Dissertation
submitted to the

combined Faculties for the Natural Sciences and for Mathematics
of the Ruperto-Carola University of Heidelberg, Germany

for the degree of
Doctor of Natural Sciences

presented by

Diplom-Physicist Christoph v. Friedeburg
born in Frankfurt/Main

Oral examination: July 23rd 2003

Derivation of Trace Gas Information

combining

Differential Optical Absorption Spectroscopy with

Radiative Transfer Modelling

Referees: Prof. Dr. Ulrich Platt

Prof. Dr. Bernd Jähne

Zusammenfassung

Ermittelung von Spurengasinformation durch Kombination der Differentiellen Optischen Absorptionsspektroskopie mit Strahlungstransportmodellierung

Die Differentielle Optische Absorptionsspektroskopie (DOAS) ist als Fernerkundungsmethode zur Messung atmosphärischer Komponenten etabliert. Zur Ermittelung quantitativer Information über Spurengasverteilungen ist eine Kombination neuer Meßtechniken, z.b. Multi-Axis DOAS, mit realitätsnaher Strahlungstransportsimulation erforderlich.
In dieser Arbeit wird das dreidimensionale sphärische Strahlungstransportmodell TRACY auf der Basis der Monte Carlo Methode zur Anwendungsreife gebracht und für die Interpretation mehrerer eigener und fremder Messungen verschiedener DOAS Plattformen angewandt. Im Gegensatz zu bisherigen analytischen Modellen sind keine Vereinfachungen der Geometrie oder der physikalischen Vorgänge erforderlich. Zusätzliche Ausgabeparameter, die sich auf Eigenschaften der Lichtstreuung beziehen, gestatten ein Verständnis der spektroskopischen Modellergebnisse und Aussagen über die Empfindlichkeit der Meßgeometrien für bestimmte Höhenprofilformen.
Speziell untersucht wurde die entscheidende Rolle der Aerosole im Strahlungstransport. Sie können Messungen derart beeinflussen, daß jedwede geometrische Näherung der Meßempfindlichkeit zu falschen Aussagen führt. Geeignete Meßgrößenkombinationen, inkl. O_4-Absorption, lassen in Verbindung mit Modellierung der entsprechenden Szenarien jedoch Rückschlüsse auf die Verteilung der Aerosole zu. Sie und Kenntnis über Quellen und Senken eines Spurenstoffes erlaubt die Projektion mehrerer Unbekannter auf wenige Meßgrößen, was eine Ermittelung quantitativer Verteilungen ermöglicht.

Abstract

Derivation of Trace Gas Information combining Differential Optical Absorption Spectroscopy with Radiative Transfer Modelling

The Differential Optical Absorption Spectroscopy (DOAS) is an established remote sensing technique for atmospheric constituent probing. To derive quantitative distribution data of trace gas distributions it is necessary to combine novel measurement techniques like Multi-Axis DOAS with realistic radiative transfer modelling. In this thesis three three-dimensional spherical Monte Carlo based radiative transfer model TRACY is brought to operational status and employed for the interpretation of several own and existing measurements with different DOAS platforms. In contrast to established models, no approximations and simplifications of geometry or physical processes are needed. Additional model output parameters describing the scattering of the light allow for the understanding of the spectroscopic model results and for conclusions on the geometrie's sensitivity to certain trace gas distribution shapes. The decisive role of the aerosols in radiative transfer was investigated. They were found to influence measurement to an extent rendering any geometric approximation of the measurement sensitivity invalid. Combination of measured quantities including O_4 absorption with modelling allow for conclusions on their abundance. They, in conjunction with knowledge on sources and sinks of the considered species, allow for the projection of unknown parameters onto measurable quantities, which facilitates the derivation of quantitative distributions.

Contents

1. Introduction

Spectroscopic measurements using the „Differential Optical Absorption Spectroscopy“ (DOAS) are a method to probe the entire atmosphere for atmospheric trace gases. Both the chemistry in the lower atmosphere can be investigated to assess the influence of anthropogeneous pollution and natural processes, as well as the trace gas abundances in the stratosphere to monitor ozone chemistry in the polar vortex.
DOAS is a remote sensing method taking advantage of the molecular absorption of light which is unique to each trace gas. After light of either natural or artificial origin has passed a distance through an absorber, the absorption is analysed and quantified to conclude on the trace gas concentration integrated over the light path. Not only one species, as in the case of most e.g. chemical in-situ instruments, but multiple species can be detected simultaneously.
Near the ground, systems using artifificial light focused onto a mirror in a fixed distance (“Long Path” instruments) allow for precise determination of both concentration and geometry.
Though, when higher atmosphere regions are to be investigated, these devices cannot be used any more. DOAS then depends on light from the sun, scattered in the atmosphere.
The sensitivity of the measurement is then governed by the effective path the photons contributing to the recorded light have taken through the atmosphere and the trace gases contained therein. I.e. if the light has traversed a given altitude layer on a geometrically very short path, the trace gas absorption, in spite of high concentration within this layer, may be lower than compared to the case of a layer within which the light has covered a very large distance.
The parameters affecting the light paths are various. The positions of the sun during the spectra recording, the sphericity of the earth and the atmosphere, horizontal variations of the trace gas concentrations, in addition to the vertical ones, liquid and solid aerosol particles in e.g. pollution plumes and clouds scattering the light in various ways as well as the attributes of the DOAS instrument’s incoupling optics must be taken into account. They also change with time, and so do the light paths. Last but not least, the trace gas concentrations to probe change themselves, e.g. due to photo-chemical reaction with increasing solar radiation amount. The measurement signal itself does not contain information on the vertical (or, more generally expressed, the spatial distribution) of the trace gases in question.
Strictly speaking, scattered light DOAS can only detect the presence of a trace gas, and under assumptions made, derive statements on the rise and decrease of the abundance. It cannot tell the concentration as a function of location.

So a necessary step to derive quantitative data is the modelling of the light path, and thus the sensitivity for layers and contained species, with a Radiative Transfer Model, RTM.
RTM there already exist several. Mostly solving analytically the radiative transfer equation, they predict radiative quantities reaching an instrument from a given direction, and which absorption strenghts they have taken up on their way. The analytical codes are capable to solve a large variety of DOAS problems with high accuracy and speed.
But there are limitations to these models. Either they are limited to two dimensions, or to plane parallel geometry, neglecting sphericity, or to e.g. only two scattering events.

Furthermore not all possible viewing geometries are supported, e.g. those used with balloon or aircraft mounted apparatus. Even the most established and tested models are limited in such ways, e.g. they calculate only the direct solar light beam propagation in full sphericity, but the scattered light in only a spherical approximation, or they cannot treat trace gas concentrations that vary with solar position. In case of multiple scattering with various phase functions, the calculations are very sophisticated and cost-intensive in order to maintain a sufficient numerical accuracy. So the codes cannot model all DOAS situations. Moreover, usually parameters which are related to the locations of the scattering events, and it is these locations separating a long and slant path through a given layer from a short one, are not contained in the model's output.

So there is a need for a RTM which is capable of dealing with all physical parameters affecting the light paths, supporting all DOAS geometries used, treating multiple scatterings with varying phase function in as high a precision as desired, and all at the same time.

An approach to achieve this goal is the Monte Carlo technique. It uses random numbers to decide on the outcome of physical processes with several possibilities, of which the relative frequency is for large numbers described by e.g. exponential laws.

A Monte Carlo RTM uses a series of random numbers to establish photon paths between a light source and the detector, and uses these paths to model a measurement. Though also slow when multiple and sophisticated scattering is taken account of, the Monte Carlo technique is a robust method applicable in theory to all measurement situations, and may be considered a necessary complement to the analytical codes to form a part of a package capable of handling all measurement situations currently used and in the future devised.

The sensitivity information, parametrized as "Air Mass Factor", AMF, is in this thesis investigated in the dependence on several parameters. Especially the behaviour with the aerosol load, playing asignificant role in the multiple scattering, is quantified. Comparisons and relations between modelled AMF and measured SCD for different geometries and for trace gases as well as the O_4 absorption is used to gauge the aerosol load to conclude on the correct absolute AMF.

The AMF, be it from an analytical code or a Monte Carlo based one, is only one part in the quantitative retrieval of trace gas data from a DOAS measurement. Two more indispensable requirements must be addressed.

The first is a sufficient quality of the spectral evaluation. High noise or systematic errors in the measured data worsen the signal beyond retrievability and reduce the sensitivity to variations in the trace gas profiles.

The second is a robust approach to solve for the equation system composed from the sensitivities, the measurements and the unknown concentrations. Standard equation system solving algorithms only work if the components of the system (except for the vector to be derived) are known. Numerical problems impose more restrictions if numbers varying within several orders of magnitude are present.

Moreover, in most cases not all relevant parameters affecting the light paths are known. In these cases the algorithm must be capable of using other measurable parameters than the mere trace gas signals, and presenting multiple solutions in case of ambiguities.

This thesis does address all three components.

The most important part is the development of a Monte Carlo RTM based upon the technique of "backward Monte Carlo", and enhanced by several features, including scattering parameters and variable geometry. Investigations with the model for a variety of DOAS geometries are performed and the behaviour of the sensitivities explained.

For measurements made within the frame of this work, numerical evaluation techniques are developed for future use.

Finally, the concluding chapter will present an algorithm to derive concentration profiles in spite of crucial input parameters being unknown.

2. The Atmosphere

The atmosphere is the primary research subject of the measurements described in this work. It contains the air we breathe, including the other gaseous species, the clouds and particles, and it modifies the solar radiation impinging on it. This chapter is designed to provide a brief overview on the atmosphere's composition and structure.

2.1 Vertical structure

2.1.1 Hydrostatic equation

The atmosphere is in first approximation a gaseous spherical layer attracted to the planet by its gravity. This leads to a pressure at sea-level altitude of

$$p_0 = 1.013\ bar = 760\ Torr = 1\ atm \tag{2.1.1}$$

This pressure results from the weight of the gas layer. At ground level, and at temperature of 25 °C there, it has density ρ_0 of $2.5*10^{19}$ molecules*cm^{-3}. According to Boyle-Mariotte's law the density is proportional with pressure, which decreases with height; increase in height by *dh* leads to a pressure decrease by:

$$dp = -\rho g dh \tag{2.1.2}$$

When eliminating ρ using the relationship $p/\rho = p_0/\rho_0$, (2.1.3) yields *p(h)* to be:

$$p(h) = p_0 e^{-g\rho_0 h / p_0} \tag{2.1.3}$$

with $p_0/(g\rho_0) = H$ "scale height", which has, for air with temperature 25 °C, a value ≈ 8.4 km.

$$H = \frac{p_0}{g\rho_0} = h_0 \approx 8.4km \tag{2.1.4}$$

This description surely is an oversimplification; e.g. the temperature varies not only with altitude, but also with solar radiation intensity. Briefly the following sections are to cover the layers of the atmosphere and the distribution of its various constituents.

2.1.2 Molecular-viscous layer and Prandtl's layer

The very lowest layer, immediately adjacent to the respective surface, is the "Molecular-viscous layer" which is governed in ist dynamica by molecular viscosity and, in case of rough

surfaces like soil or concrete, as well by horizontal pressure variations caused by obstacles. The layer thickness is some mm.
The next layer is Prandtl's layer, defined by the dominance of the friction force caused by the nearby surface over any other forces such as pressure. This layer has thickness of 50 m, strongly varying between 20 and 200 m with e.g. wind force.

2.1.3 Ekman's layer and the planetary mixing layer

From the surface through Prandtl's layer upwards, the wind changes its direction from its vector at ground level to the direction prevailing in the "free atmosphere". The tip of the vector describes a spiral called "Ekman's spiral".
In addition to this process, the warming of the earth surface and accumulating heat during daytime leads to the rising of air parcels near the ground, which again sink when cooling, which causes convection; wind-induced turbulences, e.g. in the vicinity of small mountains or river valleys, lead to turbulences which mix the gases in this part of the atmosphere and prevent the formation of homogeneous layers. For this reason this layer also is called "mixing layer". The top altitude varies between some hundreds of metres during night and about 1 km at daytime.
This layer is the most interesting one to those interested in e.g. anthropogeneously influenced chemistry, for example in urban ereas. It is this layer where nitrogen and sulphur oxydes, aromates as well as dust and soot particles are emitted into by heating and other processes involving combustion, and react with the original atmosphere components (e.g. nitrogen and oxygen) to various species such as HONO and NO_2. This chemistry is sensitive to solar radiation and thus is driven not only y the diurnal and annual cycles of human activity, but also by the diurnal and annual variation in impinging radiation intensity.

2.1.4 The troposphere

The next atmosphere regions can be defined by different categories; one is the temperature, governed by radiation. For the following see [*Roedel 1991*]. Close to the ground, the temperature is influenced by heat flux from the ground. With increasing altitude, adiabatic cooling leads to a drop in temperature. The content of water vapour also plays a role for the temperature profile; the warmer the surface, usually the highest the water vapour concentration near it. The vapour absorbs impinging solar radiation and reemits it. Close to the ground, the radiation gets reabsorbed by the vapour, but with increasing altitude and decreasing concentration, more radiation can escape into the upper atmosphere layers and ultimately into space, which results in a radiative cooling. These effects lead to a negative temperature gradient within this atmosphere region. With increasing altitude, the temperature drops in a nearly linear way by between 0.5 K and 1 K per 100 m and reaches a minimum of between –50° and –55° C at 10 – 13 km altitude in mid-latitudes and of –80° C at 18 km in the tropics. This layer of negative temperature gradient with altitude is called "troposphere". The area of minimum temperature is called "tropopause", it separates the troposphere from the atmosphere above.
In the tropics, the solar radiation is strongest, which leads to a warmer surface, a thicker water vapour layer, and in consequence to a higher location of the temperature minimum with lower temperature. This temperature profile in the troposphere leads to a convective movement, since warmer air masses from below rise while cooler one from higher above sink; this causes a constant, albeit, near the tropopause, slow mixing of the entire troposphere. The troposphere hence is linked to the chemical processes in the mixing layer; the winds in it carry reaction products to remote areas. And variuos clouds form in the troposhere, they also being

influenced by anthropogeneous pollution. The part of the troposphere above the mixing layer is called “free troposphere”, abbreviated FT.
Ths distribution and transport of the various chemical species within the mixing layer troposphere are subject of intense research using in situ and remote sensing apparatus on ground as well as on board of research aircraft.

2.1.5 The stratosphere

The stratosphere is the atmosphere region above the tropopause; it extends to an altitude of 50 km. The radiative cooling in the higher troposphere and the absorption of solar radiation in the upper stratosphere, e.g. by ozone, lead to an increase in temperature with altitude. This prevents the development of convection and causes a largely constant layer structure giving this area the name (“stratos” (greek) = layer). The temperature at each altitude can be derived from the equilibrium between absorption and emission. It rises to a maximum of a few °C at an altitude of 50 km, which is called the “stratopause”.
Below 40 km, 99% of all gases of the atmosphere are located. Among them is the ozone, situated in a layer around 25 km which absorbs a large part of the solar UV light. It is also the stratosphere, where in the polar winters the “polar vortex” is formed by stratospheric winds, encapsulating the air masses over the pol caps from the lower latitude air. Halogen compounds, of partly natural, partly anthropogeneous origin, rise up in the stratosphere and react with nitrogen to so-called “reservoir species”. In winter, though, the extreme cold leads to formation of “Polar Stratospheric Clouds” from droplets and ice particles; their surfaces host heterogeneous reactions liberating the halogen compounds from the reservoirs and making them reactive radicals which destroy, in catalytic reactions, the ozone, causing the forming of the “ozone hole”.
To understand the chemical reactions involved in this destruction as well as in the production of the educts was among the main motivations for the investigation of the stratosphere with remote sensing techniques such as DOAS, e.g. from balloons, and attempts to quantitative profile retrieval using radiative transfer modelling.
Also outside the vortex, the stratosphere is host for clouds such as high altitude cirrus clouds, composed mainly from ice particles.

2.1.6 The mesosphere, thermosphere and exosphere

The mesosphere is adjacent to the stratosphere, reaching up to 85 km altitude. Similar reasons as in case of the troposphere, i.e. a decreasing concentration with height of absorbing ozone and an increase in radiative cooling efficiency cause again a negative temperature gradient. The temperature drops to <-90 °C. Meteors from space mostly burn up in the mesosphere. The top boundary of the mesosphere is called “mesopause”.
The thermosphere extends from the mesopause to up to several hundreds of km. Absorption of high-energy radiation of the sun heats the thermosphere to temperatures of up to 1700 °C, which is the origin of this region’s name. The Aurora Borealis is generated there from high-velocity solar charged particles accelerated in the earth’s magnetic field and ionizing the molecules.
The thermosphere also houses “low earth orbits” of e.g. the U.S. “Space Shuttle” and the “International Space Station” ISS.
The exosphere finally denotes the transition between the atmosphere and the interplanetary space, extending from the top of the thermosphere to 1000 km.

2.1.7 The ionosphere and the heterosphere

In addition to the temperature and radiation, other categories can be used to characterize atmospheric regions.
The ionosphere begins at 50 km altitude (the stratopause) and reaches up even higher than the exosphere does, to 1500 km altitude. It is characterized by the occurence of electrons generated by the ionization of molecules. The electrons reflect and damp the radio signals and is highly sensitive to solar activity and the interaction of charged solar particles.
Specific sub-layers are the "D-layer" between 50 and 90 km altitude and the "E-layer" between 85 and 140 km. During the night, the additional "F-layer" contains the maxmum in electron concentration between 200 and 600 km.
The "heterosphere" denotes, as can be concluded from the name, the atmosphere regions were the molecules are no longer mixed but layered according to their weights. This is the case at altitudes higher than 100 km. Above 1000 km, only hydrogen is found.
As an illustration, Figure 2.1.1 may display on overview on the temperature profile for the atmosphere as described above.

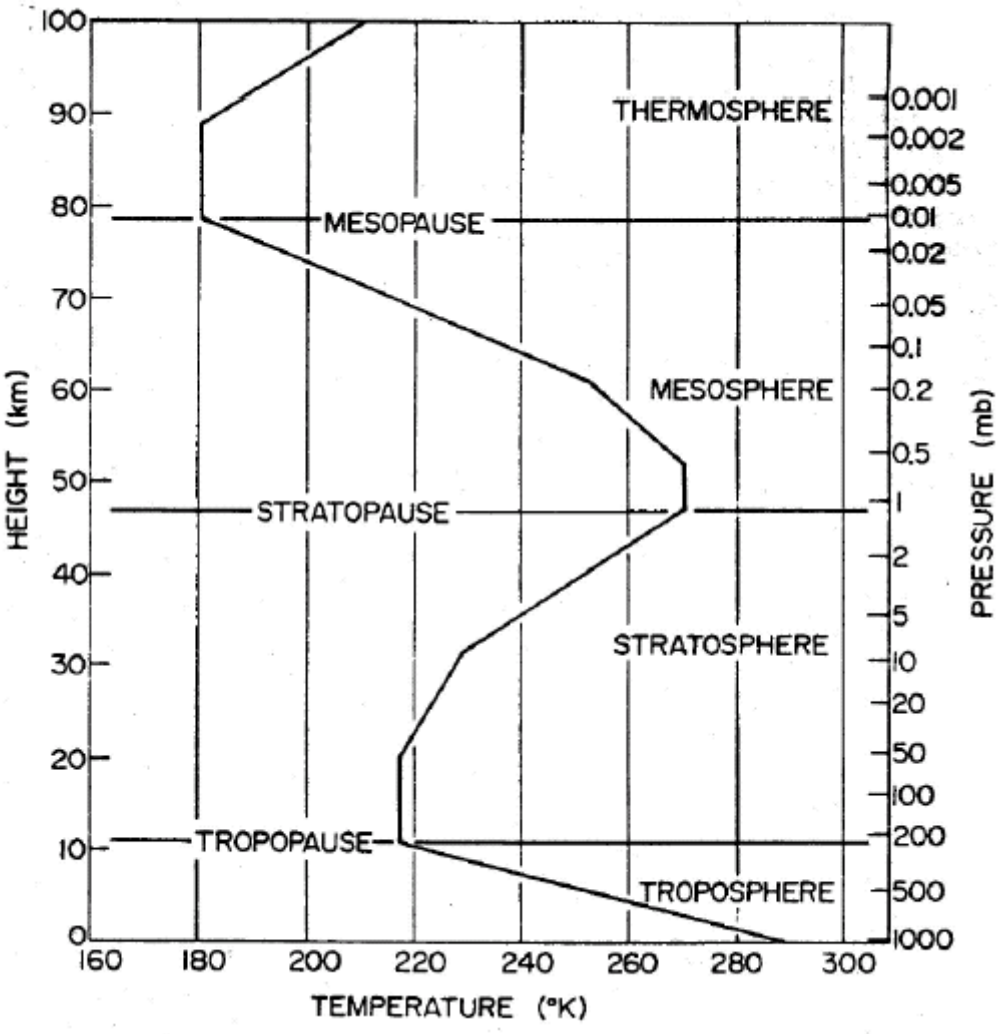

Figure 2.1.1 Vertical structure of the earth 's atmosphere. The temperature profile is an idealized one based on the US Standard Atmosphere [NOAA-S/T76-1562 1976]. The layer altitudes are governed by the temperature gradients and the sign changings of them.

2.2 Composition

2.2.1 trace gases

Table 2.1 provides data on the main permanent gaseous constituents of the atmosphere; the figures have been remaining constant during the past 10000 years. They do not reflect the importance for e.g. chemistry and radiative budget.
In addition to these permanent species gases are contained which are subject to permanent production and destruction or uptake by each other as well as by aerosols and surfaces. Their abundances can be given in concentration [cm^{-3}], which is molecule number density, in volume-%, or in "mixing ratios", which are the ratios of molecules of the considered gas per unit volume divided by the number density of the air.

Table 2.1.1 Permanent gaseous constituents of the atmosphere [*Roedel 1991*]

component	Chemical symbol	molar mass [u]	volume [%]	mass [%]
Nitrogen	N_2	28.02	78.09	75.73
Oxygen	O_2	32.00	20.95	23.14
Argon	Ar	39.94	0.93	1.28
Neon	Ne	20.18	$18.2*10^{-4}$	$10.5*10^{-4}$
Helium	He	4.003	$5.24*10^{-4}$	$0.724*10^{-4}$
Krypton	Kr	83.8	$1.14*10^{-4}$	$3.3*10^{-4}$
Xenon	Xe	131.3	$0.087*10^{-4}$	$0.39*10^{-4}$
air	-	28.97	100	100

Among them are:
- CO_2 (350 ppm[1]),
- CO (ca. 0.1 ppm),
- O_3 (0.05-5 ppm),
- Halogen species (several hundreds of ppt(parts per trillion) in the troposphere)
- nitrogen oxides (e.g. NO, NO_2) (0.01-50 ppm),
- sulphur compounds (0.1-100 ppb (parts per billion))

and many others.

The carbon compounds, especially CO_2, play a significant role as "climate gas". Produced by fossil fuel burning since the beginnings of the industrialization, the mixing ratio as listed above has been steadily increasing since the 19th century to today's value. The interactions between the CO_2 load and the biosphere as well as the ocean are subject of research since the net uptake rates are yet unknown. CO_2 can be measured with chemical in situ detection methods as well as with spectroscopy in the IR wavelength range; the new SCIAMACHY instruments can probe the atmosphere in the IR, and the efforts to retrieve CO_2 are underway.
Halogen species are crucial to the ozone chemistry and the ozone hole formation. Part of them have been emitted to a large part as chlorofluorocarbons (CFCs) by anthropogeneous action; the emission rates have been reduced by the Montreal protocol, but since these species are very stable, they persist within the atmosphere. Other sources are natural, e.g. emissions from the oceans and volcanic activity.

[1] ppm = parts per million, i.e. one molecule of the trace gas per one million air molecules;

It is beyond the scope of this chapter to give an overview on all trace gases, their sources and sinks and their photo-chemical relations. More information on specific species are given in the sections addressing their measurement with DOAS in chapters 9 and following.

2.2.2 Aerosols and clouds

Aerosols are a general term to describe solid or liquid particles floating in the atmosphere. The liquid particles are droplets, consisting of mainly water, as in troposheric clouds or fog, or acid. Solid ones are e.g. dust and soot particles. The particle distributions are usually given in either mass per volume or number density, see e.g. [*Roedel 1991*]. In continental air the values in latter unity range between 10^3 cm^{-3} for clean to 10^5 cm^{-3} for extremely polluted environments, for clean maritime air 10^{-2} cm^{-3} – 10^{-3} cm^{-3} are found. The number density drops off rapidly with altitude, to just a few hundreds of particles per cm^3 above 5 km. The mass concentrations are between 30 and 150 $\mu g m^{-3}$ over continents. Figure 2.2.1 shows the range of number density distributions with altitude measured by various authors.

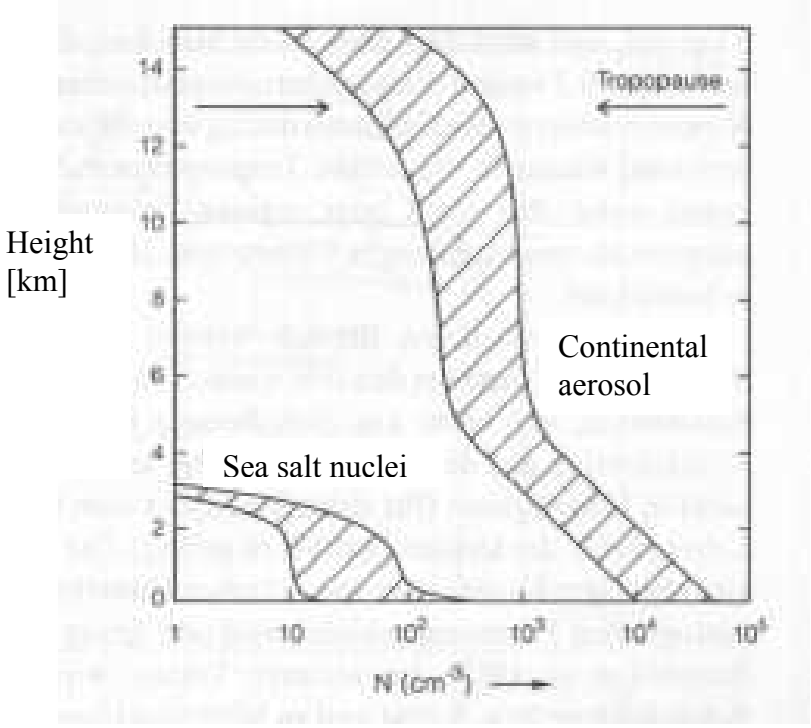

Figure 2.2.1 Tropospheric aerosol profiles in number density, taken from [Roedel 1991]

The aerosol size distributions and the chemical composition of the particles are determined by the geographic location of emission sources, type of emission, and transport, transformation and removal processes. Aerosol particles typically are of dimension 10 nm – 10 μm. The size spectra are often described in terms

$$n^*(r) = \frac{dN(r)}{d\,log(r^*)} \qquad r^* = r/r_0,\ r_0 \text{ unity distance} \qquad (2.2.1)$$

Apart from freshly generated aerosols or particles produced by singular events, e.g. volcanic eruptions, i.e. when considering aged aerosols and of sizes greater than about 0.1 μm these size spectra often can be approximated by $n^*(r) = r^{-s}$ with $s \approx 3.5 \pm 1$. These distributions are called Junge-distributions after Christian E. Junge. Different expressions of the size spectra are by volume V and mass m, i.e. $dV/dlog(r^*)$ and $dm/dlog(r^*)$, respectively. Often there are, even for a given type of aerosol, see below, multiple local maxima, named modes, of these

size distributions, which then are called e.g. bi-modal distribution in case of two modes. They can be attributed to production process and age of the respective particles.
Two primary production mechanisms generate new particles: The one is the nucleation out of the gas phase of vapours produced from chemical reactions, the so-called homogeneous nucleation. The second is the transfer of already existing particles on the ground, e.g. dust or droplets, into the atmosphere by the wind. Already floating solid particles can serve as nuclei for heterogeneous nucleation of gases.
For the following see [*Stamnes 2002*] [2] and references therein, as well as the concise overview in [*Sanghavi 2003*]. Main tropospheric aerosol types can be distinguished using various categories. The aerosol measurement and retrieval algorithm of the space based OMI instrument [e.g. *Stamnes 2002*] uses five main types according to their production processes:

- urban-industrial aerosols originates from fossil fuel combustion; the size of the particles depends on relative humidity, the absorption properties on the soot content, which is highly variable. An example is H_2SO_4, itself generated from the oxidation of SO_2, into the liquid phase by homogeneous nucleation.
- carbonaceous aerosols, generated from natural and anthropogenic combustion processes and biomass burning.
- desert dust aerosols, injected into the atmosphere by the wind, can be transported in elevated layers over several thousands of kilometers naturally produced oceanic aerosols; in clean marine environments, the aerosols consists mainly of sea salt. In the coastal regions, continental aerosols can be mixed in.
- volcanic aerosol transferred into the atmosphere in eruptions; the main component is sulfuric acid; the layer height and size distribution are highly variable and depend e.g. on strength of the eruption blast, altitude of the volcano and prevailing winds.
- oceanic or sea salt aerosol, generated e.g. from the skin of bursting bubbles and ejected into the atmosphere.

This list is not complete. Also classifiable as aerosols are ice particles forming the “Polar Stratospheric Clouds” (PSC) which play a crucial role in wintertime ozone depletion. See chapter 11, section 11.1 for details. Each aerosol type consists of sub-types according to their optical properties; these are governed by parameters such as size, reflectivity (which e.g. for soot is low) and refractive index of the liquid governing light transmission and reflection through/off such a particle. Table 2.2.1 lists aerosol classifications and properties, i.e. radius of two modes, fraction of the second mode, and refractive index.
In the light of these classes, table 2.2.2 lists the background aerosol distribution for three latitudinal zones. In general, the tropospheric aerosol load of an atmospheric column at a given location consists of a background aerosol component of local origin residing in the lowest 2 km of the atmosphere. In addition, an elevated layer of carbonaceous or mineral aerosols is often present. These free-troposphere aerosol layers result from the long-range transport of material from distant biomass burning and desert dust sources. The seasonal cycle of agriculture related biomass burning and dust lifting in the major deserts of the world is generally well known, the long-range transport is determined by prevailing meteorological conditions. At slightly above the tropopause altitude (ca. 20 km) an aerosol layer resides formed from gaseous sulphur compounds rising up from the troposphere, the “Junge layer”. It consists mostly of sulphur acid droplets of radii between 0.1 and 1 μm.
Source are e.g. carbonyle sulfide, emitted from oceans, and CS_2 from biogene decomposition processes.

[2] http://eospso.gsfc.nasa.gov/eos_homepage/for_scientists/atbd/docs/OMI/ATBD-OMI-03.pdf

Table 2.2.1 (taken from [*Stamnes 2002*])

Aerosol size distribution and refractive index for the selected OMI aerosol models. Several of the five major types are divided into sub-types according to amount of absorption or the vertical, log-normal distribution. These sub-types can contain a number of aerosol models that differ in particle size distribution and/or refractive index. The industrial and biomass types have a bi-modal distribution. The mean particle radius and its standard deviation are given separately for both modes. Aerosol number concentration is normalized to unity. The relative contribution of the second mode to the number concentration is represented by the fraction m2.

Type	Sub-type	Model	Mean Radius (μm)		Standard Deviation (μm)		Fraction of m2	Ref. index
			m1	m2	m1	m2		
Industrial	IS	IS1	0.078	0.497	1.499	2.160	$4.36\ 10^{-4}$	1.4
		IS2	0.088	0.509	1.499	2.160	$4.04\ 10^{-4}$	1.4
		IS3	0.137	0.567	1.499	2.160	$8.10\ 10^{-4}$	1.4
	IA	IA1	0.085	0.641	1.560	2.004	$7.00\ 10^{-4}$	1.45
		IA2	0.090	0.676	1.560	2.004	$6.84\ 10^{-4}$	1.45
		IA3	0.109	0.804	1.560	2.004	$6.95\ 10^{-4}$	1.45
Biomass	BL	BL1	0.074	0.511	1.537	2.203	$1.70\ 10^{-4}$	1.5
		BL2	0.087	0.567	1.537	2.203	$2.06\ 10^{-4}$	1.5
		BL3	0.124	0.719	1.537	2.203	$2.94\ 10^{-4}$	1.5
	BH	BH1	0.076	0.665	1.492	2.075	$2.07\ 10^{-4}$	1.5
		BH2	0.080	0.705	1.492	2.075	$2.05\ 10^{-4}$	1.5
		BH3	0.097	0.866	1.492	2.075	$1.99\ 10^{-4}$	1.5
Desert Dust	DL	DL3KS	0.052	0.67	1.697	1.806	$4.35\ 10^{-3}$	1.53
		DL5KS	0.052	0.67	1.697	1.806	$4.35\ 10^{-3}$	1.53
		DL3KN	0.052	0.67	1.697	1.806	$4.35\ 10^{-3}$	1.53
		DL5KN	0.052	0.67	1.697	1.806	$4.35\ 10^{-3}$	1.53
	DH	DL3KS	0.052	0.67	1.697	1.806	$4.35\ 10^{-3}$	1.53
		DL5KS	0.052	0.67	1.697	1.806	$4.35\ 10^{-3}$	1.53
		DL3KN	0.052	0.67	1.697	1.806	$4.35\ 10^{-3}$	1.53
		DL5KN	0.052	0.67	1.697	1.806	$4.35\ 10^{-3}$	1.53
Oceanic	MS	MS	0.030	0.240	2.030	2.030	$1.55\ 10^{-4}$	1.4
	MA	MA	0.030	0.240	2.030	2.030	$1.55\ 10^{-4}$	
	MC	MC	0.030	0.240	2.030	2.030	$1.53\ 10^{-2}$	1.4
Volcanic[b]	V	V	0.230	-	0.800	-	-	1.45

[a] Wavelength-dependent with (H)igh or (L)ow absorbance and (S)pherical or (N)on spherical particles.
[b] Only used in case of eruptions

Table 2.2.2 Geographical distribution of background aerosol sub-types (taken from [*Stamnes 2002*])

Latitude zone	Land	Ocean
30°N 90°N	IS	MS,MC,IS
30°S 30°N	IA	MA,MC,IA
90°S 30°S	IS	MS,MC

Clouds are formed from either water droplets condensating from the water vapour in the air, or from ice particles such as in case of the PSC. The water clouds can be distinguished by the number density of droplets, the radii of those droplets as well as the content of liquid water contained within these clouds. A classification is done e.g. in the scheme by [*Stephens 1978*]. The altitude distributions of these cloud types are listed in Table 2.2.4.

Table 2.2.3 cloud type classification scheme [Stephens 1978]

Cloud type	Number of drops [cm^{-3}]	liquid water content [gm^{-3}]	Mode radius corresponding to maximum number of droplets [µm]
Stratus I (St I)	440	0.22	3.5
Stratus II (St II)	120	0.05	2.25
Stratocumulus I (Sc I)	350	0.14	3.5
Stratocumulus II (Sc II)	150	0.47	7.5
Nimbostratus (Ns)	280	0.50	3.5
Altostratus (As)	430	0.28	4.5
Fair weather cumulus (Cu)	300	1.00	5.5
Cumulonimbus (Cb)	72	2.50	5.5-6.5

Table 2.2.4 altitude ranges occupied by the cloud types listed [Stephens 1978]

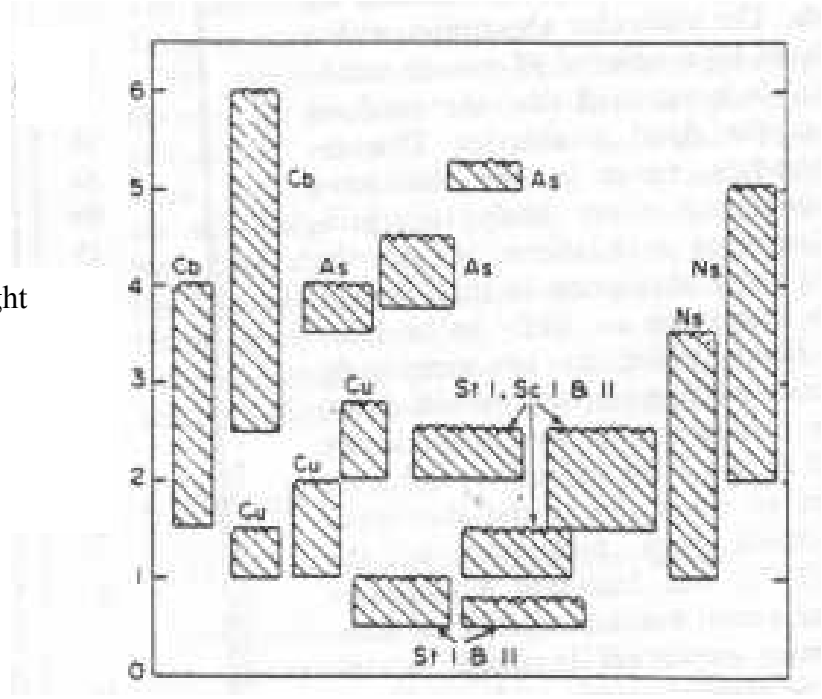

These clouds influence the retrieval of trace gases by reflection of the impinging solar light, which leads to shielding of trace gas concentrations below.
Due to multiple scattering of photons within clouds, the absorption by interstitious gases can be strongly enhanced, e.g. by molecular oxygen and O_4. The latter is a dimer of two oxygen atoms, with a concentration which is proportional to the squared molecular oxygen concentration, i.e. exponentially decreasing with altitude with a scale height half that of the air. This profile is largely independent from other trace gases. For this reason O_4 absorption provides a tool for investigation of clouds and their altitudes in remote sensing. Other attributes are the white colour and high albedo. See chapters 9 and 12 for an application.

3. Differential Optical Absorption Spectroscopy

The „Differential Optical Absorption Spectroscopy“ (DOAS) was invented at the end of the seventies as a remote sensing technique for the detection of atmospheric trace gases [*Platt et al. 1979, Platt et al. 1980*]. The theory is explained and derived in detail in [*Platt 1994*, *Stutz und Platt 1996*]. DOAS determines the integrated concentration of the trace gas in question along the light path by means of its optical absorption. For this a light source and a detector system are necessary. The latter records and spectrally decomposes the light emitted from the source that has reached the detector. The trace gases present along the light path absorb the light at wavelengths unique to the respective molecular structure. From the strength of the absorption conclusions can be drawn about the trace species's concentrations. This remote sensing technique allows for the measurement in areas which are only with great difficulty accessible to in situ devices, such as the free troposphere, or of trace gases which cannot be detected with handy in situ techniques, such as radicals like OH and NO_3. High-power lamps can serve as light sources, but for the applications to be investigated in this thesis the sun is used as source; this may happen directly or using the solar light reflected off the moon. But the most common solar light DOAS application involves the use of light scattered in the atmosphere.
So far, out of the electromagnetical spectrum mostly the wavelength between 240 and 400 nm (ultraviolet, UV) and between 400 and 790 nm (400 – 700 nm represents the visible light receptable by the human eye, VIS, see Figure. 3.1) are used. The new SCIAMACHY[1] instrument on board of ENVISAT[2] extends the range to 2380 nm in the infrared (IR). Figure 3.2 presents an overview on all trace species measurable by SCIAMACY and its predecessor instrument, GOME[3].
A range of measurement geometries for scattered light are employed defined by the direction the instruments (see below) are "looking" into. They are:

- Zenith-sky, looking straight into the zenith from a ground based station or from an aircraft
- Nadir, looking downward parallel to the surface normal from a satellite, balloon or aircraft
- Off-axis, looking neither in Zenith-sky nor in Nadir (nor in direct light) geometry, but from an angle "off" these thus defined "axes"
- Limb, looking,usually from a satellite, balloon or aircraft, slightly above or below the horizon
- Multi-Axis ("MAX"), looking into multiple directions sequentially or simultaneously

Other designations (e.g. "DAX" for Dual-axis) denote combinations of the geometries listed above.

[1] (Scanning Imaging Absorption Spectrometer for Atmospheric CHartographY)
[2] ENVIronment SATellite
[3] Global Ozone Monitoring Experiment

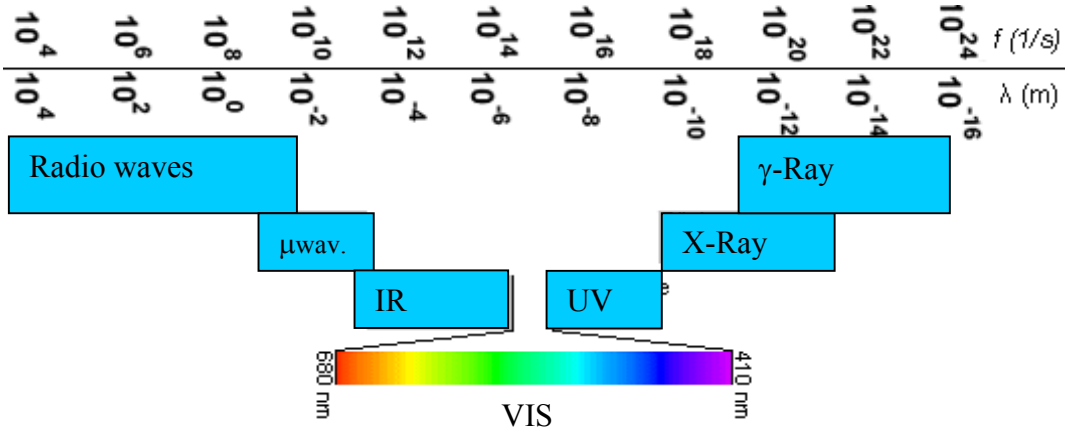

Figure 3.1 Electro-magnetic spectrum; so far DOAS uses VIS, UV and most recently IR.

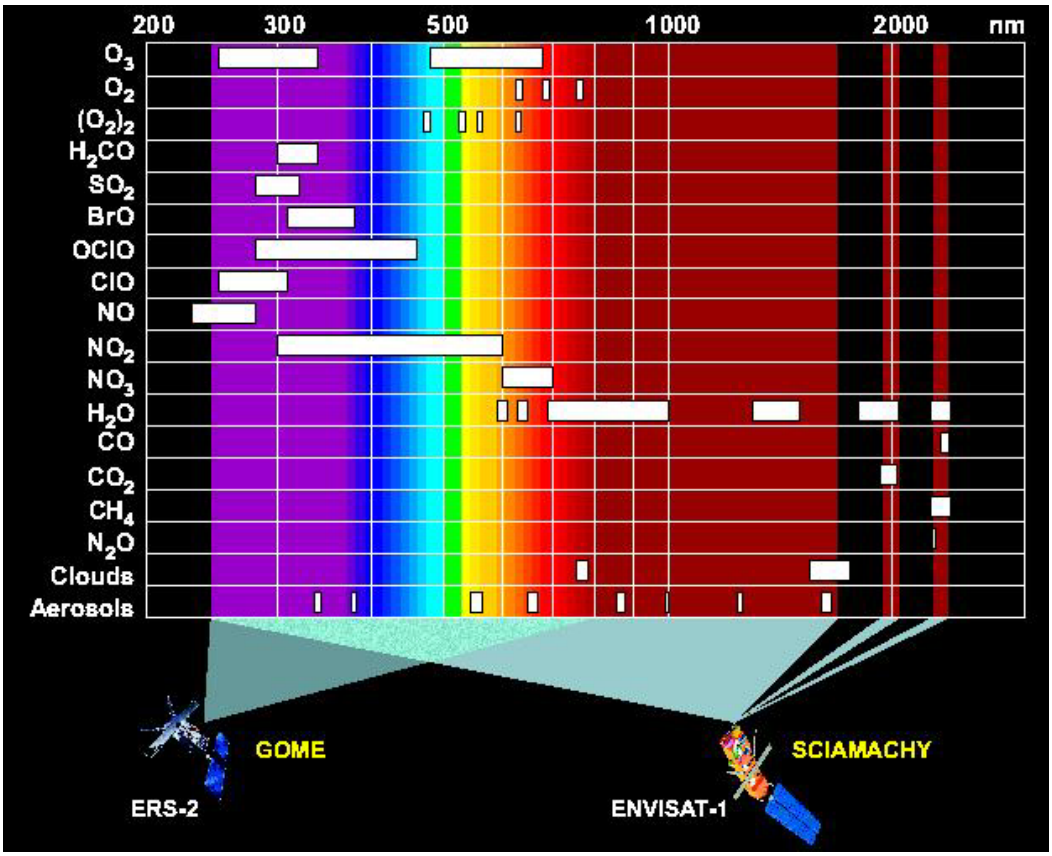

Figure 3.2 Wavelength ranges of GOME and SCIAMACHY satellite DOAS instruments and absorption windows of trace gases detectable with DOAS [IUP Bremen homepage[4]]

[4] http://www.iup.physik.uni-bremen.de/sciamachy/index.html

3.1 Principle

A DOAS detector device consists of a spectrograph with incoupling optics and a detector unit. The incoupling optics, in most cases a telescope, is aimed into a given direction out of which it collects the light scattered into it; the light is usually transferred into the entrance slit of a spectrograph by use of one or multiple quartz fibres. For more details on such an instrument refer to instrumental sections 8.1 and 9.1.2, 9.2.2, 10.1, 11.2, 12.1 of this work[5]. The spectrograph's grating is adjusted to decompose light of wavelengths within a given interval $[\lambda_a, \lambda_b]$ The light is imaged as a line or rectangle along the "dispersion axis" X with the wavelength of the light changing from λ_a to λ_b from one end to the other. This image, the actual spectrum, is recorded with a detecting device and analysed for trace gas absorptions. The absorption at one specific λ is described with Lambert-Beer's law:

$$I(\lambda) = I_0(\lambda)e^{-\sigma S} = I_0(\lambda)e^{-\tau(\lambda)} \tag{3.1.1}$$

I_0 denotes the intensity of a light beam prior to covering of an absorbing distance, I the remaining intensity after this distance, σ the wavelength-dependent absorption cross section of the absorber in units cm² and S the "Slant Column Density" (SCD) in cm^{-2}. The product of S and σ is τ, the optical density, also abbreviated OD, and like σ wavelength-dependent. S represents the concentration c integrated over the light path L:

$$S = \int_0^L c(l)\,dl \tag{3.1.2}$$

While the SCD S is defined along the slant path covered by the light used in the (real or simulated) measurement, the Vertical Column Density VCD V is defined along a light path which is parallel to the local surface normal and reaches either from the instrument's location up into the zenith or from a space borne sensor down to the earth's surface.
If we consider not continuous intensity values but photons, then τ describes the probability of a photon corresponding to wavelength λ covering the considered distance without getting absorbed. With $\tau = 1$ only the fraction e^{-1} of N originally emitted photons of a collimated light beam reaches the end of the distance. From (3.1.1) τ is derived as the natural logarithm of the ratio I_0/I :

$$\tau(\lambda) = \ln\left(\frac{I_0(\lambda)}{I(\lambda)}\right) \tag{3.1.3}$$

With more than one absorber present, the optical densities add, which implies that they can considered independently from each other. Each absorber i adds to the total absorption with its σ_i for photons corresponding to the wavelength λ considered. It must be noted here that that σ_i can also depend on temperature T, hence altitude of the trace gas. τ can be expressed as:

$$\tau(\lambda) = \sum_i \tau_i(\lambda) = \sum_i \sigma_i(\lambda, T)S_i \tag{3.1.4}$$

In addition to molecular absorption scattering processes reduce the direct beam intensity; these are scatterings off molecules like the elastic Rayleigh scattering or the inelastic Raman scattering as well as the Mie scattering off aerosol particles such as cloud or fog droplets. The spectral characteristica relevant to direct beam attenuation are expressed using the extinction coefficients κ_{Rayl} and $\kappa_{Mie.}$ They are defined through:

[5] In the chapters to follow, the DOAS device may be briefly named "detector" or "instrument".

$$dI = I\kappa dl \tag{3.1.5}$$

Since the aerosol droplets in general are of size similar or lager than the photon`s wavelength, the extinction coefficients display wavelength dependences which are much weaker ("broad-banded") than those of molecular absorption cross sections, which are typically "narrow-banded":

$$\kappa_{Rayl} \propto \frac{1}{\lambda^4} \qquad \kappa_{Mie} \propto \frac{1}{\lambda^n} \qquad \text{n=1..4}^6 \tag{3.1.6,7}$$

The Rayleigh and Mie scattering are explained in more detail in the following chapter. Be they treated here only as far as the DOAS principal theory is concerned.
In addition to the absorption and scattering processes apparatus-related effects affect the measurement. Among these are e.g. wavelength-dependent detection efficiency of the detector element, and losses and straylight due to reflection within the instrument; they also are in general broad-banded. An exception is the "Etalon"-effect resulting from reflection interferences within e.g. a protecting quartz cover of the detector element. If we comprise these apparatus-effects with the symbol $I_{app}(\lambda)$ we can express $I(\lambda)$ with:

$$I(\lambda) = I_0(\lambda) \bullet \exp\left[\sum_{i=0}^{m} \sigma_i(\lambda) c_i l\right] \bullet \exp\left[\kappa_{Rayl}(\lambda) l + \kappa_{Mie}(\lambda) l\right] + I_{app}(\lambda) \tag{3.1.8}$$

DOAS separates the extinctions into the broad-band ones $\sigma_i^{broad}(\lambda)$ and the narrow-band $\sigma_i^d(\lambda)$; the latter constitute the "differential" cross sections of the gaseous absorbers numbered with i. They are usually derived by dividing (3.1.8) by I_0, and applying an appropriate high-pass filter H to the logarithm of the right-hand-side. This filtering suppresses $\sigma_i^{broad}(\lambda)$ without significant $\sigma_i^d(\lambda)$ reduction. In theory:

$$\sigma_i^d(\lambda) = H(\sigma_i(\lambda)) \tag{3.1.9}$$

This H operator also changes the optical density to the differential optical density $\tau^d(\lambda)$:

$$\tau^d(\lambda) = \sum_i \tau_i^d(\lambda) = \sum_i \sigma_i^d(\lambda) S_i \tag{3.1.10}$$

and accordingly (from 3.1.4):

$$\tau^d(\lambda) = H\left[\ln\left(\frac{I_0(\lambda)}{I(\lambda)}\right)\right] \tag{3.1.11}$$

Figure 3.1.1 illustrates the relationships between intensities I, I_0 and the differential optical density τ_d. I_0' denotes I_0 with subtracted broad-band extinctions. In the logarithm of I_0' the narrow-band absorption structures appear as ditches. The high pass filtering interpolates $ln(I_0'(\lambda))$ in the interval $[\lambda_1, \lambda_2]$.
Finally by division by σ_i' the S_i, the Slant Column Densities of the trace gases are obtained. Their measurement is the goal of the Differential Optical Absorption Spectroscopy.

[6] n depends on the particle size distribution

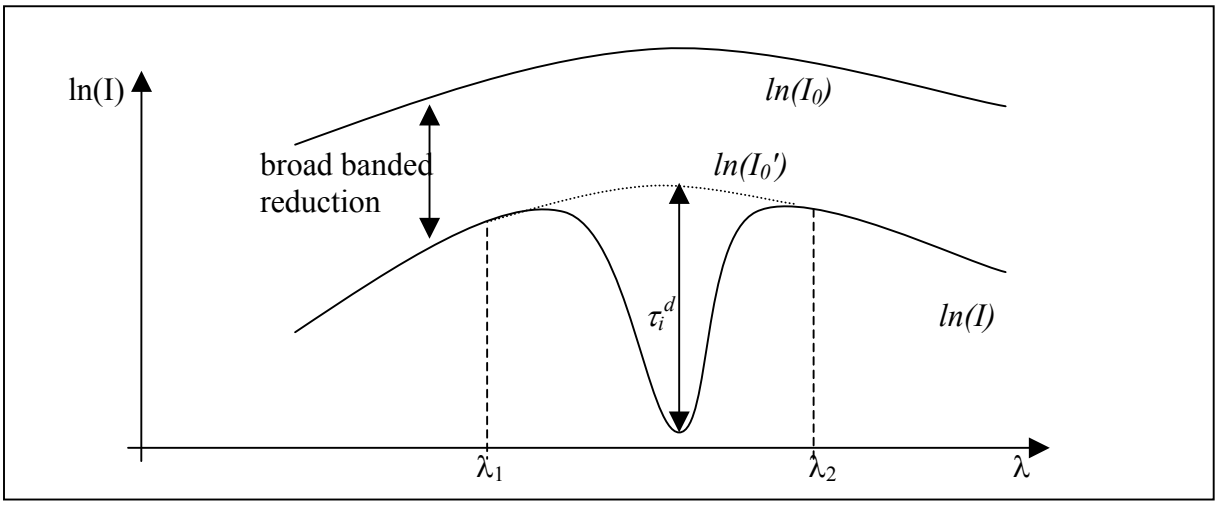

Figure 3.1.1 relations between the logarithms of the intensities and τ_i^d; τ_i^d is derived by interpolation between λ_1 und λ_2 in the funktion ln(I(λ))

3.2 Apparatus-related influences

3.2.1 Convolution with the Instrument Function

In practice, as briefly outlined above, the recording, storing and evaluation of the spectrum *I(λ)* are subject to several more effects complicating the formulae in the previous section. First of all the light source does possess spectral characteristics which e.g. depend on the emission lines of the gas filling. They can be mathematically described as own broad- and narrow- banded features which add themselves to the absorption structures.
From the limited resolution of an optical system results a change of the spectrum which e.g. involves the broadening of recorded emission lines. This alteration is described by convolution of *I(λ)* with the Slit Function *T(λ)*, also named Instrument Function. *T(λ)* depends e.g. on the entrance slit width, the refractive gratings, mirrors and other components of the spectrograph. The resulting spectrum is *I*(λ)*.

$$I^*(\lambda) = I(\lambda) * T(\lambda) \tag{3.2.1}$$

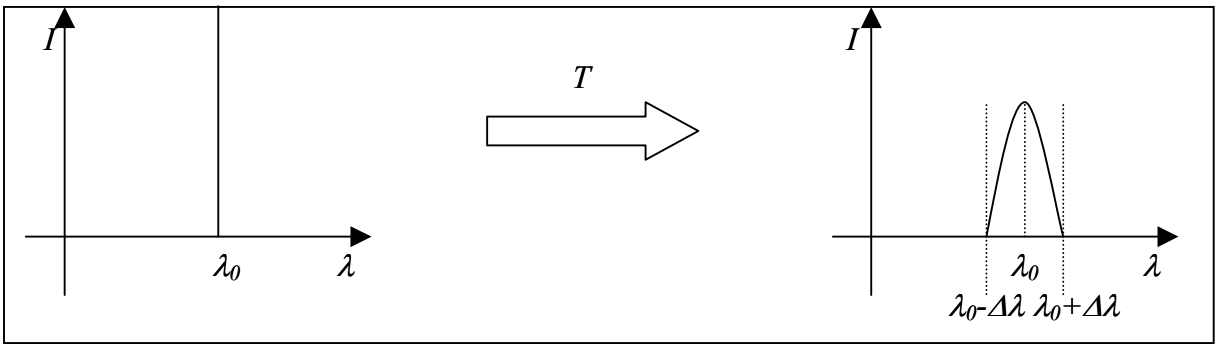

Figure 3.2.1 The effect of the Slit Function S on emission or absorption lines; a line of assumed zero spectral extension at λ_0 gets broadened, so also at $\lambda_0 \pm \Delta\lambda$ a significant signal is recorded.

$T(\lambda)$ is defined as the apparatus' response to a signal const*$\delta(\lambda)$[7], i.e. in our case a line without any extension along the spectral axis, which is broadened into a gaussian shape with an intensity > 0 within the intervals $[\lambda \pm \Delta\lambda]$. E.g. the optically very dense, but narrow-banded water vapour absorption lines are mapped to broader peaks with lower optical density at the line centre as compared to the original line. A standard method to derive $S(\lambda)$ is the recording of atomic lines, which usually, i.e. with the light sources commonly used, display a FWHM (Full Width at Half Maximum) of only 10^{-3} nm, a value smaller by two orders of magnitude than the resolution of commonly used DOAS spectrographs and thus not significantly affecting the derivation of $T(\lambda)$ from the recorded lines. Their FWHM is used as the spectrograph's spectral resolution. Spectra of higher resolution than this can be convolved with the derived $T(\lambda)$; their features then have the broadness they would have if the spectrum was measured with the spectrograph considered.

3.2.2 Discretization

The recording and storage of $I^*(\lambda)$ is performed in discretization. The detecting unit is attached, e.g. bolted, to the spectrograph and in DOAS applications consists of an array of m photo diodes or CCD elements, "pixels", which in the following are numbered by j. They are aligned along the dispersion axis X. Each of them receives the intensity $I(j)$ which is the intensity integrated over λ' within an interval $[\lambda(j), \lambda(j) + \Delta\lambda(j)] \in [\lambda_a, \lambda_b]$ see Fig. 3.2.2.

$$I(j) = \int_{\lambda(j)}^{\lambda(j+1)} I^*(\lambda')\, d\lambda' \tag{3.2.2}$$

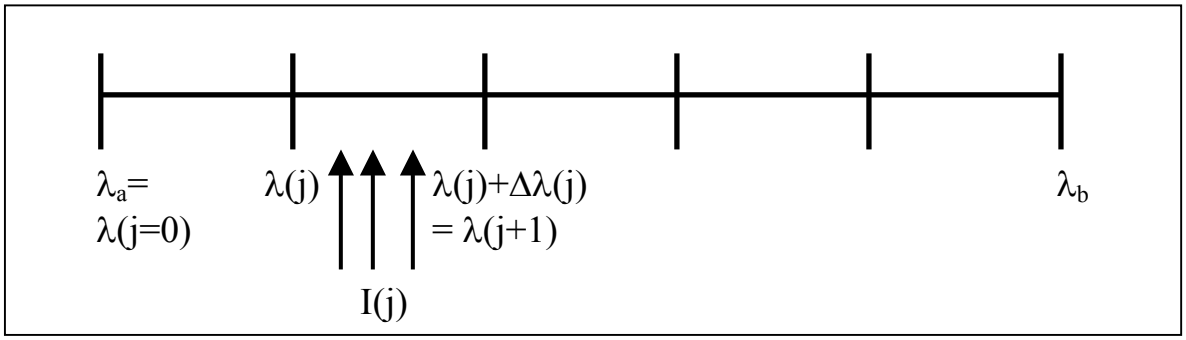

Figure 3.2.2 Overview on the discretization of the wavelength and the recorded intensity

The mapping of the pixel number $j=1,..,m$ to the intervals $[\lambda, \lambda+d\lambda]$ is governed by the "dispersion relation" Γ of the system; it can be expressed by:

$$\Gamma : \lambda(j) = \lambda(0) + \sum_{n=1}^{m} A_n \cdot j^n \tag{3.2.3}$$

with A_n the coefficients of a polynomial and j the pixel numbers. In practice Γ depends on the spectral range $[\lambda_a, \lambda_b]$, and the number and extension along L of the illuminated pixels. A typical value for a pixel interval is about 0.1 nm per pixel. Γ may be modified by e.g. changes in temperature or pressure, which can cause contractions or deformations of optical and mechanical components or a change in the air's refractive index. Countermeasures employed

[7] $\delta(\lambda)$ = "Delta function"

are the use of insulation and thermostat devices to keep the spectrograph at a constant temperature as well as flooding its airtight housing with e.g. nitrogen at constant pressure.
A measurement is the exposure of the detecting unit to the output light of the spectrograph, realized e.g. by the opening of a shutter located in the system's optical axis, for a time interval Δt. During this time, the photons which are part of any $I(j)$ excite electrons; e.g. in a CCD element electrons are excited to occupy a higher state within the band structure of the semiconductor material, where they are kept within an externally created electrical potential well. In good approximation the number of photon-excited electrons (in the following named "photo-electrons") which gather within a pixel potential well during Δt is linear in $I(j)$. So is the potential created by these electrons which is measured in the "read-out" process, digitized, sent to a computer and stored as measurement value of $I(j)$. The logarithm of $I(j)$ is expressed as:

$$\Im(j) = \ln I(j) = \ln I_o(j) - \sum_{i=0}^{m} \sigma_i(j) c_i L - (\varepsilon_{Rayl}(j) + \varepsilon_{Mie}(j) + \varepsilon_{app}(j)) + N(j) \qquad (3.2.4)$$

with $\sigma_i(j)$ as broad- or narrow-banded trace gas absorption cross sections, c_i the respective trace gas concentrations integrated over the light path L. $N(j)$ denotes the noise which consists of the noise of $I(j)$ itself (resulting from the photon noise) and the noise of the detector "background" signal, resulting e.g. from dark current electrons excited not by light, but by their own thermal energy. In Eq. (3.2.4) this background is omitted, since it is an additive term to $I(j)$, which is easily obtained from a measurement without light and, once obtained, subtracted. We now have a sum of terms, partly related to broad band effects, partly to the trace gas absorptions. The latter terms are the ones to derive.

3.3 Numerical evaluation

To solve for Eq. (3.2.4) and obtain $S_i = c_i l$ as well as their error, we first must subtract the background from $I(j)$ as already mentioned above. The high-pass filter must be applied. A numerical smoothing filter reduces the noise. This filter e.g. works by replacing each $I(j)$ by an algebraic function of $I(j \pm k)$, k e.g. = 1 or higher. This filter is essentially a low-pass filter. Its parameters must be selected carefully to only reduce the noise without significantly affecting the $\sigma_i^d(\lambda)$ (the differential cross sections, see Eq. (3.1.9)): the smoothing method can lead to a reduction of low $\sigma_i^d(\lambda)$ beyond detectability in the fitting. After this $I(j)$ can be logarithmised, and the process of numerical reconstruction of $\Im(j)$ can commenced. The following routine was developed by [*Stutz und Platt 1996*]. $\Im(j)$ is iteratively approximated (= fitted) by a function $\Re(j)$ defined by:

$$\Re(j) = P_r(j) + \sum_{i=1}^{k} a_i \cdot s_i(d_{i,0}, d_{i,1}, \ldots)(j) \qquad (3.3.1)$$

with s_i as absorption features of trace gases i, mapped to the pixel j of the detector with the parameters $d_{i,n}$, which themselves are governed by Γ. The parameters a_i are the representations of the Slant Column Densities S_i. P_r is a polynomial used to reproduce the broad-band features of $\ln(I(j))$; their reproduction removes them out of the sum term in Eq. (3.3.1) and thus serves as high-pass filter.

$$P_r(j) = \sum_{h=0}^{r} b_h \cdot j^h \qquad (3.3.2)$$

The degree r of the polynomial also is adjusted, its coefficients b_h belonging to the unknown variables in Eq. (3.3.2).

3.3.1 Reference spectra

The terms a_i must be derived from the fitting, since they are in theory proportional to the desired Slant Optical Densities for the wavelength corresponding to a given j. The $s_i(j)$ are the input data to the procedure, they are called the reference spectra. For many trace gases investigated with DOAS, the reference spectra can be measured. A cuvette is filled with synthesized trace gas. With a light source of well known spectrum and a detector setup a convolved and discretizised mapping of $\sigma(\lambda)$ can be measured for this specific trace gas. In the ideal case the detector system used for this is the same as the "original" one to be used in the field measurement. If this is not the case, $\sigma(\lambda)$ is convolved with a different instrument function $U(\lambda)$ and discretizised with a different Γ' onto channels $j' = 1,2,...$ of a spectrum $\sigma(j')$.
Usually $\sigma(j')$ is available as file which also contains data on Γ' and/or a table $j' \rightarrow \lambda$ enthält. This also constitutes a source of error. For many trace gases, such as gaseous H_2O, so far no high resolution spectra do exist. In these cases the absorption lines are calculated using models taking into account the molecular energy states. But if e.g. the change of the optical density of a line with temperature or pressure is not precisely known, the considered lines are approximated with default values or even left out. The necessary discretization of the modelling as well as roundings generate more errors. Thus it is recommended to use only reference spectra with as high a resolution as possible to obtain. It should be high compared to the spectrograph's. The higher the resolution of $\sigma(j')$, the closer are the $\Gamma(\sigma(j'))$ to spectra recorded with the original detector, and the better they can be used in Eq. (3.3.1) But even high resolution spectra still bear their Γ', which is not negated by the convolution with Γ. This implies that the convolved reference never is identical to a reference measured with the original instrument. An example are the Fraunhofer spectra recorded from the Kitt Peak mountain observatory [*Kurucz et al. 1984*], which regularly generate problems, especially when using them in the evaluation of spectra recorded at ground level. The extremely high optical densities of single Fraunhofer lines causes the convolution to be imperfect. In addition, the measured spectra are affected by the "Ring effect" (see below) due to multiple scattering which does not occur in comparable strength at mountain altitudes.
In these cases it is advisable to use a measured spectrum which contains, for e.g. photochemical reasons, significantly less absorption of the trace gas investigated, but displays similar Fraunhofer and e.g. water vapour absorptions, affected by the same environmental variables as the spectra to evaluate. Subtraction of this logarithmized "internal" reference spectrum effectively removes the absorptions present in both spectra and leaves "behind" the trace gas absorption searched for. An example is the use of a spectrum recorded in bright daylight to correct for the Fraunhofer structures in spectra recorded during sunrise to search for nitrate radical. The nitrate radical is photolysed rapidly by direct sunlight. Should theory expect any absorption to remain in the internal reference spectrum, it must taken account of in the later examination of the Slant Column Densities.
The reference spectra must not necessarily contain absorption features. They also can represent any effects on the measured spectra which vary with e.g. solar elevation and are not known in their magnitude. One example is the Ring effect [*Grainger et al. 1962, Bussemer 1993*]. This effect occurs due to multiple scattering, e.g. when measuring at ground level, and is caused by inelastic rotational-Raman scattering. Photons may be absorbed by molecules, excite them to higher or lower energy states, and get re-emitted with lower or higher energy, i.e. higher or lower wavelength. When considering a strong absorption line, it is easy to find

that a greater absolute number of line wing photons will change their wavelength to the line centre wavelength than vice versa. This leads to a reduction in optical density. The effect can be reproduced in so-called "Ring-spectra" calculated from e.g. the measured spectrum [*Bussemer 1993*].
Another effect is caused by the solar "Centre-to-Limb-Darkening", abbreviated CLD. The solar radiation originating from the solar disk centre is effectively emitted from a higher depth, with higher temperature, than ist counterpart from locations nearer to the solar rim (or limb). The intensity at wavelengths at the wings of Fraunhofer absorption lines decreases from the centre to the limb, while the intensity in the line centres is in approximation equally low regardless of the point of origin on the disk. This results in a decrease in optical density of the Fraunhofer lines from the centre to the rim. Under certain circumstances, e.g. when observing direct light from a balloon in limb geometry when the sun is partly covered by the horizon, the recorded light origins to a greater percentage from the rim than is the case if the entire solar disk is in the instrument's view. The result is a variation in the Fraunhofer lines in the measured spectrum. Failure of taking account of this may lead to large errors in the further evaluation. Two approaches have been developed to overcome this problem, one is described in [*Bösch 2002*], the other one in chapter 13, section 1.4. They both ultimately make use of a reference spectrum displaying the effect and used to represent it as if it was an additional absorber.
The cross section spectra (be they of external or internal origin, and either representing an absorber or an effect) are in the following expressed as the convolved and discretisized spectra $\sigma_i(j)$.

3.3.2 Numerical fitting

The algorithm is tasked to find three groups of variables for the construction of $\mathfrak{R}(j)$: (see Eq. (3.3.1-2))

1. the b_h of the polynomial
2. the a_i as parameters of s_i (the $\sigma(j)$), in the following also named "fitting coefficients"
3. the $d_{i,n}$ as discretization parameters of $\sigma(j)$

The routine is combination of two algorithms. First values for a_i and b_h are derived using a linear-least-squares fit. They serve as input for a Levenberg-Marquardt-Fit (LM) [*Levenberg 1944; Marquardt 1963*] for the calculation of initial values of $d_{i,n}$. These again are used for a second iteration of the linear fit, with the results in turn being used in a second LM and so on. After each iteration the values are used to construct the "artificial" spectrum $\mathfrak{R}(j)$. The quantity χ^2 is calculated:

$$\chi^2 = \sum_{j=0}^{n} [\mathfrak{I}(j) - \mathfrak{R}(j)]^2 \tag{3.3.3}$$

If the new χ^2 is smaller than the previous one, or falls below a user defined threshold, or if the variables diverge, the routine aborts.

3.3.3 Error calculation

Several sources of error are to be considered in a DOAS evaluation, some of them already having been briefly mentioned above. This section serves to provide an overview on them.
The most important error is the photon noise, which related to noise in the *I(j)*. It can "hide" features of low optical density, which then cannot be derived by the evaluation. To reduce the noise already during the measurement, a high saturation level of the spectrum is recommended, achievable with long enough integration times. The next error to be noted here is the following:
Physically during the measurement the exponential attenuation of the intensity by the trace gases happens prior to the convolution of the recorded spectrum in the instrument. DOAS convolves the trace gas cross sections before applying the fit, i.e. the convolution and application of the e-function are interchanged. This can cause a systematic error.
Further sources of error are is the Ring effect which alters the absorption line shapes, as well as the solar Centre to Limb Darkening effect occurring for certain measurement geometries.
The changes in Γ and also T caused by environmental variable variations can result in e.g. drifts of the measured spectra by several pixels. These drifts can and do occur even during a series of measurements and constitute one of the error sources of DOAS.
In the following, an error estimate for the numerical evaluation process is given. For a detailed error investigation see [*Stutz and Platt 1996*].

A linear lest-squares fit will give the best possible result and the correct errors if several assumptions are valid, of which the ones concerning the reference spectra we will consider here.

1. The errors in pixel intensity $\Delta I(j)$ are of finite variance. Since they are mainly caused by photon noise, this assumption can be considered justified.
2. The $\Delta I(j)$ are independent from each other. This is not the case, since the smoothing, and especially the convolution with the slit function, replaces every ln(I(j)) by a linear combination involving ist neighbour values. (see above).
3. There are no systematic errors in *I(j)*. If there is one, e.g. caused by varying pixel sensitivity, this usually broad-band effect must be eliminated by high-pass filtering.

The linear fit estimates $\Delta I(j)$ and calculates the errors of a_i and c_h. Errors in Γ are disregarded. To minimize them is the task of the LM. The LM finds a minimum in χ^2, but does not garantuee this minimum to be the absolute one, and not only a local minimum. The latter can occur when in the case of a cross section feature or peak periodically recurring in wavelength a spectral shift according to Eq. (3.3.2) is large enough to generate a phase shift. An example is ozone. Another possibility is that a cross section spectrum which in the chosen wavelength range mainly consists of one or two relatively broad-band but comparatively weak absorption lines erroneously is attributed to a prominet, similar looking spectrum of a stronger, different absorber. But even without these events errors in $\Delta d_{i,n}$ do occur, resulting from the already mentioned noise.
To investigate the effect of errors in $d_{i,n}$ on the linear fitting result, *Stutz und Platt* [*1996*] employed the Monte Carlo method: a test spectrum M was composed from the sum of several trace gas spectra G_i; the Γ of one of the spectra was varied by shifting and squeezing. A function $\Re$

$$\Re = 1 + \sum_i a_i G_i \tag{3.3.4}$$

was linear-fitted to M and the parameters a_i investigated. The G_i were chosen in a way that ensured that the a_i in the case of identical Γ for G_i and M were 1. The result was an error $\Delta a_i = 1\text{-}a_i$ of up to 30% at a shift of G_i by 5% of the considered wavelength range. This error was defined as φ_i. φ_{ig} denotes the error of the i. coefficient caused by the shift and squeeze of the g. spectrum. Since a shift can occur in both directions, the considered g. spectrum was in another test shifted once to the right, once to the left by a value found to be typical for $\Delta d_{i,n}$. the average of the resulting errors $\varphi_{ig+/-}$, φ_{ig}, does represent the influence of the g. spectrum's shift. The relative error $\Delta_{sh}a_i/a_i$ is then calculated as square sum of φ_{ig} over g. The total error $\Delta_{tot}a_i$, in turn is the gaussian sum of the errors Δa_i, the linear routine's error, and $\Delta_{sh}a_i$ under assumtion of mutual independence of these errors. It is $\Delta_{tot}a_i$, upon which the stated error of the fitting routine relies.
Vor the validation of these considerations *Stutz und Platt* [*1996*] again used a test spectrum, to which they added white noise. The error well described the statistical fluctuations in the result, caused by variation in the counterparts of a_i in M.
In another test the spectrum's components were shifted with respect to each other prior to their addition. This generates errors in $d_{i,n}$; they are linear with the *OD* of the noise and were larger than the estimated error by up to 100%. The test spectrum lacked prominet structures: The *OD* of single "lines" was never greater than 3%; the noise "hid" these structures. As long as the relative error of the a_i is smaller than 0.5, the observed statistical error agrees with the calculated total error.

3.3.4 Influence of noise

A different investigation was carried out to quantify the influence of noise. A linear increase of $\Delta d_{i,n}$ with the noise was observed. Most important is the noise's influence on the detection limit D_{det}, since strong noise "hides" lines of low OD. As a quantitative relationship between D_{det} and the relative noise ρ for n pixels *Stutz und Platt* [*1996*] found:

$$D_{\text{det}} \approx \rho \cdot \frac{6}{\sqrt{n-1}} \tag{3.3.5}$$

3.3.5 Residual structure

The last issue to be covered in this section is the residual structure *R(j)* or residual. It is the difference between $\mathfrak{I}(j)$ and $\mathfrak{R}(j)$, thus does represent those structures of $\mathfrak{I}(j)$ which the fit could attribute to neither one of the absorbers nor the polynomial. It can serve as indication for the detection limit of a given absorption if it is defined as the optical density which is euqal to or greater than that of the residual. If the residual was caused by noise only, each single pixel would assume a random-caused value. In theory it is a random structure varying with each spectrum evaluated. In practice, though, the residual tends to be broad-band, the pixels are not independent from each other. A residual can be approximated by a gaussian noise spectrum which is smoothed. This artificial residual can then be used for testing of sets of reference spectra by fitting them to it as if it was a measured spectra to evaluate. For a given reference the result coefficients display a variance with an average which is not zero. The 2σ-deviation, which is the 66th smallest (in absolute value) coefficient γ_{66}, divided by the average output error Δ yields a correction factor F, with which to multiply the error given out by the routine to obtain the total true error. Typical values for this factor are 3 to 6.

3.3.6 Mutual reference spectra compensation

Usually small residuals are correlated with small errors. However, it may occur that two reference spectra which are very similar to each other compensate for each other in the fitting. Typically this happens if two reference spectra for the same absorber, but measured or calculated for different pressures or temperatures are used in the fit, this e.g. to account for the trace gas being present in the troposhere as well as in the stratosphere.
The fit may in one of ist trials attribute to the low-temperature references a positive coefficient much larger than appropriate for the optical density of the absorber present in the spectrum, which it subsequently must compensate for by use of a similar but negative coefficient for the high-temperature counterpart.
The residual may be small, the given out errors may be small as well, but the coefficients nevertheless are worthless. This effect can be prevented by fitting e.g. the high-temperature cross section and the difference between the high- and the low reference.
The coefficients of the absorbers in question must not vary too strongly (e.g. by more than 50 %) when altering e.g. the polynomial's degree or the degree of the smoothing operation. If they do, the probability for a substantial error (e.g. the minimum in χ^2 being only a local one) is very high, in spite of seemingly low errors. For each DOAS evaluation, some sensitivities studies are recommendable to check whether the coefficients behave in an understandable way. The sound evaluation of the measured spectra constitutes the fundamental of the trace gas investigation and of any further processing of the derived Slant Column Densities.

3.4 Air Mass Factor

3.4.1 Classical Air Mass Factor

The Slant Column Densities obtained by a DOAS evaluation of measured spectra represent the integrated concentration over the light path, as explained above. We cannot derive conclusions on the location of trace gas. For a ground based zenith sky measurement it could be located high up in the stratosphere as well as within the planetary boundary layer, or even immediately in front of the instrument as part of an anthropogeneously generated pollution plume. The SCD contain no information about the vertical distribution, or the "vertical profile", of the trace gas.
In most cases, though, some information about the trace gas is available. As for NO_2, we can expect significant abundances near urban centres, especially during rush hour. For BrO, chemical models predict a triangular-shaped profile with a FWHM of 10 km centered at 20 km altitude. As is to be shown in section 4.5, the path the light has taken into our instrument governs the sensitivity of the measurement to the profile.
The Solar Zenith Angle SZA, the angle between the direction to the sun and the local earth surface normal, is one of the parameters determining this path.
Two measurements at two different SZA, with the light traversing a given vertical layer from two different angles, usually yield two different SCD while the profile remains constant (photochemical profile variations left aside in this). A quantity not dependent on solar position is the VCD. To compare trace gas abundance differences between e.g. rural and urban regions, the VCD is the more interesting parameter. To convert the SCD into VCD, we use the "Air Mass Factor" AMF. The AMF A is defined by:

$$A = \frac{SCD}{VCD}$$

(3.4.1)

The SCD originally are derived from the optical densities ("slant optical densities", SOD) according to Eq. 3.1.4, we can analoguously define a "vertical optical density" (VOD, V_O) as optical density obtained from the VCD. We define the formula for the air mass factor [*Solomon 1989*] to:

$$A(\lambda) = \frac{ln\left(\frac{I_0(\lambda)}{I(\lambda)}\right)}{V_O(\lambda)} \tag{3.4.2}$$

Although only the wavelength-dependence is displayed in this formula, the AMF for scattered light observation depends on a large variety of parameters, e.g.:

- the vertical profile shape and position,
- the viewing geometry,
- the sun's position in the sky,
- the scattering, by molecules, aerosols or the earth surface,
- the extinction of the light along ist path by other trace gases and by aerosols,

The relations are outlined in more detail in section 4.5.

3.4.2 Box AMF

The dependence of the AMF on the vertical profile that is the subject of the measurement constitutes a certain impediment to the retrieval of that profile.
In retrieval theory [*e.g. Rodgers 1976*] different approaches have been developed and defined relating the measurement to a characteristical quantity.
One of them is the "weighting function" WF. Its task is to define the result of a measurement as integral or sum over the contributions of the e.g. trace gas present within the grid cells of a given vertical or even three-dimensional discretization.
An SCD measured is the integral over all trace gas abundance present along the path (see above):

$$S = \int_0^L c(l)\,dl \tag{3.4.3}$$

If we use discretization in this, we can write (3.4.3) as a sum:

$$S = \sum_{i=1}^{n} c_i(\Delta l_i)\Delta l_i \tag{3.4.4}$$

In this, Δl_i denotes the length of the ith light path segment out of a total of n, of which the sum is just the total light path L. $c_i(\Delta l_i) = c_i$ is the trace gas concentration averaged over the path segment Δl_i. This Δl_i can be defined with respect to cells, also numbered with i, of a spatial discretization; e.g. in a spherical shell atmosphere, this cell is a vertical layer. The concentrations c_i can be defined as assumed uniform concentrations within the cells. The weighting function assigns each of the c_i a weight, which governs the contribution of each c_i to the total SCD measured. The larger the Δl_i in this example, the higher the weight for the c_i considered. In Eq. 3.4.4, the weight is identical to the geometrical path segment Δl_i. But this

formula is valid only if attenuation can be neglected. But in scattered light DOAS measurements, this weight is also dependent on attenuation and scattering.

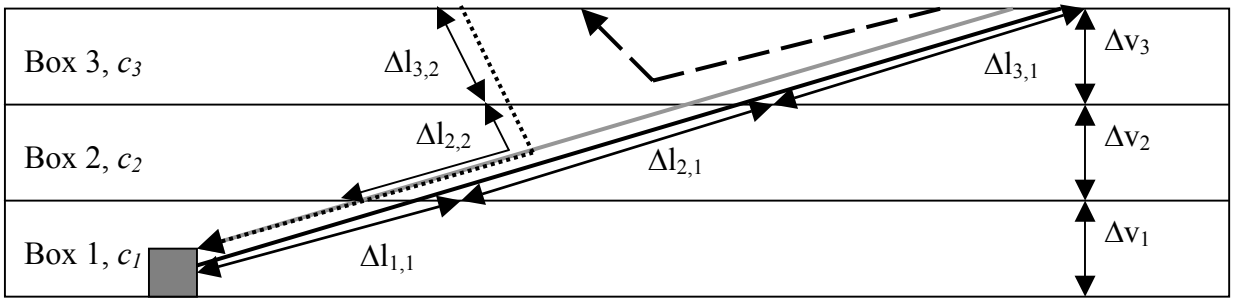

Figure 3.4.1 On the motivation for Box AMF. The straight black line represents the geometrical line of sight. Photons which would cross boxes 1 and 2 along this LOS can get scattered into different directions and do not contribute to the measurement. On the other hand, photons can get scattered into the instrument within a box which leads to a different measurement signal contribution than obtained geometrically.

Refer to Figure 3.4.1. The gray square be the detector. The space is discretizised in three boxes, Box 1, 2 and 3, uniformly housing trace gas concentrations c_1, c_2 and c_3. The straight black line denotes the geometrical line of sight. The gray arrow represents light travelling along the line of sight without attenuation, be this light path # 1. It covers, within these boxes the path segments $\Delta l_{i,1}$ (i = 1, 2, 3, second index is light path number j = 1), which depend on pure geometry. The weight of the concentrations c_i is thus $\Delta l_{i,1}$. If there is attenuation of the light on its way into the detector, the weights are altered: The long-dotted arrow represents light that gets attenuated along its way, i.e. in this case scattered in a different direction, and thus does not contribute to the measurement. The short dotted arrow represents light that gets scattered into the detector within Box 2, be this light path # 2; this light path covers $\Delta l_{1,2} = \Delta l_{1,1}$ within Box 1, but distances $\Delta l_{2,2}$ *and* $\Delta l_{3,2}$ smaller than $\Delta l_{2,1}$ and $\Delta l_{3,1}$ within Box 2 and 3. This reduces the contribution, i.e. the weight, of c_2 and c_3 to the measurement.
(3.4.4) can take account for this by addressing the grid cells by a quantity uniformly identified for all cells, e.g. the vertical extension Δv_i, and expressing Δl_i as product of Δv_i and an appropriate factor A_i:

$$S = \sum_{i=1}^{n} c_i \Delta v_i A_i \tag{3.4.5}$$

The A_i introduced here is like an Air Mass Factor for only the cell denoted by Δv_i. Please note that i serves as the actual grid cell identification, since the vertical extensions may be not the same for all grid cells. Strictly speaking, the A_i as used in (3.4.5) is the classical AMF for a weak absorber confined to (and uniformly distributed within) the i^{th} grid cell. Since several light paths contribute different amounts of light to a scattered light measurement, we must use the sum over these light paths. The A_i can be defined as fraction of the recorded light multiplied by the path segment length covered within the considered cell divided by its vertical extension.

$$A_i = \frac{\sum_{j=1}^{m} I_j \Delta l_{i,j}}{\Delta v_i \sum_{j=1}^{m} I_j} \tag{3.4.6}$$

In this formula the total intensity is expressed in the denominator as sum over m intensities I_j of which each has travelled along a specific light path. This individual light path did carry this intensity through the considered cell i along distances $\Delta l_{i,j}$. This $\Delta l_{i,j}$ must be understood here as derived only geometrically. Attenuation due to aerosols and trace gases influence the A_i insofar as the I_j as well as their sum may be modified; a strong extinction within the cell by soot particles, for example, reduces the I_j travelling along long $\Delta l_{i,j}$ which in turn reduces the A_i. If the optical densities of the trace gas is small as compared to the e.g. aerosol scattering, it can be neglected. Even for strong absorbers like O_3 absorption bands can be chosen where the absorption is small[8]. This neglection entirely separates the A_i from the trace gas. This trace gas independant A_i be henceforth called Box AMF.
The use of Box AMF opens the possibility to use a series of SCD recorded under different conditions (e.g. telescope elevations) and the Box AMF in a linear equation system.
The k^{th} out of o SCD may be expressed as:

$$S_k = \sum_{i=1}^{n} c_i \Delta v_i A_{i,k} \tag{3.4.7}$$

which is the same as in (3.4.5) but with the $c_i = c(v_i)$. Use for each of the S_k yields an equation system:

$$\begin{aligned} S_1 &= c_1 \Delta v_1 A_{1,1} + c_2 \Delta v_2 A_{2,1} + \ldots + c_n \Delta v_n A_{n,1} \\ S_2 &= c_1 \Delta v_1 A_{1,2} + c_2 \Delta v_2 A_{2,2} + \ldots + c_n \Delta v_n A_{n,2} \\ &\bullet\ \bullet\ \bullet \\ S_o &= c_1 \Delta v_1 A_{1,o} + c_2 \Delta v_2 A_{2,o} + \ldots + c_n \Delta v_n A_{n,o} \end{aligned} \tag{3.4.8}$$

In (3.4.7) and (3.4.8) $A_{i,o}$ are the Box AMF for the grid cell i and the measurement conditions (e.g. telescope direction) that led to S_k. This LES can be expressed as matrix with the products $\Delta v_i A_{i,o}$ as matrix components, the trace gas concentrations c_i as left-hand-side vector and the S_k as right-hand-side vector. The solution of (3.4.8) yields the c_i which are the vertical profile of the trace gas. Eq. 3.4.7 expresses a measurement as weighted contributions from different parts of the line of sight, i.e. the probed air mass, with the concentrations within a given volume weigthed with the fraction of measurement light passing the volume as well as with the distance covered within it. For this reason, the A_i can be interpreted as the "weighting functions" for the above formulated DOAS retrieval problem [*Rodgers 2000*]. For use of Box AMF see also [*Schulte 1996*] and [*Bösch 2002*]. Eq. (3.4.8) can be written in matrix form with Box AMF matrix **A**.as "forward model function" relating the unknown profile vector to the known SCD. The condition of A, in conjunction with the measurement noise on the SCD vector, governs the solvability of the problem. This can also be assessed with the averaging kernel of **A** [*Rodgers 1976*]. Chapter 14 will demonstrate a solution approach to an ill-conditioned **A**.

[8] The applicability of the assumption has to be determined in sensitivity studies prior to use.

4. Atmospheric scattering

In the previous chapter, section 3.1 briefly the influence of scattering processes on measured spectra was mentioned. This chapter will discuss them in detail, since they play a crucial role for the transfer of light through the atmosphere.
First the Rayleigh scattering will be covered, in the second section the aerosol scattering and after this the scattering off the earth surface and off clouds.

4.1 Rayleigh scattering

The Rayleigh scattering describes the scattering of light by the molecules of the air. The scattering centre vertical distribution thus obeyes the air density.

4.1.1 Molecular dipole radiation

The molecular dipole radiation is based upon the polarization of the electron cloud of an air molecule by the electromagnetic field of the impinging radiation. The following is based upon the classical Maxwell equations. The field separates the average locations of the positive charge of the molecule cores and the negative one of the electron cloud; the harmonic oscillation described by the frequency (hence the wavelength) of the light induces an oscillation of the same frequency of two centres of charge of the molecule (Fig. 4.1). Be these charges $+e$ and $-e$, and the maximum distance between their respective average locations a, then we can approximate the molecules by two point charges separated by a distance a. The norm p_0 of dipole moment vector then is (at its maximum):

$$p_0 = |\vec{p}_0| = ea \tag{4.1.1}$$

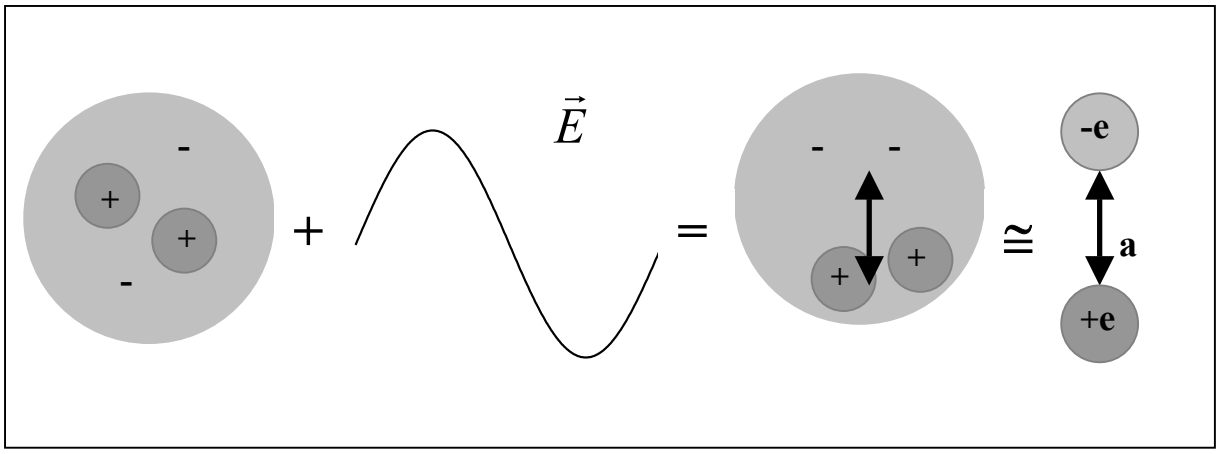

Figure 4.1.1 representation of an air molecule, e.g. N_2, as oscillating dipole

The time dependent expression is (with $\omega = 2\pi\nu$, $\nu = c/\lambda$):

$$\vec{p}(t) = \alpha\vec{E}(t) = \alpha\vec{E}_0 e^{-i\omega t} = \vec{p}_0 e^{-i\omega t} \tag{4.1.2}$$

In this equation α denotes the "polarizability" relating the electrical field to the polarization it achieves to induce in a given molecule.
The energy density [Jm^{-3}] of the field [e.g. *Greiner 1991*] is given by:

$$w = \frac{\varepsilon_0}{2}\vec{E}^2 \tag{4.1.3}$$

Since the energy propagates at the speed of light, *c*, this results in the energy flux upon the molecule ϕ [$Jm^{-2}s^{-1}$] to be:

$$\phi = \frac{\varepsilon_0 c E^2}{2} \tag{4.1.4}$$

Since the dipole itself starts to oscillate, it acts as a source emitting dipole radiation. At any distance *r* from the centre point between the two oscillating charges, given this distance to be large as compared to the wavelength λ, the electric "far field" vector E_f resulting from this induced radiation is:

$$\vec{E}_f = \frac{1}{4\pi\varepsilon_0 c^2 r^3}\left(\frac{d^2\vec{p}}{dt^2}\times\vec{r}\right)\times\vec{r} \tag{4.1.5}$$

and the magnetic far field vector H_f:

$$\vec{H}_f = \left(\frac{d^2\vec{p}\times\vec{r}}{dt^2 cr^2 4\pi}\right) \tag{4.1.6}$$

The vectors or *r*, E_f and H_f form an orthogonal system while propagating. The "Poynting vector" *P* describes the momentary energy flow [$Jm^{-2}s^{-1}$] along the *r*-vector.

$$\vec{P} = \vec{E}\times\vec{H} \tag{4.1.7}$$

Since the absolute values of the electric and magnetic field vectors are equal, we can express the former in terms of the latter and insert into (4.1.7), which yields:

$$\vec{P} = \frac{1}{16\pi^2\varepsilon_0}\left(\frac{d^2\vec{p}}{dt^2}\times\vec{r}\right)^2\frac{\vec{r}}{c^3 r^5} = \left(\frac{d^2\vec{p}}{dt^2}\right)^2\frac{sin^2\theta}{16\pi^2\varepsilon_0 c^3 r^2} \tag{4.1.8}$$

In Eq. (4.1.8) θ denotes the angle between the axis of oscillation and the *r* vector. The essential of this *sin(θ)*-term is that the dipole does not radiate into the direction of its oscillation. To obtain the total average amount *Q* of radiated energy per unit time through the surface of a sphere of radius $R >> \lambda$ centered at the dipole's position we have to integrate the

right-hand-side of (4.1.8) over one oscillation period T as well as over the area of a unit sphere. The integration over the solid angle, equivalent to integration over θ and φ

$$\int_0^{\pi}\int_0^{2\pi}\sin\theta d\theta d\varphi \tag{4.1.9}$$

yields factor 2π*4/3, which leaves

$$Q=\frac{1}{6\pi\varepsilon_0 c^3 T}\int_0^T\left(\frac{d^2\vec{p}}{dt^2}\right)^2 dt \tag{4.1.20}$$

The dipole moment is a function of time. If we assume the oscillation of the dipole to be harmonic, we can express it as in the right-hand-side in Eq. (4.1.2). Due to the energy having to propagate from the dipole itself to the location at distance r, the time series in Q is delayed by r/c, the dependence on t actually is on $(t-r/c)$. Integration over time now yields:

$$Q=\frac{\omega^4 p_0^2 T}{12\pi\varepsilon_0 c^3 T} \tag{4.1.21}$$

Replacing in here ω by $2\pi/T$ and after this cT by λ, we finally find:

$$Q=\frac{4}{3}\frac{\pi^3 c p_0^2}{\varepsilon_0\lambda^4} \tag{4.1.22}$$

In this we find the dependence on the fourth power of wavelength we have already mentioned in (3.1). It means that the shorter the wavelength is, the higher the energy radiated from the dipole. Since the total energy must be conserved, this energy Q is taken from the initial field energy Q_I of the impinging radiation. Hence the fraction $q_S = Q/Q_I$ of scattered energy is by far greater for short wavelengths, such as the UV, than it is for longer wavelengths in the VIS or the IR.

4.1.2 Rayleigh cross section

If we divide this energy, divided by a unit of time, by the energy flux [$Jm^{-2}s^{-1}$] in (4.1.4) and use (4.1.2), which again introduces the polarizability α, we obtain the cross section

$$\sigma_R=\frac{8\pi^3\alpha^2}{3\varepsilon_0^2\lambda^4} \tag{4.1.23}$$

This was first derived by Lord John William Strutt Rayleigh (1842-1919). The scattering of this kind is hence named Rayleigh-scattering, in the following often denoted with a subscript "R".

Since any energy Q of radiation of wavelength λ is equivalent to a number N of photons of energy $h\nu$, with $\nu = c/\lambda$, q_S consequently denotes the fraction of photons scattered out of a direct light beam by Rayleigh scattering when crossing a volume with scattering centres. The polarizability of this volume in turn depends e.g. on the density of such scattering centres

with their electric charges within the volume. The polarizability of a single nitrogen molecule equals [*Greiner 1991*] that of a conductive sphere of radius r_{N2} = 1.2 Å, which is:

$$\alpha_{N2} = r_{N2}^3 = 1.7*10^{-24} \text{ cm}^3 \tag{4.1.24}$$

If we consider red light of wavelength 650 nm = 6500 Å, and use this value as well as (4.1.24) in (4.1.23), we obtain a value for σ_R of $2.1*10^{-27}$ cm^2. A typical value for ground level of the air density ρ is $2.7*10^{19}$ cm^{-3}. Hence the mean free path length l_R for Rayleigh scattering as derived from $1/(\rho\sigma_R)$ is 180 km for λ = 650 nm. For blue light of λ = 470 nm it is only 49 km. At low solar elevations, such as during sunrise and sunset, the sun appears red at the horizon. This results from the blue parts of the spectrum having been scattered out of the direct beam when entering the lower, and dense, atmosphere. The clear sky appears to be of blue colour; this is a consequence of the blue light being scattered and reaching the observer not only from the sun, but from out of the entire upper hemisphere.

4.1.3 Rayleigh phase function

The Rayleigh scattering is not isotropic. If we are interested in the scattering characteristics, we want to know in which direction the light is scattered into and with which probability. So we define the scattering angle θ' to be the angle between the incident and the radiated light, which converts the $sin(\theta)$ into a $cos(\theta')$-dependence (see Figure 4.1.2). If we do not integrate (4.1.8) over the solid angle of the entire sphere, but over a small solid angle centered around a given angle θ and divide by the flux, we obtain a $cos^2(\theta')$-dependence of the "differential" Rayleigh cross section:

$$\frac{d\sigma_R}{d\Omega} = \frac{\pi^2\alpha^2}{\varepsilon_0^2\lambda^4} cos^2(\theta') \tag{4.1.25}$$

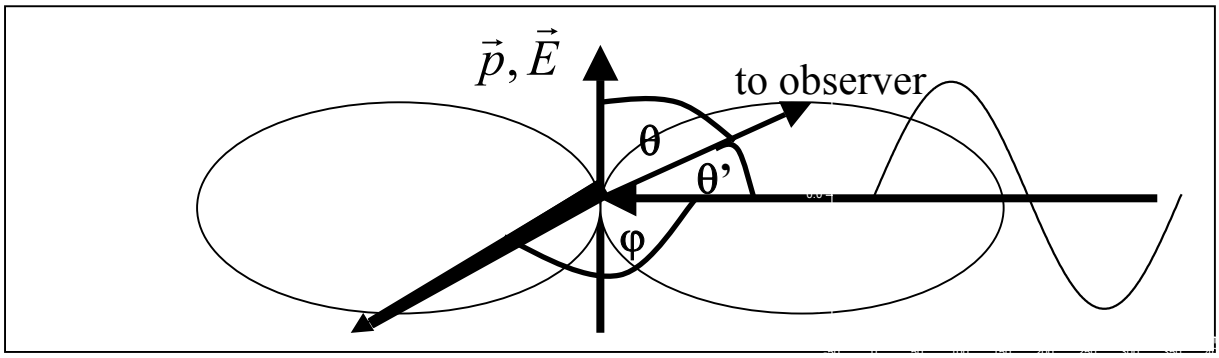

Figure 4.1.2 image of the scattered energy distribution of Rayleigh scattering as projected onto the scetch plane. The 3D-structure resembles a "doughnut" shape.

Qualitatively this is understandable, since the dipole does not radiate in the direction of his oscillation; so if θ = 90, we find the left-hand-side in (4.1.25) to be zero. The three-dimensional shape of that characteristics is a doughnut-shaped ring around the dipole axis. There is no dependence on the scattering azimuth angle φ. When considering N single photons, (4.1.25) the phase function represents the probability that a scattered photon gets scattered into a specific direction.

4.1.4 Polarization

Please note that this relationship applies to an electric field vector of incident radiation which encloses the angle θ' with the emitted dipole radiation. In Fig. 4.2 the scetch plane is also the scattering plane containing both the Poynting vectors of incident and emitted radiation as well as the electric field vector. The light thus is "polarized" parallel to the scattering plane. When solar light enters the atmosphere, it is originally unpolarized, i.e. the angle ψ between the observer's line of sight and the electrical field vector of exciting and thus of dipole radiation is equally distributed. If this angle is 90°, then the line of sight and dipole axis are perpendicular to each other, and ψ no longer is θ' but becomes φ, hence does not govern the energy flux into the direction of the observer. The angle θ (refer to Fig. 4.2) is then 90° for all ψ, and the $sin(\theta)$ becomes 1. See Fig. 4.3 for an illustration. At scattering angle 90°, no light polarized parallel to the scattering plane can reach the observer. If we use $I_{||}$ for the intensity of this light and $I_{\perp}$ for the intensity of perpendicularly polarized light, a "depolarization factor" p_R can be defined (with value 0 if $I_{||} = 0$ and the light is fully polarized):

$$p_R = \frac{I_{||}}{I\perp} \tag{4.1.26}$$

Since each electric field vector of incident radiation can be decomposed into vectors parallel and perpendicular to the line of sight, there will (again assuming the incident light to be not polarized) be total electric field vectors parallel and perpendicular to the scattering plane which are equal in absolute value. The total radiation reaching the observer then is the sum of two halves in (4.1.25):

$$\frac{d\sigma_R}{d\Omega}_{nonpol.} = \frac{\pi^2\alpha^2}{2\varepsilon_0^2\lambda^4}(1+cos^2(\theta'^{|}\,)) \tag{4.1.27}$$

which yields the average differential Rayleigh cross section for incident non-polarized light and scattering angle θ'. This differential cross section is also named "phase function" $\phi_R(\theta')$.

More accurate calculations, taking account of e.g. the anisotropy of the polarizability of nitrogen and oxygen molecules, have been performed by [*Penndorf 1957, and Chance and Spurr, 1997*]. The latter paper contains a new fit to the data giving an average polarizability (with n refractive index, $N_0 = 6.02205*10^{23}mol^{-1}$ Avogadro's number)):

$$\alpha = \sqrt{\frac{(n-1)^2}{4\pi^2 N_0{}^2}} \tag{4.1.28}$$

and a fit to their exact Rayleigh cross section in units [10^{24} cm^2] with $\lambda' = \lambda^{-1}$ [μm^{-1}]:

$$\frac{3.9993*10^{-4}\lambda^{|4}}{1-1.069*10^{-2}\lambda^{|2}-6.681*10^{-5}\lambda^{|4}} \tag{4.1.28}$$

which is to be used in this work. They also derived a more accurate $\phi_R(\theta')$ taking into account the p_R of the considered light. But since we will (to be described later) treat the light as corpuscular radiation with one defined polarization axis per particle, and since for the average

(non-polarized) phase function the $(1+\cos^2(\theta'))$ –dependence of $\phi_R(\theta')$ prevails, the $\phi_R(\theta')$ in Eq. (4.1.27) will be used in this work, polarization so far ignored.

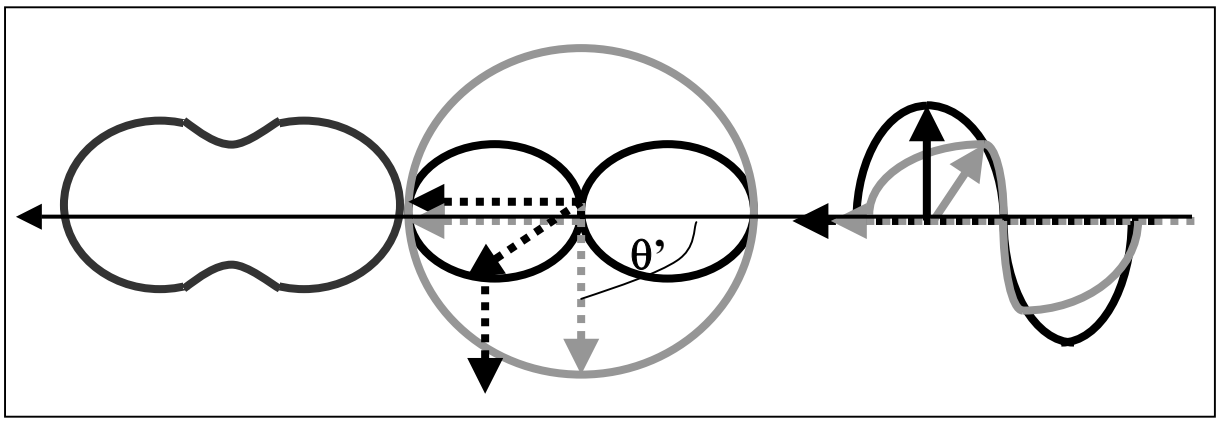

Figure 4.1.3 Polarization characteristics of the Rayleigh scattering. Depicted in gray is radiation polarized perpendicular to the scattering plane, in black parallel. At a scattering angle θ' of 90° (downward pointing arrows) no parallel-polarized light can be scattered by one event. In dark gray, to the left, the total phase function is depicted for unpolarized light.

This polarization characteristics of the Rayleigh scattering can be observed e.g. in zenith viewing geometry especially at sun elevations around 0°, when the scattering angle is θ' for both polarization directions, but θ is 0 for the one and around 90° for the other. It can be taken advantage of. If we refer to Fig. 4.3 and consider two scatterings of each $\theta' = 45°$ instead of one with $\theta' = 90°$, we find that the resulting Rayleigh cross section for "parallel " polarized light, which is just the right-hand-side in Eq. (4.1.25) with $\theta' = 45°$ and to the power of two, is non-zero, i.e. 0.5 if we normalize (4.1.25) to unity at $\theta' = 0°$. This means that multiple scattering weakens the polarizing effect. When measuring it with e.g. polarization-sensitive instruments (e.g. DOAS devices equipped with polarization filters) we can, comparing the polarization with values calculated for the assumption of single scattering, conclude on the importance of multiple scattering. Since in the follwing we will only consider the scattering angle unless stated otherwise, we redefine θ to be this scattering angle.

4.1.5 Raman scattering

The Rayleigh scattering is an elastic process since it preserves the total energy of the incoming and outgoing radiation. But this conservation is not necessarily the case in scattering processes. In fact, the Rayleigh-scattering is only the elastic special case out of the general molecular scattering.
The molecular structure with electron clouds allows for the excitation and de-excitation of rotational and vibrational states. In the wavelengths commonly used for DOAS, the VIS and the UV [1], the energy of the photons complies with rotational excitation and de-excitation. As a consequence, photons change their wavelength when suffering such an event.
This is then called Raman scattering. The scattering centres again are the atmosphere molecules. The Raman scattering is what causes the Ring effect in scattered light spectra. Since the Radiative Transfer Model developed in this thesis does model the radiative transfer for one wavelength at a time, Raman scattering is not yet implemented. Appendix A contains

[1] IR DOAS applications are currently under development, e.g. [*Frankenberg, pers. comm.*]

a section outlining an approach to implement Raman scattering within the frame of the routines and algorithms present in the code.

4.2 Aerosol scattering

Molecular scattering applies to particles with dimensions small as compared to the wavelength. In addition to it, also scattering of larger particles with radii comparable in order of magnitude λ alters the transfer of light through the atmosphere. These particles are the aerosols and cloud droplets. Their types, origins and vertical distributions are outlined in section 2.2.2. The optical properties for a given wavelength are as various as are the physical ones, depending on i.e. size, shape, reflectivity and many more. Research is still ongoing to derive e.g. phase functions, since in many cases only numerical or empirical methods are usable. The scattering off spherical droplets, as they are found in e.g. clouds or fog, is described analytically in Mie theory, and is called Mie scattering.

4.2.1 Mie scattering

The Mie scattering off spherical liquid droplets can be compared to diffraction at a pinhole with diameter comparable to the wavelength. Interference results in minima and maxima when regarding the scattered intensity as function of the scattering angle. Depending on the angle between droplet surface and direction of incident light, the light may get reflected off the droplet, or it may enter and exit it and get twice refracted.

4.2.2 Mie cross section

To calculate the exact cross section and phase function $\phi_{Mie}(\theta)$involves highly complex computation including the size, refractive index of the liquid, and the incident angle. Since the cross section depends not only on the wavelength, but also on the size (e.g. radius r) of the particle (and the "pinhole"), Mie theory uses the size parameter $\alpha = 2\pi r/\lambda$.
Figure 4.2.1 depicts two examples of Mie extinction functions $E(\alpha)$, normalized to the particle cross section, for two refractive indices n as a function of the size parameter.

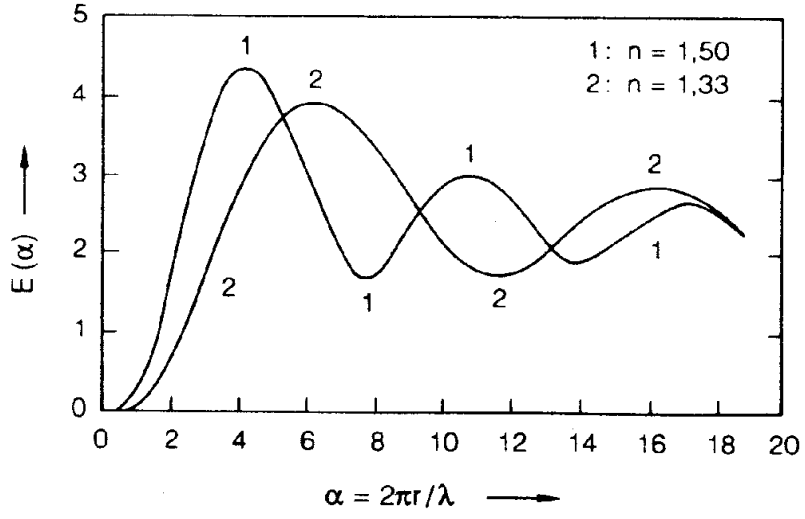

Figure 4.2.1 Mie extinction function $E(\alpha)$, normalized to geometrical particle cross section as a function of size parameter α for two refractive indices, taken from [Roedel 1991].

Since usually we have not only one single aerosol of one size, but a mixture of droplets of several sizes, we can derive a macroscopical extinction coefficient $K_e(\lambda)$ by integrating over $E(\alpha)$, multiplied by the geometrical cross section and the size distribution $n(r)$:

$$K_e(\lambda) = \int_0^\infty \pi r^2 E(\alpha) n(r) dr \tag{4.2.1}$$

In case of aerosols larger than 0.1 μm, the aerosol size distributions often obey a r^{-s} law, s about 4; when inserting this in (4.2.1) and converting it into a function of α alone (see *[Roedel 1991]*), we obtain a simple relation between $K_e(\lambda)$ and λ:

$$K_e(\lambda) = const. \cdot \lambda^{3-s} \tag{4.2.2}$$

This shows the wavelength dependency of the Mie scattering for aerosol mixtures to be far smaller than the one for Rayleigh scattering.

4.2.3 Mie phase function

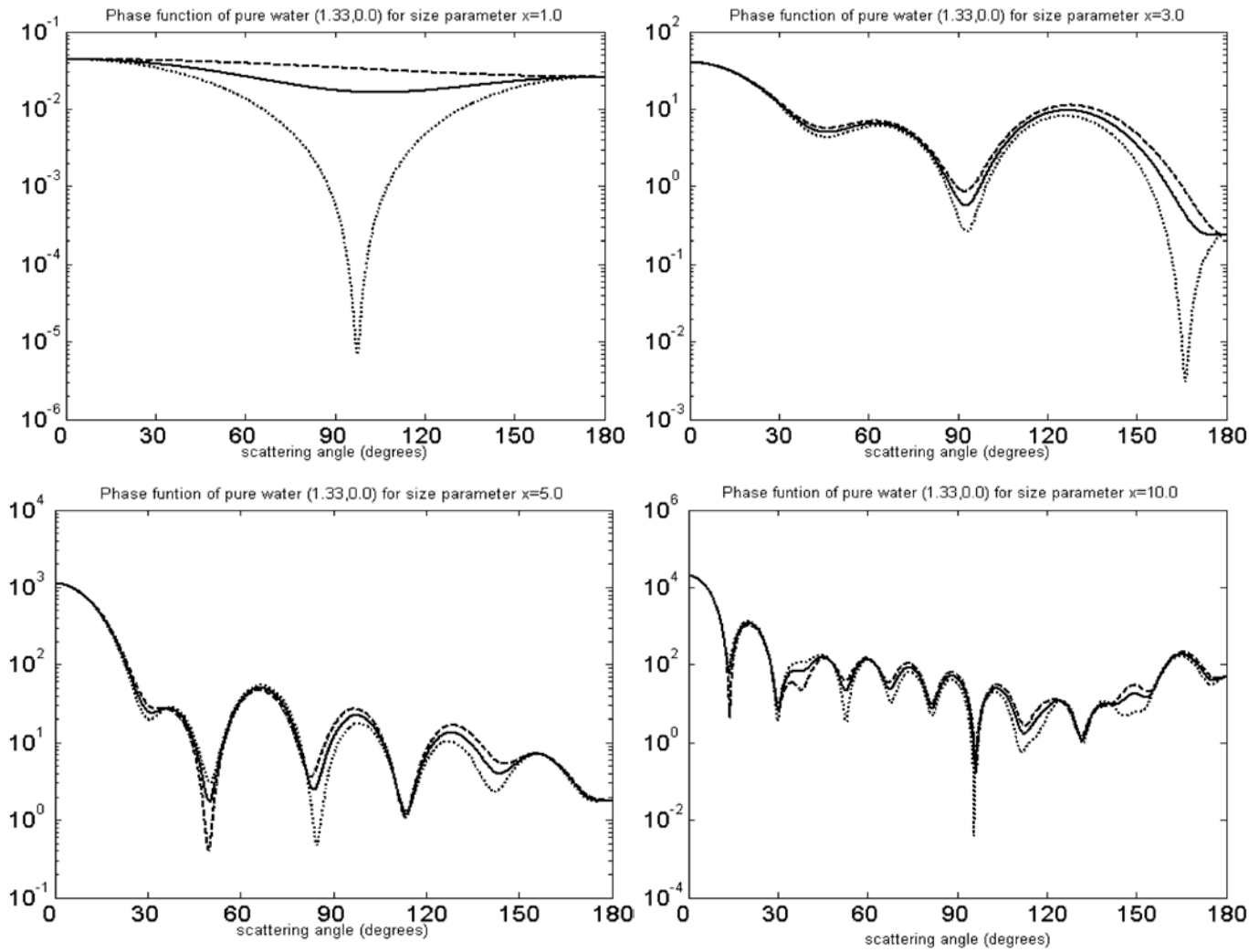

Figure 4.2.2 Phase functions computed with Mie theory by [Sanghavi 2003] for different size parameters. The development of local "interference" maxima with increasing α can be seen. The dashed and dotted lines denote the phase function for light polarized parallel and particular to the scattering plane, the straight lines the function for depolarized light.

Figure 4.2.2 shows the phase functions for four values of the size parameter, calculated by [*Sanghavi 2003*]. Clearly the development of multiple interference structures with increase in α can be seen. But also the function's forward-peakedness rises. This becomes more evident if the functions are regarded in polar diagrams without log scaling (Figure 4.2.3).

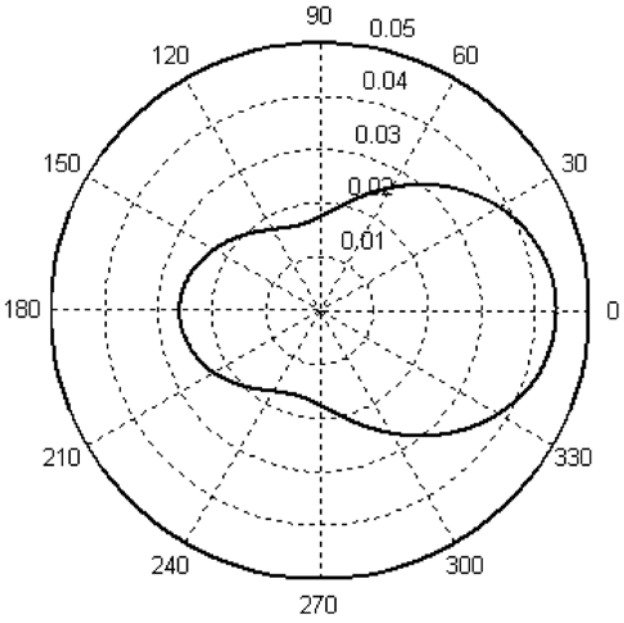

Phase function of pure water (1.33,0.0) for size parameter x=1.0

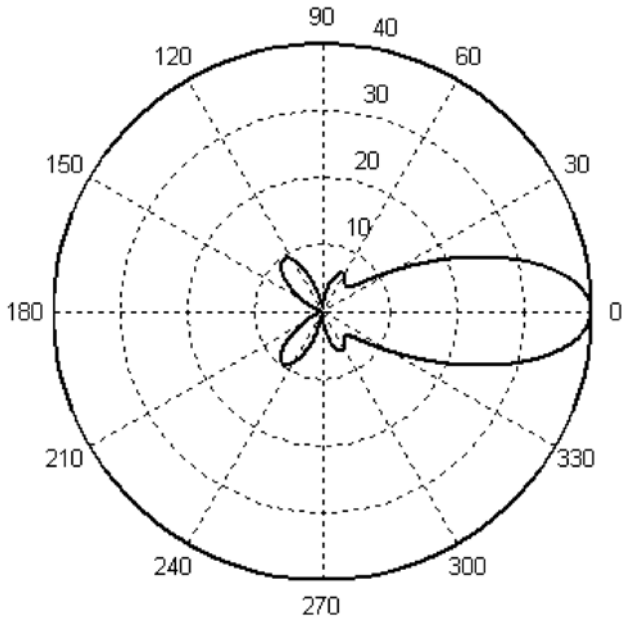

Phase function of pure water (1.33,0.0) for size parameter x=3.0

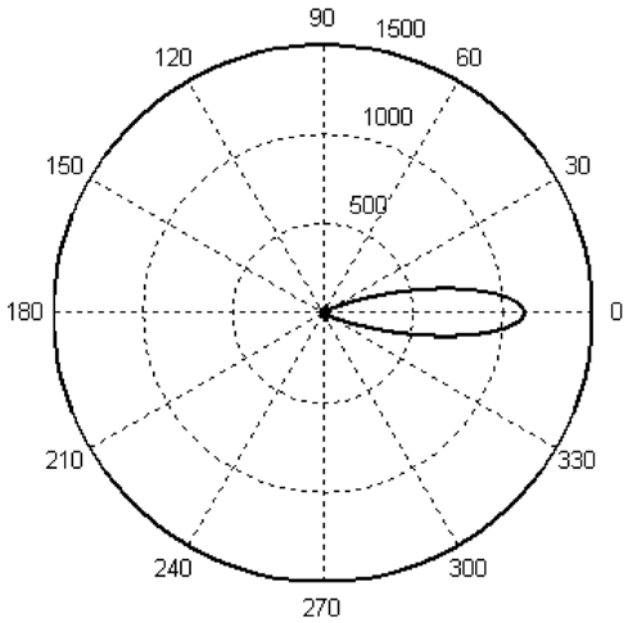

Phase function of pure water (1.33,0.0) for size parameter x=5.0

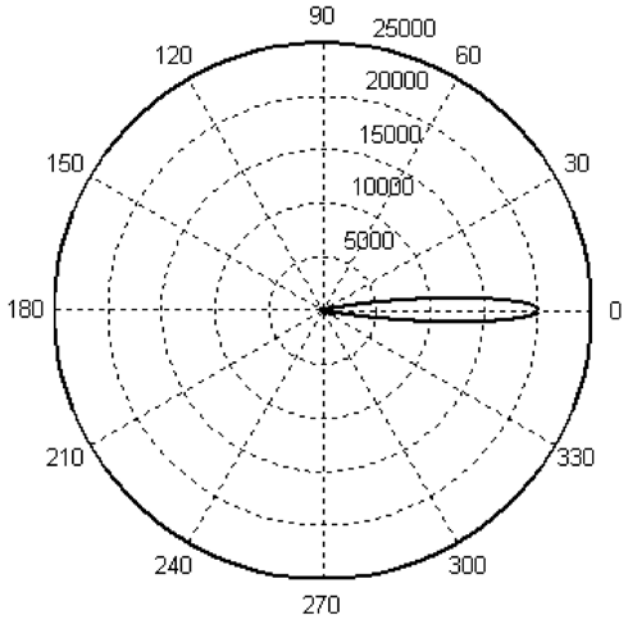

Phase function of pure water (1.33,0.0) for size parameter x=10.0

Figure 4.2.3 Phase functions computed by [Sanghavi 2003] for the same parameters as above and depolarised light, but plotted into polar diagrams. With rising α, the functions become stronger forward-peaked. This can be explained with larger "pinholes" where the light can pass through without altering direction.

The phase function of an aerosol mixture is derived as an average over the aerosol sizes present weighted with the size distribution. This averaging over phase functions of different size parameters reduces the local minima and maxima or even makes them vanish. An approximation for the phase function of aerosol mixtures is given by the Henvey-Greenstein functions [*Henvey and Greenstein 1941*]:

$$\theta_{Mie,HG}(\theta) = \frac{1-g^2}{(1+g^2-2g\cos(\theta))^{\frac{3}{2}}} \tag{4.2.3}$$

with the assymetry coefficient *g*; it describes the degree of "forward-peakedness" of a scattering process; *g = 0* is isotropical scattering, and the phase function becomes unity for all scattering angles, while with *g = 1* all intensity is scattered in forward direction. For atmospherical aerosols *g* is between 0.6 and 0.7 [*Perliski 1992*]. The resulting phase functions for this g-range are very similar to each other; the display a monotonuous decrease with increasing scattering angle.

4.2.4 Aerosol absorption

The aerosols do not only scatter light elastically, but also absorb it. To parametrize this effect, the single scattering albedo ϖ is defined:

$$\varpi = \frac{\kappa_S}{\kappa_S + \kappa_A} \tag{4.2.4}$$

with κ_S and κ_A as extinction parameter for scattering and absorption, respectively.

In continental air, the "e-length" (defined as the distance after which an intensity has been attenuated to 1/e of its original intensity) is for 400 nm 25 km, for 600 nm 45 km.
For Rayleigh scattering, it is 22 km and 116 km, respectively. The wavelength dependence thus is far weaker.
For each aerosol type, described by its number density, its cross section and its ϖ an extinction coefficient κ_E can be derived which usually varies with altitude.
The vertical extinction coefficient profile, the single scattering albedo as well as the phase function are used in this work to model the effect of aerosols.

4.3 Surface scattering

The last scattering process to be covered in this chapter is the scattering off a large surface. The most important parameters is the albedo ω defined as the ratio between incident and reflected intensity, I_i and I_r:

$$\omega = \frac{I_r}{I_i} \tag{4.3.1}$$

Typical values are given in Table 4.3.1.

Table 4.3.1 Albedo values for different surfaces

surface	ω
Earth average with clouds	30 %
ocean	5 %
Urban areas	10 %
Ice, clouds	70-80 %

The albedo is wavelength dependent, and for many surfaces decreases in the UV.
The scattering does not happen as in case of a specular reflection e.g. off a mirror. The most widely adopted characteristics is the Lambertian reflection. The Lambertian "phase function" is (with normalization factor π^{-1} for integration of the cosine over an hemisphere):

$$\phi_{Lamb}(\theta) = \pi^{-1} cos(\theta) \tag{4.3.2}$$

For an individual photon, the probability to get reflected into a direction r with angle θ to the surface normal scales with $cos(\theta)$.
But an illuminated Lambertian surface of given albedo displays the same brightness to the observer, regardless of the viewing angle.
If we consider an area A on which N photons are impinging per unit time, and a receiver which has an area a (which is situated within A) within the field of view, we find that if we look not in nadir direction, but from an angle θ onto A, the field-of-view-area will increase with $cos(\theta)$ while the number of photons reflected into this direction per unit area decreases with the same factor. This leads to a constant signal in the detector.

But this brightness does depend on the cosine of the incident angle θ'; a light source which radiates a given number M of photons onto an area perpendicular to the light beam axis will deliver, when tilted by θ' against the "nadir" direction, only $Mcos(\theta')$ per unit area which are available there for reflection, i.e. the larger this angle is, the lower the reflected intensity.

4.4 Cloud scattering

Most water clouds are essentially conglomerates of water droplets, as outlined in chapter 1. There are usually several Mie scatterings of photons within a cloud; after 7 to 8 of them, the photon direction has lost any connection with the original one [*Pfeilsticker, pers. comm.*]. The assessment of the paths of photons within clouds is a subject of intense research.
Nevertheless, for a variety of applications, including satellite remote sensing operations, the clouds can be parametrized in an easier, more phenomenological way.
One parameter is the coverage, which is defined by how large the fraction of a given area of earth surface is that is covered with clouds. Coverage 0 describes a clear sky, coverage 100 % an overcast one. The cloud top of most cloud covers can be approximated by a lambertian reflector as described in the previous section, with an albedo between 70 and 80% for optically thick clouds.

A fraction of the photons enter the cloud and get absorbed within by the droplets and interstitious gases.
Another fraction gets transmitted, but after several scatterings which alter the original direction. The photons are emitted from the other side of the cloud with directions approximately equally distributed into the 2π semisphere. The effective transmittance phase function bears the same value for all scattering angles $\theta \in [0,\pi]$.

$$\phi_{Cloud}(\theta) = const. \forall \theta \in [0,\pi] \tag{4.4.3}$$

To an individual photon, one of these processes will occur, governed by the parameters albedo and transmission.

4.5 Principal mechanisms of light scattering in the atmosphere

The Slant Column Densities obtained by a DOAS evaluation of measured spectra represent the integrated concentration over the light path, as explained in the previous chapter. We cannot derive conclusions on the location of trace gas. It could be located high up in the stratosphere as well as within the planetary boundary layer, or even immediately in front of the instrument as part of an anthropogeneously generated pollution plume. The SCD contain no information about the vertical distribution, or the "vertical profile", of the trace gas.
To obtain an information about the sensitivity of a measurement, the AMF concept is used as defined. As already stated, the AMF is influenced not only by the measurement geometry but also by the scattering. This section outlines some basic mechanisms of this dependencies.
Fig. (4.5.1) illustrates some principal dependencies of the AMF. Let us consider two wavelengths we choose for measurement in zenith sky geometry at a given sun elevation. This sun elevation is henceforth parametrized as "Solar Zenith Angle" SZA, defined as angle between the direction to the sun and the vertical path; i.e. SZA = 90° denotes a sun at the horizon. Be the SZA high, e.g. between 70 and 90°.
The solar light of both wavelengths impings onto the entire projection of the earth surface. The question is from which of those light beams photons will enter our instrument.

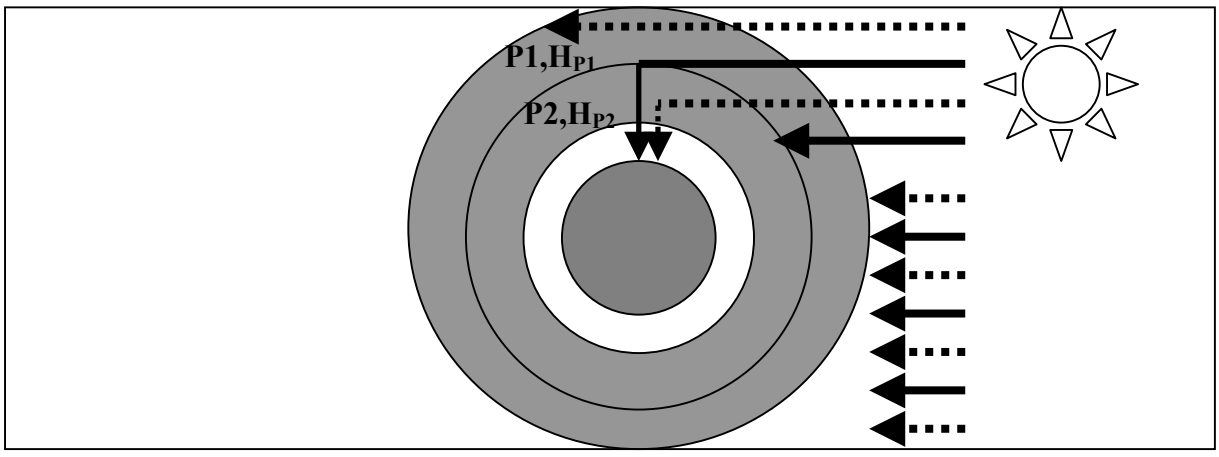

Figure 4.5.1 Possible shapes of solar light paths (straight line: UV, dashed line: VIS) through vertical trace gas profiles, represented as uniform spherical layers in gray colour

Be there two profiles of trace gas, P1 and P2, of equal shape (in our case located plumes of equal spatial extension) and concentration in [cm^{-3}], though at different centre altitudes H_{P1} and H_{P2}.
The optical density be small (so as not to influence the radiative transfer significantly in itself) and independent from environmental variables (which is, e.g. in the case of ozone, not in general the case). The VCD is thus identical for both profiles. The SCD, though, will be different. In both cases the light enters the atmosphere at an angle defined by the sun elevation. As seen in the previous sections, the cross section for molecular Rayleigh scattering is far higher for the UV, which means that in case of the UV, the light is unable to penetrate deep into the atmosphere before getting scattered; this will happen at altitude $H_{S,UV}$; in contrast, the VIS light does penetrate deep, but upon entering the deeper atmosphere with higher density, scattering occurs as well, but at an altitude $H_{S,Vis}$ which is significantly lower $H_{S,UV}$.
A fraction of the light will be scattered into the direction of the instrument, covering the last section of the light path into the detector on a vertical way. In case of P1, we see that $H_{S,UV}$ is located within the vertical layer occupied by P1, at about H_{P1}. As a result, the UV light will travel a very slant way through the layer of P1, and suffer a large spectral absorption. Its way through P2, though, is vertical, since P2 is entirely located below $H_{S,UV}$.
Thus the SCD of the UV measurement of P1 will be much higher than the VCD, but about equal to it for P2. This results to a high AMF for P1, and a low one (near 1 in this case) for P2.
For geometrical reasons as indicated in the picture, the VIS beam's way through P1 is shorter than for the UV, but through P2 it is much longer; hence the SCD in VIS for P1 is smaller than in the UV but greater for P2, and the same is valid for the AMF.
Table (4.5.1) lists the principal differences in radiative transfer for the UV and VIS in zenith sky geometry.
Of course neither light will get scattered at only one altitude, but an average altitude can be derived (see below). Taking into account the additional extinction from the scattering point downward into the detector, we can derive an effective altitude. From this effective altitude we receive the light in both cases; this altitude separates the slant from the vertical path and governs the AMF.
Figure 4.5.2 illustrates the behaviour with a very simple calculation. For wavelengths 350 and 550 nm, and SZA 70°, where neither sphericity nor refraction is of significant importance, the light paths from the top of atmosphere to each of 70 vertical layers of 1 km thickness between 0 and 70 km have been calculated geometrically; for these ways, and for the "remaining" vertical path from this altitude to the ground the Rayleigh attenuation has been calculated.
For the different altitudes themselves, the air number density was used as weight for the relative scattering probability. This yielded 70 light contributions, each with a scattering point at a given altitude, which were divided by their total sum. The resulting plot shows from which altitude we receive which fraction of the measured light.

Table 4.5.1 principal relations of scattering altitudes and AMF for the profiles P1 and P2

Wavelength	AMF P1	AMF P2	Eff. scattering altitude
UV	high	low (near 1)	high
VIS	low	high	low

These effective altitudes not only vary with wavelength, but as well with SZA. If we increase the SZA in Fig. (4.5.1), we see in Fig. (4.5.3) the geometrical paths through the atmosphere

increase. This leads to a higher attenuation, and thus to a higher importance of light beams travelling higher. The result is a higher effective scattering altitude for a given wavelength. Performing DOAS measurements at agiven wavelength for a series of SZA, the light effectively scans the atmosphere; this results in a series of different AMFs.

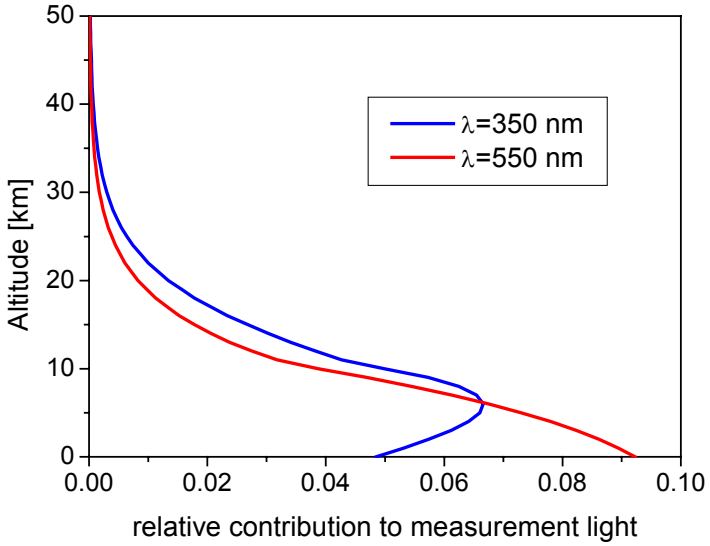

Figure 4.5.2 light contributions from 1 km altitude levels for two wavelengths at SZA = 90°. In the UV (350 nm), the most light we receive from about 7 km altitude; for the VIS we receive the most light from the air at ground level.

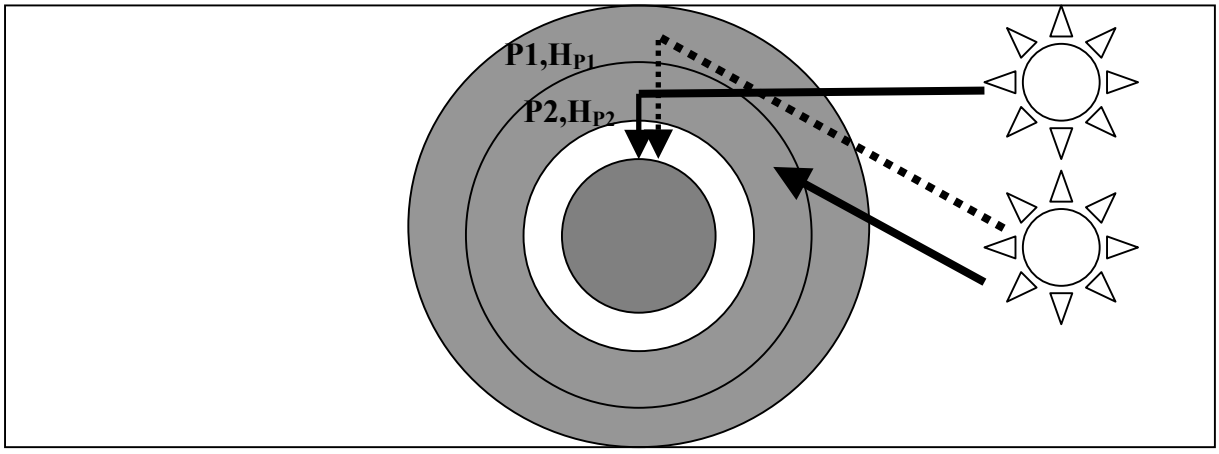

Figure 4.5.3 The reason for effective altitude variation with SZA; higher SZA increase the geometrical light paths and the atteunation (straight line: SZA = 0°, dashed line: SZA > 90°)

A first approximation for the slant light paths at SZA < 70° (i.e. without sphericity and refraction taken into account) is:

$$L = V_l/cos(SZA) \tag{4.5.1}$$

With L as slant path and V_l as vertical path, respectively.
One other effect important for radiative transfer be explained here, this one related to absorbers near the ground. See Figure 4.5.4. The measurement device be a DOAS setup

looking in zenith sky as well as with a low elevation (angle between line of sight and the local earth surface tangent). The research subject is a trace gas layer near the ground, represented in light gray. The straight lines represent the two lines of sight, the dashed ones the light entering the detector along them. We see that the light path through the absorber is longer for the slant line of sight than it is for the zenith-sky line. This leads to a higher sensitivity to the absorber near the ground for the low elevation. A first approximation for the light path is

$$L = V_l/\sin(\varepsilon) \tag{4.5.2}$$

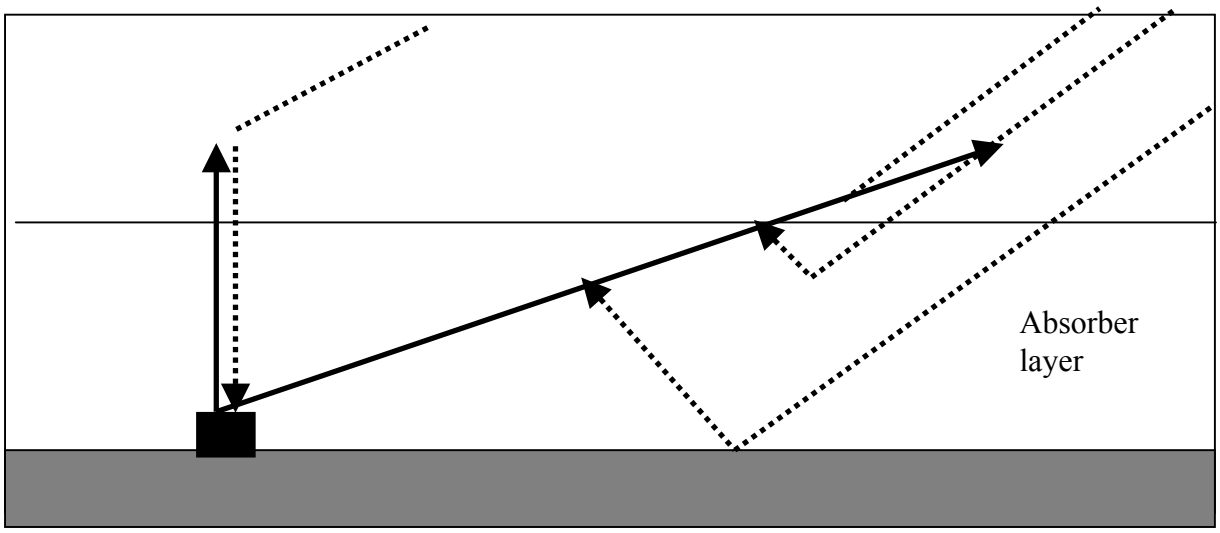

Figure 4.5.4 light paths through an absorber near ground for two lines of sight; for the slant line of sight, indicated by the long black arrow, the light path and the sensitivity to the absorber is higher than for the vertical (zenith-sky) line of sight.

Two more remarks should be added here. Since neither of the geometries are “direct light”, they depend on scattering in the same way as the zenith-sky experiment does. Since in the UV the first scattering usually occurs in the troposphere or the stratosphere (see above), the original slant path does not lead through an absorber near the ground; the terminal part of the light path which does travers the absorber solely depends on the elevation of the telescope. The influence of the SZA on the AMF of absorbers near the ground is far lower than for stratospheric ones.
The second remark is that near the ground the air number density usually is highest, and the aerosol scattering coefficient is also. For a slant line of sight covering a large geometrical distance through dense air multiple scattering influences the AMF, as indicated by the lower two of the three dashed arrows representing light paths along the slant line of sight. This multiple scattering significantly changes the light paths through the absorber. The scattering can also occur off the earth surface, and thus also depends on the local albedo.

These qualitative considerations can be performed for each of the measurement geometries used for DOAS and every combination of wavelength and environmental conditions such as aerosol load and type, albedo and cloud cover. The multiple scattering renders geometrical approximations invalid.
From these uncertainties arise the need for quantitative parameter derivation with a radiative transfer model.

5. Radiative transfer equation

The way of radiation from a source through a scattering and absorbing medium is described with the radiative transfer equation. This chapter will explain the derivation of the equation, the conversion from the continuous equation to the discrete one and finally cover the radiometric quantities. At the end the current primary radiative transfer equation solution techniques will be explained briefly. The information can be taken from many authors, e.g. [*Kirk 1991, Mobley 1994*]

5.1 Radiometric quantities

5.1.1 Photon distribution function

First we consider the number f of photons with wavelength $\in [\lambda, \lambda+d\lambda]$ which cross an area dA coming from a solid angle $d\Omega$ tilted against the surface normal n by angle θ during time dt.

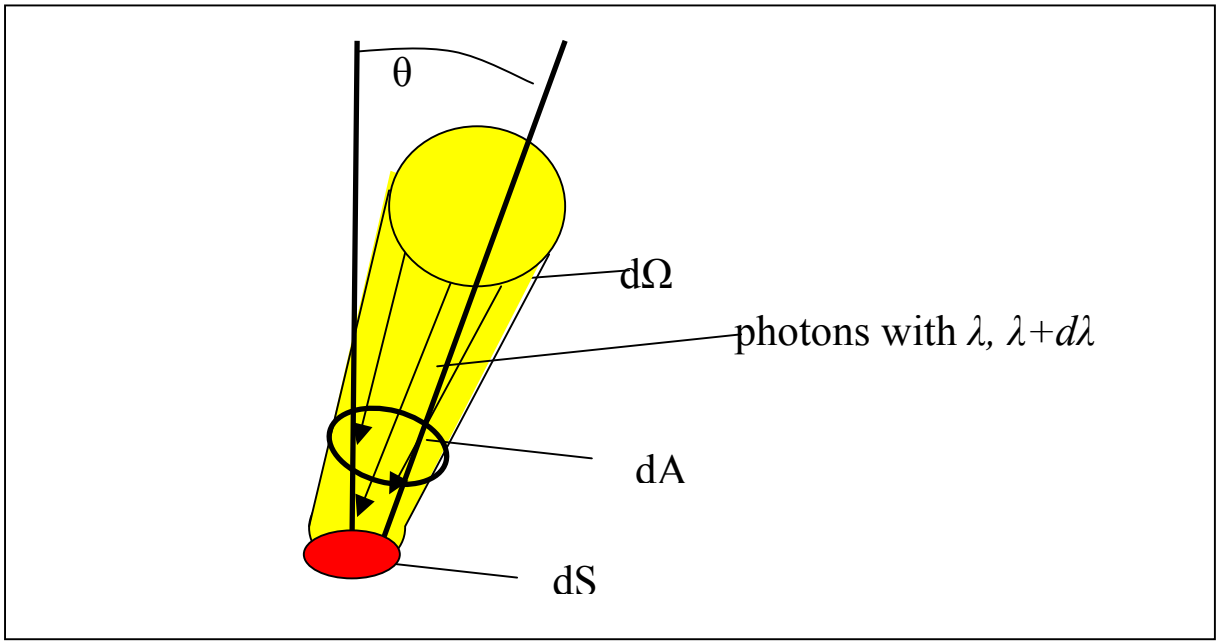

Figure 5.1.1 The angles and aeras in the definitions of radiometric quantities

This number is defined by the photon distribution function:

$$f(\vec{r},\vec{n},\lambda,t)\, c\, dt\, \vec{n}\, d\vec{S}\, d\Omega d\lambda \qquad (5.1.1)$$

f has unit [$nm^{-1}sr^{-1}cm^{-3}$]. Using the known relation between energy and wavelength $E = hc/\lambda$ (5.1.1) can be expressed in terms of energy with vector dS^ expressed as $dA\ cos(\theta)$:

$$dE = c^2\ h\ \lambda^{-1}\ f(\vec{r},\vec{n},\lambda,t)\ dA\ cos(\lambda)\ d\Omega\ d\lambda\ dt \tag{5.1.2}$$

The „radiation energy“ is defined as the energy emitted from a radiating body. The designation is *E*, in units [J].

5.1.2 Flux and intensity

The alteration of *E,* integrated over Ω and λ, with time in unit [W] is named „radiation flux“

$$\phi = dE/dt \tag{5.1.3}$$

The energy radiated from the sun per unit time is $W_s = 3.85 \cdot 10^{26}$ W.
The flux can be considered as a function of the solid angle from which it impinges, which recognizes the non-isotropy in general radiation fields with one or more light sources. The „intensity“ *I* in units [W sr^{-1}] is defined as

$$I = d\phi/d\Omega \tag{5.1.4}$$

5.1.3 Radiance

If we not only consider the solid angle from out of which our radiation impinges (be it from one or more sources of radiation) but also our area segment *dA* oriented perpendicularly to the direction of the light ξ (representing the centre axis of the incident light cone defined by $d\Omega$) we can define the „spectral radiance“[W $m^{-2}sr^{-1}$]:

$$L(\xi,\lambda) = \frac{d^2\phi}{dA\cos(\theta)d\Omega d\lambda} \tag{5.1.5}$$

The relation between the spectral radiance and the energy is given by:

$$dE = L\ dA\ cos(\theta)\ d\Omega\ d\lambda\ dt \tag{5.1.6}$$

and between the radiance and the distribution function:

$$L(\vec{r},\vec{n},\lambda,t) = c^2 h\lambda^{-1} f(\vec{r},\vec{n},\lambda,t) \tag{5.1.7}$$

5.1.4 Irradiance

In the atmosphere, as well as in other scattering media, such as the ocean, not only the radiation impinging from out of one solid angle is of relevance, but all radiation reaching *dA*. The integral over space angles yields the *spectral irradiance*. It can be defined in two ways: The „planar“ and the „scalar irradiance“; the former in turn is divided into two: the „downward planar irradiance“

$$E_d(\lambda) = \int_{\varphi=0}^{2\pi} \int_{\theta=0}^{\pi/2} L(\theta,\varphi,\lambda)\left|\cos(\theta)\right| \sin(\theta) d\theta d\varphi \tag{5.1.8}$$

accordingly in units [W m^{-2} nm^{-1}], which is the sum of all downward-directed components of L which pass an area segment *dA* dividing the upper from the lower hemisphere. The *cos (θ)* factor in (4.5) weighs the incident radiation parts which do not imping onto *dA* perpendicularly. The flux passing this area A then becomes

$$\phi_A = AE_d \tag{5.1.9}$$

In an analoguous way, E_u is the „upward planar irradiance" which is defined the same way as ist upward counterpart, but with an interation over θ running from π/2 to π.
An instrument designed to the measurement of planar irradiance in either upward or downward direction is named a „cosine detector". It usually consists of a diffusor plate designed to remove any directional charactersitics from the impinging irradiance. An example is teflon. Located below is a spectral filter (or a spectrograph), and a detecting element, like a photo multiplier.
In photochemistry the direction out of which radiation reaches a given volume element with species contained is not of relevance since the photo dissociation does not in the average depend on this. The accurate quantitity for this is the above mentioned „scalar irradiance". A different, and more common, name is the "actinic flux"

$$E_0(\lambda) = \int_{\varphi=0}^{2\pi} \int_{\theta=0}^{\pi} L(\theta,\varphi,\lambda)\sin(\theta)d\theta d\varphi \tag{5.1.10}$$

Also in unit [W m^{-2} nm^{-1}], it lacks the cos (θ)-factor and it integrates over the upper and lower hemisphere altogether. A collector accepting the radiation from out of all directions, a so called E_0 collector, has spherical shape and consists of a similar material as the diffusor plate. If the sphere is of radius r, the effective area presented to any given direction of incident radiation is accordingly πr^2. The total flux passing this area then becomes

$$\phi_0 = \pi r^2 E_0 \tag{5.1.11}$$

It is illustrative to note here that the E_0 can also be divided into radiation upwards and downwards, and since the direction does not lead to any weighting, the radiation detected could as well come in from only one direction, being equally distributed over the area the sphere does present it.
Within the sphere, the radiation is converted into a theoretically perfectly isotropical radiation field, of which a part proportional to E_0 is directed onto a detector.
For photochemistry the number of photons of a given wavelength (=energy $h\nu$, h = Planck's constant, ν the frequency) is important hitting a given volume cell per unit time. The irradiances can therefore be expressed as "quantum irradiance", in [photons m^{-2} nm^{-1}], and also per spectral interval. For additional information be it mentioned here that an often used quantity in biological research is the PAR (photosynthetically available radiation), though with its wavelength integration limits varying in literature betweeen 350 nm - 700 nm and 400 nm – 700 nm.

$$PAR = \int_{350nm}^{700nm} \frac{\lambda}{hc} E_0(\lambda)d\lambda \tag{5.1.12}$$

5.1.5 Extraterrestrial solar irradiance

The solar radiation impinges from only a small solid angle of 0.26°. In good approximation the sun is a uniformly radiating source (the centre-to-limb darkening effect to be neglected here). The irradiance impinging onto the earth`s atmosphere can be measured using instruments located on high mountains, such as the Kitt Peak, although for the UV errors by scattering and beam attenuation must be considered. The best method is to use satellite-mounted sensors. An example for a spectrum measured with such a system is given by [*Wehrli 1985*]. It has units [W m^{-2} nm^{-1}], this is a quantity of type E_0. Be this solar E_0 henceforth named S_0. Figure 5.1.2 shows the spectrum of S_0. The integration over wavelengths yields the Solar Constant S = 1368 W/m².

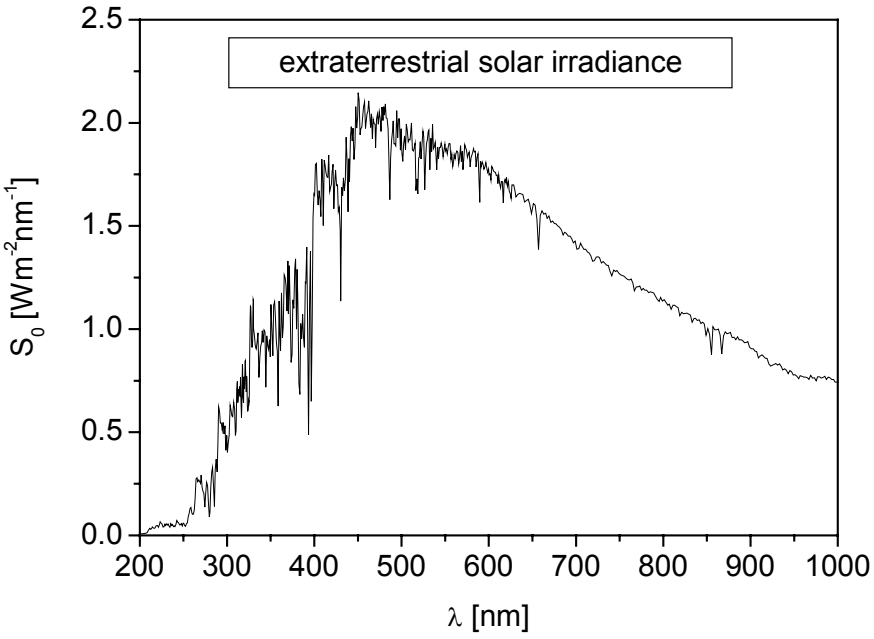

Figure 5.1.2 The extraterrestrial solar irradiance by [Wehrli 1985]

5.2 Radiative transfer equation

The temporal and spatial development of f is described with Boltzmann's equation[1]:

$$\frac{df}{dt} + \nabla_{\vec{r}}(\vec{c}f) + \nabla_{\vec{c}}(\vec{a}f) = Q(\vec{r},\vec{n},\lambda,t) \tag{5.2.8}$$

Q is the source term which comprises the net change of photons per unit time which can be described with the flux. ∇_r is the operator differentiating for *r^;* ∇c differentiates for velocity. The photons propagate with constant light speed c and are not accelerated. Thus (5.2.8) becomes:

$$\frac{df}{dt} + c(\vec{n}\nabla_{\vec{r}})f = Q(\vec{r},\vec{n},\lambda,t) \tag{5.2.9}$$

[1] *See e.g.[Thomas et al. 1999, Buchwitz 2000, Marquard 1998] for this section*

This is a continuity equation for the photon gas. When considering only our time interval *dt* which be short as compared to time scales of photon flux changes, and using (5.1.7) we find:

$$(\vec{n}\nabla_{\vec{r}})L(\vec{r},\vec{n},\lambda,t) = hc\lambda^{-1}Q(\vec{r},\vec{n},\lambda,t) \tag{5.2.10}$$

To specify Q, we consider a medium which scatters, absorbs and emits the radiation in plane-parallel geometry. We introduce the absorption and scattering coefficients β_{abs} and β_{sca}:

$$\beta_{sca}(z,\lambda) = \sum_i \beta_{sca,i}(z,\lambda), \beta_{sca,i}(z,\lambda) = \rho_i(z)\sigma_{sca,i}(\lambda) \tag{5.2.11a}$$

$$\beta_{abs}(z,\lambda) = \sum_i \beta_{abs,i}(z,\lambda), \beta_{abs,i}(z,\lambda) = \rho_i(z)\sigma_{abs,i}(\lambda) \tag{5.2.11b}$$

$$\beta_{ext}(z,\lambda) = \beta_{sca}(z,\lambda) + \beta_{abs}(z,\lambda) \tag{5.2.11c}$$

with ρ_i as number density of the scattering and absorbing matter #i and σ_i as respective cross sections.
The change in radiance then is:

$$cos(\theta)\frac{dL}{dz} = -\beta_{ext}L + \frac{\beta_{sca}}{4\pi}\int_0^{2\pi} d\varphi' \int_0^{\pi} \phi(z,\theta,\varphi,\theta',\varphi',\lambda)L\,sin(\theta')d\theta + \beta_{abs}(z,\lambda)B(T(z),\lambda) \tag{5.2.12}$$

In this z is the vertical coordinate; ϕ we already have introduced as phase function for the scattering process. The change in *L* along *z* is thus governed by:

- extinction, proportional in strength to the radiance available for extinction
- contribution of photons from scattering out of the surrounding 4π sr
- emission, proportional in strength to the absorption

If we consider our atmosphere and if we look at VIS and UV wavelengths, we find that excited electronic states get de-excited by collisions, hence we have no emission, and the last term disappears. Introducing the vertical optical depth τ:

$$\tau(z,\lambda) = \int_0^{\infty} \beta_{ext}(z',\lambda)dz' \tag{5.2.13}$$

and the single scattering albedo

$$\omega(\tau,\lambda) = \frac{\beta_{sca}}{\beta_{ext}} \tag{5.2.14}$$

and inserting them into (5.1.12) we obtain (omitting the dependencies):

$$\cos(\theta)\frac{dL}{d\tau} = -L + \frac{\omega}{4\pi}\int_0^{2\pi} d\varphi' \int_{-1}^{1} \phi L d\cos(\theta)' \tag{5.2.15}$$

This the integro-differential form of the radiative transfer equation (RTE).
If we neglect multiple scattering, we lose the second term because scattering only reduces the radiance at a given point along *z*. The remaining equation is solved with

$$L = L_0 e^{-\tau/\cos(\theta)} \tag{5.2.16}$$

which we recognize to be Lambert-Beer's law for a radiance L0 propagating along a direction tilted by θ against the vertical axis. The solution of the RTE shall be the subject of the following sections. The goal is to derive *L* for a given location within a model atmosphere.

5.3 Analytical solution approaches to the RTE

5.3.1 Two Stream Approximation

One of the basic radiative transfer models is the Two Stream Approximation. It uses the following assumptions:

- Plane parallel atmosphere
- Horizontal homogenity, the sideward flux into a volume and out of it cancels out
- Energy transfer is performed by radiation only, i.e. no convection present.

Consider a plane parallel atmosphere. The light of wavelength λ and intensity *I* is impinging from an angle θ (Fig. 5.3.1). The transmission *T* through a layer of thickness *dz* between altitudes z_1 and z_2 with optical density τ is

$$T = \frac{L(z_2)}{L(z_1)} = e^{-\tau/\cos(\theta)} \tag{5.3.1}$$

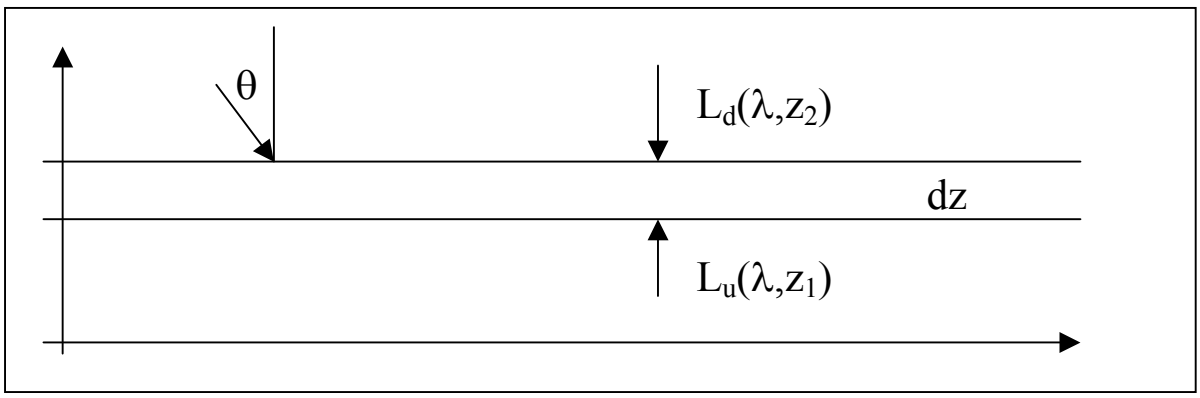

Figure 5.3.1 Situation of the Two Stream Approximation for solution of the RTE

Because the radiation does imping from all directions instead of one only we have to integrate over the surrounding sphere:

$$T(z_1, z_2) = \frac{1}{\pi} \int_0^{2\pi} d\varphi \int_0^{\pi/2} e^{\tau/\cos(\theta)} \cos(\theta)\sin(\theta) d\theta \tag{5.3.2}$$

We can now separate the radiance into the downward component L_d and the upward-directed L_u, defined as integral of L over the lower and upper hemisphere, respectively.
$L_d(z)$ at altitude z also is composed from the downward contributions of scattering centres at all altitudes above z, weighted each with the transmission $T(z,z')$ from any z' down to z (see scenario in section 4.5):

$$L_d(z) = \int_z^\infty L(z')T(z,z')dz \tag{5.3.3}$$

$$L_u(z) = L_d(0)AT(z,0) + \int_0^z L(z')T(z,z')dz \tag{5.3.4}$$

The same applies to $L_u(z)$. The latter formula contains as first term the light reflected off the ground, which is just L_d at $z' = 0$ multiplied with albedo A and weighted with transmission from 0 to z. The net radiance is the sum of both components:

$$L(z) = L_u(z) - L_d(z) \tag{5.3.5}$$

5.3.2 Discrete Ordinate Method

In the Two Stream Approximation the radiation at a given location is divided into the upwelling and the downwelling part. This approach can be made more differentiated, hence more accurate, by considering not two but four, six or more directions (Figure 5.3.2).
The radiance is then formulated as um over these directions or "ordinates".

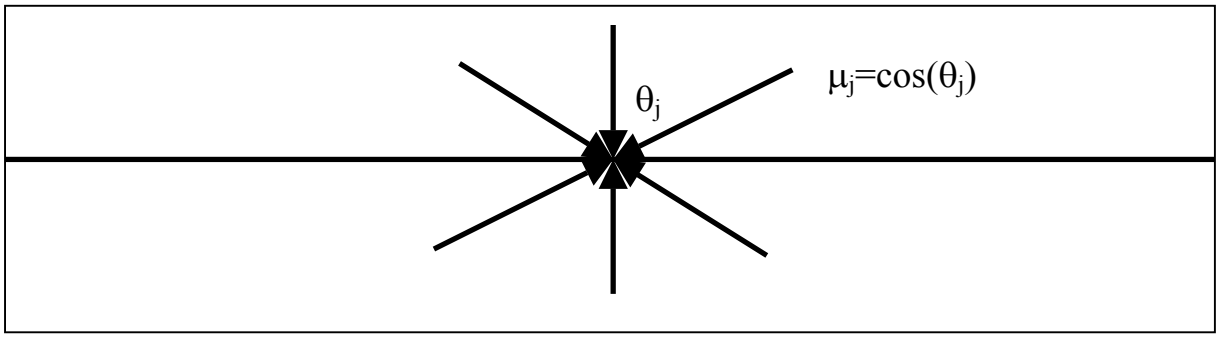

Figure 5.3.2 Discrete Ordinate Method; the radiance incoming at a given place is calculated along several directions

$$\int_{-1}^{1} d\mu L(\mu) \approx \sum_{j=1}^{m} w_j L(\mu_j) \tag{5.3.6}$$

Here, μ_j denote the discrete ordinates, expressed as cosines of the angles to the vertical. The w_j are the "quadrature weight", chosen so that (5.3.6) is fulfilled approximately.
This approach is the "Discrete Ordinate Method" [*Dahlback and Stamnes 1991*]

A prominent example for this method is DISORT, developed and operated by NILU (Norway) and IASB-BIRA (Belgium) [*Kylling 1995*]. DISORT features are:

- full treatment of MS and
- refraction
- pseudospherical geometry (direct beam only)
- treatment for aerosol scattering, cloud scattering, ground albedo
- supported viewing geometries: zenith, nadir, off-axis.

5.3.3 Finite Difference Method

The Finite Difference Method separates the direct from the diffuse radiation, the latter being defined as radiation which has been scattered by atmosphere particles once at least. The source is the solar radiance L_0 impinging from an Solar Zenith Angle θ. As in the case of the Two Stream Approximation the radiation is separated in the downward and upward radiance components; for the direct radiation they are:

$$L_{d,dir}(z,\cos(\theta),\varphi) = L_d(z,\cos(\theta),\varphi)e^{-\tau(z)/\cos(\theta)} \tag{5.3.7}$$

$$L_{u,dir}(z,\cos(\theta),\varphi) = AL_0\cos(\theta)e^{-\tau_0/\cos(\theta)}e^{-(\tau_0-\tau(z))/\cos(\theta)} \tag{5.3.8}$$

A again is the albedo, τ_0 the total optical density of the atmosphere. The equations for the diffuse field contain the scattering contributions from the upward and the downward radiation. The RTE for the upward diffuse radiation is:

$$\cos(\theta)\frac{dL_u}{dz} = -\beta_{ext}L_u + \frac{\beta_{sca}}{4}\int_0^{2\pi}d\varphi'\int_0^{\pi/2}\phi(z,\theta,\varphi,\theta',\varphi')L_u\sin(\theta')d\theta \tag{5.3.9}$$

$$+\frac{\beta_{sca}}{4}\int_0^{2\pi}d\varphi'\int_0^{\pi/2}\phi(z,\theta,\varphi,-\theta',\varphi')L_d\sin(\theta')d\theta$$

The equation for the downward field is composed in an analoguous way. The L_u is the total upward radiance, being the sum of the upward direct and the upward diffuse radiance.

$$L_u = L_{u,dir} + L_{u,diff} \tag{5.3.10a}$$

$$L_d = L_{d,dir} + L_{d,diff} \tag{5.3.10b}$$

Eq. (5.3.7)-(5.3.10) can be combined to form two coupled integro-differential equations for the upward and downward diffuse radiance.
As next step the vertical coordinate z is discretized into vertical levels Z numbered 1 to N_z.
The propagating light also is separated into N_μ "streams", denoted by their angle of propagation θ with $cos(\theta) = \mu$.
Then the derivation of L by z (see left hand side of the RTE) is approximated by:

$$\left.\frac{dL_Z}{dz}\right|_{z(Z)} \approx \frac{L(Z+1)-L(Z-1)}{z(Z+1)-z(Z-1)} \tag{5.3.11}$$

The term in the denominator of the right hand side in (5.3.10) is a "finite difference". (5.3.10) can be inserted in RTE for all vertical levels Z , which then can be written in matrix form. The solution of the matrix yields a vector with the radiances for each vertical level.

A widely used example for this method is SCIATRAN, developed by the IUP Bremen [*e.g. Buchwitz et al., 1998*]. The features are:

- full treatment of multiple scattering (MS),
- refraction
- in spherical geometry (direct beam only)
- treatment for aerosol scattering, cloud scattering, ground albedo
- supported viewing geometries: zenith, nadir, off-axis.

5.3.4 Other methods

Other methods of solution of the RTE (5.2.15), not to be explained here, are e.g.:

- The Spherical Harmonic Method
- The Doubling-Adding Method.

5.3.5 Raytracing methods

A technique allowing for fundamental statements on radiative transfer for e.g. Zenith-sky geometry is to compute the attenuation from the sun through a layered (either plane parallel or spherical) atmosphere to "scattering" points distributed along the line of sight, and then "down" from these points into the detector. An example is "AMFHD" [*Frank 1991*].

5.4 The Monte Carlo approach to the RTE

The Monte Carlo approach is a method to model physical processes which are governed by processes with multiple known outcomes occurring with known probabilities. They are simulated by generating random numbers and mapping them to the probability of a given process result. If a process can have two different results, expressed as parameters a_1 and a_2, and one with probability p_1, the other with p_2, the sum of these two must necessarily be one; a Monte Carlo approach generates a random number R out of the interval [0,1]; if R is smaller than p_1, then a_1 is chosen as valid output parameter to base further calculations upon, otherwise it is a_2. If a large number of N model runs are performed, a percentage of N that is just p_1 will yield a_1, while the rest will result in a_2.
In radiative transfer, the propagation of a single photon through a scattering medium is subject to random processes. Though the attenuation of a light beam obeys a well known exponential function, the collision of a single photon with a scattering centre can happen at the very beginning or at the very end of a given distance to cover, just as a radioactive nucleus can emit an alpha particle now or in a thousand years. The probability for the photon to get scattered on its way to a given point is known. So a random number can be used to decide

about this, and a large number of random experiments will reproduce the attenuation of the light beam consisting of a large number of photons.
At the place of scattering, the photon can be scattered into any direction, the probability of a scattering being governed by the respective phase function. Here also a random number can be used to decide which direction this individual photon gets scattered into.
If there were six directions, each occurring with the same probability as in the case of isotropical scattering, a dice-throwing would generate a random number which would decide about the direction. This section will show how to relate the RTE to this scheme.

5.4.1 Relation between MC and the RTE

Consider a light source in a scattering medium emitting a radiance L_0. Since radiance and intensity I_0 in their above definitions are related by an area of our choice, we can identify the one with the other. Both expressions may be used in the following.
We want to know which fraction of this intensity will reach an area segment A. If the light beam is not directed onto A directly, we depend on scattering. A large variety of light paths are possible. We can define each by

- A number n of scattering events e_n and
- the locations R_n of these scatterings.

The location of the source be R_0, the first scattering location be R_1. The distance between these two places, $|R_1\text{-}R_0|$ leads to an attenuation of I_0 by T_1. So at R_1, the intensity

$$I(R_1) = I_0 T_1 \tag{5.4.1}$$

Is received. Now the scattering location must be regarded as an infinitely short, but nonnegative elongation dr of the preceding path segment. The intensity $I_{1\to 2}$ scattered from any point along dr into the direction of R_2 depends on (see integral term in (5.2.15))

- the intensity reaching this point I_1
- the scattering centre density at dr, ρ, assumed uniform within our experiment
- the scattering cross section σ, assumed constant within our experiment
- and the integrated phase function value $\phi(\theta_1)$

The integrated phase function value $\phi(\theta_1)$ must be understood as integral of the phase function over a solid angle defined by an infinitely small scattering angle interval $\theta_1 \pm d\theta$. θ_1 is the scattering angle necessary to continue the path along the second chosen segment. At this point, we must consider the light as not perfectly collimated but as radiance defined for this solid angle. With solid angle 0, the integral of the phase function would be zero, and so would the probability to scatter "into" this solid angle. dr, ρ and σ, and the phase function $\phi(\theta_1)$ form the probability P_1 of a scattering taking place and directing the photon into the appropriate direction:

$$P_1 = \phi(\theta_1)(1 - e^{(-dr\rho\sigma)}) \tag{5.4.2}$$

The formula for $I_{1\to 2}$ follows to:

$$I_{1\to 2} = I(R_1)P_1 = I_0 T_1 P_1 \tag{5.4.2}$$

To derive the intensity (radiance) I_n finally reaching the area segment along the specified way we must successively form the product of transmissions along the path segments and the scattering probabilities at the scattering locations.

$$I_n = I_0 \prod_{i=1}^{n} T_i P_i$$

(5.4.3)

The total intensity I reaching the detector can also travel along paths with any other number m of scattering events: I_2 may denote the intensity traveling along a path with 2, I_3 with 3 scattering events.

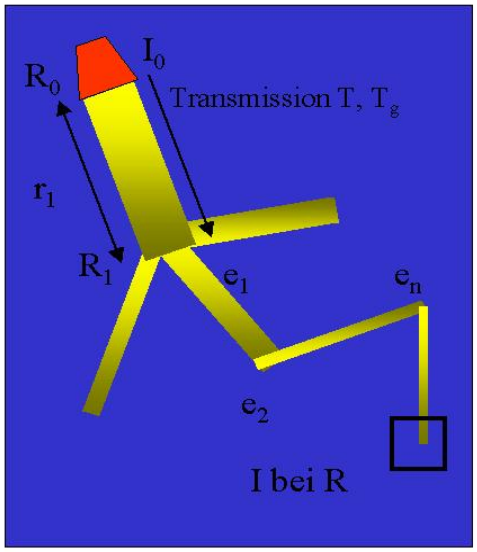

Figure 5.4.1 A light path with n scattering events between source and area segment. The colour shading indicates the attenuation along each segment. The transmission T_g denotes possible attenuation by gas absorption.

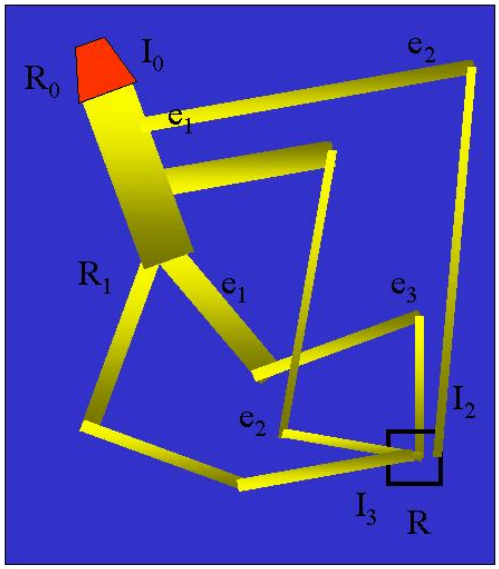

Figure 5.4.2 Light path with varying numbers of scattering events

Naturally the intensity reaching the aera segment does not travel there along one path only, but along multiple ones. If I_0 consists of a finite number of N photons, the number of paths between source and area segment (detector) will also be finite, as will the number of paths with any given integer number of scattering events. Be J_n the sum of all intensities along a total of m paths with n scattering events such as I_n:

$$J_n = \sum_{j=1}^{m} I_{n,j} \tag{5.4.4}$$

The total intensity I reaching the detector can also travel along paths with any other other number m of scattering events: I_2 may denote the intensity

$$I = \sum_{k=1}^{\infty} J_k \tag{5.4.5}$$

This intensity I is the light reaching the detector along all paths possible.
When including $k = 0$ we also take account of direct light, which of course must be weighted with the transmission T_0. Since the direct light treatment is simple, its inclusion into (5.4.5) straight forward and since DOAS measurements mostly feed of scattered light, we will disregard it in the following.
As apparent in Fig. (5.4.2), at the detector location, the terminal segments reach the detector from any angle out of 4π sr. Thus I represents a sum over (spectral) radiances L. E, the scalar irradiance, comprises all those L. When recalling the RTE for the radiance change along a vertically oriented dz , replacing L by E, which renders useless the cosine term and omitting the direct light term, and replacing the integration over angles θ and φ by integration over 4π, we find (beβ_{sca} appropriately normalized):

$$\frac{dE}{dz} = \frac{\beta_{sca}}{4\pi} \int_0^{4\pi} d\Omega \phi(\Omega, \Omega^{|}) E \tag{5.4.6}$$

The right hand side describes all intensity (or radiance, when considered per solid angle interval) getting scattered onto our segment from out of the surrounding sphere. We can now discretize the unity sphere into O segments $d\Omega_o$. Each of these sphere segments will be passed by intensities I_o which are the sum of all intensities scattered by $n \in [0,\infty]$ events. These intensities are just what is integrated over in (5.4.6). Thus we can convert (5.4.6) into a summation:

$$\frac{dE}{dz} = \frac{\beta_{sca}}{4\pi} \sum_{o=1}^{O} \phi(\Delta\Omega_o, \Delta\Omega^{|}_o) E \Delta\Omega_o \tag{5.4.7}$$

The term $\phi(\Delta\Omega_o, \Delta\Omega'_o)$ describes the probability for a photon reaching a scattering location from solid angle interval $\Delta\Omega_o'$ to get scattered into $\Delta\Omega_o$, i.e. through the unity sphere segment we integrate over. This indicates that each scattering location contributing to either the integral in (5.4.6) or the sum in (5.4.7) itself is fed from the entire surrounding 4π.
This means that any contribution E_o, defined at the unity sphere surface section defined by $\Delta\Omega_o$ in itself is the sum of contributions of scattering surrounding this surface section.

- Since we freely can discretize E_0 in its components E_0,s scattered at distances s from the detector, weighting them with the appropriate transmissions Ts,
- since we can discretize them into the contributions which have suffered a given number of n scatterings
- and since we can bring dz to the right hand side in (5.4.7) to combine with β_{sca} to P_i

we find that (5.4.7) describes the light scattered onto our detector area along all possible paths in the same way as (5.4.5) does.

This means that a Monte Carlo experiment using the known physical parameters of attenuation and scattering will reproduce the radiation field generated by a source and measured with a detector.
The advantage of the Monte Carlo technique to RTE solution is that any scattering process and any geometry can be modelled with equal accuracy. No approximations to e.g. pseudo-spherical geometry and no limitation to e.g. direct beam are necessary. Moreover, the derivation of information on the scattering locations can be derived, which yield valuable insights into the reasons for the e.g. SZA-dependency of a given AMF.

5.4.2 Backward Monte Carlo technique

The strict Monte Carlo experiment is to "fire" photons out of a light source along initial directions governed by the aperture of that source; e.g. in case of the sun the half solar aperture angle of 0.267° [*Meeus 1992*] is used. Then random numbers govern the entry of the photons into a model atmosphere, where they are scattered, by which scatterer, and in which direction. The photon direction is accordingly altered at each scattering location modelled. In their random walk, eventually the photons will either leave the atmosphere or reach the altitude (zero for simulated ground based measurements) where the modelled detector is located. There, the impact location and the incident angle are compared to the detector specifications. Each radiative transfer process can be modelled and reproduced with accuracy, and no approximations are needed. The absorption would be modelled by the destruction of the photon and the abort of the path calculation.
The problem in this is that the detector must reproduce realistic dimensions and aperture angle, i.e. the photon not only must reach the detector altitude, but must actually hit the detector, and do so from a solid angle defined by the line of sight and the aperture angle.
When comparing a calibrated radiometer measurement of the radiance out of a solid angle defined by 5° around zenith, we find the irradiance computed from the measurement to be smaller than the extraterrestrial solar flux by a factor of order of $1*10^{-4}$ in bright daylight, even lower for aerosol loads present. This reduction is caused by the attenuation and absorption in the atmosphere as well as by the directional entrainment of the aperture angle. If we use a detector of detector area 1 cm^2, which is a realistic figure for e.g. DOAS telescope lenses, and model the solar irradiance by photons impinging onto the projection of the sphere formed by the planet and the atmosphere of 70 km altitude, we find that the detector covers a fraction of order of $1*10^{-18}$ of the total surface. This results in a total probability for one single photon to get "recorded" by the instrument of order of $1*10^{-22}$. For a simulation of a scattered light measurement one photon is not sufficient, since a representative image of all photon paths contributing to the measurement is desired; as will be shown later, at least 1000 photon recordings are necessary. This results in the requirement to model $1*10^{25}$ photon paths for one single simulation. To reduce the illuminated area of the earth to a segment of e.g. 100 km centered at the detector increases the probability by orders of magnitude, but by far not sufficiently so. Hence this approach is not recommendable.

An effective solution to this problem was formulated by e.g. [*Blättner et al. 1974*].
Equation (5.4.5) consists of a sum of products. These products are valid also for photons coming from the detector and hitting the source. This means that (5.4.5) describes as well the intensity emitted from a detector and reaching the source. The probability for a photon to leave the source (defined itself by its area and aperture angle) and reach a detector under the required conditions is the same as the probability that the photon leaves the detector on the way it entered it and reaches the source, i.e. follows backward the path it has in fact covered in forward direction. This is feasible, since any transmission probability (the probability that a

photon covers the distance d from one given point to another) and any scattering probability (for a given scattering angle θ to occur) are the same in both directions; especially since the phase functions known so far are in their average symmetric around the original trajectory, a scattering by 42° to the left is as probable as a scattering by 42° to the right if we follow the process in reverse direction. This approach is called "Backward Monte Carlo".
In the case of a DOAS measurement the sun is a far easier (larger) target to hit than is the comparably tiny detector placed in the field; hence it reverting the photon paths promises a far higher efficiency. But even so the fraction the sun occupies on the surface of the unity sphere surrounding the model system is of order of 10^{-6}. This is the probability that any random generated path will indeed lead into the sun.

Hence we must, at one point, deviate from strict Monte Carlo doctrine and connect the random walk path with the direct solar beam, if available for the point of the path considered, e.g. not located within the earth's shadow. The most recent example for this is "AMFTRAN" [*Marquard 1998*]. The probability p of a given path defined by n scatterings (i.e. their locations and scattering angle intervals $\Delta\Omega$):

$$p_n = \frac{I_n}{I_0} = \prod_{i=1}^{n} T_i P_i \tag{5.4.8}$$

We can consider a light beam as consisting of N photons, together with a given initial intensity I_0. At the end of the considered path, only I_n ($<< I_0$) reaches the last path point; this equals the fraction of photons out of the initial N that follows this path.
The first n-1 segments are generated by random numbers as in the case of Forward Monte Carlo; when generating a large number of paths, e.g. of the order of 1000 or 10000, I_0 is represented by all photons launched. The probabilities of paths with a given number of scatterings, scattering angle intervals and distances covered between two scatterings is reflected by the frequency the paths occur within the modelled path ensemble. Paths with improbable features, such as very high numbers of scattering events or scattering events in areas with low scattering centre density, will occur seldomly, and their contribution will be small.
In (5.4.8) we can separate the probability P_n for the last scattering event before the photon leaves the model atmosphere as well as the transmission T_n for the attenuation along the direct path between this last point and the top of atmosphere (TOA).

$$p_n = P_n T_n \prod_{i=1}^{n-1} P_i T_i = P_n T_n p_{n-1} \tag{5.4.9}$$

The product of these two quantities also is the probability for an incoming solar photon passing this scattering location to get scattered into the direction the (n-1)th photon path segment does define. It can be calculated analytically, and the intensity of the sub-beam can be scaled with it. The last segment of the random-generated light path is then artificially replaced by a segment leading into the sun. The result is a valid light beam between sun and detector. The trace gas absorption and other quantities are derived and contribute to the total result of the simulation.

6. The 3D Monte Carlo RTM „TRACY“

6.1 Previous RTM used for DOAS

Prior to models taking account of multiple scattering, analytical models were in use calculating fist the attenuation of a direct solar beam from the TOA through a layered atmosphere to one of an array points apced along the line of sight of the simulated detector, then down from this “scattering point” into the instrument, to conclude on the radiance contributins from different altitude layers as well as on the AMF of absorbers present in the model atmosphere. Examples are given in [*Noxon et al. 1987*] and [*Solomon et al. 1987*], as well as in [*Frank 1991*] (“AMFHD”), and [*Schulte 1996*] (“DAMF”).
These programs essentially are single scattering algorithms, i.e. they calculate the probabilities of paths (the intensities reaching the detector along them) with only one scattering event. For long wavelengths, e.g. in the “red” region, or in the IR, the assumption of only one scattering is feasible for Zenith-sky geometry, though not for the UV. Light paths with higher numbers of scattering (“higher oders of scattering”) can contribute significantly to the recorded signal.
The Backward Monte Carlo RTM “AMFTRAN [*Marquard et al. 1995, Marquard et al. 1998*] used the Backward Monte Carlo technique to account for multiple scattering. “AMFTRAN” served a lot of fundamental purposes, and included features such as Off-axis, or satellite-nadir, to account for the new geometry of the GOME system. A lot of effects in radiative transfer, e.g. related to O_4 measurements, could be reproduced. But “AMFTRAN” did not support all geometries needed at the time of this writing, e.g. airborne Off-axis, and very slant lines of sight in ground based Off-axis, suffered from problems with high SZA and it was limited to a fixed altitude grid.

6.2 Motivation and requirements

The considerations outlined in section 4.5 are of only qualitative nature. At SZA > 70° the sphericity complicates the geometrical calculations. The scattering angle modifies the intensities along each light path. Especially when more than one scattering event occurs, any geometrical approximations are rendered invalid.
Photons that have been scattered out of the direct path on its way to the line of sight may get scattered again and enter the instrument from a different direction. The presence of aerosols with their different phase functions further complicates the problem of deriving light paths and, hence, Air Mass Factors of one or the other kind. Many different light paths contribute to a scattered light measurement and to the spectroscopic signal derived from it.
The model presented in this work had been conceived as model to interpret the SCD from DOAS measurements. This implies the derivation of AMF for a given wavelength.

Such a model should be as close to reality as possible. This requirement includes the following list of features supported:

- Three-dimensional structure to support 3D variations in trace gas concentrations as well as environmental parameters
- Variable discretization within the structure in all three spatial axes
- Flexible and variable trace gas and aerosol load concentration input
- All scattering and attenuation processes relevant to the transfer of light of a given wavelength including albedo
- Flexible aerosol scattering parametrization
- Atmospheric refraction
- Variable detector location (latitude, longitude and altitude)
- Variable viewing direction (rotation of line of sight around two perpendicular axes)
- Variable field of view

Another, rather formal but indispensable, requirements is the usability of the code. This implies:

- Compatibility with the most widely used operating system
- User interface usable without extensive preparatory studies

The program should be usable on any modern windows PC or notebook used in scientific institutes and readily available from IT stores. Ultimately the program should be able to run on a notebook at a measurement campaign to assess the sensitivities of measurement geometries for the planned operations. The fundament to this work was done by [*Morgner 2000*] who devised elements of a flexible, object-oriented software structure as well as the geometrical routines. This included the possibility to search for a specific parameter, e.g. the scattering altitude, in a computed path.
The goal of the present work is to develop and make more efficient both the method and the code, expand the sets of control and output parameters calculated with and for, expand the object structure to support all DOAS geometries, devise a user-interface for input and result output and convert the software into a flexible, easy-to-use RTM for DOAS applications.
Special efforts were undertaken to adapt the program to the needs and points of view of a DOAS experimentalist in the field.
Many routines were combined, others completely rewritten and/or added additional functions.
In the following sections the core of this thesis, the spherical 3D RTM TRACY[1] is described.

6.3 The backward Monte Carlo implementation

The photons emerging from the atmosphere are facing a surrounding sphere out of which the sun covers only a surface fraction of $5.4*10^{-6}$ (derived from the solar half aperture angle of 0.267° [*Meeus 1992*] which the photons must hit. As already stated in section 5.4.2, the next and necessary step to gain efficiency is to model the path to a given point, and then compute the probability for the photon getting transferred into the sun analytically.
The photons are assigned a weight (representing and named the intensity of a light beam travelling along their way) that is scaled by the derived probability.
This process of "intercepting" the photon to ensure it to take its way into the sun is in this thesis named "forcing".

[1] **T**race gas **RA**diative Monte **C**arlo **Y**(I)mplementation

The forcing tactics is applied to any photon path that did not end in the sun by itself, which is true for the great majority of random generated paths. After this has happened, the forcing consists of six steps:

1. The scattering probability along the last (n-1)th modelled path segment of length L between the modelled last scattering point *LSP* and the atmosphere exit point *AEP* is derived from the integration of Rayleigh and aerosol scattering coefficients over this etape. Since this probability will be part of the "artficial" nth segment, it is named $p_{s,n}$.
2. A random number $R_l \in [0,L]$ selects the "new" scattering location between *LSP* and *AEP*.
3. A random number $R_s \in [0,1]$ selects the scatterer from the normalized sum over the Rayleigh and the (eventually multiple) aerosol scattering coefficients. If e.g. R_s is smaller than the Rayleigh coefficient (after normalizing), then Rayleigh is identified as scatterer for the "new" scattering; otherwise, it is one of the aerosols present.
4. The probability of the new nth scattering leading into the sun (i.e. for the appropriate scattering angle necessary to "hit" the solar disk) is derived from the phase function of the selected scatterer, $p_{p,n}$.
5. The photon is then set to the coordinates of the new scattering point and given the directional vector of the sun. The intensity weight is scaled with the product $p_{p,n} * p_{s,n} = p_n$.
6. The path etape between the new scattering point and the new atmosphere exit point is calculated with no more scatterings allowed. The transmission probability t_n (= 1-scattering probability) along this etape is calculated, analoguously to step 1; the photon weight is scaled with t_n as well[2].

Four cases do occur:

1. The photon leaves the atmosphere and is already headed for the sun, i.e. its directional vector encloses with the direction to the sun an angle smaller than or equal to the 0.52°. In this cases the photon weight is not altered and the path is fully contributing to the further calculations. This case is very rare in scattered light simulations.
2. The photon, after emission by the detector, is not scattered and directly hits the sun after a straight path through the atmosphere. In this case again no weight scaling is applied. This case occurs in direct light simulations.
3. The photon leaves the atmosphere after a scattering event in a direction not leading into the sun. In this case the forcing is applied as described above.
4. The photon does not get scattered and leaves the atmosphere in a direction not leading into the sun. In this case the entire path is considered as last etape (and the detector location as LSP) along which the forcing is applied.

The net effect is to add one scattering event to each path. Since the fraction of photons that have been scattered already n times that get scattered a (n+1)th time is governed by the probability of a new scattering to occur along the etape between the nth scattering and the top of atmosphere, which is just $p_{s,n}$, it is obvious that the ratios between the intensities of succesive scattering orders is reproduced. The use of each photon modelled ensures efficiency and comparable statistics for each wavelength chosen for modelling.
The following sections and chapters will entirely deal with backward modelling and/or will present and discuss results obtained with this technique.
Chapter 13, though, will briefly present an implementation of forward Monte Carlo and show application examples.

[2] In case further scattering is allowed after the forcing on the last etape, the attenuation is calculated only up to the nest scattering event. From this on, the photon is treated as if not yet forced until it emerges the atmosphere once again.

6.4 Geometrical structure

6.4.1 Coordinate system and "voxel" structure

The model employs full spherical three-dimensional geometry.
When measuring with high solar zenith angles or with slant viewing geometries, the light paths are affected by the atmosphere's sphericity. Even when investigating situations for which sphericity is not of significant importance it strictly first has to be proven to be of insignificance by modelling with sphericity and comparing to cartesian geometry model results. But at this point the derivation of "cartesian" model results is abundant since the inherently more accurate spherical calculation already exists. For this reason, the cartesian geometry has been abandoned, and the model was fixed to spherical geometry, although with variable discretization in all of the three dimensions.
The earth sphere is modelled with realistic size, its central point being the cartesian coordinate system's origin. The z-axis runs through the model earth's north and south pole, being positive in the „north", negative in the „south".

Three coordinates are used:

- ϑ, the angle between the z axis and the location or direction vector in question; it also represents the geographical latitude of any modelled location.
- Φ, the azimuth angle. $\Phi = 0$ is valid for all vectors with y = 0 in the cartesian system. Thus it represents the longitude of a given location vector.
- **Z**, the amount axis. It represents the distance from the earth centre, and thus the altitude of any given location. If any altitude is defined as "above sea level", the earth radius 6370000 is added to this altitude to yield the correct **Z**-coordinate.

In the following, these coordinates be addressed with the bold face letters introduced.
The coordinates define three dimensional grid cells, or volume pixels („voxels") within which the modelled detectors are located, and the modelled photons are to operate.
All points with a given ϑ-value form a cone, of which the tip is the system's origin. All points with a fixed Φ form a plane, which rotates, when Φ is varied, around the z-axis of the cartesian system. An finally any vectors with same **Z** value form a sphere.
This means each voxel is enclosed by three pairs of geometrical surfaces: two cones, two planes, and two spheres. It can be defined by two ϑ, two Φ, two **Z** values, which are in turn defined by the respective axis's chosen discretization. This leads to a three-dimensional numbering of the voxels used in the model. For the ϑ- and Φ-axis, the first voxel coordinate numbers, i_ϑ and i_Φ, are zero, for the Z-axis, i_Z, it is 1.
This preserves the option for the implementation of a ground voxel, within which e.g. radiatiave transfer processes within the earth's surface could be modelled. The voxel with $i_Z = 1$ is the lowest one, extending from altitude $\mathbf{Z}_1$=0 (above earth surface, as stated) to $\mathbf{Z}_2$.
The first values of the ϑ- and Φ-axis, ϑ_0 and Φ_0, are fixed to zero. If the next one, e.g. ϑ_1 is e.g. 0.785 rad (45°), the voxel with ϑ-coordinate number i_ϑ=0 is limited by the cones defined by ϑ_0 and ϑ_1 and include the „north pole".
The voxel with $i_\vartheta = 1$ are enclosed by the ϑ_1 and ϑ_2 cones and thus form a „collar" running around the „earth". The voxels with $i_\vartheta = N_\vartheta$ encompass the „south pole".
The voxels with $i_\Phi = 0$ are limited by the plane which contains the „0-meridian line" on their one side, and the plane defined by Φ_1 on their other side.
The voxels with $i_\Phi = 1$, being defined by the Φ_1- and Φ_2-planes, are adjacent to the voxels with $i_\Phi = 0$; so are the voxels bearing $i_\Phi = N_\Phi$, closing the ring around the „earth" sphere.
The discretization is freely chosen by means of an ASCII file („space.txt", see manual in the appendix) with the numbers of discretization steps for the ϑ-, the Φ- and the **Z**-axis, N_ϑ, N_Φ

and N_Z in the first line and the selected coordinate values ϑ_i, Φ_i (in units radian) and $\mathbf{Z}_i$ (in unit km, above earth surface) of the limiting surfaces in the three lines below.
The “Top Of Atmosphere”, TOA, can thus be chosen by the value $\mathbf{Z}_{Nz}$.
The defined voxels are assigned air number densities, pressures and temperatures, as well as trace gas concentrations and aerosol type extinction coefficients. From these initialization parameters, others are derived such as refractive indices and total extinction coefficients. From the aerosol extinction coefficients, the scattering and absorption coefficients are taken. Also clouds can be inserted here, as number densities of droplets of different sizes. A different cloud treatment, and the one used in this work, is the definition of a cloud layer of parameters altitude, coverage, albedo and transmission, see section 4.4. The parameters can be obtained and worked with by any routine that is given the respective voxel object.

6.4.2 Locations and directions

All modelling parameters are defined with respect to the above described geometry. Three vectors are defining the beginning and terminating segment of each photon path. These are the current photon location and direction, and the direction vector of the sun, which by definition is the terminating element of any photon path modelled in backward Monte Carlo with forcing. The initial photon location is the one of the “emitting” detector.
This position is initialized by the user with three floating point variables:

- geographical latitude in [°], the detector’s ϑ-coordinate in the spherical system,
- geographical longitude in [°], the Φ-coordinate in the spherical system,
- altitude, in units [m], defined as altitude above sea level, defining the **Z**-coordinate. For simulated ground-based operations, the altitude is near or equal zero. For balloon or aircraft campaigns it my range between 1 and 40 km; and finally for satellites, it is any value larger than the modelled top of atmosphere.

The three location parameters can be selected freely and are not limited or influenced by the spatial discretization.
The solar position vector (briefly named solar vector) is defined relative to the detector position vector with two variables:

- Solar Zenith Angle (SZA or ϑ) in [°], which is the angle enclosed by the resulting solar vector and the local surface normal. ϑ = 90° denotes a sun exactly at the horizon, e.g. during “sunrise”.
- Solar Azimuth Angle (SAZ, A[3]), in units [°]; the detector location and the local surface normal vector define a plane henceforth named “surface plane”; this plane contains a vector between the detector location and the “north pole” of the model coordinate system, i.e. the point with spherical coordinates (0,0,6370000); be this vector called “north vector”. The resulting solar vector can be projected onto the surface plane; the SAZ is then defined as angle between this projected solar vector and the north vector. A = 90° denotes a sun in the east, e.g. during “sunrise”.

Using these definitions, the solar vector is derived by the program using the detector location vector and the input ϑ and A.
Apart from a position the detector is also assigned a line of sight (and multiple ones in MAX DOAS simulations).
This line of sight, abbreviated LOS, is user-defined by again three variables.

- elevation ε in [°], defined as angle between the line of sight and the surface plane; ε = 90° denotes zenith-sky geometry, ε = 5° an Off-axis measurement with upward looking but very slant line of sight, ε = -90° a nadir measurement, and ε = -5° a slant downward-pointing operation; the latter two are realized with airborne or spaceborne platforms.

[3] Greek capital “alpha”

- azimuth φ in [°], defined as the angle between the LOS and the solar vector when both are projected onto the surface plane. The choice φ = 5° leads to a modelled line of sight which "looks" 5° past the sun, and clockwise so. With φ = 180° the device telescope points away from the sun. ε and φ, in conjunction with the detector location, define the vector of the LOS in the coordinate system.
- half aperture angle α_{ud} in [°]. It defines the maximum angle between the initial photon direction and the LOS.
- half aperture angle α_{lr} in [°] in "left-to-right" direction. If it is chosen to be negative, only α_{ud} is relevant to the modelling, defining a cone centered at the detector LOS into which the photons are emitted. The initial photon direction is derived by this LOS taken as basis, which is tilted in a random direction by an angle randomly chosen out of the interval [0, α_{ud}]. If α_{lr} is non-negative, the aperture chacateristics of the detector is elliptical: Two vectors are defined which both are perpendicular to the LOS, see below "detector" object description. In slant viewing geometry, elevation $|\varepsilon| < 90°$, one of these vectors points in "up-down" direction, the other on in "left-right" orientation. Then a random number is generated defining the scaling factors (both negative or positive) of a third vector composed from these two vectors. A large number of repetitions makes this vector describe an ellipse on the surface of a surrounding unity sphere. The angle between this vector and the LOS defines the new aperture angle α for this individual photon. Along this new vector the photon direction, initially the LOS, is tilted by an angle $\in [0, \alpha]$.
- For completeness be here listed two more parameters and flags defining the detector. The polarization-related ones are listed and explained in the respective section. The detector area a in [cm^2] denotes the light-collecting area of the instruments. Depending on this instrument, this is e.g. the area of the telescope front lens.
- The dimensionless integer cosine flag, if set to 1, weighs the outgoing photon with the cosine of the angle between the initial direction and the LOS. If the flag is 0, no such weighting is applied.

6.5 Photon unit concept

The strict Monte Carlo idea projects photons, being the modelled equivalent of real photons, with wavelength and polarization properties. One single real photon can either pass a given distance through a set of absorbers specified, or it can be absorbed. Though it is easy to implement this concept, the statistical noise would make it difficult to discern the optical density of a given species, more so if an overall OD of e.g. 1% is composed from the absorptions of several species, which all are to be distinguished from each other for AMF determination. A second problem occurs when trying to model several wavelengths of a given spectrum. Within strong absorption areas, such as the centre of Fraunhofer or water vapour absorption lines, a far smaller number, often by orders of magnitude, of photons must be used than in the case of optically thin spectral ranges. Since it is always the smallest number of photons to limit the statistically governed precision of the result, and since it is desirable to obtain the same numerical precision for the results of all wavelengths investigated, extremely high numbers of photon paths must be calculated for the spectral ranges with low absorption.
So it was decided to assign the model photons an "intensity" value or "weight".
The intensity is modified also when reflexion from a surface of albedo <1 takes place, and in the "forcing" applied at the end of an individual photon path modelling.
It will also play a crucial role in the "forcing" of the photons into the sun (see above). Furthermore, it offers an elegant way to incorporate Raman scattering.

Since photons in the strict quantum physical sense do not possess an intensity but a fixed energy, the modelled photon objects are named “photon units” PU. For ease of reading, they be henceforth also called “photons”. A model runs begins with launching a photon out of the detector and into the cone defined by the detector line of sight and the half aperture angle selected. Then the model calculates the nearest intersection point of this initial trajectory (or in general, of the current photon trajectory) to one of the current voxel’s boundary surfaces, and the distance the photon must cover to reach it.

6.6 Principal algorithms

The sections below explain how the radiative transfer is realized in the Backward Monte Carlo mode of TRACY. For a more detailed description of the various objects including the variables involved see Appendix A, for the manual Appendix B. Not covered below is the Forward Monte Carlo mode, since this so far has not been validated. For the Forward algorithm see chapter 13.

6.6.1 Decision between multiple scatterers

At this point we have a photon travelling along a given distance through a volume with given number densities of scattering particles. Here we must decide

- whether a scattering occurs,
- where along the given distance,
- and by which scatterer

This section will explain how this problem is solved in TRACY.
From the wavelength the Rayleigh-cross section σ_R is calculated. From the voxel it obtains the air number density ρ and the scattering coefficients κ_S of the N_A aerosols.
The aerosols (up to ten different types) are parametrized not only by their phase function a vertical profile of extinction coefficients, but also by a ratio $\varpi' = \kappa_{Abs}/\kappa_{Ext}$, which is equivalent in information to the single scattering albedo ϖ (see section 4.2.4), and must be chosen from appropriate data or reference. This parameter allows for the separation of a given aerosol type into a scattering part and an absorbing one. E.g. with a given number density n (equivalent, for a given cross section, to the extinction coefficient), a given ϖ' means that a fraction $\varpi'$of all interactions photon-aerosol lead to absorption of the photon, as in the case of a trace gas, while $(1-\varpi')$ results in elastic scattering. Hence we can treat the fraction ϖ' of the aerosol particles as additional trace gas to be accounted for when deriving spectroscopic parameters from the completed paths, and $(1-\varpi')$ of the aerosol particles as scatterer like Rayleigh particles. From these data the probability t of transmission without scattering is derived by:

$$t = e^{-d\left(\rho\sigma_R + \sum_{i=1}^{N_A}\kappa_{S,i}\right)} = e^{-d\kappa_{S,tot}} \tag{6.5.1}$$

This formula denotes a function $f(x)$ which is always unity at $x = 0$ and $f(x) = t$ at $x = d$.
This done, the decider generates a random number $R_T \in [0,1]$ and bases the further algorithm upon two cases:
$R_T <= t$: the photon does not get scattered. The output parameter is set to d, the absorber number of the photon to 0.
$R_T > t$: the photon is scattered. In this case the the function (6.5.1) is inverted to map R_T (which is within the interval defined by the function values of $f(x)$ with $R_T \in [0,d]$) to the abscissa:

$$f^{1}(R_T) = x \tag{6.5.2}$$

Due to the exponential character of the function a large enough number of experiments will place more x per unit abscissa axis near the value $x = 0$ than near $x = d$. This reflects real photons to be scattered out of a direct path rather at the beginning of the way along a scattering distance than at the end. This x derives denotes the place along the photon direction and within d the photon scattering takes place. The output parameter d_s is set to this x.

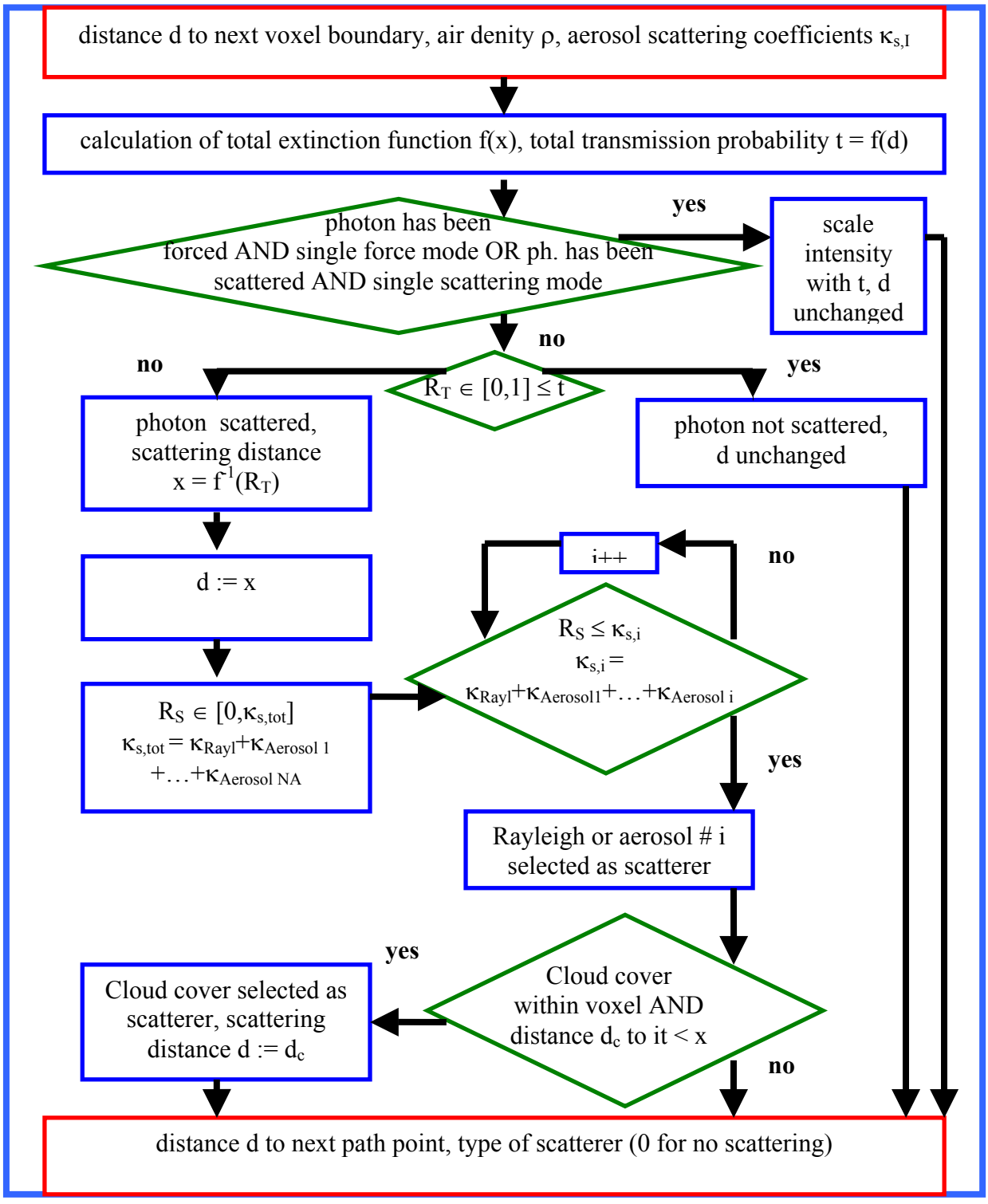

Figure 6.6.1 Flowchart for the algorithm deciding on location and type of scattering events. In red boxes the input/output data are listed.

After this, a second random number R_S is generated with $R_S \in [0,\kappa_{S,tot}]$; $\kappa_{S,tot}$ is the total extinction coefficient introduced in Eq. (6.5.1). This R_S now gets successively compared first to the Rayleigh scattering coefficient, then to the Rayleigh coefficient plus the first aerosol scattering coefficient, then to the sum of the Rayleigh and the first two aerosol coefficients and so forth until it is found to be smaller than one of these sums. If it is smaller than the Rayleigh coefficient, Rayleigh scattering is identified as “responsible” for the scattering of which the existence has been established in the first algorithm step.

If it is larger than the Rayleigh coefficient, it is successively compared to the sum of the Rayleigh and the aerosol coefficients added successively, and the relative sizes of them decide which one is the scatterer.
If clouds are present in the model, it is checked whether the cloud cover crosses the current voxel. If this is the case, it is checked whether the distance d_c to any valid intersection point of the photon trajectory with the cloud cover is shorter than x, and if this is the case as well, the cloud cover is chosen as scatterer.
A different treatment is used when the program is running in the single scattering mode or the single forcing mode and already one scattering event of either kind or a forcing operation has taken place. In this case d is left unchanged but the photon intensity weight is scaled with the transmission probability t. All this is explained in more detail in section A.2.6, where also the relevant parameters are named involved in this algorithm.
Figure 6.6.1 shows a flowchart of this routine.

6.6.2 Path points

In case a scattering event, its type and location, has been selected, the photon is placed on the scattering location. Then the phase function of the respective scatterer (see chapter 4) is used, and a random number is used to derive the scattering angle for this process. The azimuth is also random selected, for details see A.2.7. According to the angle chosen, a new direction for the photon is calculated with an algorithm avoiding multiple time consuming trigonometric calculations of a rotation matrix. Again the next voxel transition point is calculated. In case of cloud cover scattering, a first random number decides whether the photon gets reflected, transmitted or absorbed, before a second one is used for the respective process. In case of a voxel transition, the refraction, if activated by the user, is calculated with a formula using the respective two voxel’s refractive indices in Snell’s formula avoiding singularities (see A.2.8).

6.6.3 Raytracer

The *Raytracer* is the control routine tasked with the modelling of photon paths. Called from the main program for as many times as photons are to be modelled, it performs the following tasks using the appropriate subroutines. First a photon is launched. Then the next voxel intersection and the distance to it is derived. Then the decision is made on scattering type and location, as outlined above, and the selected scattering events are acted upon. Then again the next voxel intersection is calculated until the photon leaves the atmosphere. From the last scattering point, it is forced into the sun (see above). From this last scattering point, no further scattering is allowed after forcing, and the intensity of the photon is scaled with the transmission probabilities through each passed voxel on the way to the TOA.

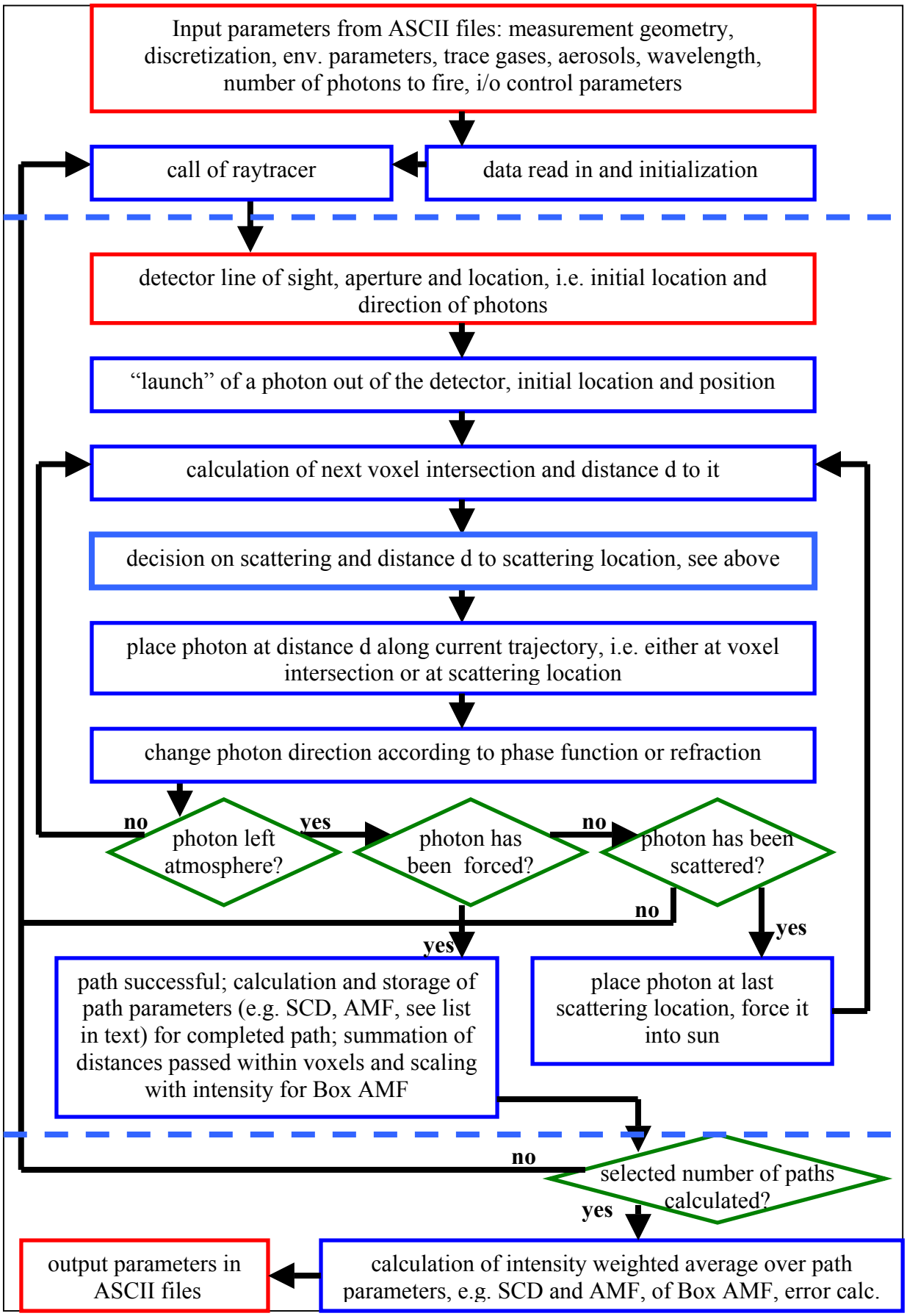

Figure 6.6.2 Flowchart of TRACY. The dashed light blue line comprises the tasks of the raytracer, above and below the line the operations of the main program are depicted. Not shown here are the subroutines, e.g. for geometrical calculations

If the photon, after a forcing, leaves the atmosphere into the direction of the sun, the path is considered successful. In case of a random photon “hitting” the sun without forcing, it is forced nevertheless. The fraction of photons hitting the sun “accidentally” is very small, and equivalent to the small fraction the solar disk covers in the sky. Nevertheless, even in model runs with just a few thousand photons such an event may occur; this would falsify the statistical image of the photon paths with the large (i.e. not reduced by forcing) statistical weight of this single path. If the photon emerges from the atmosphere without any scattering to force off, the path is rejected.
In case of a successful path, the following quantities are derived from the path, mainly by successively summing over the contributions of the path segments within the voxels:

- The SCDs,
- The SODs,
- The aerosol optical density (obtained from the aerosol absorption coefficient)
- The air column density
- The O_4 column density (as derived from the air number density)
- The geometrical path length of the photon path
- *NRS, NMS, NAS*: integers containing the number of the Rayleigh, aerosol and albedo scatterings the photon has suffered so far in its path;
- *FSP*: The location vector of the last scattering event modelled; for a real photon, it would be the first;
- *LSP*: The location vector of the first scattering event modelled; for a real photon, it would be the last;
- *FSA, LSA*: The scattering altitudes in [m] above sea level of the first and last scattering event, respectively;
- *LSD*: The distance in [m] between the detector and the last scattering event;
- Intensity weight,
- The atmosphere entry angle (the angle between photon’s atmosphere exit direction and the local surface normal), called *Entry Angle, EA*
- The angle between the first scattering location vector and the detector location vector, called *First Scattering Angle, FSAN*
- If the calculation of Box AMF is wished, the distances passed within the selected voxels is summed over and scaled with the intensity weight.

These results are stored, and the raytracer routine then terminates, and is called again to compute the next photon path, if the selected number of paths not yet has been calculated.

6.6.4 Result calculation

After the desired number of paths has been computed, the program calculates the intensity weighted average over these quantities; in addition, from the sum of intensity weighs, it calculates the spectral irradiance (i.e. the radiances multiplied by the solid angle defined by the detector aperture, see chapter 8 for derivation) that would have been received by the detector during the simulated measurement. For all these quantities also the error is derived as intensity weighted standard deviation.
All results, the SCD, AMF, numbers of scattering events etc., their errors, as well as the Box AMF are written to ASCII files which can be read in by any common data analysis software.
Figure 6.6.2 shows the flowchart of TRACY, with the light blue dashed line separating the main program from the raytracer; note the insertion of the object deciding on scattering event and location (see flowchart in Fig. 6.6.1)

6.7 Error estimate

As stated, the errors of all parameters are given out as intensity weighted standard deviations.
In this concluding section for completeness some estimates are given on the quantity of the AMF error.
The errors are statistical ones, and thus primarily depend on the number of photon paths contributing to the result, as far as light path and scattering parameters, such as e.g. LSD and NRS, are concerned.
For the AMF, though, the situation is far more complex; the error depend on the number of scatterings the photons suffer after leaving the detector and before ultimately leaving the voxels containing the absorber. Figure 6.7.1 illustrates the relations, again using ground based geometry as an example.
For an absorber very close to the detector (i.e. the ground in this example), most photons traverse it on a similar path before getting scattered.
An absorber profile reaching up higher into the atmosphere, more scatterings occur within the absorber, increasing the variability of the path segments within.
If the absorber is located in the FT or the stratosphere, but below the LSA, a significant variability can be expected for the paths between the first and last scattering events. This increases the AMF error, especially if the profile is of narrow spatial confinement.
An exception to this are VIS wavelengths with the average NRS near 1.
In case the profile is of greater vertical extension, it may comprise the LSA, which increases the light path fraction identical to all modelled paths.
An increase in NRS may increase the variability of light paths, but multiple scattering within a profile also can lead to an average light path length stable to statistical scattering altitude variation.
The LSA and all scattering quantities vary, as already known, with wavelenth.
With higher SZA, the light paths become longer, which increases the numbers of scatterings.
When the sun is beyond the local horizon, scatterings with no direct line between location and sun lead to path aborts.
To give a quantitative estimate on the above qualitative considerations, a brief investigation was performed with the following parameters:

- U.S. standard atmosphere, 1 km discretization 0-70 km
- Ground based MAX geometry with azimuth 90°, elevations 10°, 20°, 90°
- SZA 30°, 70°, 80°, 90°, 92°
- Wavelengths 350 and 550 nm
- Photon numbers 1000 and 5000.

Four NO_2 profiles were used:

- #0 box profile at the ground, uniform concentration 10^9 cm^{-3} between 0 and 2 km
- #1 box profile at the ground, concentration $1*10^9$ cm^{-3} between 0 and 1 km, $5*10^8$ cm^{-3} between 1 and 2 km.
- #2 gaussian stratospheric profile, centered at 25 km, FWHM 10 km, max. concentration $5*10^7$ cm^{-3}
- #3 gaussian stratospheric profile, centered at 35 km, FWHM 10 km, max. concentration $5*10^7$ cm^{-3}

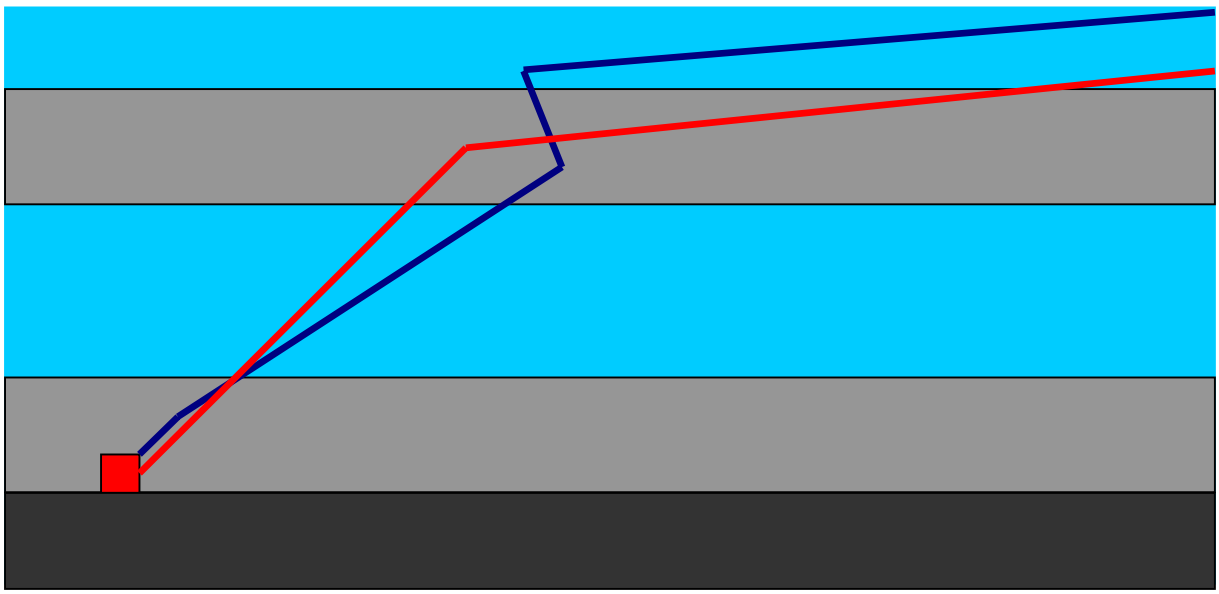

Figure 6.7.1 The profile locations, spatial extensions and the wavelength-dependent scattering parameters govern the variability of the path segments within an absorber profile and thus the AMF.

The plots in Fig. 6.7.2 show the relative errors of the AMF for the different elevations and wavelengths. The boxed lines denote the errors for 1000 photons, the straight one for 5000 photons.
The basic findings can be summarized as follows:
For 350 nm and SZA <= 90°, 5000 photons deliver AMF with a relative error of <= 5%.
For 350 nm and SZA >90°, as well as for 550 nm, higher numbers, e.g. between 7000 and 10000, are recommended.
It shall not be attempted to derive a functional relationship between the various parameters and the relative error. The figures given are meant to give the user information on the order of magnitude of photon numbers to use for his modelling.
Due to the large variety of model scenarios and measurement parameters any user is advised to perform a sensitivity study to derive the photon number nesessary to meet the needs in signal-to-noise ratio for the respective modelling enterprise.

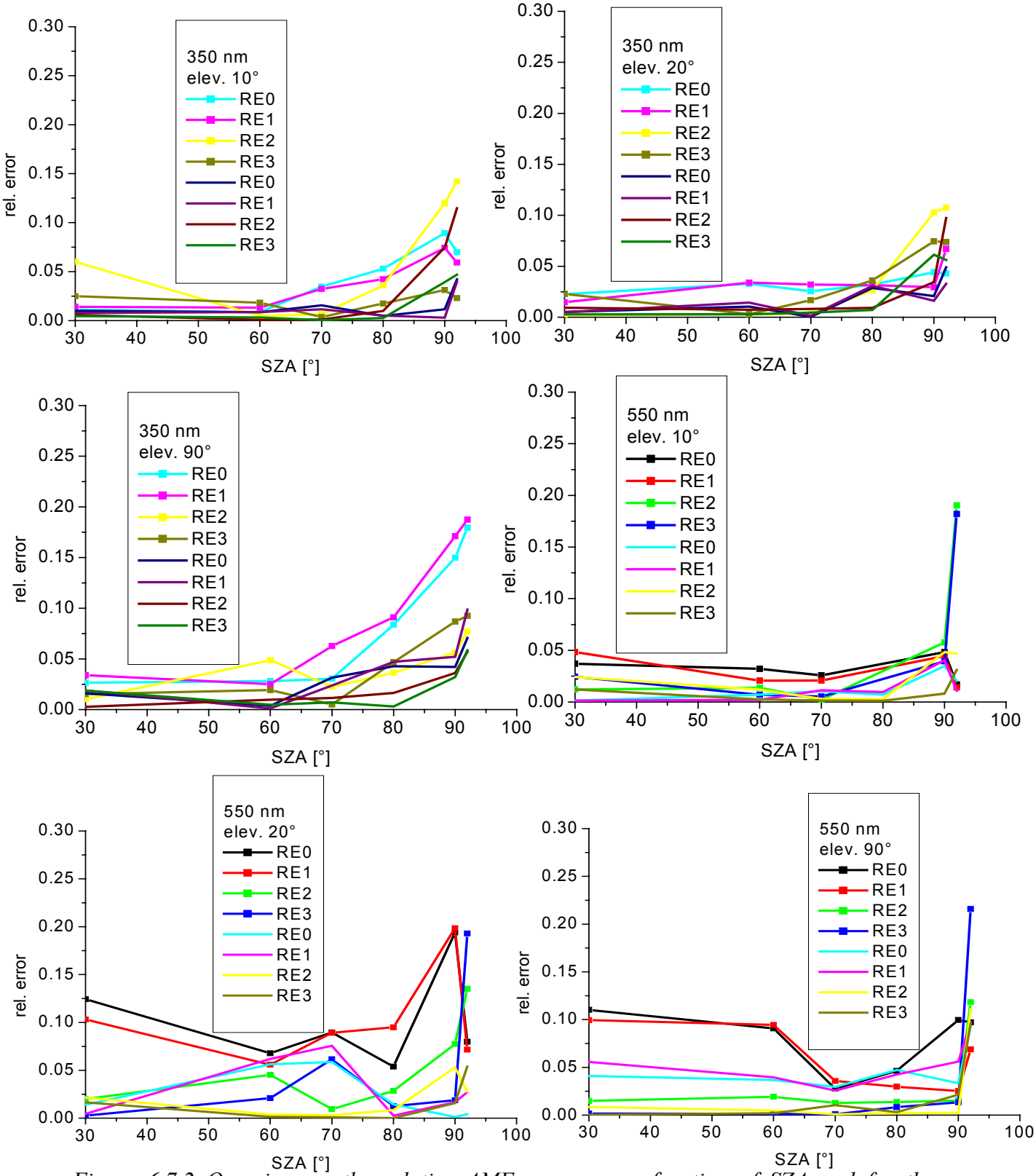

Figure 6.7.2 Overview on the relative AMF errors as a function of SZA and for three elevations, two wavelengths and six profiles as defined above. For SZA <= 90° and 350 nm, 5000 photons are needed to obtain a relative AMF error <= 5%. For 550 nm, higher photon numbers, e.g. 7000 or 10000 are recommended.

6.8 Influence of refraction

For the sake of completeness, a brief investigation on the influence of refraction on the AMF be attached here. Calculations were performed for the same profiles, wavelengths and SZA as in section 6.7, and with refraction engaged and disengaged, respectively.
Photon numbers used were 5000 for SZA < 80°, and 10000 for SZA above.
For 350 nm and slant elevations, no significant influence for either the tropospheric or the stratospheric profile could be seen for the slant elevations. The tropospheric AMF is largely governed by the elevation and the *LSD*, which shortens the paths and reduces the effect of their curvature. A slight tendency to higher stratospheric AMF for SZA > 90° was well within the error of between 1 and 2 %. This finding for stratospheric absorbers is in agreement with [*Frank 1991*]. For 350 nm and elevation 90°, i.e. Zenith-sky, the tropospheric AMF below SZA < 92° tend to be smaller by some % with refraction included than without. E.g. for 85°, the difference for the AMF of the O_4 profiles is ca. 8 %. [*Frank 1991*] states reduction for this SZA (albeit 475 nm, SZA 86°) of 7.5 %.
For 550 nm and 90° elevation, ca. 7% deviation of the O_4 AMF at 90° SZA derived with TRACY compare less well to 15° predicted by [*Frank 1991*] for 90° and 575 nm.
Differences of similar quantity can be seen in all elevations for the tropospheric test profiles between SZA 80 and 88°, due to more deeply located last scattering events and longer remaining direct paths to the sun, allowing for curvature, but not at SZA above, where the differences become insignificant again. For 550 nm and stratospheric AMF, again no significant tendency can be made out for the SZA modelled.
As a conclusion we can note that below 80°, the refraction seems to be without influence for ground based observations. Due to this finding and the (yet) approximative character of refraction treatment after the last scattering, refraction is not included in the following chapters.

6.9 Runtime estimate

The time TRACY needs to compute 1000 photon paths depends on the number of voxels to calculate intersection points with, as well as of number and type of scattering events to compute for. Table 6.8.1 lists some typical values for 30° SZA and the two wavelengths and three elevations used for the error estimate. The figures are valid for a 2 GHz Pentium IV CPU with 256 MB RAM, the error is the standard deviation over three runs.

Table 6.8.1 Computation times for 1000 photon paths on 2 GHz P-IV CPU. Error is 5s.

	350 nm clear sky	550 nm clear sky	350 nm aerosols	550 nm aerosols
elevation 5°	1’25’’	1’5’’	2’	1’40’’
elevation 10°	1’20’’	55’’	1’50’’	1’25’’
elevation 90°	1’	35’’	1’15’’	50’’

7. Validation

So far TRACY, an entirely newly written code, had not been validated against other models. Within the framework of the European project "QUILT"[1] a workshop on radiative transfer (RT) modelling activities within the QUILT project has been held at IASB-BIRA on October 3-4, 2002. The most important established models participating were

SCIATRAN
- operated by the Insitute for Environmental Physics of the University of Bremen [*e.g. Buchwitz 2001*]
- using Finite Difference Method
- treating the direct beam including refraction in full spherical geometry
- treating full multiple scattering (MS) in pseudo-spherical geometry, iteratively solving the RTE to achieve convergence for full sphericity

UVspec/DISORT
- operated by the Norwegian Institute for Air Research (NILU) [*Kylling 1995*] and
- using Discrete Ordinate Method
- treating the direct beam including refraction in pseudo-spherical geometry
- treating MS higher orders in plane parallel geometry with spherical geometry

UVspec/DISORT - modified version
- operated by the Belgian Belgian Institute for Space Aeronomy (BIRA-IASB)[*Hendrick 2002, pers. comm.*],
- treating the direct beam including refraction in full spherical geometry

Other models were either single scattering models or supported 2nd order of scattering only.
In the following comparison results for MS mode are shown for SCIATRAN, Uvspec/DISORT and TRACY. All of them include treatments for aerosols, clouds and ground albedo.

7.1 Zenith-sky NO_2 and BrO with diurnal variation

In the first exercise, calculations of SCDs in zenith-sky geometry were performed. The scenario included diurnal (i.e. photo-chemical) variation of the respective input profiles.
These were calculated using the photochemical box model PSCBOX [*Hendrick et al., 2000; Errera and Fonteyn, 2001*] with daily initialization with chemical fields for 12h UT extracted from the 3D CTM SLIMCAT multi-annual run output [*Chipperfield, 1999*] at the location of Harestua (60°N, 10°E, Norway). The resulting profiles for a set of SZA were extracted as matrix ASCII files[2] to serve as input for the RTM.

[1]" Quantification and Interpretation of Long-Term UV-Visible Observations of the Stratosphere"
[2] One line for each SZA, each line containing concentration for one altitude layer

In addition to the species to probe, fixed p, T and air total number density profiles as well as fixed NO_2 and O_3 concentration profiles were provided.

The other parameters were:

- Fixed altitude grid: 0-120 km/1km layer thickness
- Fixed wavelengths: 352 (BrO) and 422 nm (NO_2)
- Fixed ground albedo value (0.20)
- Fixed cross sections sets
- Aerosol scattering and refraction not included

Figure 7.1.1 displays the input profiles for a variety of the SZA used. While NO_2 abundances at a given altitude decrease with decreasing SZA due to photolysis, BrO concentrations rise.

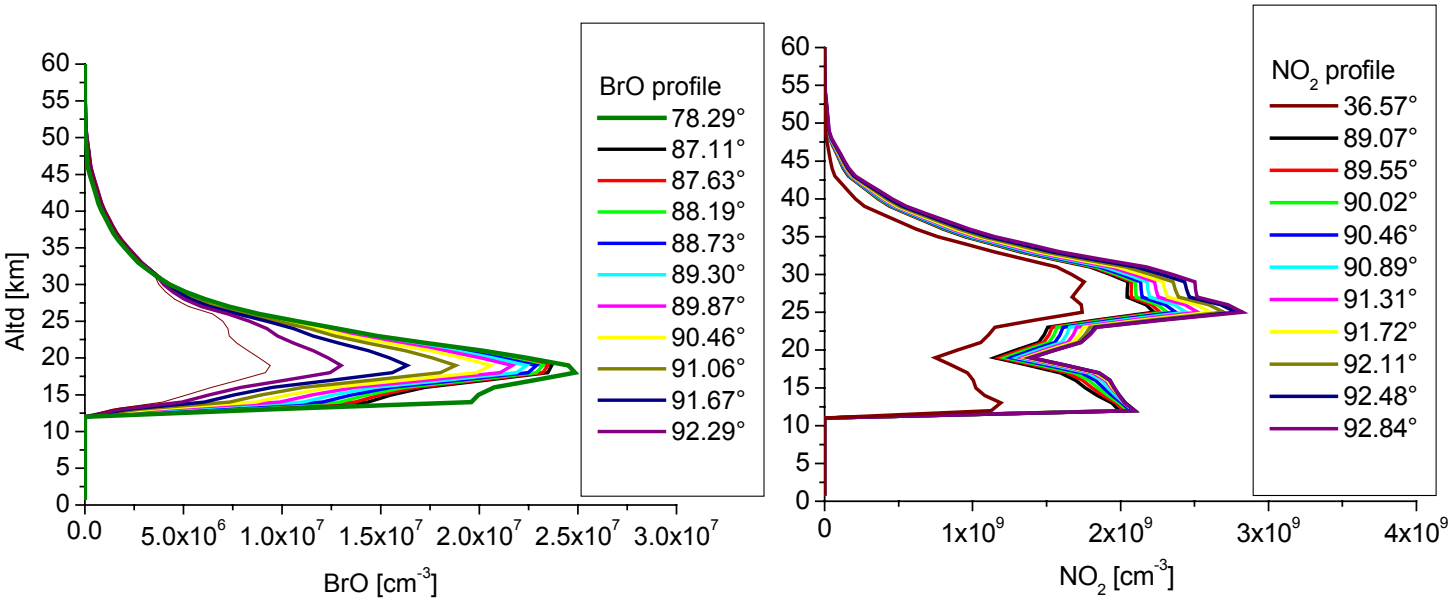

Figure 7.1.1 Input profiles for zenith-sky radiative transfer intercomparison exercise.

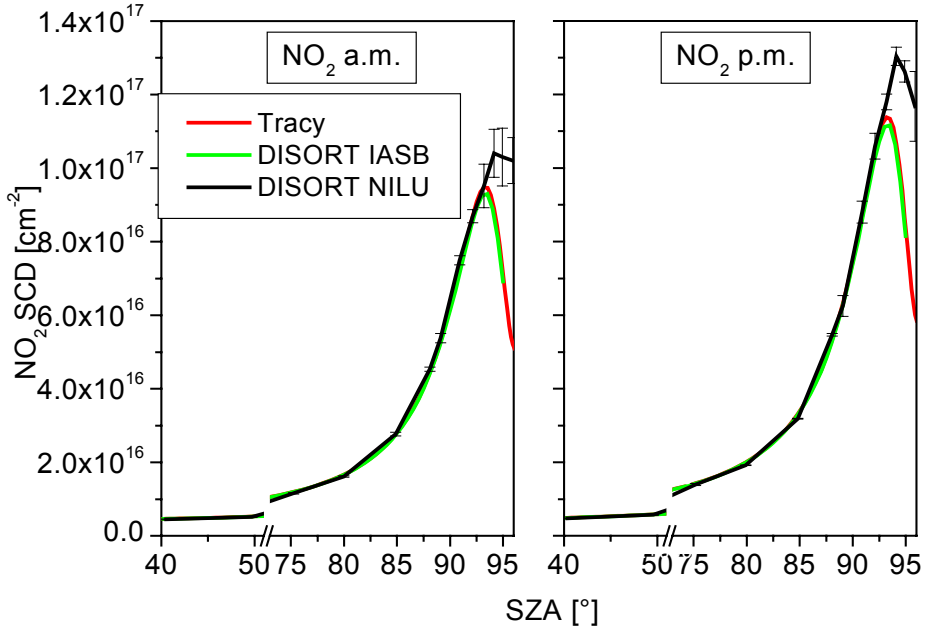

Figure 7.1.2 modelled SCD for NO_2 in zenith-sky for TRACY, DISORT/IASB and DISORT/NILU; for SZA <= 92.5°, all three codes show excellent agreement. Above 92.5°, TRACY models systematically higher SCD than the DISORT implementations.

Figure 7.1.2 shows the results for NO_2, Figure 7.1.3 for BrO. The SZA ranged from 40° (NO_2) and 78° (BrO) to ≈> 96° in steps oriented to the ones of typical measurements of these species.
For NO_2, below SZA = 92.5°, all three models, i.e. TRACY and the two DISORT implementations[3], show excellent agreement. Above this SZA, TRACY SCDs are systematically higher; the difference increases with SZA.

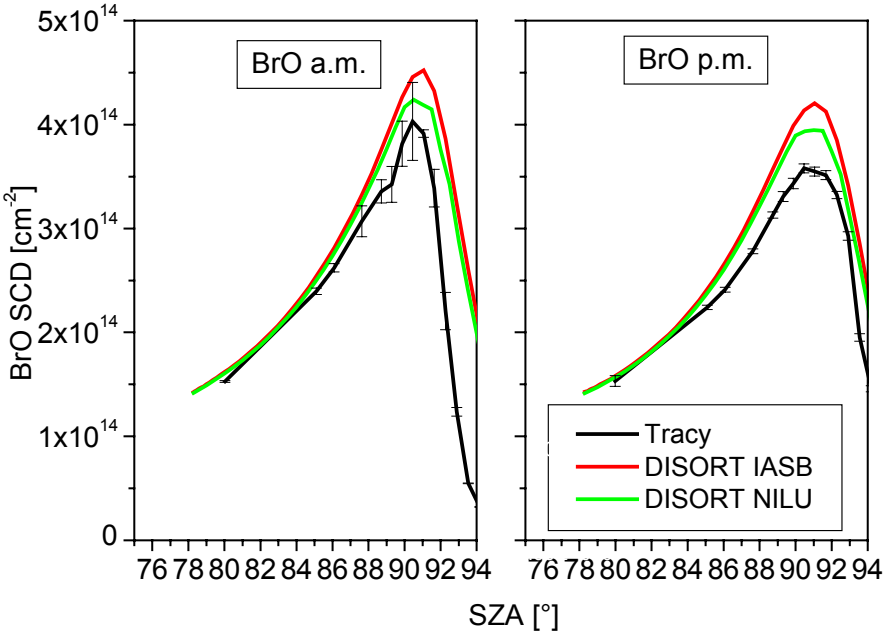

Figure 7.1.3 modelled SCD for BrO in zenith-sky for TRACY, DISORT/IASB and DISORT/NILU; for SZA > 85°, TRACY models systematically smaller SCD than the DISORT implementations.

For BrO, a smaller SZA range was modelled for. Below SZA = 85°, again all three models show good agreement. But above this SZA, TRACY models SCD which are much smaller, again with the difference to the competitors increasing with SZA. Around 90°, the differences between TRACY and DISORT/NILU is similar to that between the two DISORT implementations.
The SCD of TRACY are consistent with the *LSA* and *FSA* moving above the layers of significant BrO abundances with sinking sun, but this only indicates TRACY's internal consistency, not her correctness. Similar parameters of the other codes to compare with were not available.

A drawback became apparent of the backward Monte Carlo treatment. With higher SZA, high photon numbers (i.e. >10,000, e.g. 20,000 for UV wavelengths and SZA > 93°) are needed to obtain sufficient accuracy. The dataset for the sunrise scenario was redone after the workshop with 30,000 photons to ensure the deviation of the SCD was not statistical.
For SZA > 94° the signal-to-noise ratio was so low that it was decided to focus on the SZA below. The shorter range as compared to NO_2 is explained by the larger vertical extension of the NO_2 profile, which tends to "average out" statistical variations of Box AMF for thinner layers located within the profile.

The reason for the deviations can be of twofold origin.

[3] SCIATRAN results so far are not available due to data interface problems with the 2D trace gas matrices

First, TRACY was the only MC RTM in the comparison, i.e. treated the calculation of incoming irradiance and light propagation in a completely different way as the analytical codes do. This can lead to systematic variations which to investigate is a necessary future work to assess which approach (if any) is the more accurate one.
Second, as stated above, DISORT does not treat MS in full spherical geometry but in a plane parallel atmosphere. Since we have, especially for UV wavelengths, multiple scattering in real measurements, the treatment of sphericity may cause discrepancies. Supporting this is the fact that the differences become larger with increasing SZA, i.e. with increasing influence of the earth's curvature.

7.2 Off-Axis HCHO

The second scenario was Off-Axis based; the profile to probe was a (fixed) HCHO profile as generated from the model package for urban areas. It is shown in Fig. 7.2.1, left panel.
Again provided were O_3 and NO_2 profiles, as well as p, T and number density profiles.
Additionally an also model-derived aerosol load was used (see Fig. 7.2.1, right panel).

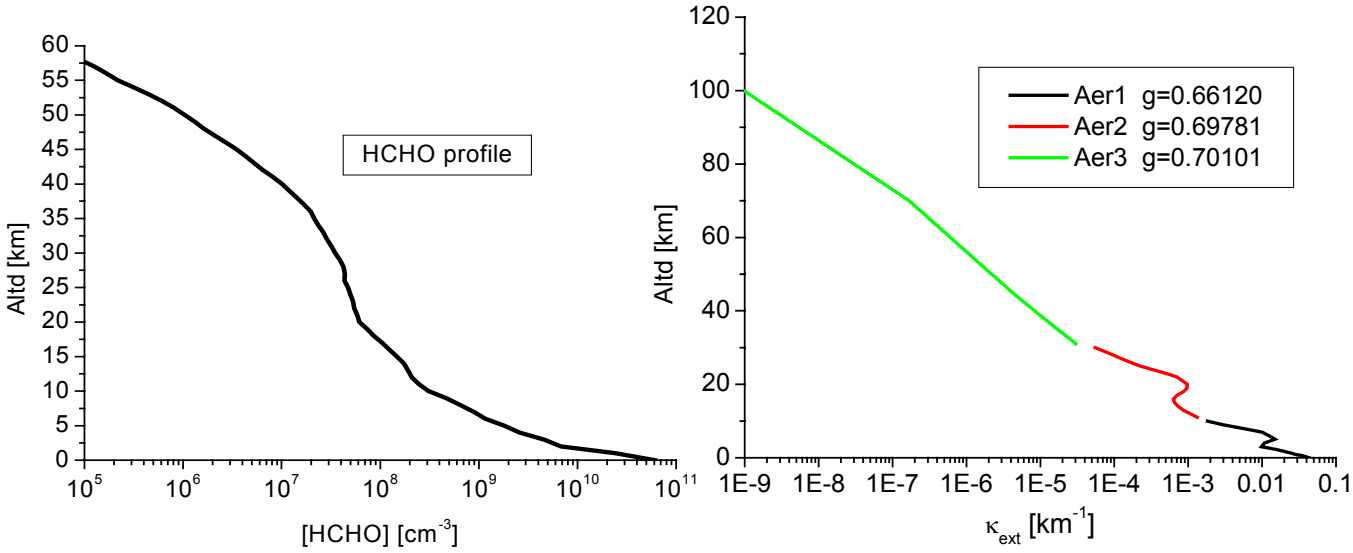

Figure 7.2.1 Left panel: HCHO profile used for the off-axis exercise; please not the log abscissa. Right panel: extinction coefficient vertical profile (also shown with log abscissa) for the aerosol load used in the exercise. The legend gives the asymmetry coefficients from which the phase functions were to calculate.

The other parameters were:

- Fixed altitude grid: 0-3 km/200 m layer thickness;
- 3-120 km /1km layer thickness
- Fixed wavelength: 356 nm
- Fixed ground albedo value (0.20)
- Fixed cross sections sets
- Refraction not included

The viewing geometries were

- Elevations 5°, 10°, 20°, 30°, 40°, 90°
- Azimuths 30°, 60°, 90°, 120°

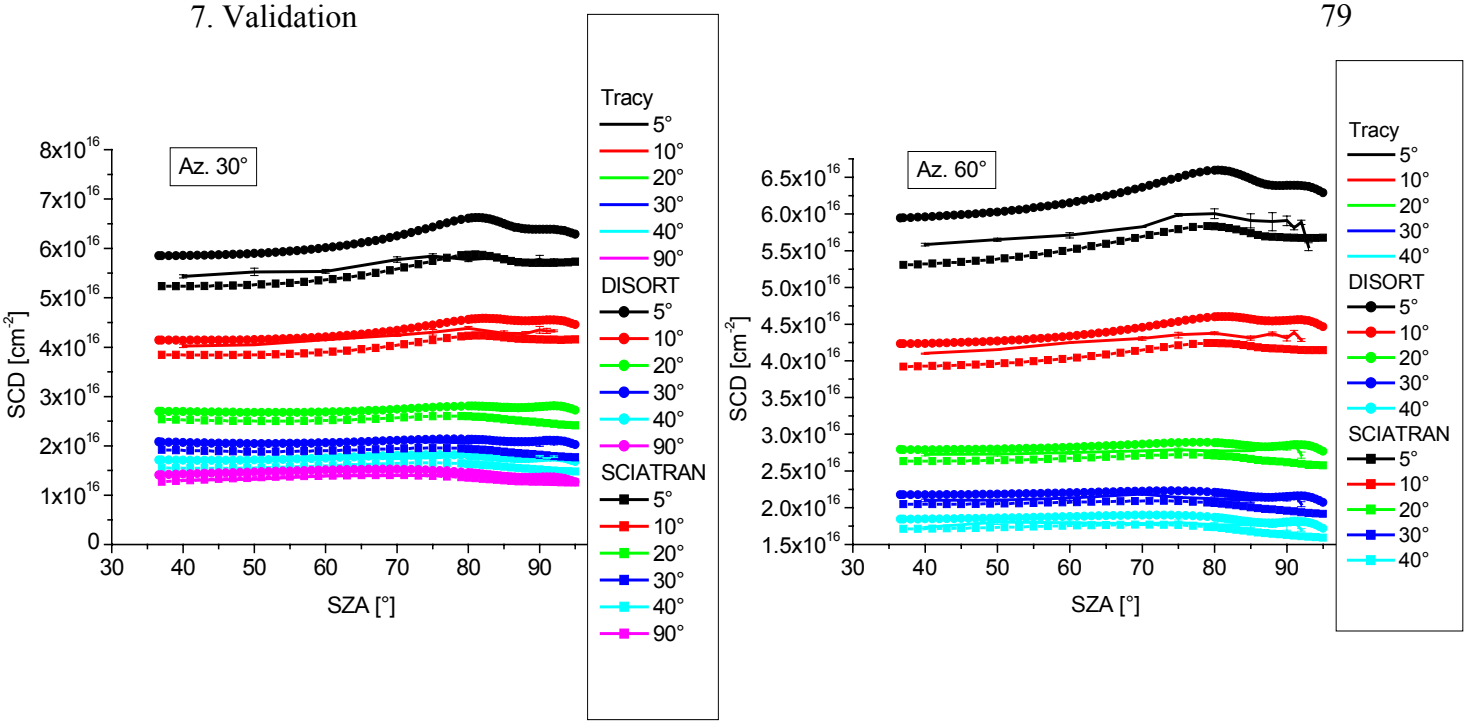

Figure 7.2.2a HCHO SCD for azimuths 30° and 60° of TRACY, DISORT/IASB and SCIATRAN. Note the inclusion of elevation 90° (zenith-sky) for azimuth 30°. The overall agreement is good. But SCIATRAN and DISORT have differences of up to 10% and larger. TRACY SCD are in between the two analytically derived datasets.

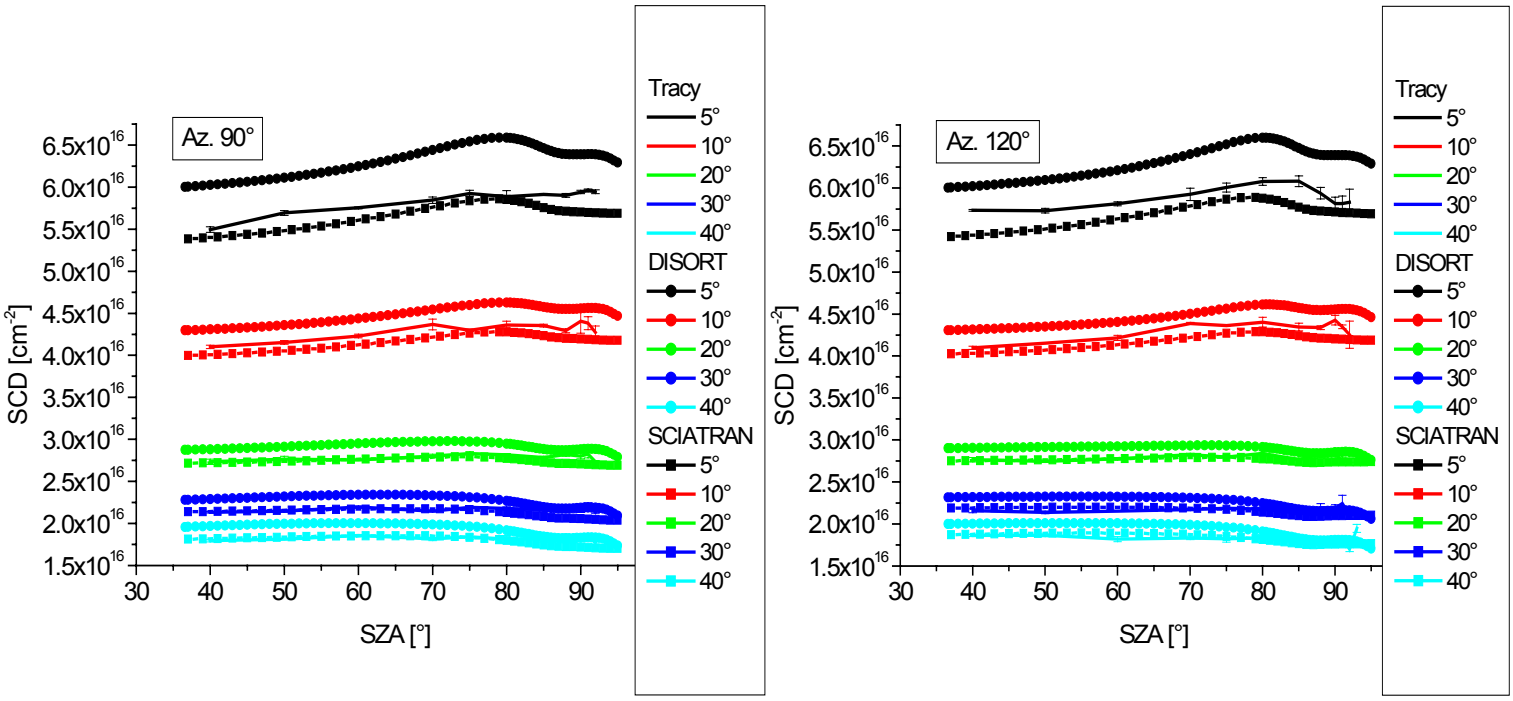

Figure 7.2.2b HCHO SCD for azimuths 90° and 120° of TRACY, DISORT/IASB and SCIATRAN. The same statements as for Fig. 7.2.2 apply.

Figures 7.2.2 a and b show the results; zenith-sky is included in the plot for azimuth 30°.
The findings can be summarized as follows.
The overall agreement is good for all three models, but not excellent. The differences are largest between the two analytical codes (up to more than 10% for low elevations), with TRACY being situated in between.
Near the ground, where scattering governs the path through the absorber in a stronger way than is the case for the stratosphere, the different treatments of the RTE obviously influence the result. Again the differences are a matter which must be investigated by all partners participating.
The exercise also served the assessment of the influence of the azimuth angle on the SCD.
Exemplary for elevation 5°, Figure 7.2.3 shows the comparison between the four azimuth angles used.

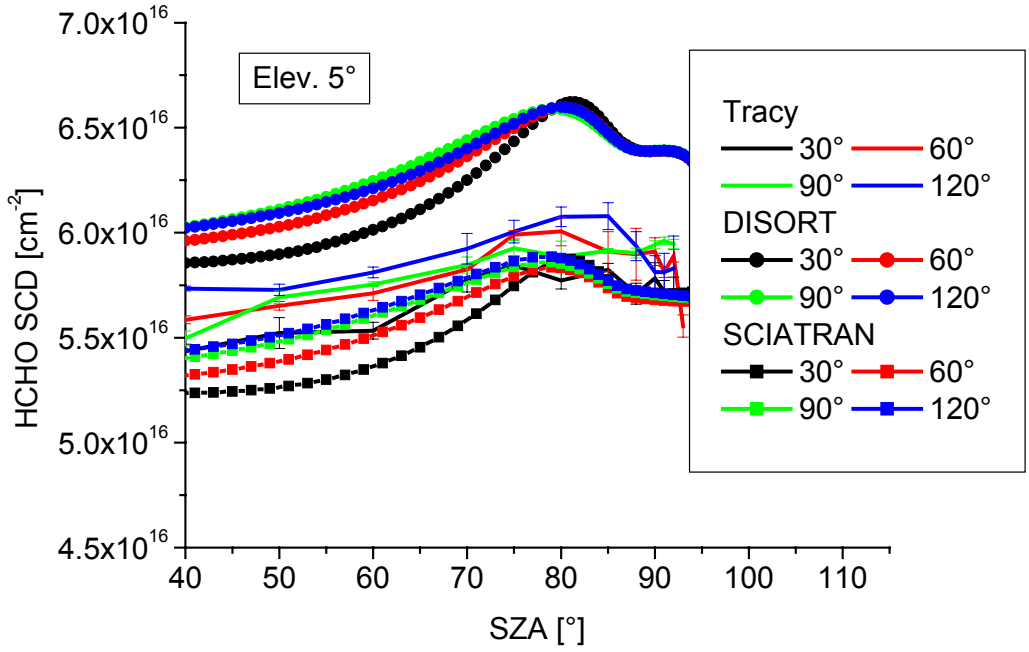

Figure 7.2.3 Comparison between the SCD modelled for the four azimuth angles for TRACY, DISORT/IASB and SCIATRAN.

In general we find an increase in SCD with increasing azimuth for all three models. A maximum is reached around 80° SZA.
This can be explained with the competing effects of slanter path of the incoming light and the increase of scattering, attenuating the light coming in near the ground and leading to a higher contribution of light scattered higher above, and traversing the trace gas layers on a path less slant.
The specific behaviour is though different. DISORT models the largest SCD for 90° up to SZA = 80°, then the SCD for 30° becomes the greatest.
SCIATRAN and TRACY "agree" in modelling the highest SCD for 120° azimuth and for all SZA. This is understandable when imagining the light paths. The light recorded by the detector gets scattered in a distance depending e.g. on local aerosol load and albedo, but not on SZA. In the "extreme" case of 90° SZA, and azimuth small (e.g. 1°) the scattering point is located nearly on the direct line between the sun and the detector.

When we turn the instrument to azimuth 180°, the incoming solar light must literally "pass us by", and in doing so cover more distance within the trace gas layer near the ground than in the other case.

7.3 Off-Axis NO_2

A third scenario, also Off-Axis based, treated NO_2 under the influence of azimuth. The calculations shown were performed with and without aerosols for 422 nm wavelength.
The measurement geometries used were the same as in the case of HCHO, so was the albedo. Vertical discretization was 1 km. Figure 7.3.1, left panel, shows the ozone and NO_2 profiles used as input, the right panel the aerosol profile.

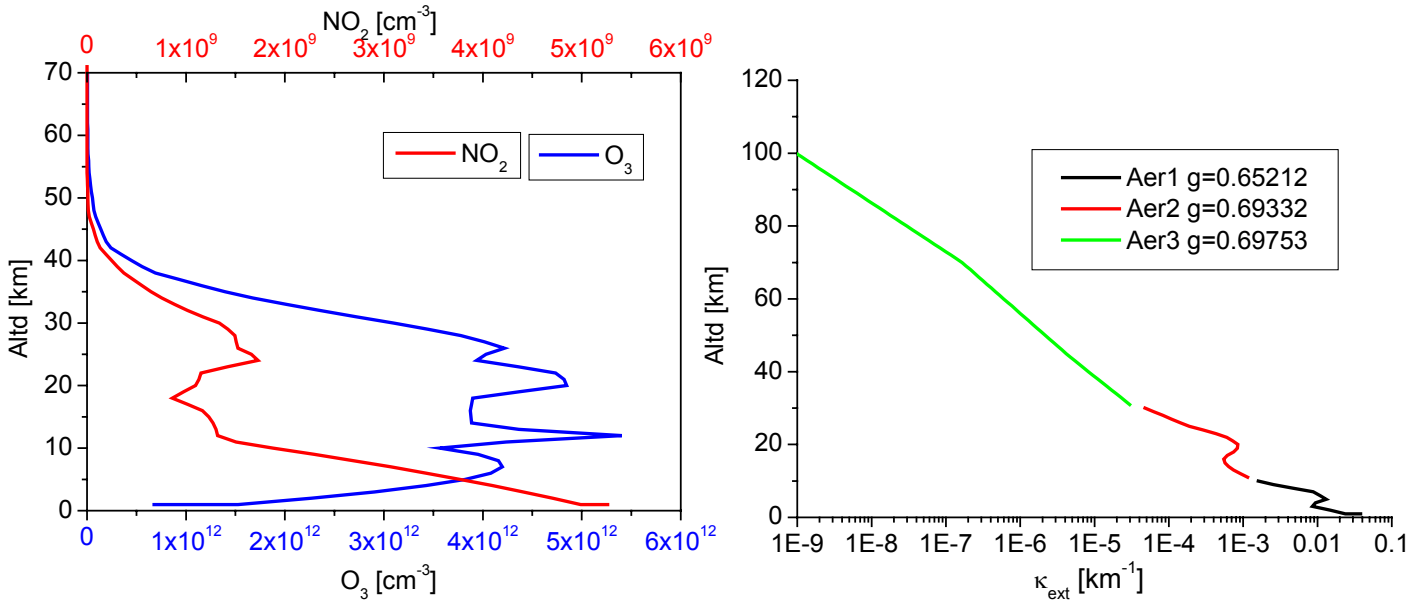

Figure 7.3.1 Input profiles for ozone, NO_2 and aerosols used for the Off-Axis-NO_2 comparison.

Figures 7.3.2 and 7.3.3 exemplary show the SCD for azimuths 60° and 120°. (Figures by [*Hendrick, pers. comm.*]). The solid lines represent the calculations without aerosols, the dashed lines with aerosols, and TRACY results are depicted in green. To keep the result delivery deadline as well as the errors below 2%, the high SZA were not computed for this plot due to the high computation time. Calculation for SZA 94°, 95° and 96° afterwards with 50000 photons for 40° elevation, 60° azimuth yielded SCD of $9.3*10^{16}$, $9.1*10^{16}$ and $8.5*10^{16}$, respectively, with errors of around 10%. Hence TRACY delivers higher SCD for high SZA, which does not surprise in the light of the zenith sky calculations, but it reproduces the drop in SCD for highest SZA, albeit for higher ones as do the analytical competitors. It must also be noted that there are also differences between the results of the analytical RTM for high SZA. Nevertheless, the agreement for the SCD handed in originally is excellent. It can be assumed that treatment of sphericity plays, here again, a decisive role.
Interesting is assessment of the aerosol influence. In Figure 7.3.4 [*Hendrick, pers. comm.*] the ratio SCD calculated with aerosols divided by those calculated for pure Rayleigh is plotted, the elevations and azimuths as well as the colour codings being identical to Figures 7.3.2 and 7.3.3.

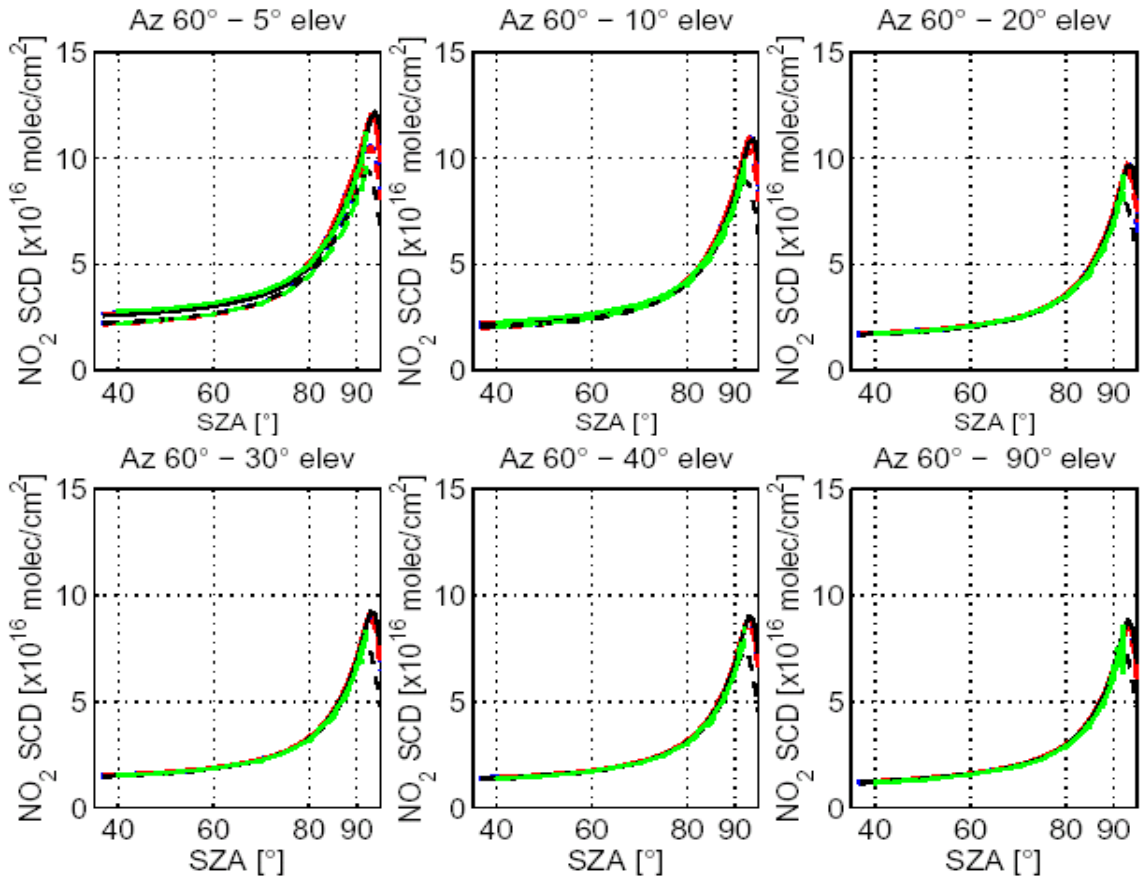

Figure 7.3.2 SCD for NO_2, modelled with and without aerosols (dashed and solid lines, respectivel)y for azimuth 60°; the colour is blue and red for DISORT IASB and NILU, respectively, black for SCIATRAN, green for TRACY. TRACY SCD error is <= 2%.

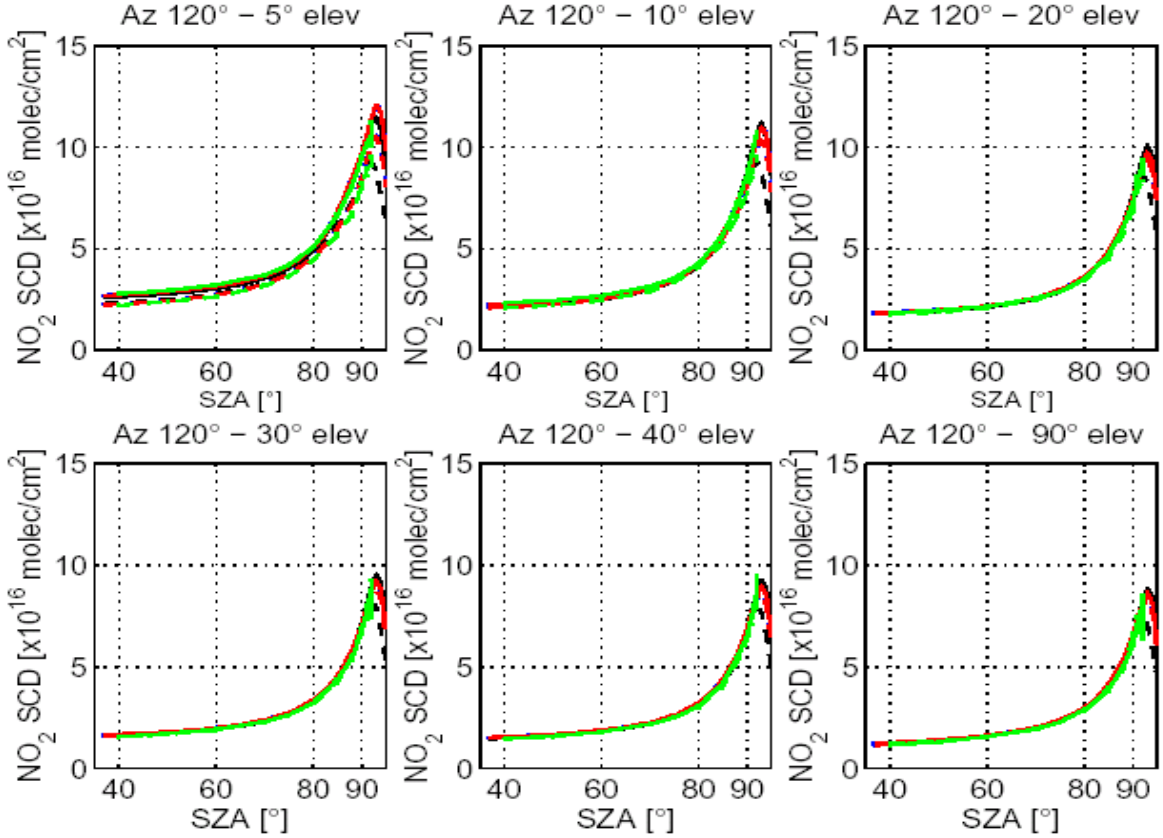

Figure 7.3.3 Same as Fig. 7.3.2, but for az. 120°. The agreement for SZA <= 90° is good.

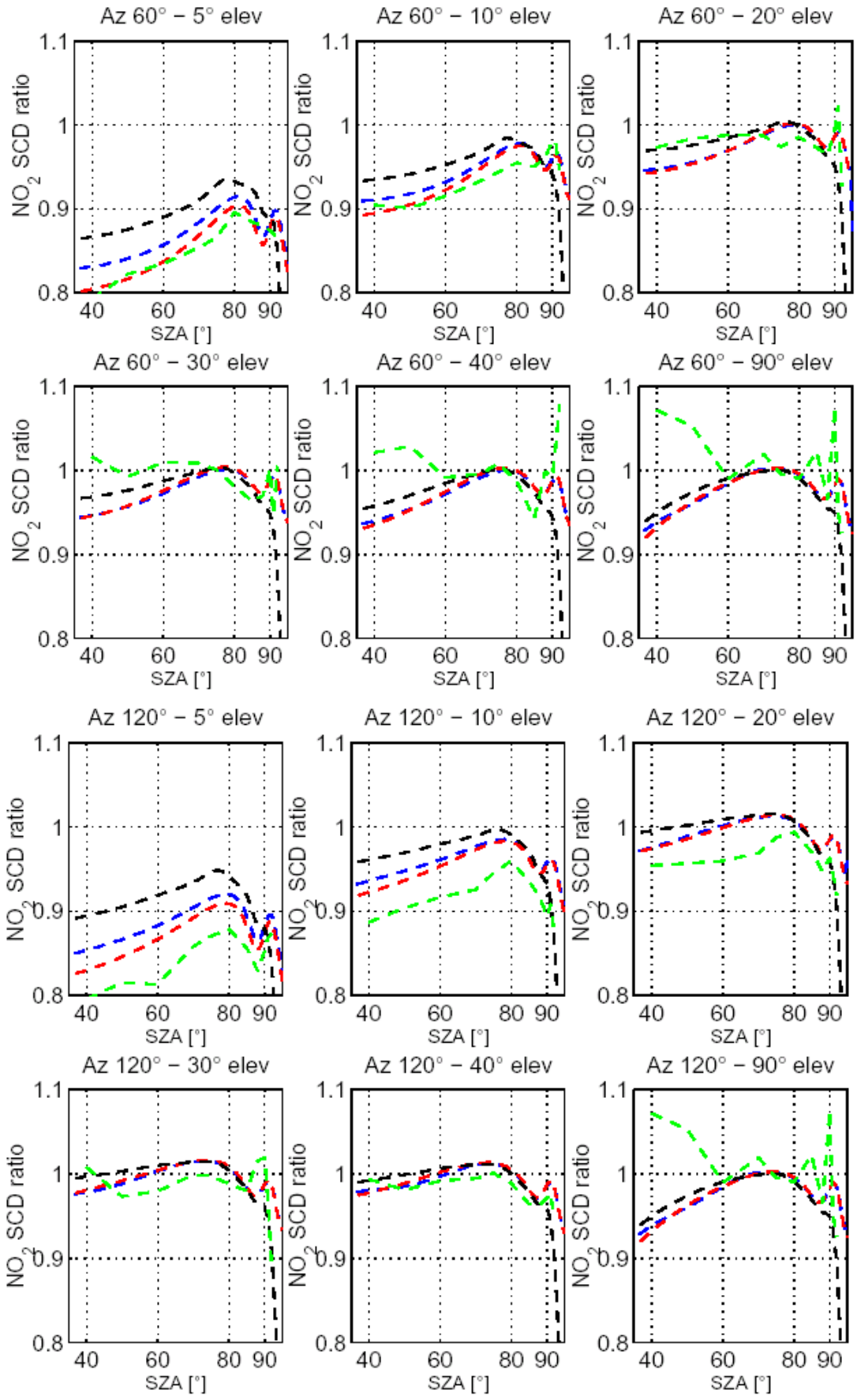

Figure 7.3.4 Ratios of SCD calculated with aerosols by those without aerosol influence. The overall behaviour of the series is reproduced, but differences for high elevations must be noted. Colours are: blue/red : DISORT IASB/NILU, black : SCIATRAN, green : TRACY

For low elevations, the differences between TRACY and the other models are in the order of those between the analytical models; the overall shape of the ratios as function of SZA is reproduced. For high elevations, i.e. 30°, 40° and 90°, we must note differences for low SZA, i.e. the ratio for TRACY SCD is >1, while it is <1 for the analytical RTMs. For 90°, also the behaviour around 90° differs from the other results, but this can be attributed to statistical noise due to smaller numbers of scattered photons in zenith-sky geometry. TRACY obviously "sees" an increase of the AMF for high elevations due to multiple scattering-induced light path enhancement within the aerosol load used.

As summary result, differences at high SZA and for stratospheric absorbers occur; they may arise by both the treatments of multiple scattering and of sphericity being performed differently by the participating models.
They precise reasons must be found and eliminated.
Overall, the newly implemented and developed full spherical 3D MC RTM TRACY competed agreeably with the established and powerful analytical packages for the exercises and wavelengths shown.

8. Application to absolute radiometry

Since DOAS can measure several species simultaneously, conclusions can be drawn on the abundances of educt and product species within a probed air volume; in conjunction with chemical reaction constants, the chemical equilibria can be derived and statements on the reaction of the abundance one species by (e.g. anthropogeneous) alteration of another's can be made [*e.g. Geyer 2000*].
But the driving force behind the reaction, production and destruction of many species, including e.g. NO_2 and HCHO, is the solar radiation. E.g. the U-shape of the diurnal variation of stratospheric NO_2 (chapter 9) results from production during night and photolytical destruction at sunrise. An important requirement for the input of chemical models are, apart from data on gaseous species concentrations, the "concentration" of the "reactant" photons available per unit volume and time available for trace gas photolysis.
The DOAS devices generate spectra of which the "counts" can be, using data on the e.g. PDA's quantum efficiency and the ADC, in theory converted into numbers of photons per spectral channel. But for several reasons this is not realized:

- The spectrographs are partly not temperature-stabilized, leading to variations e.g. in the dispersion relation
- The detectors are cooled, but not stabilized to given temperature, leading to e.g. dark current variations
- Variations in dark current alter the signal in a broad-band way
- So do offset variations
- VIS straylight falsifies the signal in the UV

The task of measuring radiometric quantities in absolute calibration requires the instrument to be stable against component shifts by movement, temperature changes and surface degradation. Equally important is the separation of UV and VIS light signals from each other. In the UV region, the increase in incoming irradiance between 300 and 350 nm leads to large differences between adjacent spectral channels. A device as used for DOAS measurements projects the entire spectral interval through the spectrograph's mirrors and gratings and onto a detecting array. Since the stray light of a given wavcelength present in any spectrographic device is proportional to the incoming light of that wavelength, stray light from a channel with high intensity will interfere with measurement light from a lower intensity spectral interval, and can be in the same order of magnitude. These reasons (among others, depending on the specific layout) prevent most DOAS devices from measuring light in absolute quantities such as radiance. To do so it is necessary to reduce the spectral interval projected onto the detecting element and to suppress stray light. This can only be done using a scanning spectrometer. For this reason a calibrated scanning spectro radiometer was purchased.

8.1 Calibrated scanning spectro radiometer

The spectro radiometer, henceforth abbreviated SR, composed by „Gigahertz Optics“, measures the irradiance [W $nm^{-1}m^{-2}$], per spectral channel between 250 nm and 600 nm, downwelling from a hemisphere.

8.1.1 Incoupling optics

The light impings onto a Teflon ball of 1 cm diameter embedded in a black steel tube. The Teflon ball accepts light impinging from all directions out of the 2π hemisphere opposite of the tube, i.e. it is suited to measure the acitinic flux. The light forms a diffuse radiation field inside of the ball, of which a part proportional to its energy content enters a bundle of quartz fibres with length 2.95 metres. They conduct the light into a device forming from the fibre's exit surfaces a slit of dimensions 20 mm (height) to 0.75 mm (width), the latter figure matching the double monochromator's entrance slit width.

8.1.2 Spectrograph

The core element is a set of two spectrographs of the Czerny-Turner type by Bentham, model DMc 150. Each is equipped with an entrance slit of 0.75 mm width, and a holographic grating of 2400 grooves per mm on a motor driven turret. The focal length of each one is 150 mm.
From the entrance slit the light illuminates a first mirror which directs it into the grating. The turret motor serves to turn the grating around its vertical central axis to project only a the first orders of a narrow spectral interval onto the second mirror; within this second mirror's focal plane the exit slit is located.
Since in theory this slit can be made so narrow that only electromagnetic waves of an infinitely small spectral band can pass, this system is called a monochromator.
From the exit slit it enters a second spectrograph which is identical to the former one. The second spectrograph's grating is turned in a manner coordinated with the first grating's movement and projects an even smaller spectral interval onto the second mirror and onto the system's exit slit, which has the same width as the entrance slit.
This combination of two monochromators accordingly is named a double monochromator.
The focal length of the combined system and the grating yield a dispersion D of 1.35 nm per mm. From the dispersion D and the slit width B the formula $B = \Delta\lambda' / D$ the spectral bandwidth $\Delta\lambda'$ of the light emerging from the exit slit is computed to be 1 nm. A measurement of mercury line's FWHM shows the device's practical resolution $\Delta\lambda$ to be 1.05 nm. This means that the measurement at a nominal wavelength λ_0 generates a value valid for a wavelength range $\Delta\lambda$ of 1.05 nm centered at λ_0.
The spectral range supported by the system's gratings and turrets is 250 to 600 nm. The wavelength data given out by the system are not accurate. At the time of this writing, an offset of 1.3 nm makes a nominal wavelength smaller in reality.
The twofold selection of a narrow bandwidth by projection onto a slit reduces the straylight significantly as compared to DOAS devices. To limit the effects of temperature contractions and shifts, the system is built from ceramics instead of steel.
To probe a given spectral range, the turrets must be turned to sequentially project a small sub-interval of the total one to the photomultiplier which serves as detector element. This process is called scanning. The duration of a scanning of a spectral range of e.g. 200 nm can be 5 to 15 minutes, depending on light conditions. This constitutes a drawback limiting the temporal resolution.
Behind the system's entrance slit a filter wheel is located. At the time of this writing, it holds a shutter to perform dark current measurements, an UG 5 filter to suppress VIS light to enter

when measuring in the UV, and an order sorting filter to prevent higher orders of UV light to act as straylight when measuring in the VIS.

8.1.3 Photo multiplier

The detection element is a Peltier cooled photo multiplier operated at a high voltage of 750 V and cooled to –10°C. It accepts the light emerging from the double monochromator's exit slit and converts it into a photo current. It is sensitive to light between 250 and 600 nm.

8.1.4 Energy supply, controlling and detection electronics

An electronics rack module supplied with the system, to be mounted into a rack or to stand alone, is equipped with a transformator to convert the power line 220 V into the 750 V necessary to operate the photo multiplier. The voltage is displayed on a LCD; from the readout the uncertainty is estimated to be 1 V.
A second component feeds the peltier unit of the detection head and controls the temperature to be constant at a preset value. The uncertainty, also concluded from a readout LCD, is 0.1 °C.
The photo current is fed into an amplifying module ranging over five decades (from an amplification factor of 1E6 to 1E10). Its output in units [nA] is fed into an ADC, which delivers digitized signals to the controller board in the PCI slot of a PC via an IEEE interface bus. The board is also connected, with a second IEEE bus cable, to the double monochromator, where it controls the turrets and the filter wheel.
Figure 12.2.2 shows the assembled SR.

Figure 12.2.2 assembled spectro radiometer: a) electronics module, b) double monocromator, c) quartz fibre bundle

8.1.5 Control software

Two control softwares are in existence.
"AUTOSCAN" is a DOS program supplied by the manufacturer; it allows for variable wavelength steps, either equidistant ore freely chosen. The generated output in [nA] is written to an ASCII file in the "NASA AMES" format, i.e. a block containing the wavelengths chosen, followed by lines containing e.g. the date, the CPU clock times of scan begin and end, dark current data and other scan parameters, followed by a block of the "nA" values. The file is then closed and given a number preceded by a prefix chosen by the user.
Several scan parameters, must be input by the user upon each launch of the program.

"SRCon" is a program written by the author based upon DLLs supplied by the manufacturer. It allows to freely select the wavelengths to be probed within the spectral range desired, and perform either a fixed number of scans, or to operate within a specified range of solar zenith angles, which it calculates from the CPU clock time using a ephemerid-based high precision module (see below).
The time and date as well as the SZA and the solar azimutal angle before and after each scan are written, along with the output currents in nA, to an ASCII file, which can be read in by any data analysis program for processing.

8.1.6 Calibration

The actual throughput of the system depends on a variety of parameters, including the quartz fibres aperture angle, the sensitivity of the detection unit, the accuracy of the slit etc, each of them being subject to tolerances.
Therefore it is necessary to calibrate it when attempting to measure absolute energies.
The calibration is performed using a NIST traceable lamp operated by [*Birger Bohn, pers. comm.*] of Research Centre Jülich[1]. This calibration is valid within a given wavelength range and under strictly defined conditions of operating current, voltage and temperature.
The calibration sheet (see Figure 12.1.3) lists the spectral planar irradiance of the lamp at a defined distance of 70 m. The incoupling optics is placed at exactly this distance facing the lamp. The calibration light then hits the Teflon ball from a deviation angle of 0° ± 0.4°; since the deviation of the cosine of 0.4° from 1 is negligible, the planar irradiance is equivalent to the actinic flux which makes this calibration valid. For details see [*Hofzumahaus et al. 1999*].
A scan is performed using the wavelength step sequence [$\lambda_1, \lambda_2, \ldots, \lambda_n$] that is intended to be used for the measurement planned, and from the photo current output I [nA] a conversion factor F_i for each wavelength channel [$\lambda_0-\Delta\lambda$, $\lambda_0+\Delta\lambda$] is derived.
Application of this conversion factor to the photo current output in the measurement yield the amount of energy that has impinged onto the Teflon ball per second at the time of recording within this very wavelength channel, meaning the irradiance in [W m^{-2} nm^{-1}].
Figure 12.1.3 shows the calibration lamp output in irradiance at a distance of 70 cm and the SR response in [nA] for the calibration of June 26th 2002.

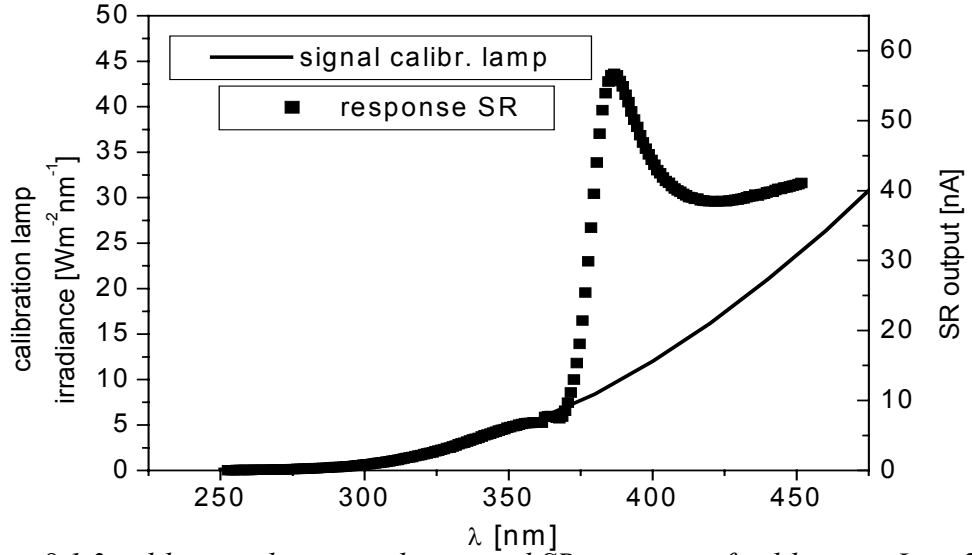

Figure 8.1.3 calibration lamp irradiance and SR response of calibration June 26th, 2002. The increase in signal above 380 nm results from the removal of the UG5 UV pass filter.

[1] Calibration sheet by German Calibration Service (DKD) DKD-K-10601, March 18th 1996

8.1.7 Calculation of photolysis frequencies

The photolysis frequency mainly depends on the cross section σ [cm^{-2}], which governs the sensitivity of the molecule‘s electron structure to photons of a given energy. But the cross section is modulated by the quantum yield *q* [], which is a measure of the fraction of photons hitting a molecule that actually leads to a photo dissociation, and not only to an e.g. excitation of a vibrational state. Usually the quantum yield is unity in the UV, and decreases monotonously when increasing the wavelength into the visible. Integration over the photolytically relevant wavelengths of the product of number of photons, cross section and quantum yield results in the photolysis frequency *J*:

$$J = \int_0^\infty \gamma(\lambda)\sigma(\lambda)q(\lambda)d\lambda \tag{8.1.1}$$

The measured irradiance E(λ) is measured in channels channels n ∈ [1,..,N] each representing (as stated above) an interval centered (and represented by) at λ(n). E(n(λ)) yields the number γ(λ(n)) of photons per second and unit area impinging onto the Teflon ball with energies matching λ(n). The unit of this quantity is [s^{-1} cm^{-2} nm^{-1}]. Multiplication with the convolved cross section and quantum yield results in the number of photolysis events per second within the channel; integration over all channels finally yields the photolysis frequency *J* in [s^{-1}], given that the probed wavelength range comprises all relevant wavelengths.
From the multiplication with the photolysis frequency with any actual trace gas concentration the absolute amount of molecules per cm^3 is derived that would get photo dissociated per second for a given concentration. The integration of course in fact is a summation:

$$J = \sum_{n=1}^{N} \gamma(n(\lambda)) \cdot \sigma(n(\lambda)) \cdot q(n(\lambda)) \tag{8.1.2}$$

This quantity can be used for chemical models.
This calculation is perfomed with the program “Sierra” (Spectral *J* from radiometer data, SJRa). It reads in ASCII files with the

- SR response to the calibration lamp,
- the cross sections and quantum yields of the trace gases,
- the file with the wavelength steps
- and the file with the data measured in the field.

Taking into account the wavelength offset, it performs above calculations and writes the results line by line to an ASCII file.

Photolysis frequencies show a sharp rise during sunrise. During a SZA decrease in the morning of 2° the photolysis frequency rises by one order of magnitude.
But during this time, the absolute values of J still are low, leading to large scan durations during this critical time. To increase the time resolution, the following feature was incorporated into the program.

The user may choose not to scan the entire spectral window within which a given species is photo-dissociated, but to omit spectral intervals $\Delta\lambda_A$ and $\Delta\lambda_B$ at both ends of the spectral range. The program then loads the high resolution Kurucz spectrum [*Kurucz 1984*] (the same used for spectral evaluation), averages channel-wise to obtain the measurement step width and

uses a user-specified set of channels to scale the Fraunhofer spectrum to the measurement, then using it as extrapolated measurement.
This method can neither be recommended during sunrise and sunset, when the ratio of UV to VIS radiance changes quickly, and nor for large $\Delta\lambda_A$, $\Delta\lambda_B$, i.e. > 30 nm on the long wavelength side. With $\Delta\lambda_A = 0$ and $\Delta\lambda_B <= 30$ nm, the photolysis frequency of NO_3, to give an example, is reproduced within 3% accuracy for SZA < 80° with the method as compared to a measurement spanning the entire necessary spectral window[2].

The usual wavelength step size used is 1 nm. Another method to reduce scan times is the measurement with the same resolution, but a larger stepwidth of e.g. 2 nm or 5 nm.
The latest version of "Sierra" linearly interpolates wavelength "gaps" in the measured data to obtain a stepwidth of <= 1 nm before processing them to photolysis frequencies. E.g. with data measured for 342 and 344.4 nm two values are interpolated between them, for 342.8 nm and 343.6 nm.
The following data are result of an exemplary investigation of this method`s accuracy for NO_2. For other trace gases, a specific sensitivity study is necessary.
As basis five spectra of a measurement campaign in Rome, June 2001 did serve, taken from a clear day around noon. J_{NO2} had been measured between 276 and 435 nm. The total time to record both spectra was ca. 22 min. The standard deviation of the J-values was 3.7%, which can be used in approximation as the noise of the photolysis frequencies induced by atmospheric turbulences, dust load variations overhead etc.
From the raw data, three data sets were generated from the total 160 channels:
"2nm1st" The first nA-value is used, after that every second one, i.e. channel # 1, 3, 5,….
"5nm3rd" The third nA-value is used, after that every fifth one.
"5nm5th" The fifth nA-value is used, after that every fifth one.

Then the data sets were processed by "Sierra". Table 8.1. 1 gives the deviations in % of the J from the interpolated data to the J of the original data, recorded with 1 nm stepwidth, averaged over the five spectra.

Table 8.1.1 Deviations of photolysis frequencies calculated from interpolated data to the J calculated from the data recorded in 1 nm stepwidth
From these data, it can be concluded that for NO_2 a stepwidth of 5 nm is sufficient to generate data with accuracies better than 3%.

dataset	Deviation of J in % from original data
"2nm1st"	0.26
"5nm3rd"	2.6
"5nm5th"	2.3

To accurately use the photolysis frequencies in a model, precise SZA are a necessary requirement.
Part of the above software package is a module using an ephemerid file (JPL) used by the United States Naval Observatory for a precise calculation of solar and lunar zenith and azimuth angles. This file contains data on the movement of all relevant bodies in the solar system affecting the earth orbit and rotation.
Most other SZA calculation software and software routines use polynomials fitted to these or other ephemerid data. The software was made available by [*Gernot Burkhardt, pers. comm.*]

[2] Even with this method, the integration time might smooth out the true atmospheric variability.

of the Astronomical Calculation Institute. After converting the Fortran code to C with translation software, the module was fitted with a user interface accepting date, UT, latitude and longitude. It then converts the time into Julian date which in turn serves as input for calculation of the coelestial angles.
The first version of the evaluation code "Sierra" contained that module to add the SZA information to the photolysis data.
Since "SRCon" now contains the module in itself and stores the data to its output file, the "Sierra" version using "SRCon" output is freed of this task.
The SZA software module also has been made a program in itself, "SZAUSN".

8.2 Conversion of TRACY output to radiances

Among the output parameters of TRACY are the following:

- the number N_P of photons contributing to the signal, i.e. of the successfully completed paths,
- and the intensity weight sum I, i.e. the sum over all intensity weights of the photon paths, after attenuation by aerosols and those trace gases chosen to influence them by the user (e.g. ozone).

N_0 is the number of photons launched.
To the input files of TRACY an ASCII file containg the solar irradiance by [*Wehrli 1985*] was added, from which the value for the modeled wavelength, $S_0(\lambda)$is taken.
We consider only the spectral quantities per unit time, i.e. per nm and per second, in the following.
Consider a situation where the sun forms a hollow sphere, i.e. occupying the entire 4π solid angle, radiating the number of photons N_0 representing S_0, i.e. the photons emitted from the solar disk apparent in the sky would distribute over a sphere with given radius (be it 1 AU or unity) and from their converge on us.
If the detector was a ball (such as the Teflon ball) without any optical obstacles such as tripods or cylinders, and if there was neither a scattering atmosphere nor absorbing gases or particles therein, the detector would record just N_0, i.e. each photon from the sun would reach the detector, and vice vs.
If we reduce the sun in solid angle, e.g. "shrink" it back to the disk of $\alpha_S = 0.28°$ half solid angle, then it only covers a fraction F_S of the unity sphere around us (π cancels out):

$$F_S = \sin^2(\alpha_S)/4 \qquad (8.2.1)$$

Then of all N_0 photons launched from the (still spherical) detector in backward mode only the fraction F_S would hit the sun, i.e. $N_P = F_S * N_0$.
But in reality, the detector would measure the same N_0 (coming from the sun) as before. This means that the number N_P must be divided by just F_S to obtain the physically correct result.

On the other hand, if we reduce the aperture angle of the detector (so far 4π) to a value smaller than this, e.g. by shielding a part of the "Teflon sphere" leaving free only a fraction representing the chosen aperture angle, we see that of the N_0 photons launched from the hollow sun only a fraction F_D would enter the detector and contribute to the signal. F_D is calculated in the same way as F_S with the difference that the half aperture angle of the detector is used instead of α_S.
But when launching N_0 from out of the detector in backward mode, we find that they all would hit the sun. Again to restore the consistency, we must multiply the number by F_D.

When we insert an atmosphere, the weight of the photons will be reduced by attenuation and the scattering probabilities.
The average probability P of the photons to reach the sun along the paths modeled is just

$$P = I/N_0 \tag{8.2.2}$$

So $P = 1$ for neither attenuation nor scattering, and all photon launches successful. So the N_0 must be weighted with P as well to form N_W. So the fraction of N_0 that reaches the detector after all factors applied is:

$$F=N_W / N_0 = (F_D/F_S)*P \tag{8.2.3}$$

The spectro radiometer is calibrated for irradiance. Nevertheless, what it records with the photo multiplier unit are numbers of photons, which are converted to irradiances by comparison with calibration data. S_0 also is an irradiance, which is represented by photons. So the fraction F also applies to the radiance.
So the following algorithm must be carried out to derive the modeled irradiance $E_M(\lambda)$:

$$E_M(\lambda) = S_0(\lambda)*F = S_0(\lambda)*P*(F_D/F_S) \tag{8.2.4}$$

This calculation, taking the detector aperture angle from the *Detector* object, has been added to the *AMFCalculator* incl. error calculation.
The irradiances can easily converted into radiances by dividing them by any appropriate angle. With this capability added to TRACY, it is capable of calculating the diffuse part of the radiation forming photolysis frequencies. Future work is the (straight forward) adding of a module calculating the direct part of the radiation analytically.
Ultimately TRACY will be able to deliver photolysis frequencies.

8.3 Modeled radiances

For a first and qualitative study, again aerosol loads derived from the HCHO SCD RT modeling comparison was used, as was in section 9.1 and 9.3 as well as in chapter 10.
For the troposphere, three aerosol extinction coefficients for ground level were chosen for a sensitivity study, 0.1 km^{-1}, 0.4 km^{-1} and 1 km^{-1} plus clear sky, albedo 10% for urban areas.
This extinction coefficient's logarithm then reduced linearly with altitude in the same way as the selected aerosol load for the MAX DOAS investigation. The phase function and the rest of the aerosol load was taken from the HCHO RTM intercomparison. Figure 8.3.1 shows the resulting plot. The quantity plotted is irradiance out of 5° around zenith.
In boxed lines the measured values are shown; the spectro radiometer incoupling optics was fitted with a black plastic tube narrowing the field of view to 5° half aperture angle around zenith. The day chosen was a clear (i.e. without clouds) day, the 22th of February 2003, one of a series of days when the SR was available in between two measurement campaigns. Among the scanned wavelengths 350 and 420 nm were chosen for the absence of strong gaseous absorptions adding uncertainty.
We see strong variations in irradiance for the different aerosol loads. This is in compliance with [*Hugh Coe, pers. comm.*] (see also section 14.3), who modelled photolysis frequencies of NO_3 and likewise found variations by a factor of rougly three for different aerosol scenarios, i.e. for clear and continental air. So again the aerosol load must be known prior to modelling if we need e.g. accurate photolysis frequencies.

But on the other hand, with the spectro radiometer we can measure these frequencies, and the irradiances can provide us with another tool, apart from O_4 measurement, to conclude on aerosol. When comparing the modeled to the measured data, it can be concluded from the 350 nm dataset that the extinction coefficient was 1 km^{-1} on that day. The match, in this case, with the 420 nm is not as good, indicating different optical aerosol properties for the two wavelengths. Also the vertical distribution assumption may play a role. It is interesting to note that the maximum in modelled irradiance is not with clear sky, but with the low aerosol load, which is attributable to multiple scattering winning over attenuation, and so for both wavelengths. Derivation of ratios for different wavelengths and SZA should overcome this ambiguity and eventually even allow for statements on aerosol single scattering albedo. The sensitivity of UV actinic fluxes to atmospheric aerosol has been investigated by [*Jeong 1999*] A detail investigation is among the future work and may also combine the spectro radiometer, fitted with tubes for different aperture angles, with the Multi-Axis technology (see next chapter) to compare the directional irradiances for different elevations. Since low elevations can be expected to be affected stronger by aerosol loads near the ground, the results may lead to further information on aerosol parameters.

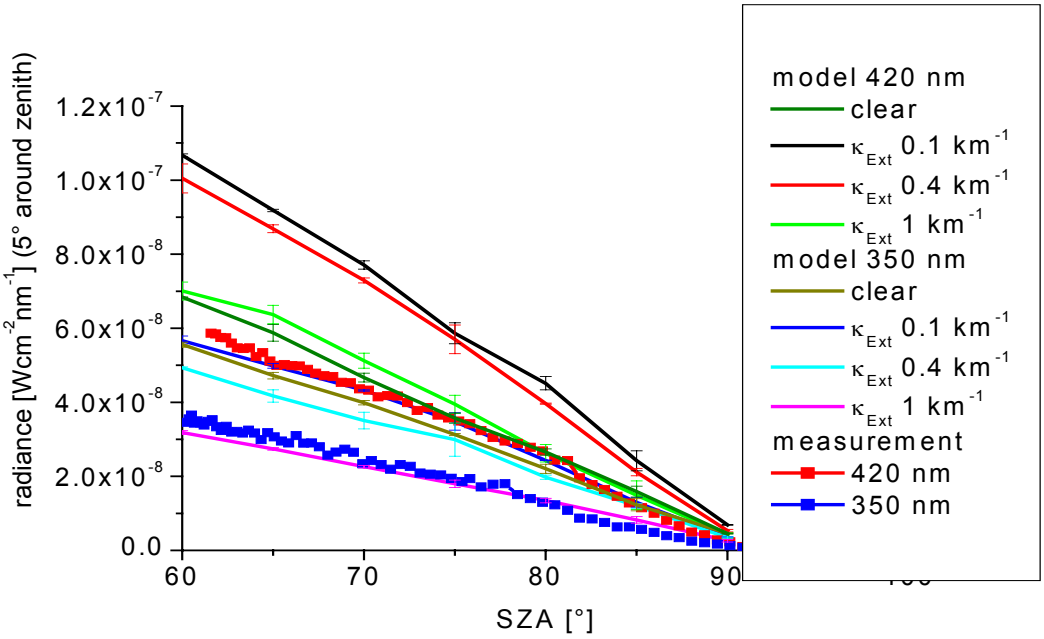

Figure 8.3.1 Modeled irradiances out of 5° around zenith for different aerosol loads (see legend and text); The irradiance thus provides us with another measurable quantity to conclude on aerosol. In dotted lines the measured data. Note the maximum in modelled irradiance at aerosol extinction coefficient (ground level) of 0.1 km^{-1}.

8.4 Addition of polarization

The wavelengths chosen are subject to multiple scattering at all SZA. This abates the influence of polarization. In case of longer wavelengths, the fraction of single-scattered photons increases, so that the respective SZA constitutes the scattering angle.
To further complete the model's capabilities, polarization was implemented by modifying the scattering routines for Rayleigh scattering. Mie scattering also has polarization attributes, their characteristics being, though, as complicated as the phase functions in their relation to size parameters, refractive indices etc. But the modifications described below can straight forward

be applied to the Mie scattering as well. For details see A.2.13. The photon was assigned to normalized vectors representing the electric and magnetic field vectors. In the Rayleigh-scattering algorithm, instead of the scattering angle θ the angle θ' is calculated as angle between previous and new photon direction in the plane defined by the previous direction and *Polaris*. The phase function is

$$\phi(\theta') = \cos^2(\theta') \qquad (8.4.1)$$

The second angle necessary for a 3D scattering now is the angle between the new direction as projected onto the plane defined by the previous direction and the "magnetic" vector. The phase function for this is unity. Both angles are derived using the phase functions and random numbers. Two control parameters to input have been added; they are the optical densities for light polarized along two axis which are perpendicular to each other as well as the detector's line of sight. For definition see Appendix A. The initial weight of a photon to be launched can thus be scaled according to a randomly selected polarization vector. The concept of Stokes-vectors was not used, because the above scheme is easy to handle and to adapt to existing routines, and any desired (e.g. elliptical) polarization of the light can be obtained by "mixing" appropriate numbers of photon polarization axis with specific directions. Figure 8.4.1 shows an exemplary series of relative radiances with assumed perfect polarization filter for zenith sky geometry, aligned in east-west and north-south direction, respectively, and for a sun shining in the east for the entire sunrise in a pure Rayleigh case. Hence finite OD for light polarized perpendicular to the filter's axis, finite transmission of the optical component, and azimuthal movement of the sun have not been taken into account for this qualitative test.

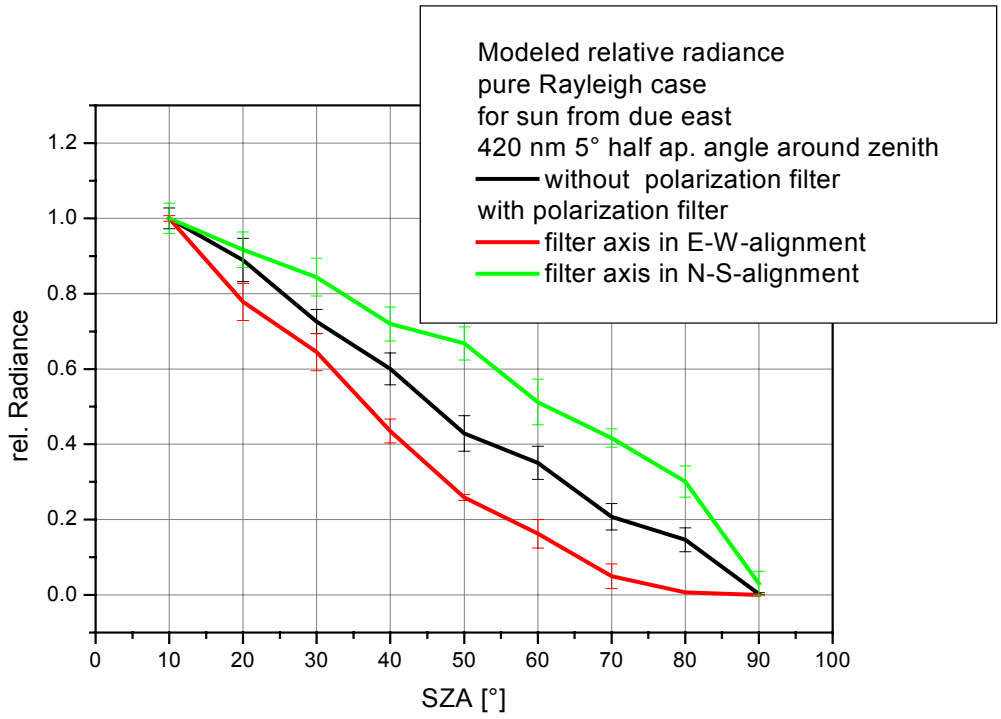

Figure 8.4.1 Modeled relative radiances for an idealized polarization filter and fixed solar azimuth of 90°. Clearly in axis alignment to East-West the polarizing effects of the filter and the Rayleigh scattering combine to suppress the greatest part of the signal around SZA 90°.

When the filter polarization axis (the axis incoming light must be polarized parallel to to pass the filter) is aligned in East-West direction, the appropriately polarized light is suppressed by the Rayleigh scattering characteristics around SZA 90°. The result is a greatly reduced signal, fed only from multiple scattered light, as compared to the other filter axis position.

8.5. Polarization characteristics of the SR with a polarization filter

Lack of clear days prevented measurements of sufficient quality. Nevertheless, a system of SR and polarization filter has been characterized by [*Grätz 2003*] under supervision of the author. Using a halogen lamp, emitting (in theory) white, unpolarized light, the effect of turning an UV polarization filter in different angles with respect to the SR UpDown-Axis was investigated for the spectral range the SR is usable for. The SR was fitted with the tube to suppress straylight, and the assembly was horizontally aligned to a system of halogen lamp (with stabilized power source) and a focusing lens. Shown in Figure 8.5.1 is the attenuation of the lamp signal as ratio of the measured signal with filter divided by the signal without for a representative set of wavelengths. 10 scans were performed, the errors shown are the square sums of the standard deviations with and without the filter.
The conclusion to be drawn is that the spectro radiometer does have its own polarization charactersitics, induced by its gratings and mirrors, and that the quartz fibres do not destroy the polarization of incident light by transmitting it. Hence this must be taken into account when measuring polarized light with any filter. For more quantitative investigation a filter optimized for VIS light could be used, to focus on wavelengths with less influence of multiple scattering perturbing the polarization effects, and with known polarization properties. For an example see Figure 8.5.2; it shows the optical densities for light polarized parallel and perpendicular to the filter axis as a function of wavelength.

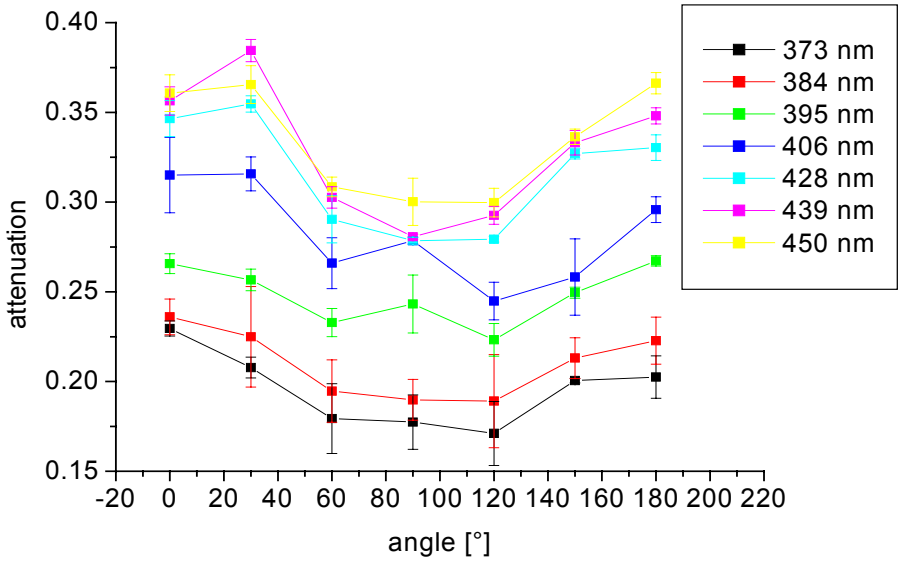

Figure 8.5.1 Attenuation by the filter when turned in its axis with respect to the detector's Up-Down axis.

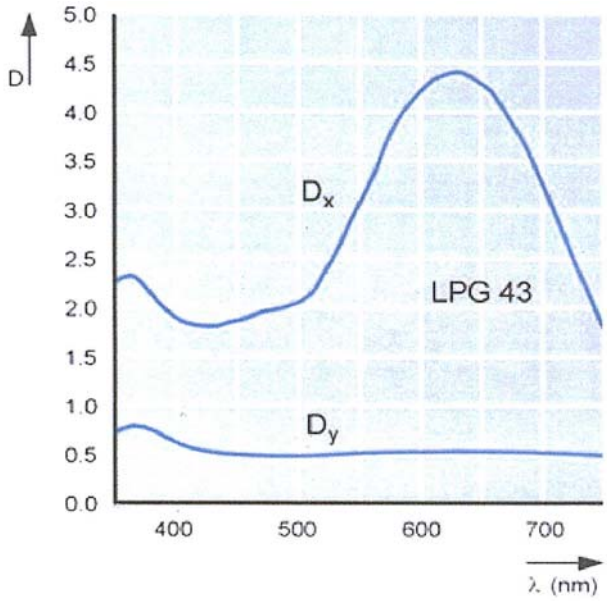

Figure 8.5.2 Polarization characteristics of Schott LPG 43 polarization filter [taken from Schott homepage[3]*.*

Transmission experiments with a stabilized lamp could yield a plot like 8.5.2 for the spectro radiometer itself, to enhance, by affixing of the filter in well defined positions, the capabilities of the SR by the one for investigations on the polarization of scattered light.

[3] *http://www.schott.com/german/*

9. Application to ground based DOAS

An important application of TRACY in the light of a possible matrix based profile retrieval is the Multi-Axis DOAS. The following sections will cover a series of measurements of different trace gases and the relationships between the AMF and scattering parameters.

9.1 Sequential MAX-DOAS of BrO Alert/Canada 2000

9.1.1 Role of tropospheric BrO and campaign objectives

BrO is a halogen compound important for ozone chemistry both in the stratosphere and in the troposphere. For a detail discussion of the BrO chemistry see [*Hönninger 2002*] and references therein from which this section has been adapted to provide some background knowledge on the species of which the measurements are to interprete.
The destruction of tropospheric ozone by bromine (or chlorine) does occur in two cycles:
Cycle 1:

$$X + O_3 \rightarrow XO + O_2 \quad (9.1.1)$$

$$Y + O_3 \rightarrow YO + O_2 \quad (9.1.2)$$

$$XO + YO \rightarrow X + Y + O_2 \quad (9.1.3)$$

$$XO + YO \rightarrow XY + O_2 \quad (9.1.4)$$

$$XO + YO \rightarrow OXO + Y \quad (9.1.5)$$

The net reaction is:

$$2O_3 \rightarrow 3O_2 \quad (9.1.6)$$

Cycle 2:

$$X + O_3 \rightarrow XO + O_2 \quad (9.1.7)$$

$$OH + O_3 \rightarrow HO_2 + O_2 \quad (9.1.8)$$

$$XO + HO_2 \rightarrow HOX + + O_2 \quad (9.1.9)$$

$$HOX + h\nu \rightarrow OH + X \quad (9.1.10)$$

With the net reaction:

$$2O_3 + h\nu \rightarrow 3O_2 \quad (9.1.11)$$

Since the 1980s researchers from various Arctic stations have reported events of sudden ozone depletions in the polar boundary layer after sunrise [e.g. *Oltmans and Komhyr 1986; Rasmussen et al. 1997*]. The presence of bromine compounds were discussed as possible reasons [e.g. *Finlayson-Pitts et al. 1990; LeBras and Platt 1995*]. DOAS measurements from different platforms [e.g. *Hausmann and Platt 1994; Wagner and Platt 1999; Frieß 2001*] confirmed the presence of BrO abundances and allowed for conclusions that a large part of the bromine abundance was located in the boundary layer, with mixing rations between 10 ppt and 30 ppt near the ground.
There are still many open questions concerning tropospheric bromine chemistry, the source and sink mechanisms and the influence of reactive Br on a global scale.

Organobromine compounds, halocarbons, emitted from natural sources are potential precursors for reactive bromine compounds in the troposphere. For typical mixing ratios and tropospheric lifetimes of brominated hydrocarbons see [*Hönninger 2002*] and references therein. Macroalgae and phytoplankton are responsible for a part of the total production of volatile brominated organic substances in the oceans and therefore for their release to the atmosphere. But the atmospheric abundances and degradation rates of organobromine compounds cannot sustain the sudden increases of reactive bromine of up to 10 ppt/h observed in the arctic boundary layer during polar spring. Also, the observation of up to 180 ppt BrO in the Dead Sea valley [*Hebestreit 2001*] suggests a more effcient production process must exist which releases reactive bromine from salt surfaces present both in the Arctic as salt covered sea ice surface as well as in the Dead Sea valley

The mechanism suggested to cause the observed sudden BrO enhancements in the boundary layer is the autocatalytic release of bromine involving heterogeneous reactions on sea salt surfaces [e.g. Vogt et al. 1996]. The release of reactive halogens from acidic sea salt surfaces occurs via the uptake of gaseous HOBr:

$$HOBr_g \rightarrow HOBr_{aq} \tag{9.1.12}$$

$$HOBr_{aq} + (Cl^-)_{aq} + (H+)_{aq} \rightarrow (BrCl)_{aq} + H_2O \tag{9.1.13}$$

$$(BrCl)_{aq} + (Br^-)_{aq} \rightarrow (Br_2Cl^-)_{aq} \tag{9.1.14}$$

$$(Br_2Cl^-)_{aq} \rightarrow (Br_2)_{aq} + (Cl^-)_{aq} \tag{9.1.15}$$

$$(Br_2)_{aq} \rightarrow (Br_2)_g \tag{9.1.16}$$

$$Br_2 + h\nu \rightarrow 2Br \tag{9.1.17}$$

$$2(Br + O_3) \rightarrow 2(BrO + O_2) \tag{9.1.18}$$

$$2(BrO + HO_2) \rightarrow 2(HOBr + O_2) \tag{9.1.19}$$

net:

$$HOBr + (Br\text{-})_{aq} + (H+)_{aq} + 2HO_2 + 2O_3 + h\nu \rightarrow 2HOBr + H_2O + 4O_2 \tag{9.1.20}$$

Here, (aq) denotes the aqueous phase, i.e. reactions on deliquescent sea salt aerosol or the surface layer of freshly frozen sea ice. This bromine release mechanism is also illustrated in

Figure 9.1.1. The generation of two HOBr molecules for each one taken up by the sea salt surface is what causes the rapid production of reactice bromine. This auto-catalytic mechanism can lead to an exponential increase of bromine in the gas phase, which led to the term “bromine explosion” [*Platt and Lehrer 1997*].

The following conditions are necessary (among others) to sustain the above reactions:

- The acidity must be high enough (pH < 6.5) by uptake of gaseous HCl or other strong acids. Therefore e.g. sea ice surfaces strongly enriched in sea salt are needed. These are present as surface brines (a liquid layer with a high salinity on the frozen sea ice) and frost flowers on freshly frozen sea ice.
- The meteorological conditions must prevent boundary layer air from mixing with free tropospheric air. During late winter and early spring, strong inversion layers in the lowermost 1000m of the polar atmosphere ensure this to be the case.
- The autocatalytic bromine release and the subsequent destruction of ozone requires light (Br_2 photolysis), so bromine explosions only occur after polar sunrise.

The released bromine causes the destruction of ozone in the marine boundary layer. When all ozone is consumed, reactive Br is converted to HBr and either taken up by the aerosol or deposited at the surface as bromide (Br^-).
After the inversion layer break-up more ozone enters the PBL from higher altitudes.
The photolytic lifetime of BrO at a solar zenith angle of 70± ranges between 30 s and 100 s depending on surface albedo, etc.

$$BrO + h\nu \rightarrow Br + O \qquad (9.1.21)$$

The only other important reaction channel of BrO besides the photolysis reaction (9.1.21) are the BrO self reaction and cross reactions with other halogen oxides:

$$BrO + BrO \rightarrow Br + Br + O_2 \;\; 85\% \qquad (9.1.22)$$

$$BrO + BrO \rightarrow Br_2 + O_2 \; 15\% \qquad (9.1.23)$$

The BrO lifetime with respect to the self reaction is given by the inverse of [BrO] multiplied by the reaction rate constant and ranges between 300 and 1200 s for mixing ratios at ground level of 40 ppt and 10 ppt, respectively.
Bromine atoms also can react with oxidized or unsaturated hydrocarbons (e.g. formaldehyde HCHO), HO_2 radicals or ozone in the following pathways:

$$Br + RH \rightarrow HBr + R \quad 2\% \qquad (9.1.22)$$

$$Br + O_3 \rightarrow BrO + O_2 \;\; 98\% \qquad (9.1.24)$$

RH denotes the sum reacting hydrocarbons. Depending on their levels the conversion time of BrO to HBr can be up to 5000 s. But the BrO self reaction is much faster, leading to efficient ozone destruction. BrO also reacts with dimethyl sulfide (DMS)

$$BrO + DMS \rightarrow Br + DMSO \;\; k = 2.6 * 10^{-13}\ cm^3 \qquad (9.1.25)$$

It might be important in the clean marine boundary layer where the only other

sink for DMS is the reaction with OH radicals. Finally Fig. 9.1.1 shows schematically the reactions involved in tropospheric bromine chemistry.

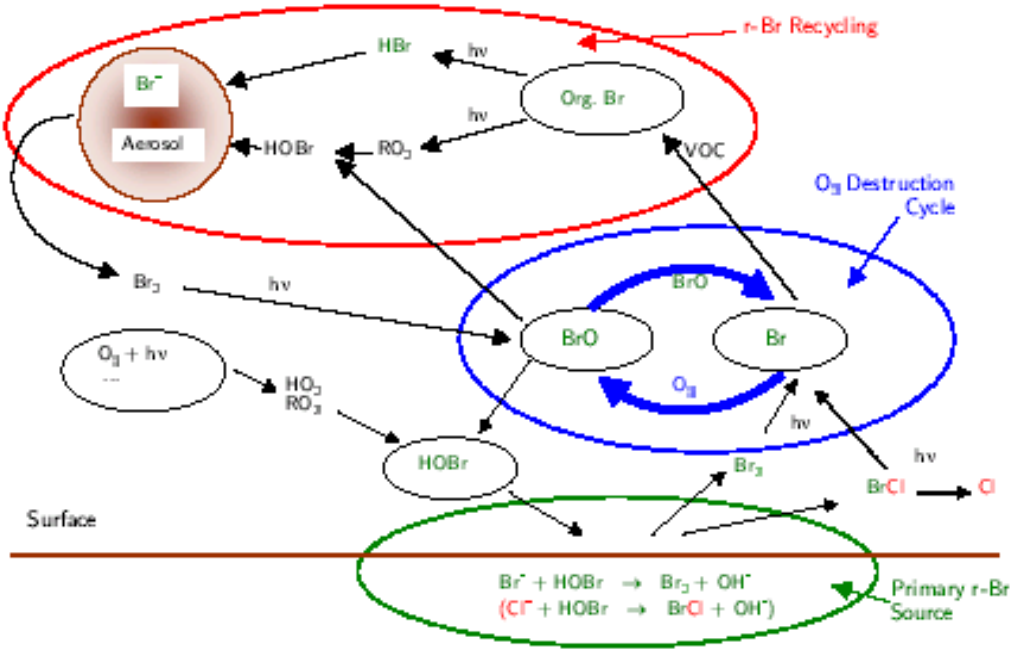

Figure 9.1.1 Tropospheric bromine chemistry with bromine explosion mechanism (taken from [Lehrer 1999])

To investigate the abundances of BrO over ice as well its vertical distribution, Gerd Hönninger [Hönninger 2002] performed ground-based measurements during the ALERT2000 campaign in Alert/Canada from April 4th to May 12th 2000. He employed a sequential MAX DOAS device to take advantage of the expected different sensitivities for BrO abundances near ground. The next two sections are courtesy of [*Hönninger 2000*].

9.1.2 Instrument

The entrance optics were adapted from the system used by e.g. [*Kreher 1991*]. It consists of a quartz lens (focal length f =100 mm, diameter d = 30 mm) and a round bundle of 25 individual quartz fibers (core diameter 100 mm, diameter of the circular arrangement d_e = 0.8 mm). This quartz fiber bundle (length l = 8 m) transmits the light from the focal point of the quartz lens to the entrance slit of the spectrometer for spectral analysis. At the entrance slit the fiber exits form a column of 25 mm height. The aperture of the telescope can be calculated from f and d_e to be less than 1°. The telescope arrangement is assembled in a dry atmosphere and sealed to prevent contamination and condensation of water on the interior optics. The stainless steel telescope housing is sealed with a UV-transmitting quartz window mounted at 45° angle which also prevents snow from accumulating in front of the telescope.
The telescope housing (half aperture angle 0.2°) is equipped with a joint system to transform the movement of a linear stepper motor drive into a change in elevation angle of the telescope. The elevations used for this operation were 5°, 10°, 20° and 90°.
The spectrograph is a Czerny-Turner model [Czerny and Turner 1930] of type ACTON Spectra Pro 500 with a focal length of 500 mm. It has a plane diffraction grating of aperture ratio f/6.9 and an entrance slit (fiber exit) width of 100 µm to support the MAX-DOAS fiber

bundle, a grating of 600 grooves/nm, dispersion 3.08 nm/mm and a spectral resolution of 0.54 nm). The quartz fibre is mounted in the focal point (entrance slit) of the first convex mirror (collimating mirror), which reflects the parallel light onto a plane diffraction grating. A second convex spherical mirror unit (focussing mirror) then focusses the dispersed light onto the detector. The wavelength region observed by the detector can be changed automatically by a computer controlled stepper motor. To minimize thermal instability the whole spectrograph unit is insulated and temperature stabilized to a few K above maximum room temperature.
For recording the spectra, a 1024 pixel photo diode array detector (PDA) is mounted in the focal plane of the spectrograph. This photo diode array from Hamamatsu (Type S3904-1024) has 1024 Si photo diodes (CMOS) of each 25µm width and a height of 2.5 mm. The PDA is cooled down to temperatures between -15 and –30 °C by a Peltier cascade to reduce dark current. Due to the cooling of the detector unit water vapor could freeze on the PDA surface and possibly cause etalon structures due to interference effects. Therefore the detector is evacuated and filled with dry argon as inert gas. Figure 9.1.2 shows a schematic drawing of the device.

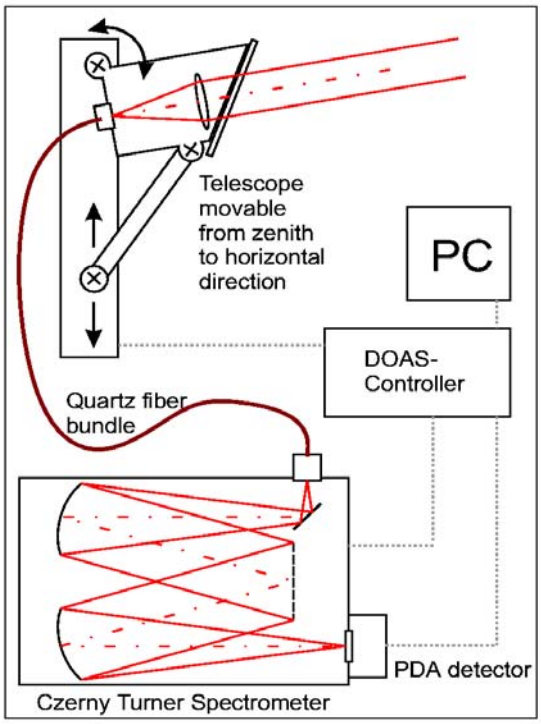

Figure 9.1.2 Sequential MAX DOAS setup operated e.g. in Alert 2000

9.1.3 Measured SCD

For a description of the evaluation algorithm see again [*Hönninger 2000*].
All spectra were evaluated against a zenith-sky referece with no tropospheric BrO, but the stratospheric signal of a quantity not known precisely.
Figure 9.1.3 shows the results for all four of the elevations in the 1th of May.
Clearly a relation between the measurement signal and the elevation can be seen: the higher the elevation, the larger the DSCD. With this experiment the usability and the potential of the novel sequential MAX DOASD was impressively demonstrated.

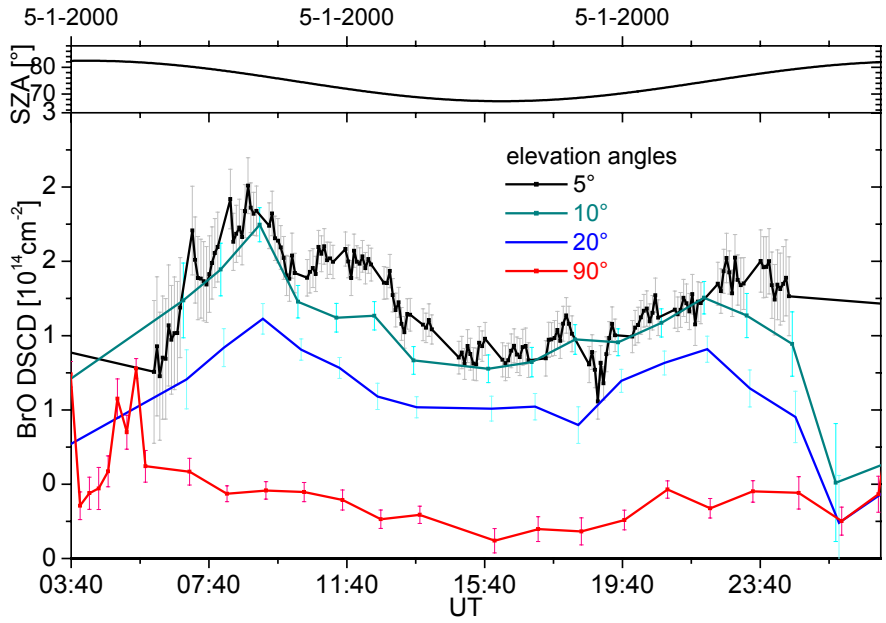

Figure 9.1.3 BrO MAX DOAS results for May 1st, 2000, Alert, Canada ([Hönninger 2002]). Clearly the differences in BrO signal for the different elevations is seen. But also it is obvious that the measurement does not obey the geometrical "1/sin"-approximation, which would deliver higher DSCD for 5° with respect to 10° (by a factor 2.

We see without further investigation that the bulk of BrO must be located close to the ground, and that is subject to meteorology, e.g. wind, on a short time scale.
If we compare this result to the geometric approximation, we find that in theory the 5° elevation should deliver DSCD which are larger by a factor of 2 as the 10° values. This is not the case, in fact at some times, the 10° signal is even a bit greater. This leads us to the question which factors do influence the radiative transfer in a way to motivate this behaviour.

9.1.4 AMF investigation

The aim of the following study is to assess the behaviour of MAX DOAS AMF for a set of profiles of various shapes and altitudes and for a representative set of environmental conditions. The sensitivities of different elevations for similar profiles are related to these AMF.
The measurement parameters were (for the first study):

- Wavelength 352 nm
- Telescope elevations 2°, 5°, 10°, 20°, 30°, 40°, 60°, 90°
- Telescope azimuth 90°, half aperture angle 0.2°
- SZA 30°

The spatial discretization in spherical layers was 100 m between 0 and 3 km, 500 m between 3 and 5 km, 1 km above 5 km, up to a TOA of 70 km. A standard atmosphere was used and interpolated to this discretization. So was a standard ozone profile from the RT intercomparison (exercise 1), [*Hendrick, pers. comm.*]. Other traces gases were not taken into account. The aerosol load was composed as follows:
Above 10 km a standard aerosol load from a chemical model scenario [*Hendrick, pers. comm.*] was selected for all cases ("Aerosol 2 and 3", see Fig. 9.1.1).
Below 10 km the aerosols are important for absorbers within the troposphere due to their influence on radiative transfer. In adaption to real extinction coefficients two loads for

"Aerosol 1" were designed, each with a linear development of the log of the extinction coefficient at 0 km to the value of Aerosol 2 (see Fig. 9.1.1) at 10 km. Three situations were modelled for the troposphere:

1. pure Rayleigh case
2. aerosol load with extinction coefficient at 0 km of 0.1 km^{-1} ("low load")
3. aerosol load with extinction coefficient at 0 km of 1 km^{-1} ("high load")

For cases 2 and 3, two types were selected:

- rural aerosol (abbreviated "RUR")
- maritime aerosol ("abbreviated OC")

The difference between both aerosol types is the phase is the phase function, shown in Fig. 9.1.2. The single scattering albedo was set to 1, since in reality it is near 1 for these aerosol types (only a few % below) and the investigation was to be kept simple to focus on key issues. The modelling was performed for two albedo values of 5% and 80%.

The profiles which were to be investigated were designed to

- represent different altitudes of possible BrO abundances
- be simple in shape in order to assess the behaviour of the AMF.

Absorbers near ground are shaped by the planetary boundary layer. This layer is, as outlined in chapter 2, separated from the FT. Trace gases within the PBL tend to be mixed thoroughly and thus form a nearly box-shaped profile.

Three sets of profiles were thus artificially composed:

- Near the ground with different vertical extensions and shapes
- In the FT, with different altitudes, but also box-shaped
- In the stratosphere, in a gaussian shape

For the profiles see Fig. 9.1.5; the numbering shall be used to refer to these profiles in the following investigations.

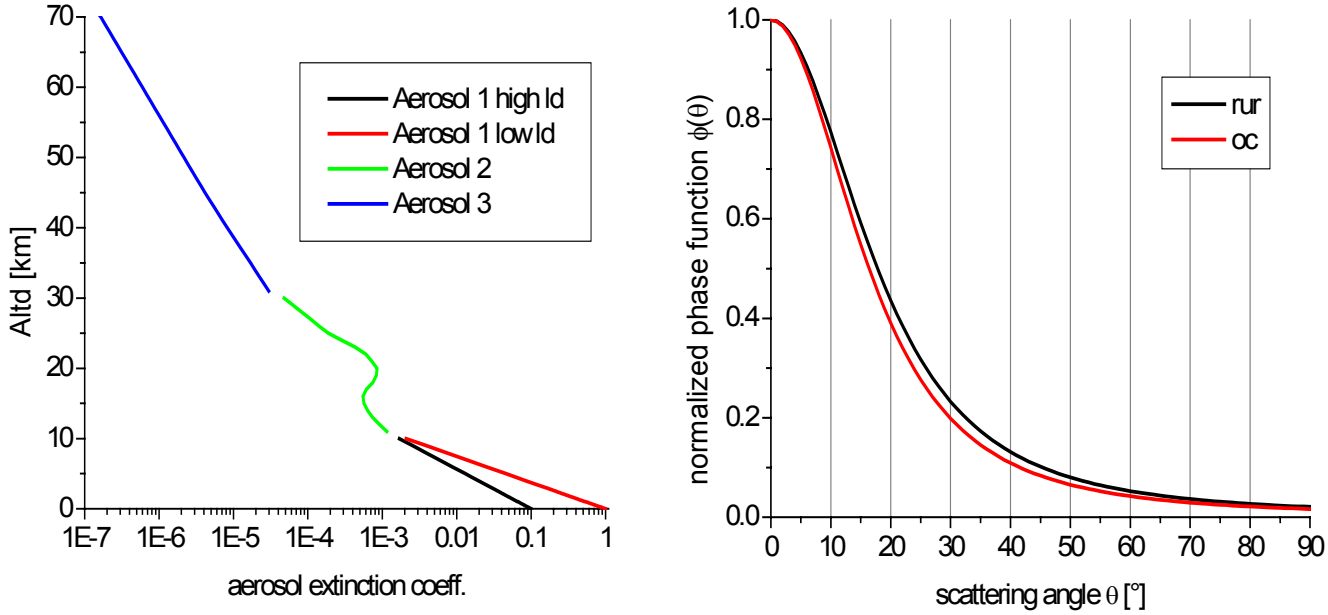

Figure 9.1.4 Left panel: aerosol loads used for the AMF investigations. In the troposphere, two loads were selected;
right panel: normalized phase functions for aerosol loads used for the AMF investigations. In the troposphere, two loads were selected.

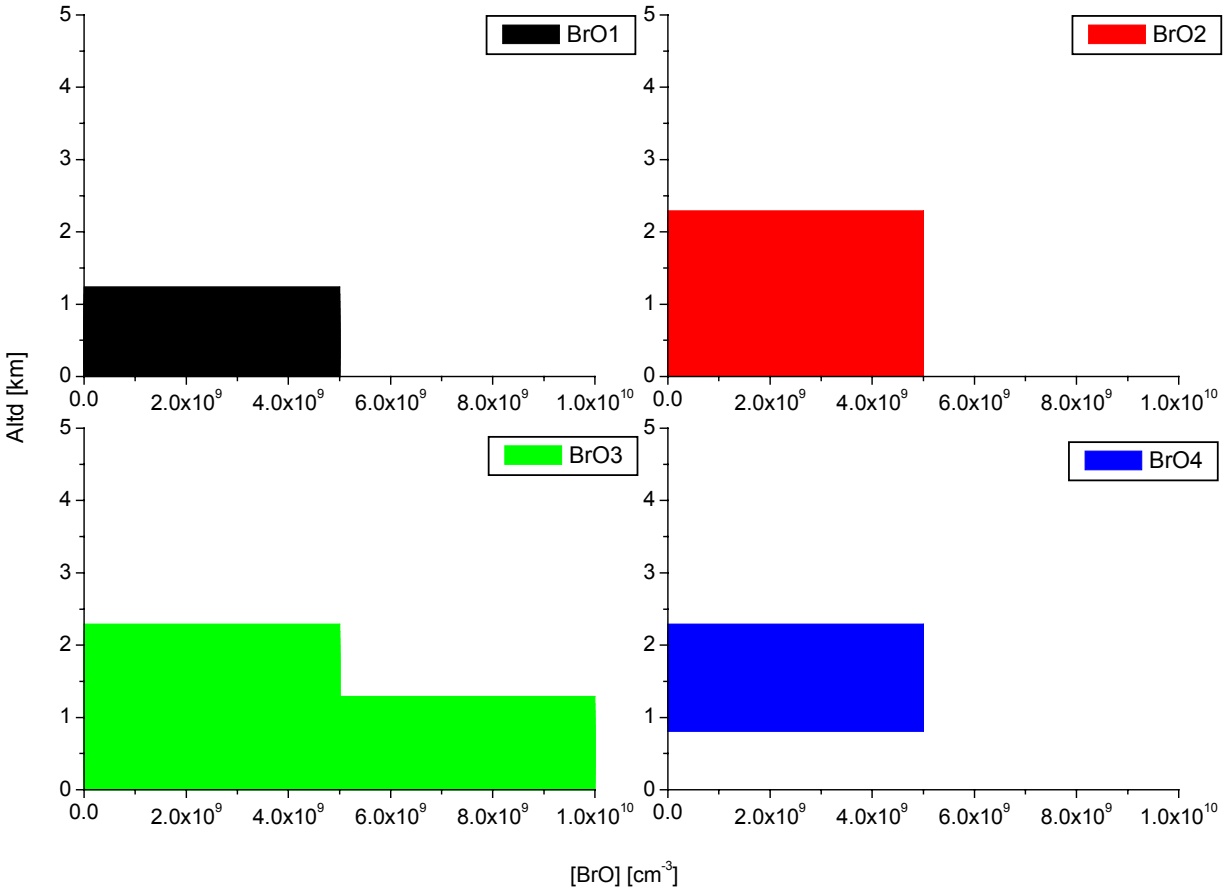

9.1.5 Near ground BrO profiles used for the investigation. "BrO1" and "BrO2" are box profiles, though of different vertical extension. "BrO3" displays a vartical gradient; finally "BrO4" is elevated off the ground. Not shown here is the O_4 profile, of which the AMF were to investigate as well.

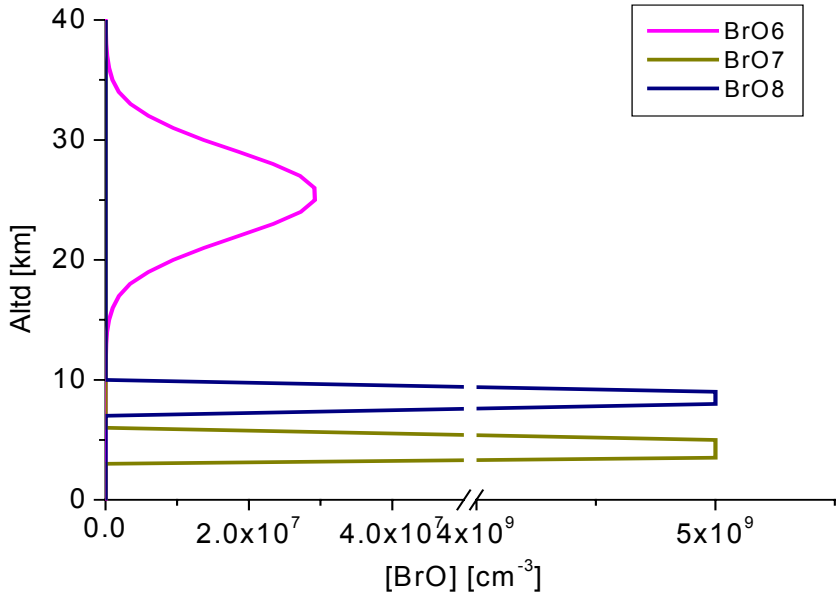

Figure 9.1.6 FT and stratospheric profiles used for the investigation. "BrO6" was a stratospheric profile of gaussian shape. "BrO7" and "BrO8" are box profiles within the FT

The investigation of the AMF for all telescope elevations consists of three parts:

- AMF for fixed SZA of 30° and fixed azimuth of 90° for all aerosol and albedo combinations for profiles “BrO1” - “BrO6” plus O_4.
- AMF for fixed SZA of 30° and variation of azimuths for pure Rayleigh and both albedoes for profiles “BrO1” - “BrO6” plus O_4.
- AMF for fixed azimuth of 90° and variation of SZA for pure Rayleigh and both albedoes for profiles “BrO1, 6, 7 ,8” and O_4

9.1.4.1 Aerosol dependency

The initial assumption is that the lower an elevation is, the longer the light path through any absorber near the ground must be, oriented at the geometrical line of sight, which in turn is approximated by 1/sin(elevation).
Figure 9.1.7 shows the results for the pure Rayleigh case.
The AMF for the stratospheric profile “BrO6” is largely independent from the elevation.
For “BrO1-3” it must be noted that the AMF for the lowest elevations falls short of the value from the “1/sin” approximation, i.e. the geometric approximation postulates an AMF of 28.7 while the modelled value is ca. 15 because of the Rayleigh scattering limiting the visibility.
For the O_4 profile, we find that the value for 2° elevation is even smaller, and the AMF rise with increasing elevations is very low.
The most striking feature is the behaviour of the “BrO4” profile. The AMF for elevation 2° is actually smaller than for 5°.
The effect of the albedo is to raise and lower, respectively, all AMF, but it has no significant effect on the elevation-dependencies.
The same shapes of the AMFs are seen with the aerosol load modelled. Figure 9.1.8 shows the AMF for the continental aerosol, 9.1.9 for the maritime aerosol, respectively, for both loads and both albedoes.

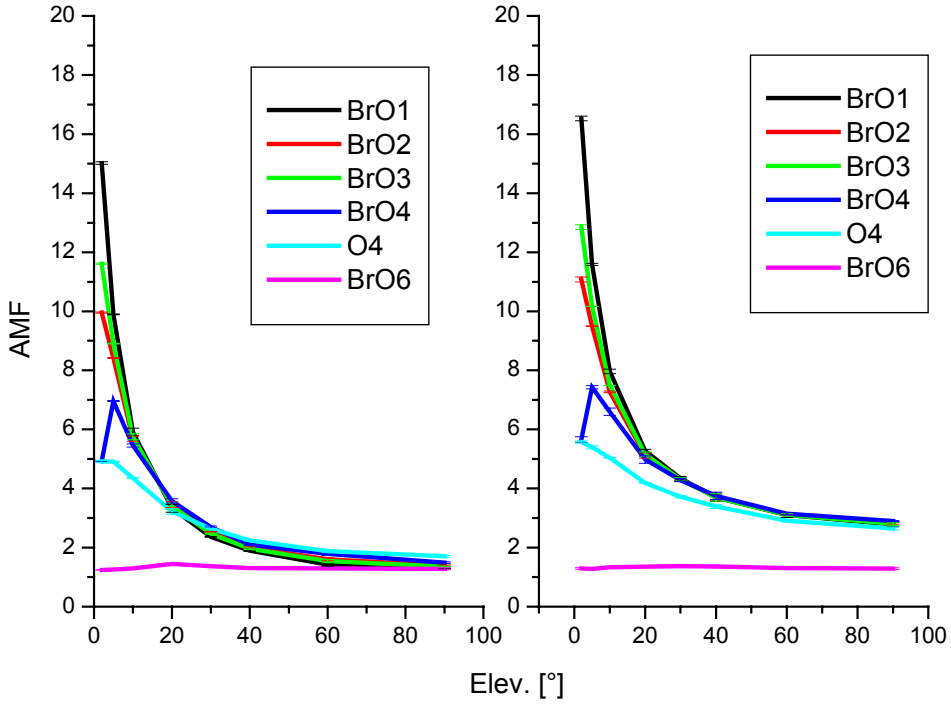

Figure 9.1.7 AMF for pure Rayleigh case and albedoes 5% (left) and 80% (right)

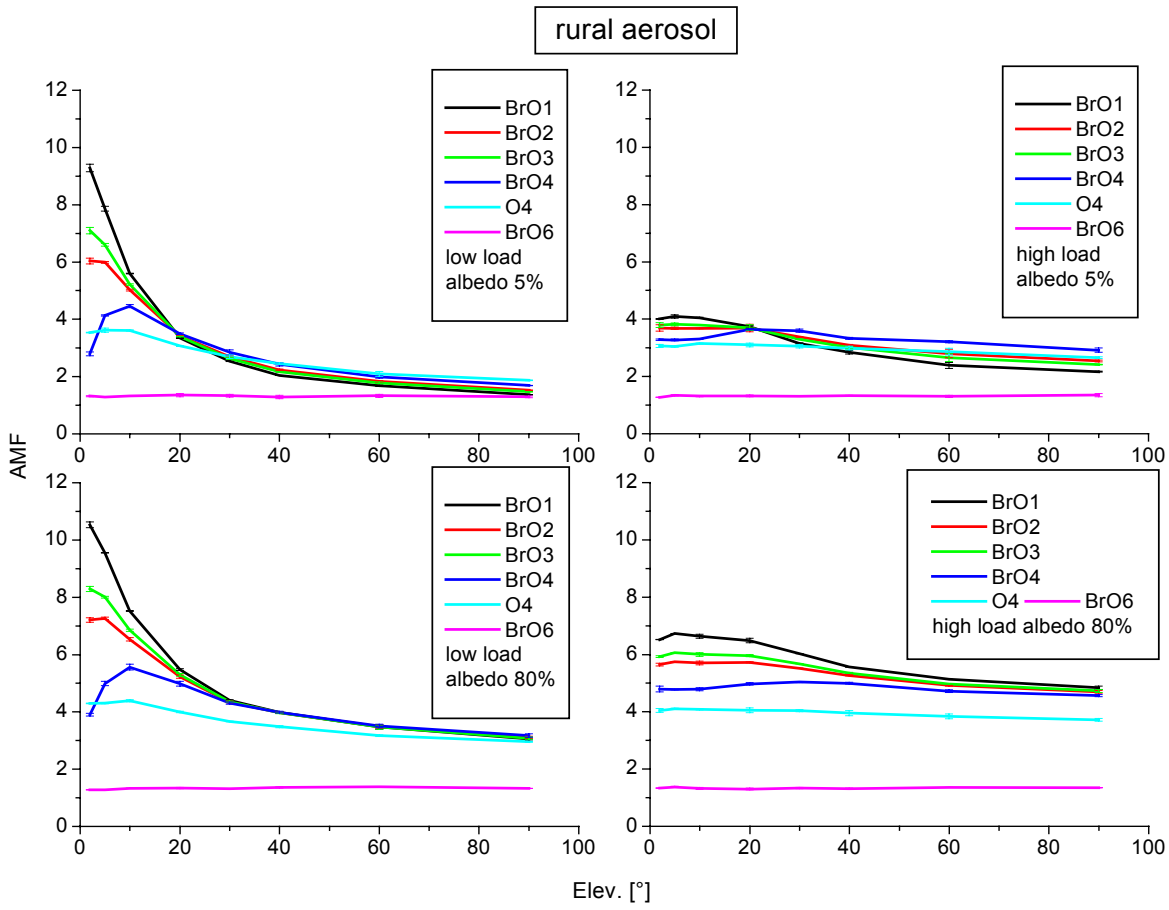

Figure 9.1.9 AMF for rural aerosol, both loads and both albedoes

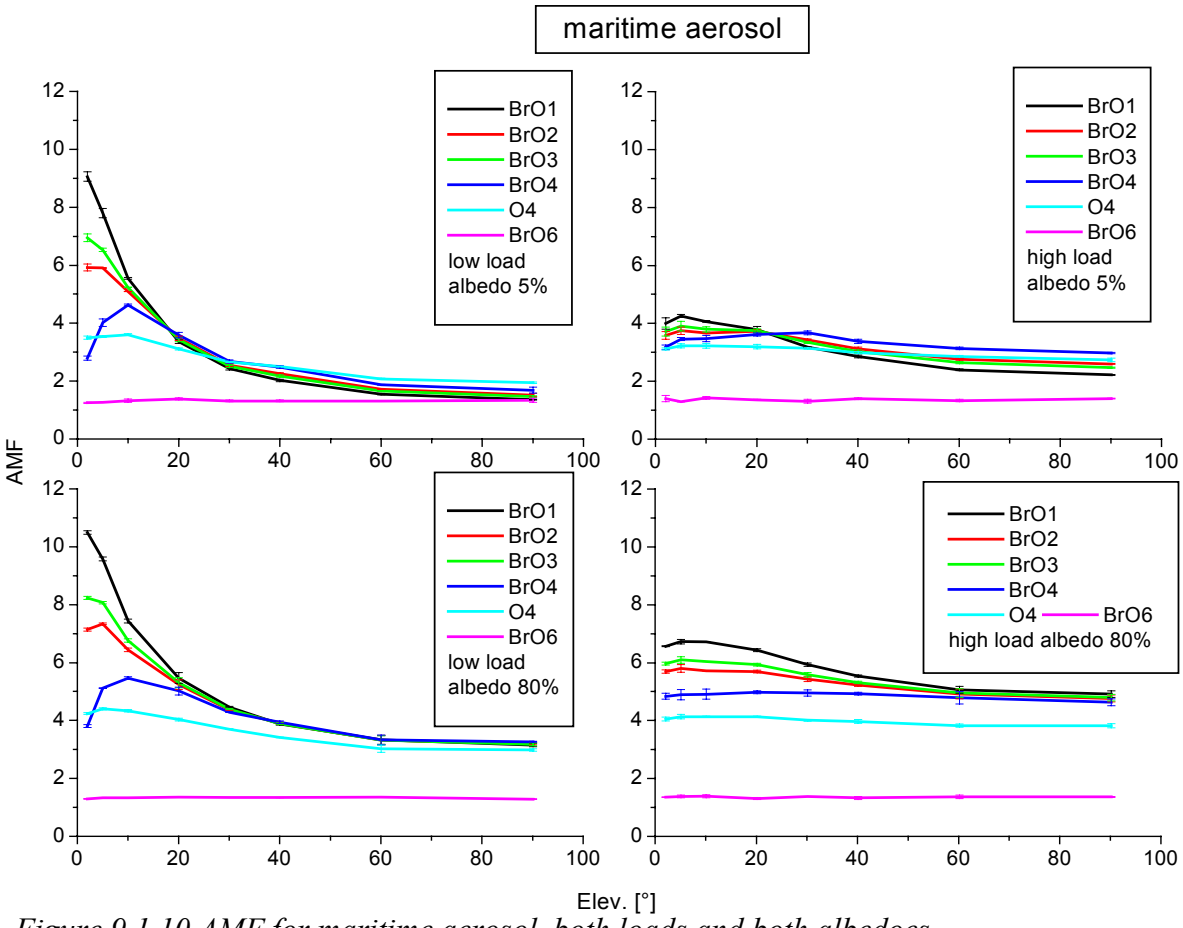

Figure 9.1.10 AMF for maritime aerosol, both loads and both albedoes

The following features are to note:

- The described effect of the AMF for "BrO4" not only prevails with aerosols added, but gets stronger. For the low aerosol load, the maximum in AMF is with elevation 10°.
- The AMF for O_4 displays a similar, though weaker effect.
- With the high aerosol load, also for "BrO1-3" the effect is observable, though with far lower overall AMF.
- With the high aerosol load, the differences between the AMF for "BrO1-4" and O_4 are reduced.
- The albedo again shifts all AMF to a similar extent.
- There are no readily visible differences between the two aerosol types used.
- The AMF for "BrO6" is again largely unaffected by aerosol load or albedo, as expected.
- The model noise is larger for the high aerosol load.

In the following, we will attempt to explain and quantify these features with model parameters. Due to the small differences between rural and maritime aerosol, only the rural one will be used for the plots to follow.
The first parameter of interest is the number of scattering events the photons suffer on average prior to enter the telescope. As outlined in chapter 6, we have available the number of Rayleigh, albedo and Mie scatterings. Figure 9.1.11 shows the former two for the pure Rayleigh case.

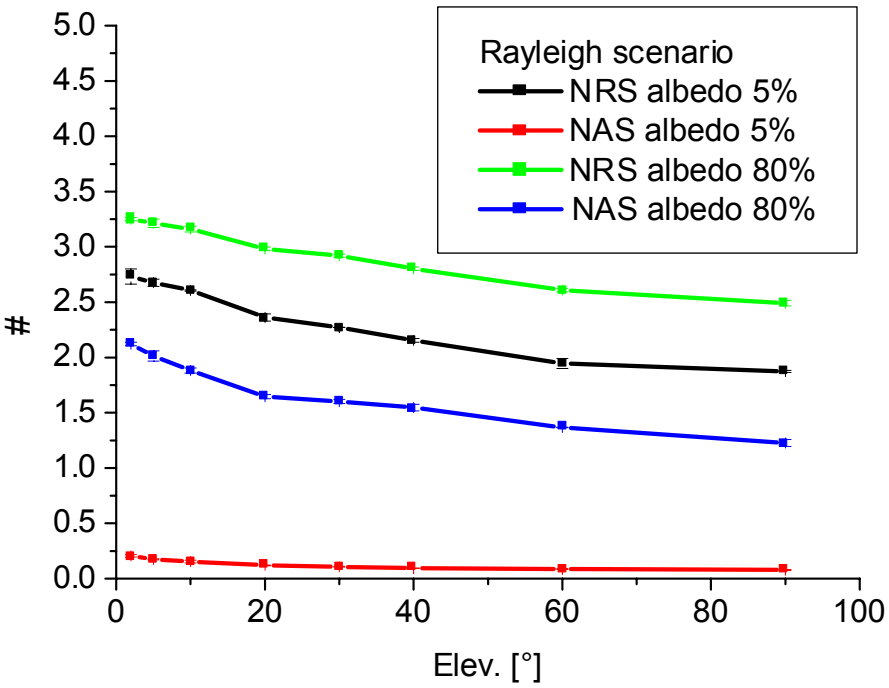

Figure 9.1.11 Number of Rayleigh and albedo scatterings (NRS and NAS, respectively) for pure Rayleigh case and two albedoes. For each scenario and each elevations we have more than one scattering; single scattering approximations of either kind are not valid.

As clearly can be seen, any single scattering approximation such as the geometrical one must be abandoned. The albedo increase from 5 to 80% significantly increases also the number of Rayleigh scatterings, since more light reaching the ground is reflected into the dense atmosphere and thus is available for further scattering. Figure 9.1.12 shows the scattering numbers for the rural aerosol, weak load case and again both albedoes.

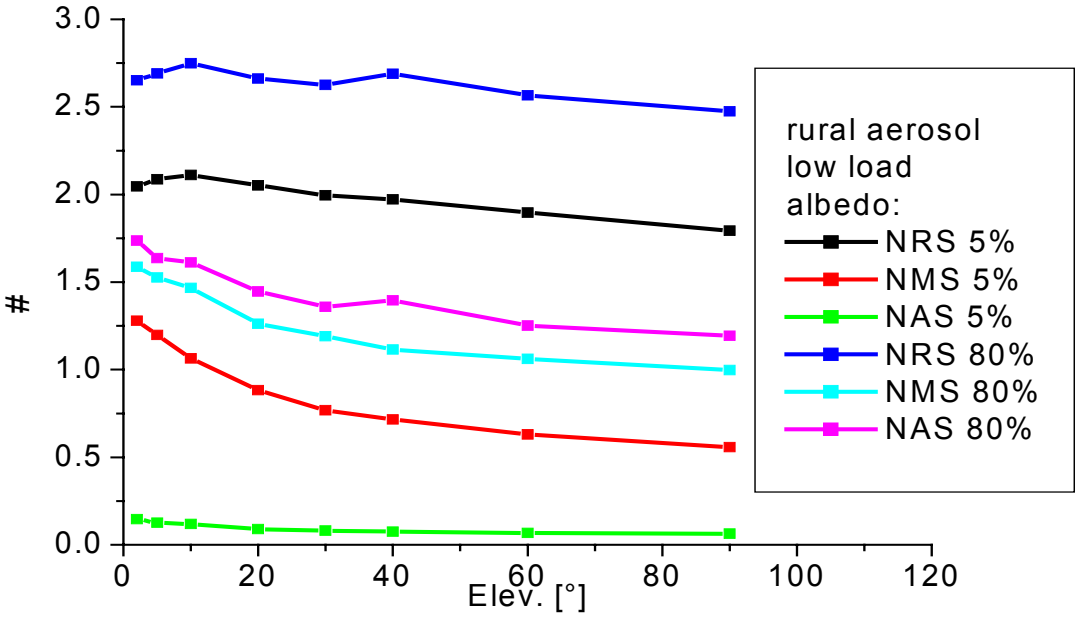

Figure 9.1.12 Number of Rayleigh, albedo and Mie scatterings for rural aerosol, low loadout, and both albedoes. As expected, the numbers increase with albedo.

We note that the total number of scatterings slightly increases due to the influence of aerosols, and that the number of Rayleigh scatterings decreases; the Rayleigh scattering loses its dominating role in the presence of strong additional scatterers. Now that we know how often the recorded light has been scattered, the next question to raise is where it has been scattered. To answer this, we consider the parameter "LSA", the altitude of the last scattering.
Figure 9.1.13 shows it for the pure Rayleigh as well as the rural aerosol/low load case.

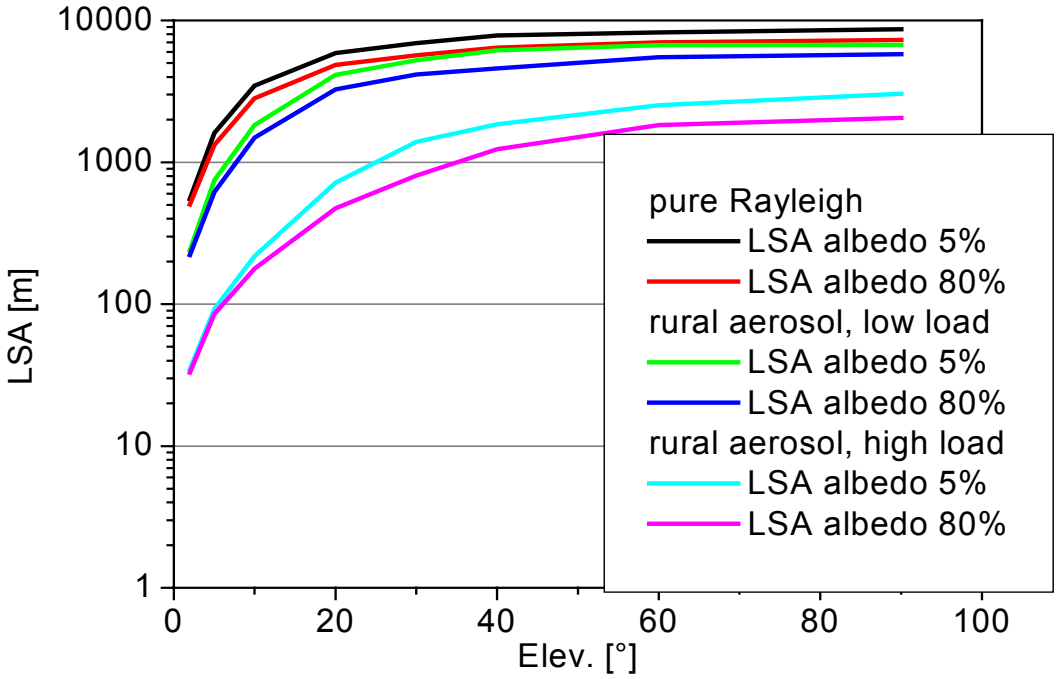

Figure 9.1.13 Last scattering altitudes (LSA) for the cases named in the legend; we find the last scattering event prior to detector entry to be lower than 1 km, even lower than 100 m for high aerosol load scenarios. It rises with elevation.

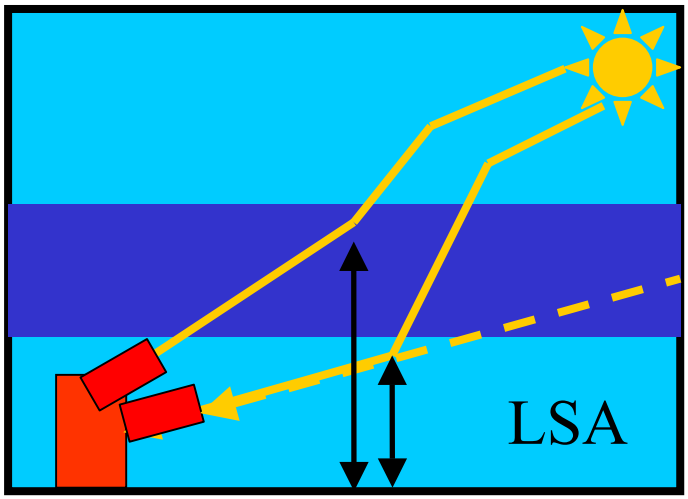

Figure 9.1.14 On the importance of the Last Scattering Altitude; for low elevations, the line of sight covers a large distance within the lower and dense atmosphere; this reduces the mean free path length and thus the LSA. The path then does not lead over a large distance through the absorber on the slant geometrical path. The path can be longer for higher elevations.

Figure 9.1.13, in conjunction with 9.1.14, explains the effect seen in the AMF.
The geometrical path is not followed through the entire verical extension of the profiles, but is shortened by scattering within the dense lower atmosphere the line of sight covers a distance which is longest for the lowest elevations.
After this scattering, the following path segments are on average less slant with respect to vertical layers than the direct line of sight (dashed line in Fig. 9.1.14). The lower the elevation is, the shorter is the first and slant path segment.
For higher elevations such as e.g. 10°, the line of sight leaves the densest atmosphere which increases the length of the first slant path segment and thus the LSA. The slant segment may reach into the atmosphere far enough to cross a given vertical layer which is not crossed by the lower elevation. This leads to the following effects observable in the figures shown:

- For profiles situated at the ground and with low vertical extensions, such as “BrO1” - “BrO3”, the AMF are smaller than estimated from the geometrical “1/sin”-approximation.
- For profiles elevated from the ground and/or with a large portion of the profile above a given LSA, such as “BrO4” or O_4, respectively, the AMF is smaller for elevations with lowest LSA. This means that the sensitivity for those profiles in our study is highest for elevations around 10°.

For stratospheric profiles, such as “BrO6”, the photons on average already have been scattered at least once before reaching the stratosphere; thus the influence of the initial path, i.e. the elevation, is largely eliminated. So the AMF for stratospheric absorbers is largely independent from the elevation.

As already mentioned, the difference in AMF for the two aerosol types used is very small. But a difference we have, which should be investigated in the light of the findings. Figure 9.1.4 shows the phase functions normalized to 1 at $\theta = 0°$. We find that a large part of the function, between 5° and 80°, is greater for a given θ for the rural aerosol than it is for the maritime.

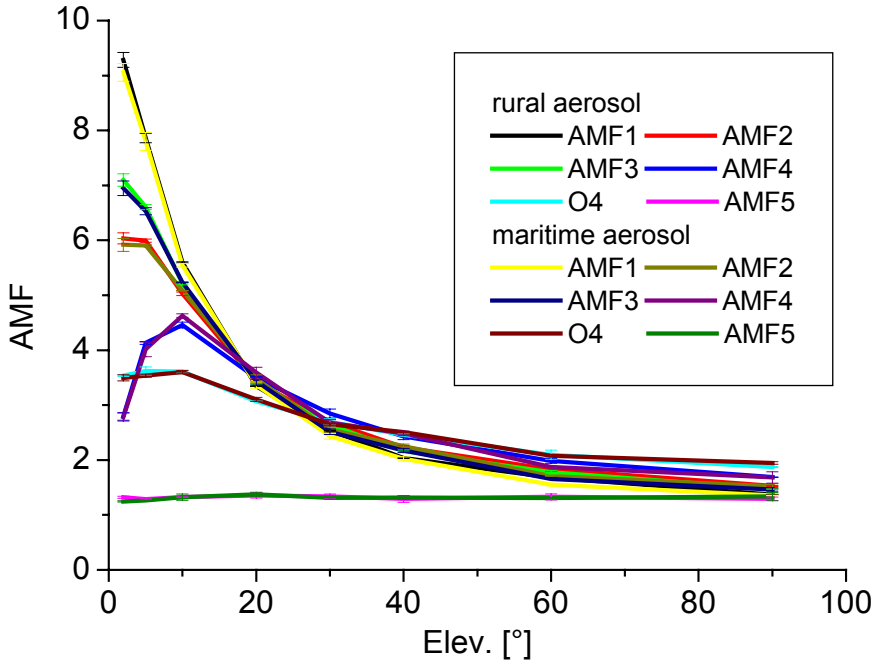

Figure 9.1.15 The effect of AMF decrease for lower elevations is stronger for maritime aerosol due to phase function being less forward peaked.

This means that rural aerosol scatters a larger part of the light into directions near the forward one, i.e. into directions resembling the light path prior to scattering. If the scattering was exclusively forward-directed, there would be no effect on the AMF at all, since the photon direction would not be altered by a scattering throwing it in the direction it had been following anyway. Thus for the maritime aerosol the described effect on AMF could be expected to be stronger. Indeed Figure 9.1.15 shows that this is the case.
But the by far stronger change in effect arises from the aerosol load strength variation, i.e. from the scattering coefficient. As already mentioned, the differences between the AMF become smaller with higher aerosol load. With the mean free path lengths becoming shorter and shorter, the fraction of the light path following any line of sight becomes smaller and less important to the total light path.
The Box AMF for the scenarios with/without rural aerosol in Figure 9.1.16 show the sensitivities for each vertical layer in the chosen discretization. They confirm the sensitivity to layers above 400 m to become smaller for 2° elevation than for 5°.
Since the aerosol load has a very large effect on the AMF we need information on it. The radiances could in theory be used for this, but usually the DOAS devices are not absolutely calibrated to allow for this. A better candidate is the O_4 AMF. The last plot for this aerosol dependence investigation shows the ratios of the O_4 AMF of 2° elevation to the others for pure Rayleigh and rural aerosol cases.
This ratio can be derived from measured values as well; using some information on the aerosol type, a set of modelled ratios could be parametrized, the parameters fitted to the ones of the measured ratio curve. From this fit the aerosol load could be concluded on to derive more accurate AMF for the profile retrieval of the interesting trace gases.

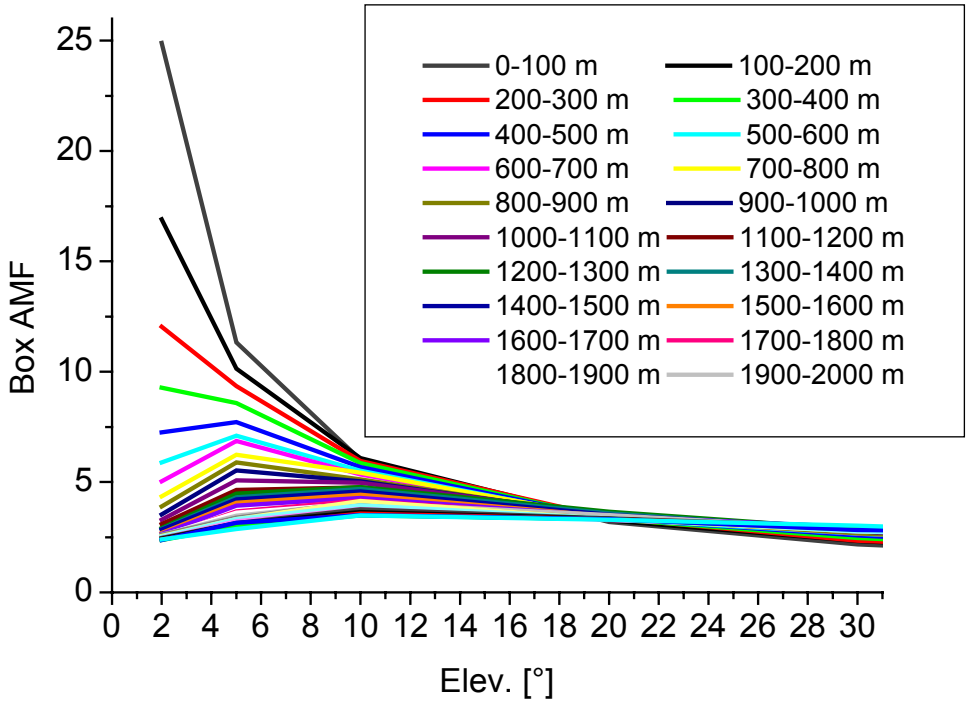

Figure 9.1.16 Box AMF for the lowest 2 km; for altitudes above 400 m they are smaller for 2° elevation instead of larger; error is <=5%.

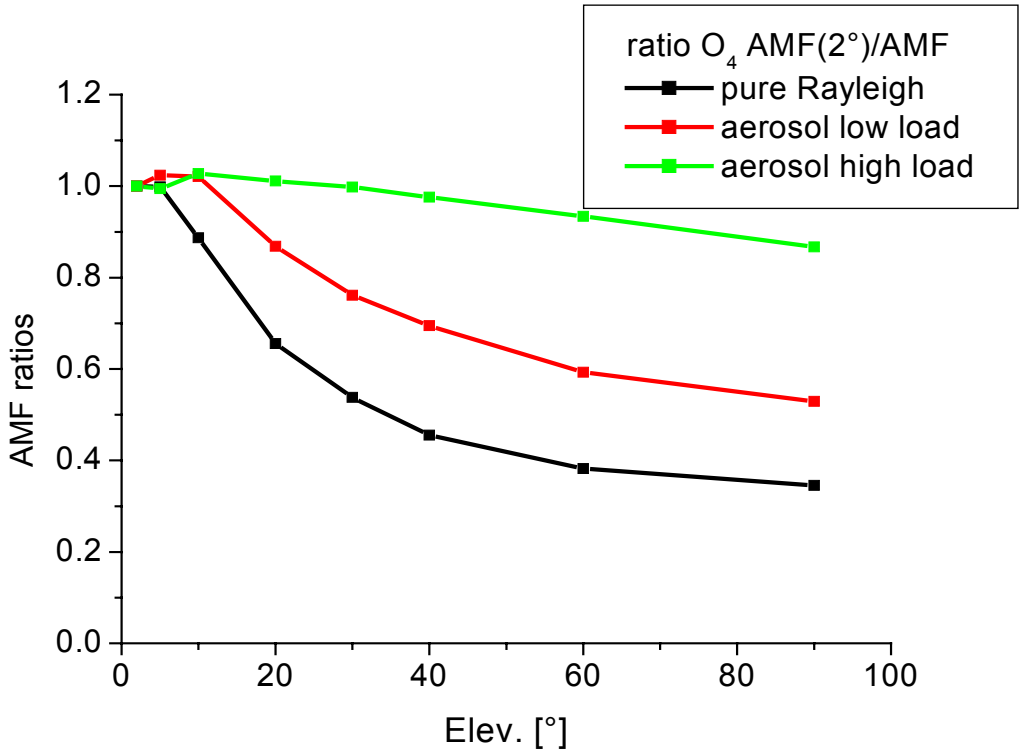

Figure 9.1.16 O_4 AMF ratios for the elevations investigated (2° = 1). Modelled ratios could be fitted to measured ones to derive the aerosol load.

9.1.4.2 Azimuth dependency

The reason for a dependence of AMF on the azimuth relies upon the fact that a solar photon, after reaching the lower atmosphere, must enter it in a place where it can get scattered into the instrument. For azimuth = 0°, this place is some point between the sun and the detector.
In case of azimuth = 180°, the scattering location is "behind" the detector, so each recorded photon must first get past the detector and cover an additional distance through the absorber near ground as compared to the situation before.
But this effect is only significant for higher SZA. For the SZA = 30°, it can be expected to be negligible compared to e.g. the influences of aerosol and albedo.
Indeed the modelling yielded this result, as shown in Fig. 9.1.17 for "BrO4".
A small tendency to higher AMF at higher azimuths can be observed, but it is hardly significant.

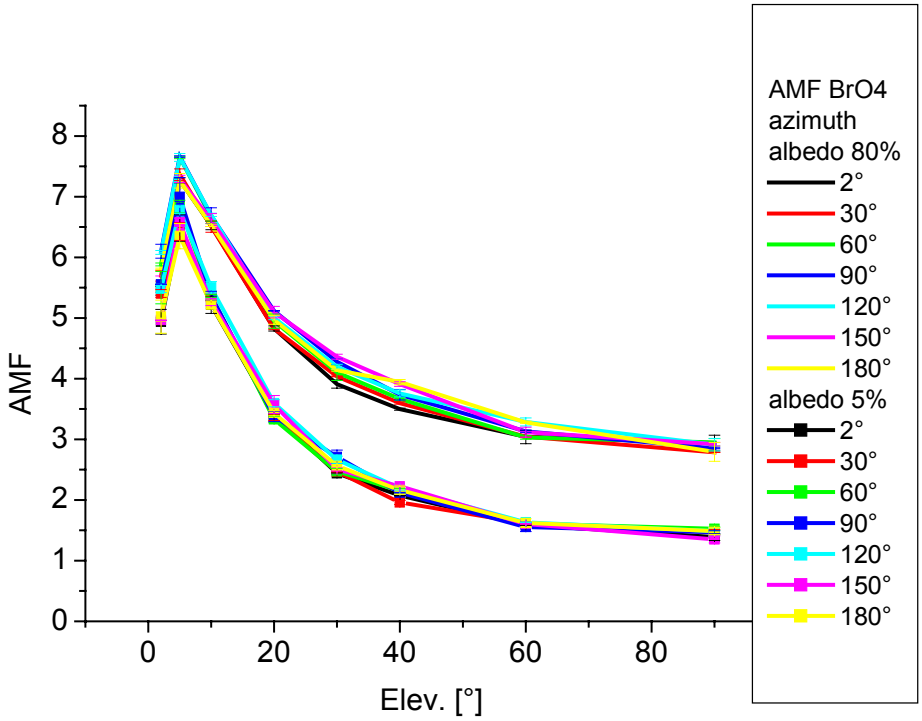

Figure 9.1.17 Azimuth-dependence of the AMF for "BrO4"; the effect is nearly negligible, as expected for small SZA (i.e. 30°).

9.1.4.3 SZA dependency

A larger role plays the SZA; as outlined in the final section of chapter 4, the SZA is mainly important for absorbers in the stratosphere, since there the location of the first scattering separates the slant path along the direction of the sun from the further, less slant path down into the dense atmosphere. The elevation only plays an insignificant role, as seen in Fig. 9.1.18.
But a dependence for absorbers near ground does exist as well, albeit a weaker one. Figure 9.1.19 shows the AMF for "BrO2" and O_4 .

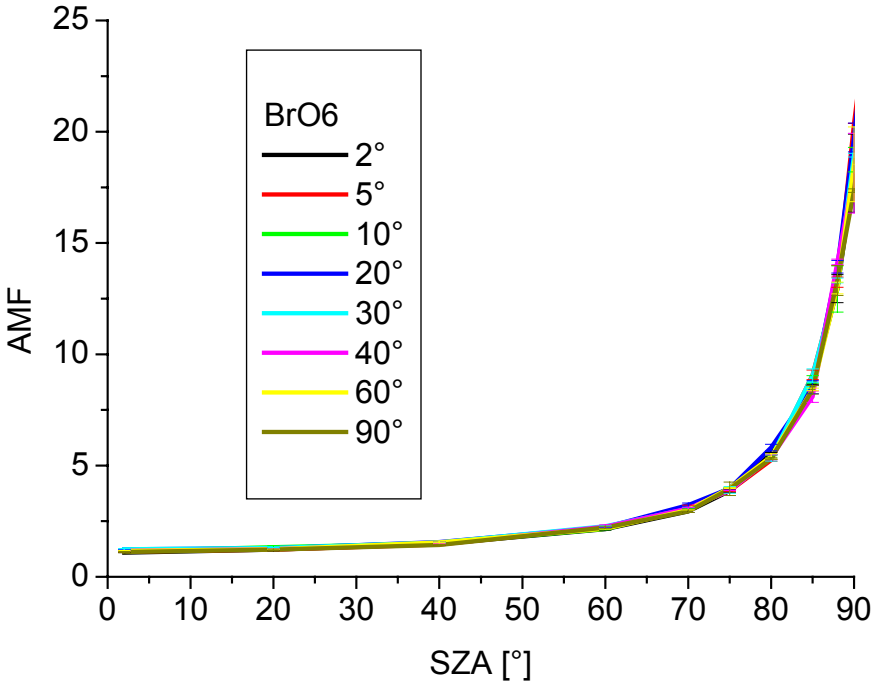

Figure 9.1.18 SZA-dependence of AMFs for "BrO6". The expected strong dependence is observed for this stratospheric absorber, so is the independence from the elevation.

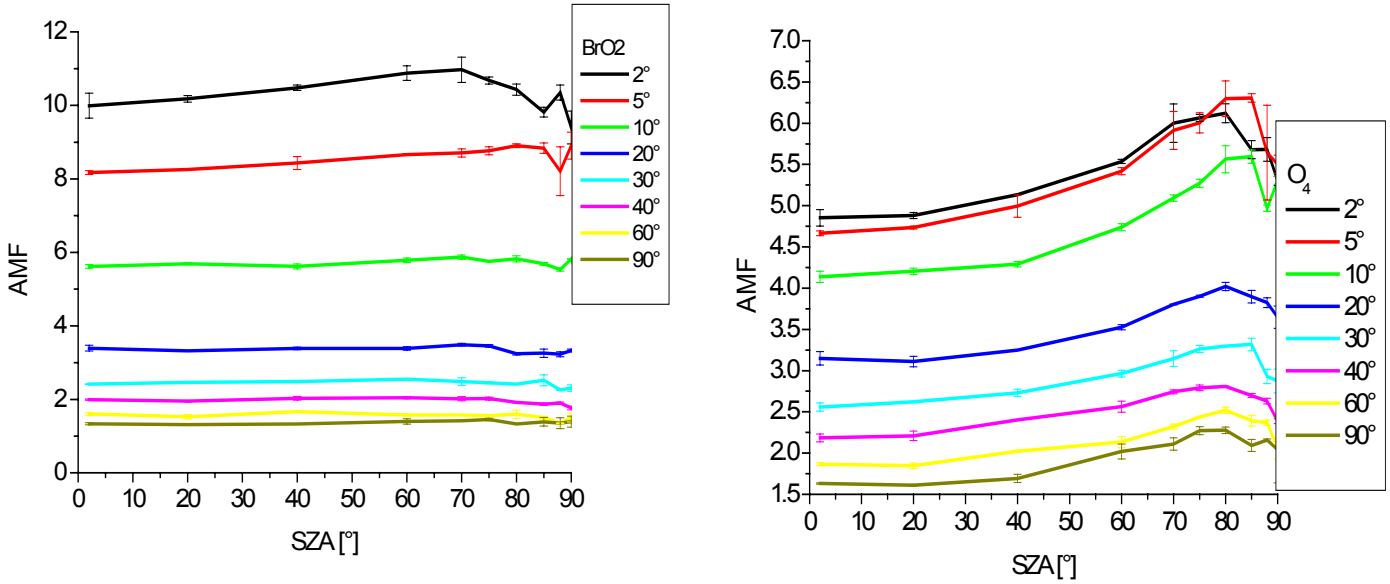

Figure 9.1.19 SZA-dependence of AMFs for "BrO2" and O_4. The elevation still dominates the AMF, but an icrease to a maximum at SZA = 70° ("BrO2") and SZA = 75° (O_4) must be noted. The reason are the different altitudes of the scattering locations.

Two features are to be noted:

- The AMF increases with SZA to a maximum at at SZA = 70° for "BrO2", 75° for O_4;
- After the maximum the AMF drops off again.
- The effect is stronger for low elevations than for high ones.
- The effect is stronger for O_4, which extends higher into the free troposphere than "BrO2" does.

To investigate the reasons, we consider again the scattering altitudes, this time of the first scattering (after the photons have entered the atmosphere) and again the last one, prior to entering the detector.

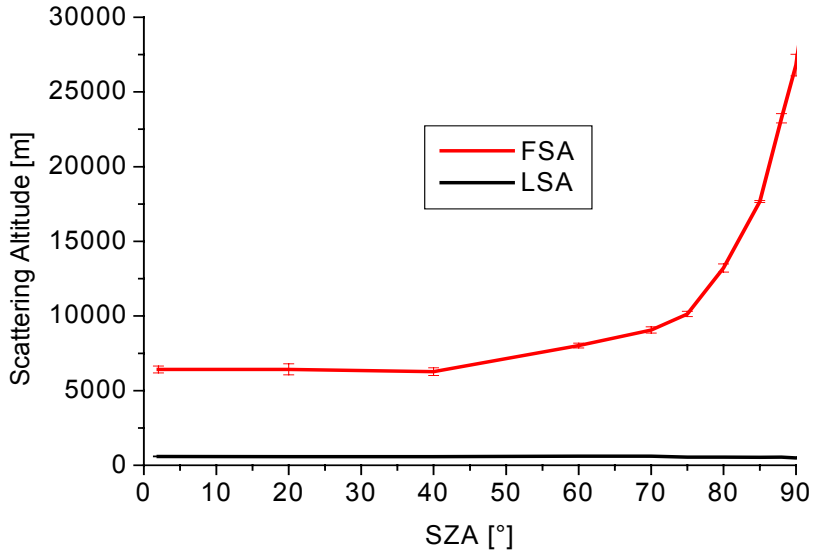

Figure 9.1.20 shows the First and Last Scattering Altitudes (FSA and LSA) for elevation 2°.

The LSA is largely independent from SZA. But the FSA increases, as readily expected from the basic considerations in chapter 4.
As long as the FSA is still within an absorber profile (which is the case for O_4 up to a greater SZA than is the case for "BrO2"), the increasing slantness of the path segment between first scattering point and the sun increases the AMF. As soon as the FSA is above the absorber, the slant path no longer crosses it, and the AMF drops off. It is the competition of these two effects that leads to the behaviour shown.
Finally the profiles in the FT, "BrO7" and "BrO8" shall be investigated, located in between the PBL and the stratospheric profiles.

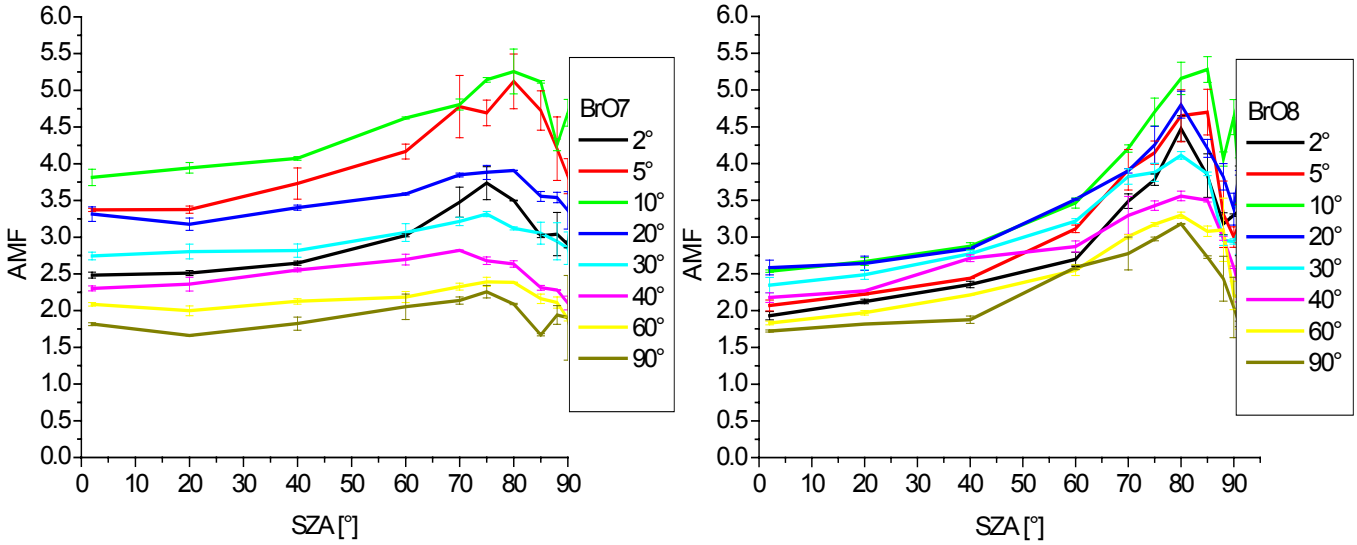

Figure 9.1.21 AMF for "BrO7" and "BrO8". The SZA dependence is larger for "BrO8", while the dependence on elevation is stronger for "BrO7".

Notable, but hardly surprising, are three effects:

- The SZA-dependence is stronger for "BrO8", located nearer to the stratosphere (in fact, immediately below it).
- The elevation-dependence is stronger for "BrO7", since it nearer to the ground.
- The elevations 10° and 20° deliver a higher AMF than 2° and 5° due to the Last Scattering Altitude.

Finally, an example plot of Box AMF for 90° elevation shows the increase in Box AMF for stratospheric layers (Fig. 9.1.22), while the low layers are largely unaffected.
Fig. 9.1.23 explains the AMF behaviour for elevation 2° for "BrO2" and O_4 (Fig. 9.1.19); the Box AMF for the FT display a similar behaviour as these AMF.

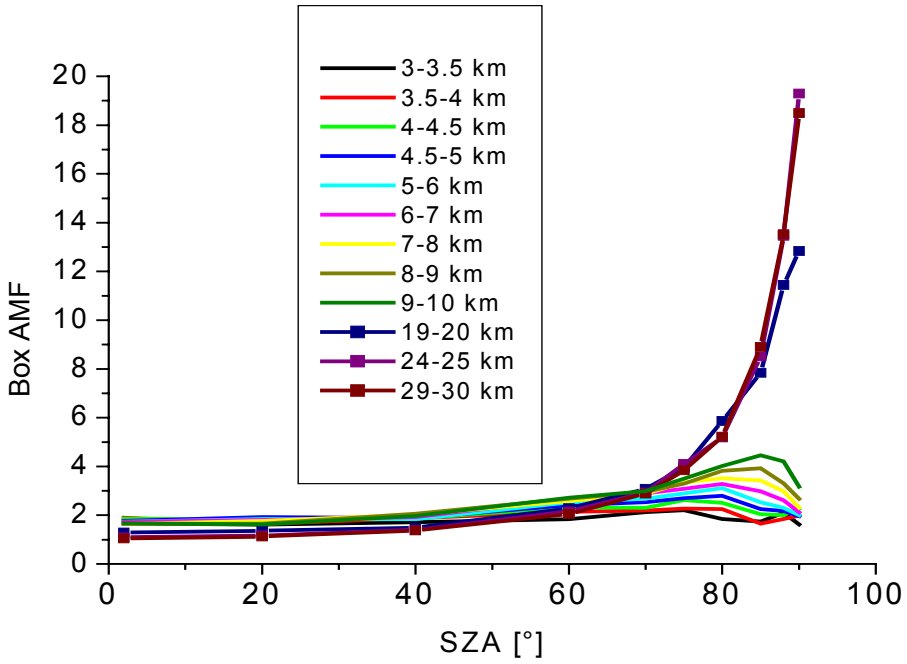

Figure 9.1.22 Box AMF for altitudes between 3 and 30 km; the strong SZA-dependence of stratospheric is readily explained with them (elevation 90°).

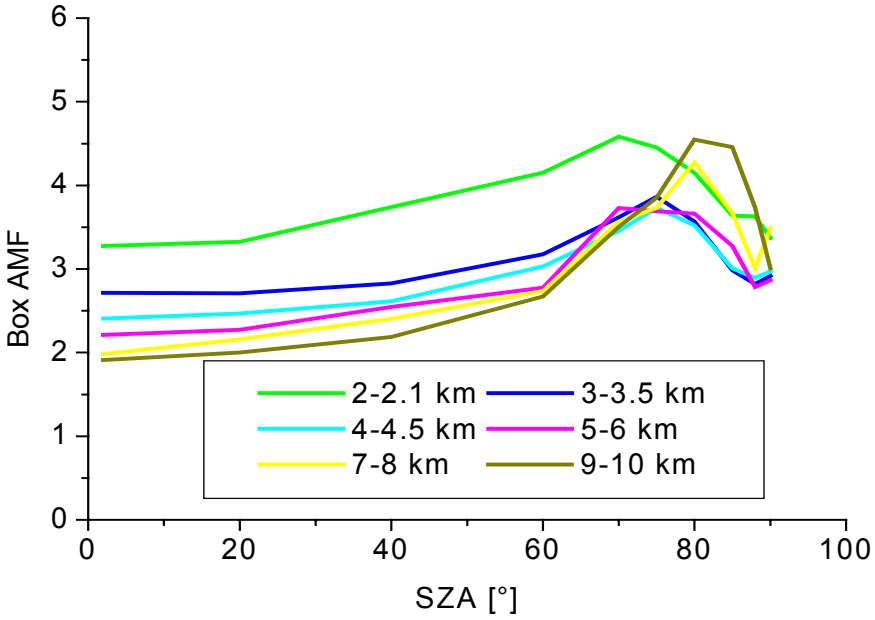

Figure 9.1.23 Box AMF for the FT; their behaviour explain the AMF series for absorbers near the ground (elevation 2°).

9.1.5 Conclusions on the vertical BrO profile

We know from our investigations that the AMF of a stratospheric profile, i.e. the measured SCD of such, is in good approximation a function of SZA, not of elevation. Since the spectra have been evaluated against a zenith sky reference, the DSCD in Fig. 9.1.3 contain a (negative) stratospheric signal. Since the AMF errors are small (<=2%) we neglect them in the following estimate. It must be noted here and in the following sections that the used aerosol distribution also is an assumption and may not be correct.
The albedo acts, as can be concluded from Figures 9.1.9 and 9.1.10, as offset to the AMF for all elevations and profiles, also in approximation.
To remove this offset, and to also eliminate the stratospheric signal, we subtract the 90°-DSCD for an exemplary dataset from the other elevation's signals.
Now we can, from the DSCD of 5°, 10° and 20°, attempt an estimate on the vertical profile present on May 1st.
When considering Fig. 9.1.3, we find the DSCD signal for 10° elevation to be only slightly smaller than for 5°, partly even within the latter value's error bars, and consistently so for the entire day. A significant difference, though, there is between the DSCD of 5° and 10° and the ones of 20°.
The albedo for the situation is 80%, since the measurement was performed on the ice surface where the BrO can supposed to get generated.
When qualitatively comparing the relations between the measured DSCD to the AMF for 80% for the profiles used in the AMF investigation, we note the following:
The high aerosol load must be ruled out, since the AMF ratios and differences, especially those for 5° and 10° versus 20° elevation, become too small in this scenario to get confirmed by the measurement DSCD. On the other hand, we have no clear Rayleigh atmosphere, otherwise the difference between the DSCD of lowest elevations would be greater. So we work with the low aerosol load. The aerosol type present in Alert was [*Hönninger, pers. comm.*] of a diamond-shaped class of ice crystals, of which the phase function is not yet available. Since the effect of phase function we have found to be existing, but negligible as compared to the uncertainties imposed by lack of knowledge on the exact extinction coefficient, we neglect this parameter.

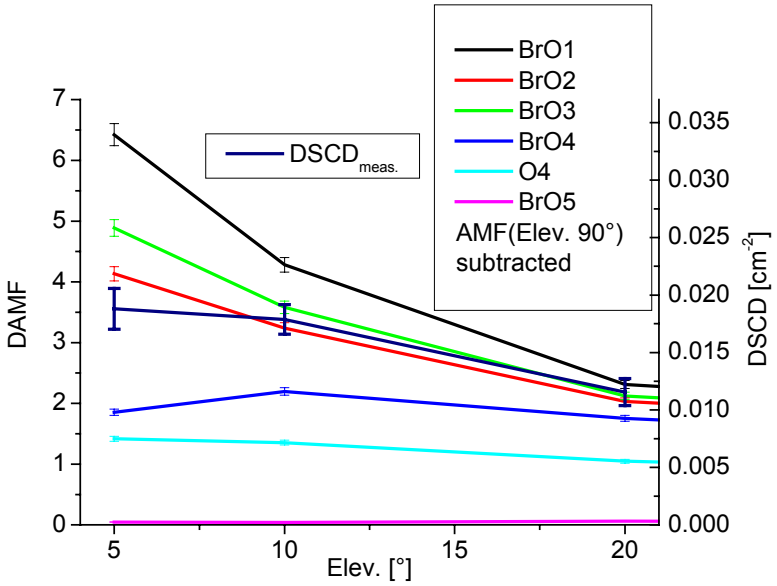

Figure 9.1.24 Zenith-corrected Differential AMF (AMF for 90° elevation subtracted) for low aerosol load, 80% albedo, to compare with the also zenith-corrected DSCD measured between 9:02 and 9:19 UT.

When considering the BrO peak value around 9:00 UT, and after subtracting the (roughly) $5*10^{13}$ cm^{-2} signal of the 90° elevation, we find the following DSCD: $2*10^{14}$ cm^{-2} for 5° elevation, a value slightly lower than this for 10°, and about 10^{14} cm^{-2} for 20°; so a factor of 2 relates the 5° and 20° signals to each other.
When now considering the AMF, for low aerosol load (this assuming to be correct), 80% albedo from Fig. 9.1.9, we must first subtract, here as well, the 90° elevation values, done so in Fig. 9.1.24, to obtain the Differential AMF (DAMF). Plotted there for comparison are the DSCD; the data has been recorded between 9:02 (5° elev.) and 9:19 UT (90° elev.). We must rule out profiles "BrO4", since we have no decrease in AMF (or DAMF) for elevation 5° as compared to 10°, and "BrO5", since there is a difference between 5° and 20°.
From the remaining data, we can form the ratios between the DAMF for 5° and the ones for 10° and 20°, listed in table 9.5.1.

Table 9.5.1 DAMF ratios (DAMF for 5° divided by the resp. DAMF)

Elevation	BrO1	BrO2	BrO3	O_4
10°	1.5	1.28	1.36	1.05
20°	2.8	2	2.3	1.35

From these data, we can rule out another two profiles, i.e. "BrO1" (since the factor of 2.8 as ratio $DAMF_{5°}/DAMF_{20°}$) is too high for the value derived from measurement, as well as "O4", since there this ratio is too low. We find from Fig. 9.1.24 and the DAMF ratios that "BrO2" provides a close, though not ideal, match with the measured data, with the ratio of 2 between 5° and 20° elevations, and the ratio between 5° and 10° closer to the measured one (about 1.1) than for "BrO3".
If we assume "BrO2" to be the correct profile, we can take this estimate one step further and estimate, from the measured DSCD of 5° elevation, the absolute concentration at around 9:00 UT c.t.. The zenith-corrected DAMF for "BrO2" and 5° is 4.14. Division of the (also zenith-corrected) DSCD of $1.9*10^{14}$ cm^{-2} by this, we obtain (roughly) $4.6*10^{13}$ cm^{-2} as VCD. The concentration that, inserted uniformly between 0 and 2 km, yields this VCD is $2.3*10^{8}$ cm^{-3}, which equals 9.2 ppt. This estimate complies well with the data from previous measurements.
The confinement of the BrO to below 2 km is supported by balloon probe soundings indicating a PBL height of up to 1.5 – 2 km. The long lifetime of BrO, once generated, makes such a vertical transport possible [*Hönninger, pers. comm.*]. With proceeding time during the day, the ratios between the elevations decrease, indicating a higher extending distribution of the BrO, which coincides with the diurnal rise of the mixing layer with rising temperature.
With more precise data on the aerosol, especially the scattering and the vertical profile, it seems possible to quantitatively derive a vertical profile of BrO for each part of the days of the campaign.

9.2 Simultaneous MAX-DOAS of NO_2 Heidelberg/Germany 2002

Tropospheric nitrogen oxydes play an important role in the quality management of urban air. The complex reactive relationships with other species already is outlined in the figure in chapter 1.
To assess the abundances of the various gaseous species as well as the types and distributions of aerosols the BAB II motorway campaign was devised. It took place from April 15th to May 15th at the A 656 motorway to the northwest of Heidelberg.

9.2.1 Role of NO_2 and campaign objectives

Precise emission data are of essential importance for all kind of atmospheric dispersion models as well as for climate change modelling on every scale. However, in many cases the anthropogenic emissions from traffic, industry and households on the one hand and biogenic emissions on the other hand are used with unknown uncertainty. Traffic emissions are usually calculated using emission factors based on idealized driving cycles and statistical data on road traffic. Up to now only in few investigations calculated emission data for roadways are compared with real world emissions [e.g. *Staehelin et al., 1995; Vogel et al., 2000*]. Especially, no comparisons were performed for the emissions of particulate matter of motorways, which also affect spectroscopic measurements. In order to check the quality of simulated gaseous and particulate traffic emissions, the project BAB II was designed by the Institute für Meteorologie und Klimaforschung (IMK) at the Forschungszentrum Karlsruhe, Germany, to determine real world gaseous and particulate traffic emissions by measuring the concentration profiles and profiles of wind at both sides of a highly frequented motorway. In addition parameters describing the traffic situation (traffic density, driving speed, motor type, type of catalyst) were obtained. Therefore, it is possible to compare measured and calculated emission data for NOx, CO, individual volatile organic compounds, and size resolved particulate matter. An overview of the measuring concept, the experimental setup and the available data are given in [*Fiedler et al. 2001*].
NO_2 is one of the main components of anthropogeneous pollution plumes like the ones near motorways. The majority of it is, however, not emitted directly; the fuel burning generates NO instead. This NO first must get oxidized, which happens by reaction with ozone.

$$NO + O_3 \rightarrow NO_2 + O_2 \quad k_{NO}(298\ K)=1.8*10^{-14}\ cm^3s^{-1}[JPL\ 1997] \qquad (9.2.1)$$

The lifetime of NO for this reaction is, for 40 ppb ozone, 51 s., which may cause, in conjunction with air movement by wind or turbulence, the maximum NO_2 abundances to exist in a different place than the one the educts were emitted.
On the other hand, NO_2 is a photolytic species dissociated by light into NO and molecular excited oxygen (see Figure 9.2.1).

$$NO_2 + h\nu \rightarrow NO + O^* \ (\lambda <= 420\ nm,\ J_{NO2} <\approx [10^{-3}\text{-}10^{-2}]\ s^{-1}\ during\ daytime) \qquad (9.2.2)$$

The excited oxygen quickly recombines with molecular oxygen to ozone:

$$O^* + O_2 + M \rightarrow O_3 + M \qquad (9.2.3)$$

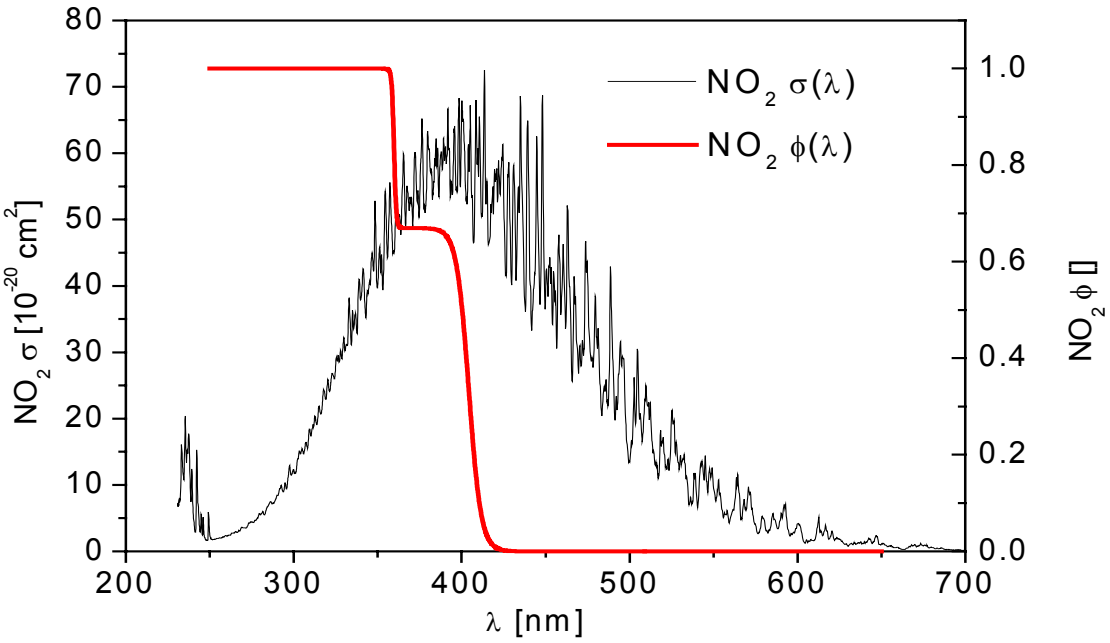

Figure 9.2.1 NO_2 absorption cross section (Harder et al., 1996) and quantum yield [JPL 1997]

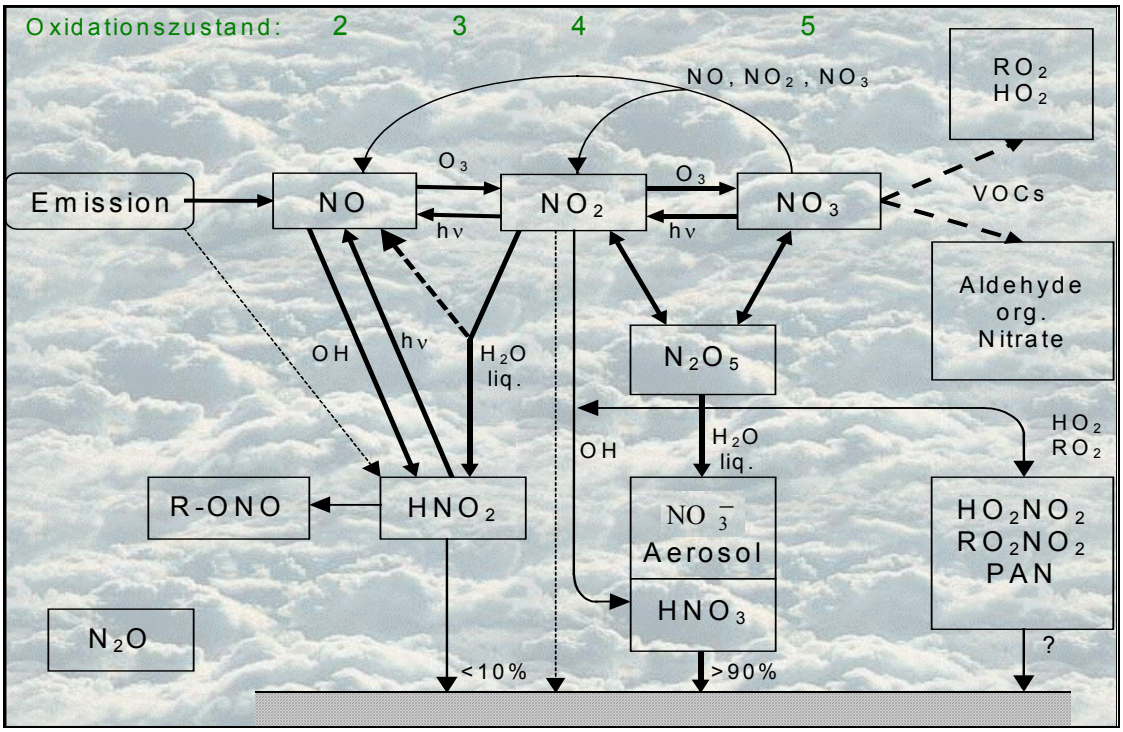

Figure .9.2.2.: Overview on the tropospheric NOx chemistry (taken from [Geyer 2000]).The green letters indicate the stage of oxidation, the species at a given arrow denotes the respective reaction partner. Species containing an "R" denote organic compounds.

This leads to a photostationary equilibrium between NO, NO2 und O3. The equilibrium constant for clear sky condition and SZA = 0° is:

$$K_{eq} = \frac{k_{NO}}{J_{NO2}} = \frac{[NO_2]}{[NO][O_3]}, K_{eq}(289K, J_{NO2,max}) = 2.1*10^{-12} cm^3 \quad (9.2.4)$$

If two of the concentrations involved and the photolysis frequency are known, e.g. by measurement, the remaing concentration can be derived. A tool for this is the "Leighton ratio"

$$\frac{[NO_2]}{[NO]} = [O_3]\frac{k_{NO}}{J_{NO2}} \quad (9.2.5)$$

These are only the most important reactions involving nitrogen oxides. A detail discussion is given in e.g. [*Ackermann 2000; Geyer 2000; Trick 2000*]. From [*Geyer 2000*] a schematic overview on the NOx chemistry is taken for Fig. 9.2.2.

9.2.2 Instrumental setup

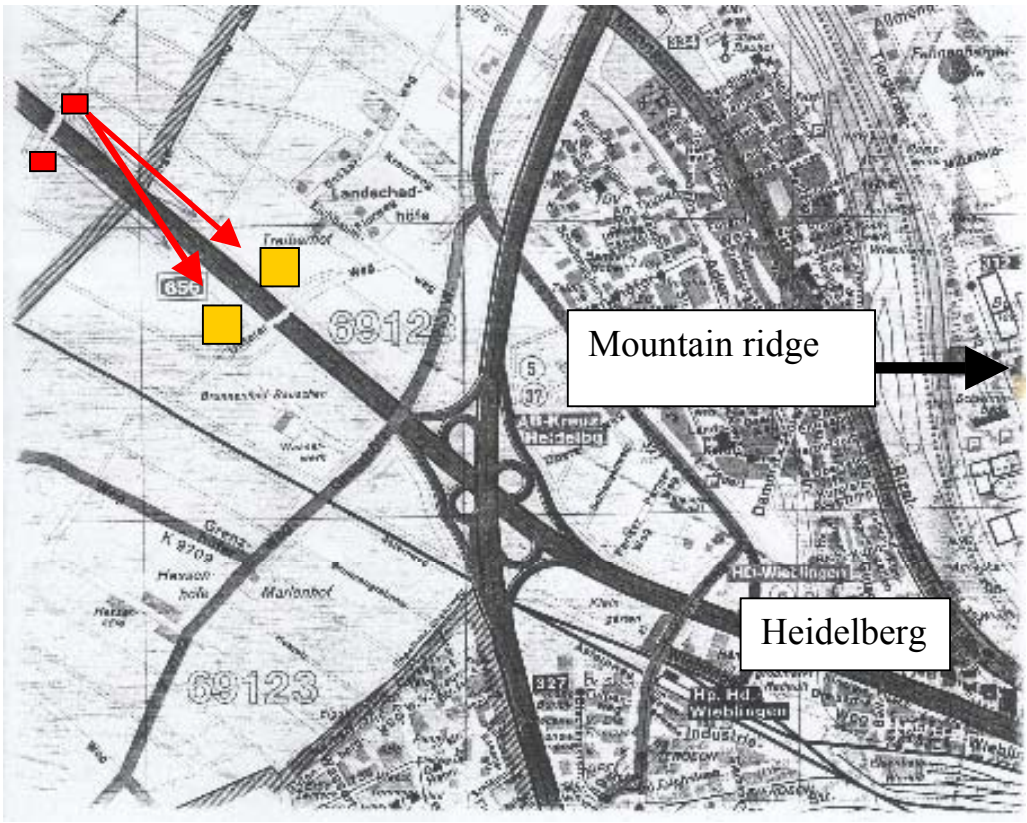

Figure 9.2.3 Measurement site of BAB II motorway campaign. To the east of Heidelberg, a mountain ridge (Odenwald) is located.
The orange boxes indicate the primary instrument locations on both sides of the motorway, the red ones the sites of the DOAS instruments; the arrows indicate the lines of sight of the sequential MAX DOAS (see below).

Figure 9.2.3 shows the location of the site; the motorway A 656 leads in north-westerly direction out of the Heidelberg urban area. To the east, the mountain ridges of the Odenwald enclose the Neckar valley. The orange boxes indicate the location of the two primary sites, one to the north of the motorway, the other on the opposite south side. Several in-situ devices monitored gaseous and particulate components of the plume. Two crane towers, one per side, contained more instruments which were moved up and down using an elevator. The distance between each tower and the motorway centre line was 80 m. The output of the in-situ instruments served as basis for calculations of the plume shape and propagation [*Bäumer et al., 2003*].
Figure 9.2.4a shows the two towers; behind them, to the left, buildings of the Heidelberg district of Wieblingen mark the outskirts of the town. The Odenwald mountains limit the view to the horizon. A haze from urban aerosols is clearly seen.

Figure 9.2.4a The two crane towers of the BAB II campaign; the crane towers and containers and support vehicles are seen. The Odenwald mountains loom bluishly at the horizon.

The picture in Fig. 9.2.4a was taken from the north-western bridge; in front of it, the two small red boxes denote the location of two wooden huts. Figure 9.2.4b shows the northern hut hunched into the bushes flanking the bridge bases. Built from wood elements, they were placed on a fundament of stones created to keep them in a stable position on the soil of the agriculturally used terrain.
The huts housed four instruments attached to the DOAS tomography division of the Institute for Environmental Physics.
The first three of them were “Long Path” devices; they emit a beam of collimated light and project it onto a retro reflector designed to reflect any impinging light back into the direction it came from. Four retros were mounted by members of the division to each tower, at altitudes

Figure 9.2.4b The northern wooden hut; it housed one of the LP devices and the simultaneous MAX DOAS device.

of 10 m, 20 m, 30 m and 40 m. The LP instruments were modified to sequentially fire their beam at all of the retro-reflectors in a rotating pattern [*Mettendorf et al., 2002*]. The goal was to apply tomographic algorithms to derive a 4D concentration field [e.g. *Laepple et al., 2002*]. They were operated 24 h, with a data backup break performed by the division's night watch post.
The fourth device, installed in the northern hut, was a simultaneous MAX DOAS device.

The instrument and its components are described in detail in [*Heismann 1996, v. Friedeburg 1999, v. Friedeburg et al., 2002*]. Figure 9.2.5 shows a schematical view.

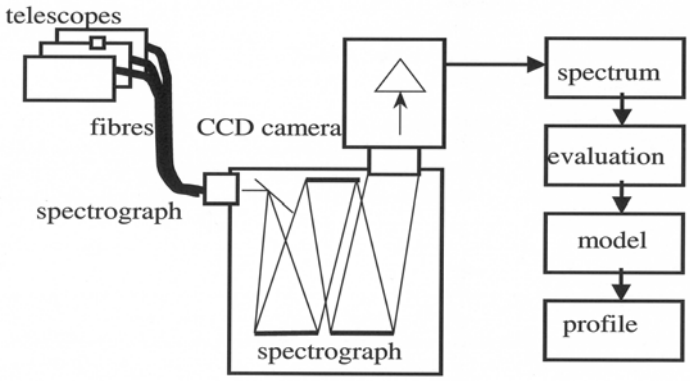

Figure 9.2.5 Schematical view of the simultaneous MAX DOAS instrument.

In contrast to the sequential MAX DOAS, it records several elevations simultaneously, which increases in theory the overal 4D resolution.

The light collecting device consists of eight simple aluminium tube based telescopes mounted in a way to facilitate manual rotation in the vertical and horizontal axes. Each telescope focuses the incoming light onto the end of one 400 micrometer quartz fibre. The mechanical construction limits the aperture angle to 0.15°. The eight fibres conduct the light into the entrance slit entrance slit (width 400 µm, height 5 mm) of a 500mm F/6.9 Czerny–Turner spectrograph (Acton Research). The spectral grating of 1200 grooves/mm, mounted on a turret, was set to cover the wavelength area between 420 and 450 nm. It disperses the light in a way that keeps the light of all telescopes separated from each other.

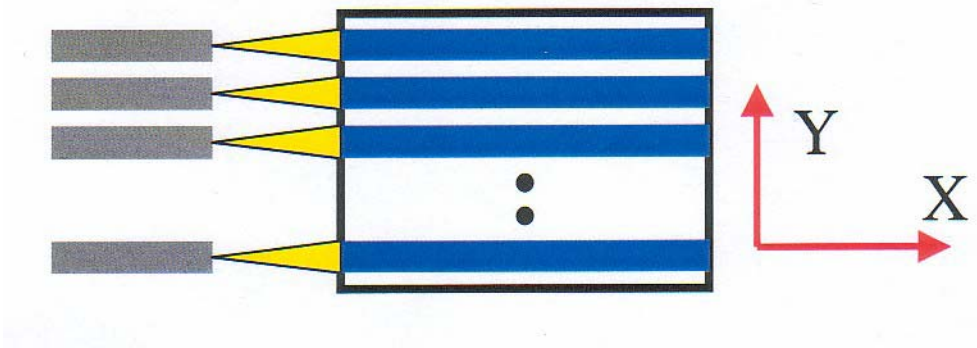

Figure 9.2.6 The (dispersed) light of each telescope is projected onto the 2D CCD chip. The vertical Y axis stores the spatial information, the horizontal X axis the spectral one.

The dispersed light of each fibre is dispersed onto a cooled 2D CCD chip 1530-P-1024S (EG&G) with 256 by 1024 pixels of size 19*19 μm^2. It is cooled to –40 °C in order to reduce the dark current. The wavelength information is recorded in the chip's horizontal axis with a dispersion of 0.029 nm per pixel. Figure 9.2.3 shows schematically the mapping of the telescope light "beams" onto the 2D CCD chip. The wavelength calibration and the instrumental function are derived by taking spectra of Neon emission lines. The spectral resolution was determined to be 0.25 nm FWHM (full width at half maximum). For the actual evaluation, a more precise wavelength calibration with respect to the measured spectrum was possible using the prominent Fraunhofer structures in the spectrum. The spectrometer is temperature-stabilized (35 °C) to minimize spectral shift. The remaining shifts were found to be ≤ 0.2 pixels.

A recording is performed by opening and closing a mechanical shutter in front of the chip for the duration desired. After closing, the chip is read out. The control software is MFC [*Gomer et al. 1979*]. A modification by [*Heismann 1996*] allows, apart from shutter operation, to separate read-out of each of the 256 pixel rows. This in turn allows for the identification of the rows illuminated by one given telescope when feeding it with collimated halogen light. Sets of 20 equidistant pixel rows on the chip are reserved for one given fibre. In between pixel lines are left out to avoid mutual interference.

After readout and conversion to a digital signal each 20 pixel column is co-added to form a spectral channel. The digital 'count number' in each channel is thus proportional to the integrated light intensity received during each exposure time interval in the same way as in case of the PDA. Depending on the available light intensities, integration times between 50 and 400 s were used. During most of the day, 50 s were sufficient; together with a few seconds for CCD read-out and data storage, this related to a temporal resolution of 1 min.

Spectra recorded in total darkness on each day were used for the detector's electronic offset and dark current correction; these "underground spectra" were found to be stable with time even over several days.

The setup was installed in the northern wooden hut. Two telescopes were directed into the zenith, three aimed near the retro reflectors mounted at 10, 20 and 30 m on the northern crane tower, the remaining three at their counterparts on the southern tower. The alignment was performed with a targeting telescope attached parallel to the telescope to be targeted. The error was estimated from the precision with which the cross hairs could be centered on the respective retro array. The horizontal distances between hut and towers was 705 m to the northern and 840.4 m to the southern tower. For the resulting telescope elevations see Table 9.2.1.
This geometry mimicked the one chosen by the IUP tomography group [*Mettendorf et al., 2002*] which facilitates comparison studies. In spite of this similar geometry, the MAX DOAS telescopes, due to their small aperture angle, did not receive reflected light from the long path instruments. The telescopes aimed at the south tower looked through the motorway plume.
When the wind came from northerly directions, the motorway plume did not interfere with the lines of sight of the three telescopes looking parallel to the motorway, which opened a free view on the plume of Heidelberg (see Figure 9.2.7). The geometrical lines of sight of the lower two elevations were limited by the mountain ridge.

Table 9.2.1 The elevations of the telescopes aimed at the retro reflectors mounted at different heights to the two towers; they were adjusted with a water level.

side	retro altitude [m]	elevation [°] (error est. 0.2°)
north	10	0.81
north	20	1.63
north	30	2.44
south	10	0.68
south	20	1.36
south	30	2.05

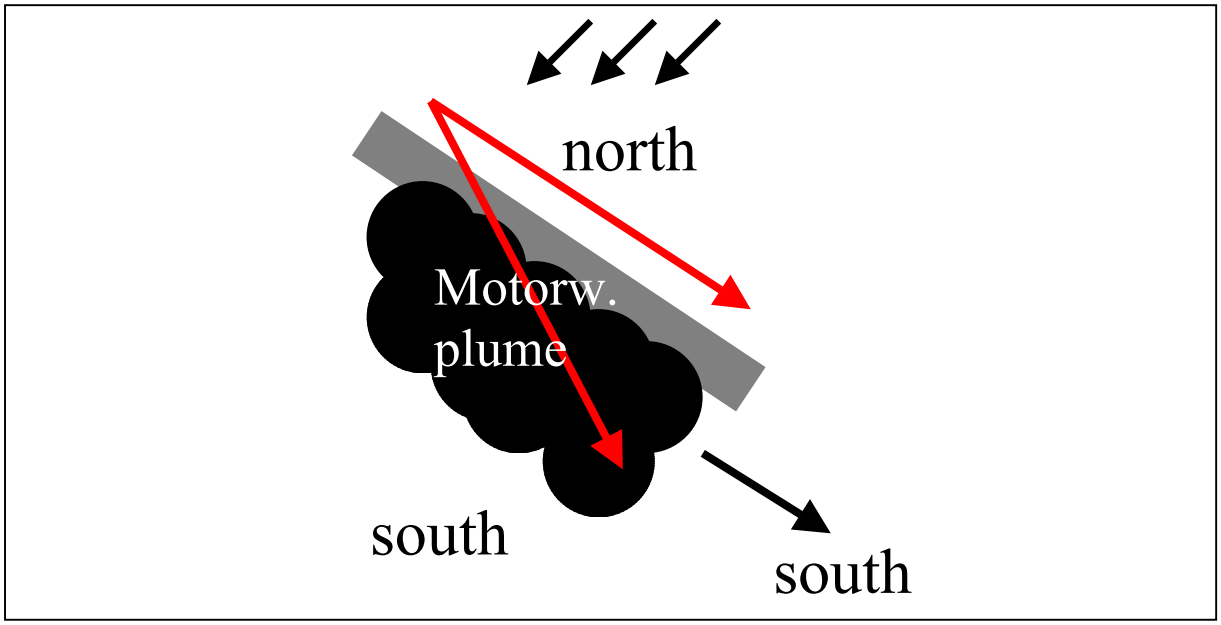

Figure 9.2.7 The two groups of lines of sight of the MAX DOAS telescopes; when northerly winds prevailed, the ones looking at the northern tower only measured the Heidelberg urban background plume, while the others probed the motorway plume.

9.2.3 Evaluation procedure and measured SCD

The simultaneous MAX DOAS technique has the advantage of high temporal resolution, i.e. one recording delivers spectra along all lines of sight.
But it has the drawback that the instrumental function varies across the CCD chip. This is e.g. due to different transmission functions of the telescopes and quartz fibres, the astigmatism of the spectrograph[1], and reflectivity variations across the grating. Another reason, and the possibly most important one, is based upon variations of the shapes (and thus, areas) of the CCD pixels on the sub-μm scale. This leads to a deviation of the recorded Neon emission lines from the gaussian shape, and differently so dependent on the rows and the wavelength of the line. This applies to any absorption line as well, which causes problems especially with narrow and dense lines such as the Fraunhofer and the water vapour lines; they then are difficult to reproduce with cross section spectra convolved with only one slit function.
This section will present two techniques to overcome this difficulty. A third one was developed by [*Bossmeyer 2002*].
The first one was used for the results below. It takes advantage of the fact that the telescopes can be turned individually at any time the operator choses. On days with clear sky and low traffic, e.g. on Sundays, all telescopes were directed into the zenith. Spectra were recorded, separately for each telescope, which are henceforth called Fraunhofer Zenith Spectra (FZS)[2].
The actual measurement spectra were, prior to further processing, divided by these FZS to remove the Fraunhofer features, and most of the water vapour absorption.
The fitting region was selected to be 430-441 nm. This region provides sufficient NO_2 structures but lacks the strongest Fraunhofer lines as well as significant water vapour absorption. A cross section spectrum of NO_2 [*Harder et al., 1996*] was fitted to derive the NO_2 SCD. Then the following steps were taken:

1. Convolution of the trace gas spectrum with the slit function of each telescope
2. Convolution of a high resolution Fraunhofer spectrum with the same slit function
3. Fit of Fraunhofer spectrum to the FZS, storage of shift and squeeze coefficients of fit
4. Application of these coefficients to trace gas cross section spectrum
5. Fit of the measurement spectrum to the FZS, which now has same wavelength calibration as the trace gas cross section spectra
6. Calculation of Ring spectra [*Bussemer 1997*], accounting for the rotational Raman scattering, from the FZS
7. Use Fraunhofer Zenith Spectrum (FZS) taken with each telescope separately as Fraunhofer reference
8. Subtract FZS from measurement spectrum
9. Fit Ring and trace gas spectra to the measured spectrum

Figure 9.2.8 shows a typical evaluation. Figure 9.2.9 the NO_2 SCD for May 10th. They in fact are differential SCD, DSCD, but be they named SCD as well for simplicity. The diurnal variation of the stratospheric NO_2, induced by photolysis during daytime and buildup at night, is clearly seen as U-shape. The stratospheric signal is superimposed on the one generated by the motorway and the city. At this point, three facts must be considered:

- The SCD derived in the fitting do "contain" the "negative" NO_2 signal of the FZS used, which has been recorded at a different time.
- The campaign goal was information on the NO_2 near the ground, to which the low elevations are sensitive.

[1] The emission lines of a halogen lamp, when fed into all telescopes, is not projected as a line onto the chip, but as a "half moon" of slightly varying thickness from the centre to the tips.
[2] The FZS must be recorded in temporal vicinity to the measured spectrum, since the slit function varies with time as well.

- The stratospheric signal is an interfering one that must be removed; since the dependence of stratospheric AMF to telescope elevation is negligible, it is nearly identical for all elevations used.

So as last step, the SCD measured with one of the zenith viewing telescopes (which were checked to be equal) was subtracted from each measured spectrum for each recording time. The SCD contained in the FZS cancelled out. The stratospheric signal of each recording time was removed. The results were six sets of purely tropospheric NO_2 ΔSCD.

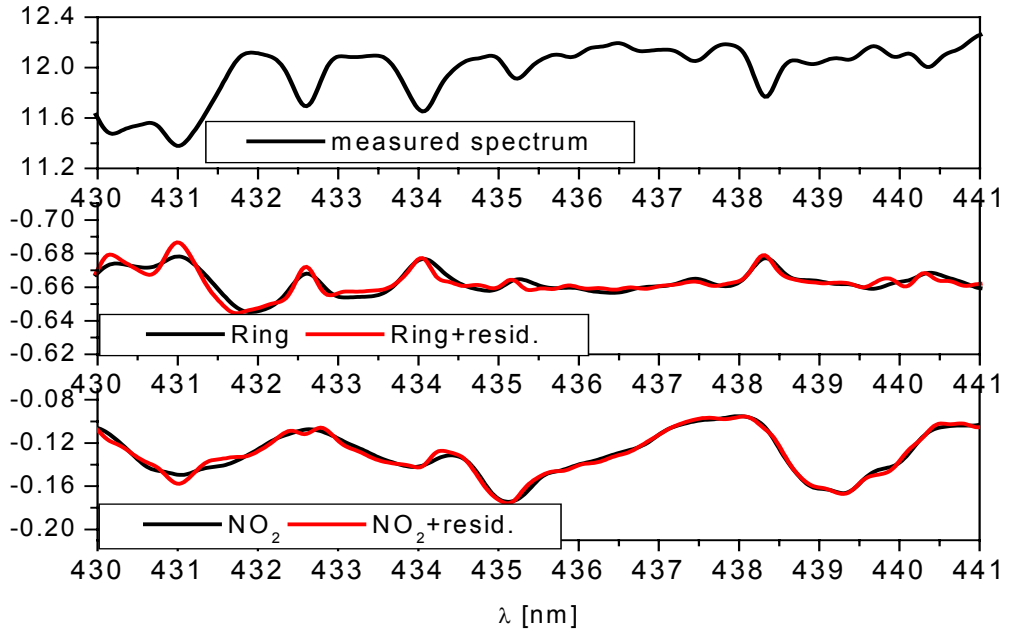

Figure 9.2.8 Result of the NO_2 DOAS evaluation described in the text. On top, a typical measurement spectrum is seen. Shown below are the comparisons between the NO_2 and Ring effect absorptions found in the spectrum (black lines) and the added residual of the fit (gray lines).

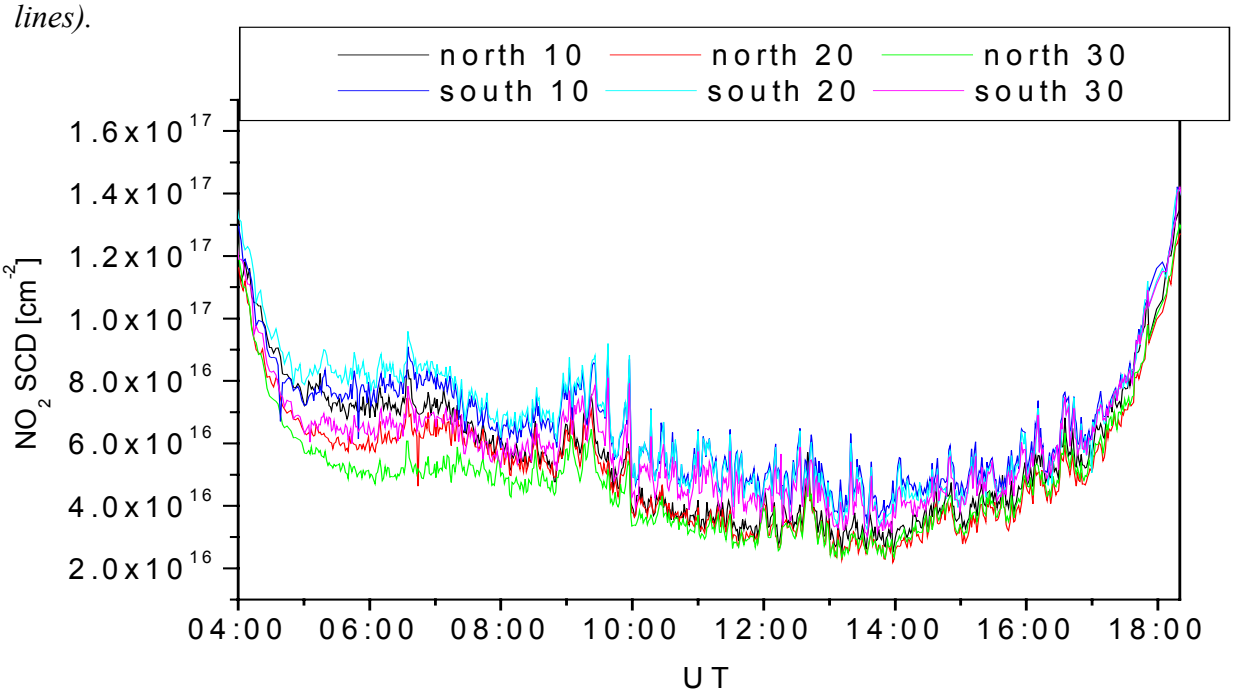

Figure 9.2.9 NO_2 (D)SCD for the six slant lines of sight for May 10th, 2003, A 656 motorway near Heidelberg. The U-shape characterizes the stratospheric NO_2 column. The subtraction of the column in the FZS falsifies the values.

Figure 9.2.10 shows the ΔSCD with the zenith signal removed for each recording time, again for May 10th, 2001.

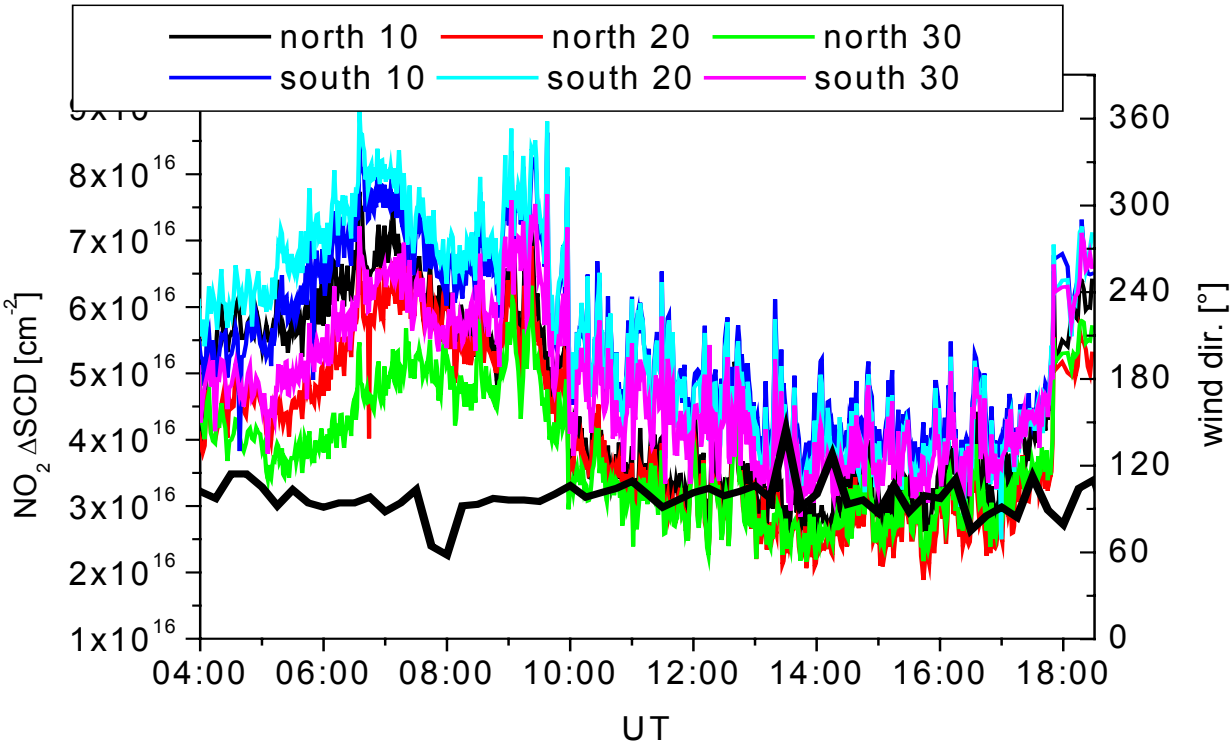

Figure 9.2.10 NO_2 ΔSCD from Fig. 9.2.9, but with the zenith sky signal removed. Now the diurnal variation of the motorway and Heidelberg plumes are seen. The black line is the wind direction.

The following plots will all refer to May 10th and 11th 2001 as example. They were days during an "Intensive Measurement Phase", IMP, during which all devices installed on site were operated to obtain a maximum of data collocation. It also were days with northerly wind prevailing, which allowed for comparison of the Heidelberg plume and the combined Heidelberg-motorway plume seen with the northern and southern looking telescopes, respectively. And it was a clear day, which made the FZS, recorded under clear sky conditions as well, applicable.

Before discussing the ΔSCD and their dependency on time and elevation, we will discuss the second approach for evaluation of CCD MAX DOAS spectra.

The first, and used, one essentially treats all telescopes and their CCD pixel areas as separate instruments. The second fits spectra of different lines of sight (and CCD chip rows) to each other, e.g. a spectrum S_{E1} of 5° elevation to one, S_{E2}, of 10°, which be called "cross-fitting". The Fraunhofer, water vapour etc. structures that do not cancel out are removed by fitting (either instrument-measured or convolved) cross section spectra. This directly yields the differences in slant trace gas column between the two lines of sight in question; the common stratospheric signal cancels out.

This approach, though, has to deal with the different slit functions. If unaccounted for they increase the residual in a way (to 1-2% for the spectra of May 10th) that prevents derivation of usable trace gas columns. One method is the "cross-convolution". Each measurement spectrum of the one elevation is convolved with the slit function of the other and vice versa.

Then a direct fitting is possible. However, depending on number and resolution of the spectra this technique may be time-consuming.
The method developed here also uses FZS. The FZS of the two elevations in question have been, as mentioned above, recorded at the same time along the same line of sight. So they contain the same absorptions. The only difference between them are the spectral effects of different slit functions.

- In the case of NO_2, the trace gas is a comparatively weak and narrow-banded absorber as compared to Fraunhofer and water vapour. So the slit function variation only has small effects on the NO_2 absorptions. But the Fraunhofer and water vapour absorptions show the effects. Their strengths are comparable in the FZS and the measured spectrum, and so are the slit function effects of S_{E1} and S_{E2}, which is not the case for NO_2.
- Division of FZS of S_{E1} and S_{E2} by each other after fitting one to the other yields a "difference spectrum", DS, that "contains" the slit function differences between both telescope-fibre-CCD regions.
- Smoothing of the logarithm FZS and using their difference as DS reduces the noise.
- Fitting of the DS together with S_{E1} to S_{E2} (or vc. vs.) removes a large part of the slit function differences and reduces the residual so that the trace gas can be evaluated.
- Use of a Ring spectrum (calculated from either S_{E1} or S_{E2} or both) still is a necessity, since the numbers of scattering events of any kind vary with elevation.

The fact that the slit function varies with time scales of days as well must be accounted for in this method (and also in the cross-convolution). Furthermore, the water vapour absorption changes with SZA; so does the strength of the Ring effect altering the shapes of the Fraunhofer lines. The slit function change then acts as additional operator. This causes the DS to be different depending on the day and SZA of the recording of the FZS used. Figure 9.2.11 shows three difference spectra for the telescopes "south 20" and "south 30", recorded May 1st and 12th, clear day, when all telescoped probed the zenith for the entire day.

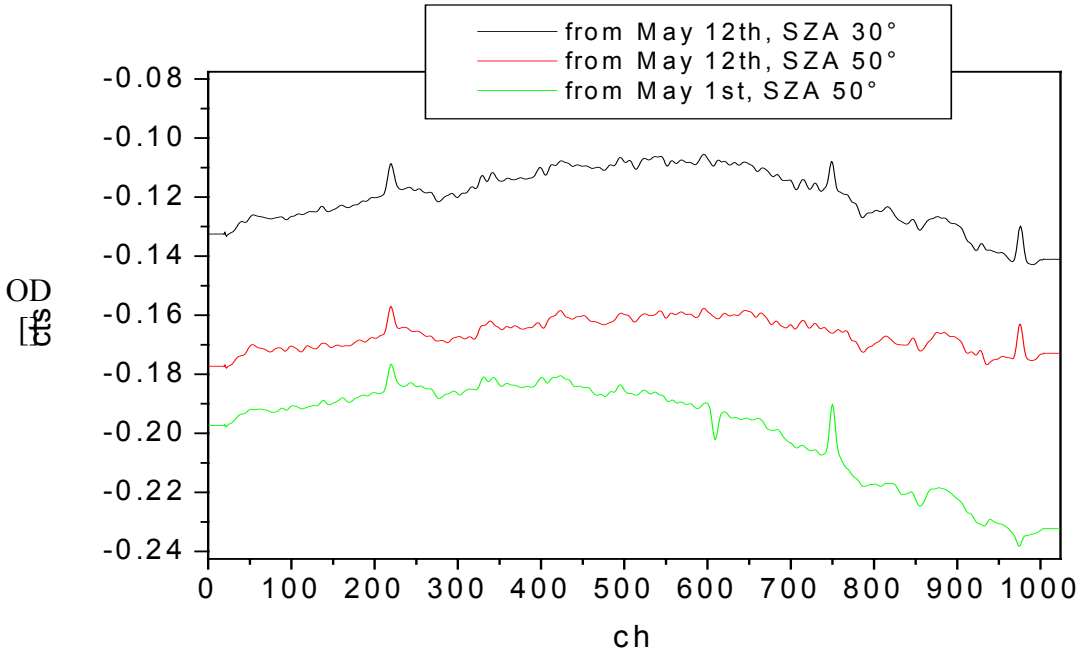

Figure 9.2.11 "Difference spectra" DS used for the fitting of spectra of different telescope-pixel row-systems. They vary with recording day as well as with SZA. The peaks denote positions of Fraunhofer lines; the spectral range is 450 to 420 nm (left to right)

Additionally, since the FZS have to be fitted to each other prior to DS derivation, the DS vary with the width of the spectral window used for the fit of the two "educt" FZS.
The method was applied to a series of sepctra of the two telescopes for 12th of May around SZA 75°. The final fit of the two measurement spectra was performed in a window of 400 channels.
A representative set of DS was selected with different days of FZS recording, SZA and window widths (400 "narr" and 800 channels "wide").
Two cross-fittings without DS, but two window widths participated in the comparison; so did a cross-convolution fit.
The derived NO_2 column differences were compared to the differences in ΔSCD derived from the first "FZS" method. Figure 9.2.12 shows the results.

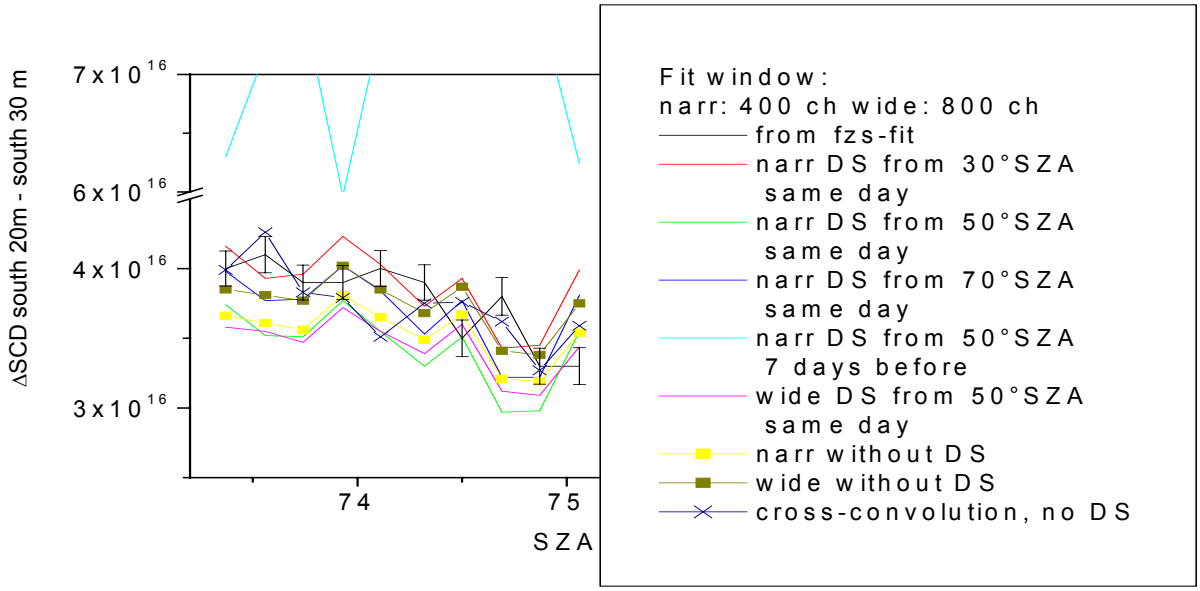

Figure 9.2.12 Fitting results for a set of spectra of "DS" method with different DS and cross-convolution method as compared to FZS fit. Apart from using a DS too old, all methods deliver similar results.

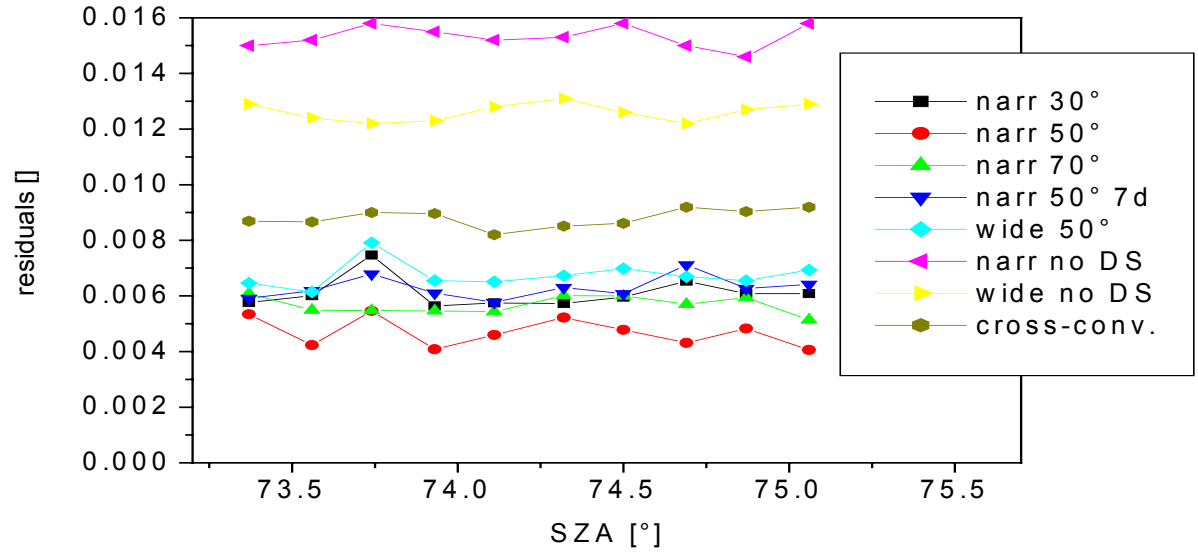

Figure 9.2.13 Residuals of the "DS" and cross-convolution fits. With an appropriate DS used (i.e. from same day as the meas. spectrum, similar in SZA and spectral window) residuals reduce by about a factor 2 as compared to cross convolution.

We find that all fits, except the fit with the DS a week old, deliver results similar to the FZS fit, though slightly beyond the FZS error. Any systematic offset cannot be made out from these spectra. It must be noted that the errors of the DS and cross-convolution fits are not included in this plot. Gauging from the FZS error, they would render all results similar within errors.
But it is also the residual that decides whether a column density can be considered significant. When in Figure 9.2.13 comparing the residuals of the approaches investigated, we find (as expected) the fits using neither DS nor cross-convolution to be unacceptable. The fit with the DS from the week before surprisingly has residuals similar in OD to the fits with DS from the same day. Together with the DS obtained from the broader window, nevertheless, it has the highest residuals, on average, of the DS fit group. The best fits are the DS of narrow width and of the same day. This means that the method is not very sensitive to SZA, which eases the logistics of the DS derivation during measurement campaigns.
The results in Figure 9.2.12 also serve as consistency check to the FZS fit used.
No we can discuss the results. Figure 9.2.10 shows clearly the rush hour in the morning, when large amounts of traffic commute into the city. The rush hour in the evening is not seen at UT 15.00 (difference LT to UT was 2 hours) but after 18.00 (20.00 LT). This must be attributed to the shop closings at 20.00 UT and the clerks leaving the city. Clerks from offices and e.g. banks do not generate such a peak at 15.00; they obviously leave Heidelberg at times scattered in between 15.00 and 18.00, and merge with the other traffic.
All signals show short time scale (1 min) fluctuations in the order of 10%.
There are, also as expected, differences in the signals of different elevations, identifiable even with the FZS zenith signal superimposed. To closer investigate them, we focus on the rush hour of this day (Figure 9.2.14).

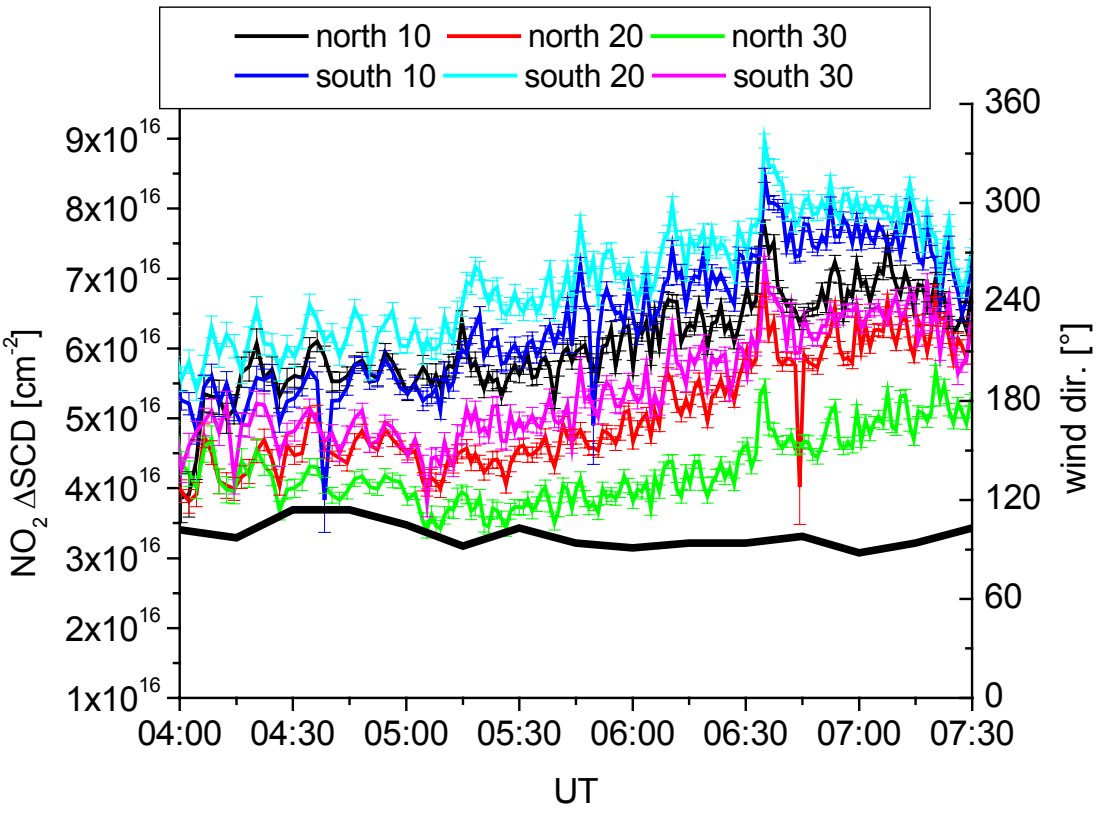

Figure 9.2.14 The morning rush hour of May 10th, 2003, on A 656 motorway. The telescopes looking through the plume and at the 10 m and 20 m retros have the strongest signals.

The summarized findings are:

- The telescopes looking southward through the motorway plume at a given retro have stronger signals than their "north" counterparts.
- The "30" telescopes measure the lowest columns within the "north" and "south" groups, respectively.
- In the "north" battery probing the Heidelberg background plume, the "10" telescope has the highest signal.
- In the "south" group probing the motorway plume and the Heidelberg plume behind, it is the "20" telescope which measures the highest NO_2 column.

We look at another rush hour, of the following day, the 11th of May (Figure 9.2.15)

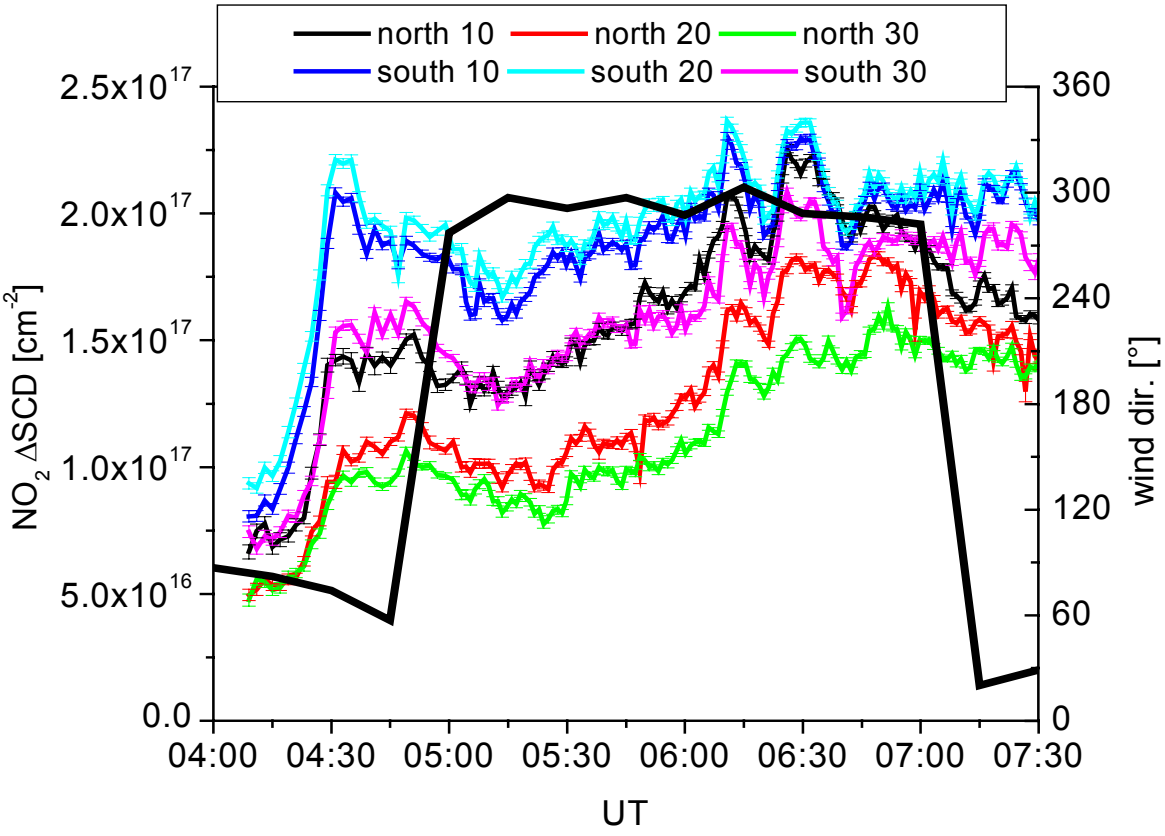

Figure 9.2.15 Rush hour of May 11th. The rush hour is more pronounced, the differences between the telescopes larger. The principal findings apply as well.

On this day with the rush hour more pronounced we find the results confirmed.
The findings reoccur here again. Within the "south" telescope battery, the "20" m consistently has the highest signal. Figure 9.2.16 shows the differences between the telescopes of the "south" group.
We first consider the light paths of the measurements before discussing the findings in the light of the findings of the AMF investigation for the BrO/Alert enterprise. Figure 9.2.17 gives an overview on the radiative transfer relevant factors.
As already stated, the Odenwald ridges are located to the east, in the direction of the telescopes. The lines of sight of the "north 10" and "north 20" telescopes ended at these mountains, in a distance of >=10 km. "North 30" looked over the mountains.

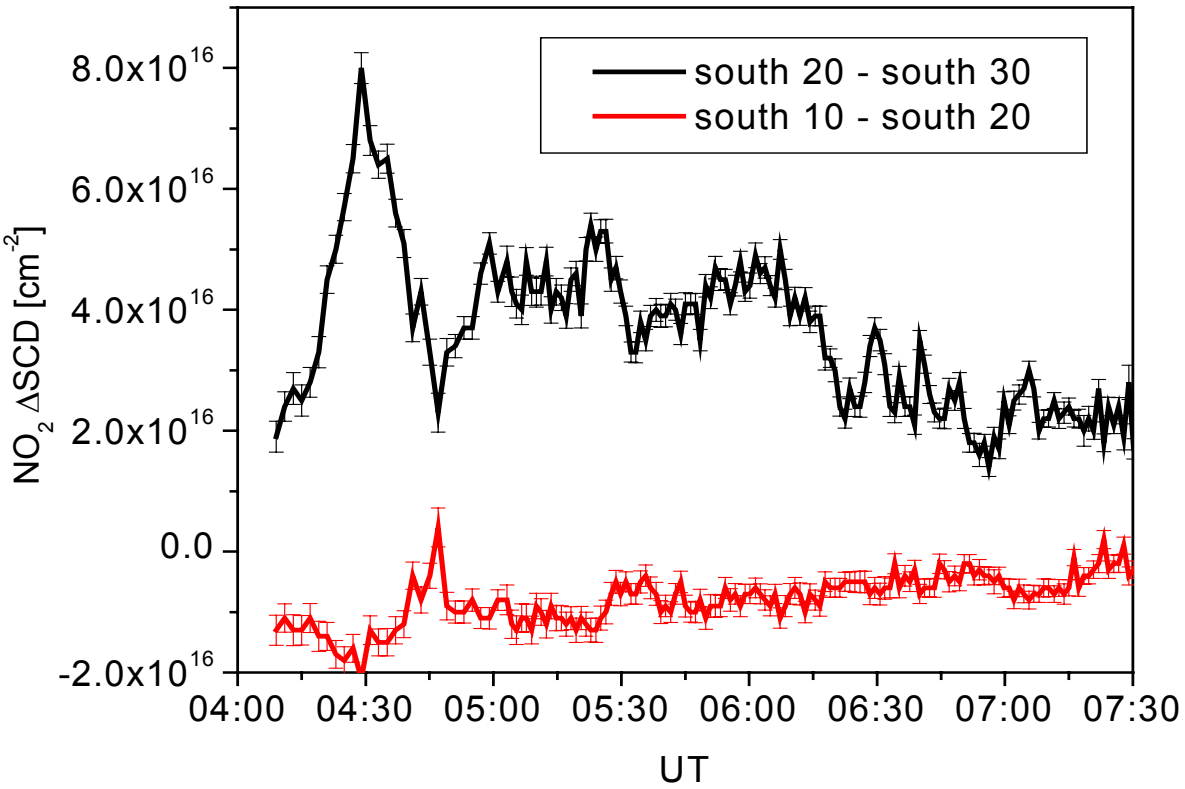

Figure 9.2.16 Differences in ΔSCD between the telescopes of the "south" group. While the line of sight of "30" clearly leaves the plume after a short distance, the "20" telescope has a slightly higher signal than "10".

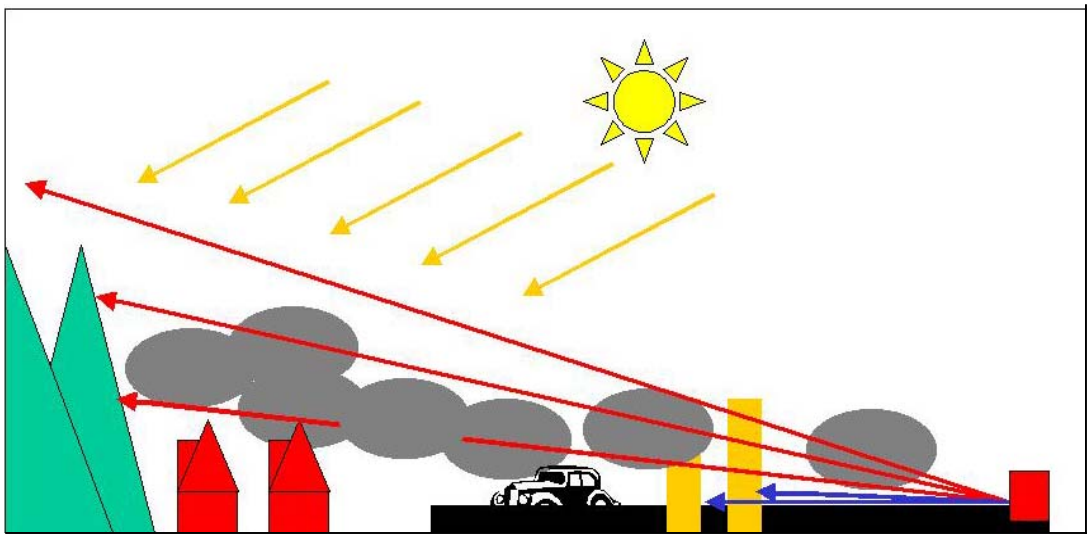

Figure 9.2.17 The mountains to the east limit geometrically the lines of sight of "20" and "30" telescopes of both groups. Behind the motorway plume, the Heidelberg plume is located. Both plumes contain aerosols affecting the light paths e.g. by reduction of the LSD. The shape of the plumes must be considered different; e.g. turbulence-induced vertical distributions can be expected to be more significant in the motorway plume.

For the "south" group, the same is true, with the difference that their lines of sight reach the mountains after about 15 km, their vectors having a larger southern pointing component.
Both the motorway and the Heidelberg plumes contain aerosols, altering the light path by scattering in addition to Rayleigh scattering.
The particulate matter composition at a motorway is a complex issue, which is why it was one of the research focuses. Droplets from heterogeneous reactions, soot from fuel combustion, and biogen dust from the agricultural fields are among the particles. The shape and size parameters still are under investigation by the respective workgroups, and the optical parameters are not yet available for a detailed investigation. Recalling Fig. 9.1.15, it is straight forward to see that e.g. variations in extinction coefficient and phase function can compensate for each other in their effect on e.g. the *LSA*. For this reason, a quantitative investigation and profile retrieval is not attempted here. But qualitative vertical profile shape statements are possible nevertheless.
When recalling Figure 9.1.13, we find that for 2° elevation (and 352 nm wavelength) the *LSA* for extinction coefficient 0.1 km^{-1} is around 250 m, the *LSD* about 7 km; for aerosol extinction coefficient of 1 km^{-1} at ground level the *LSA* is between 30 and 40 m, the *LSD* thus lower than about 1.2 km.
The lowest elevation is 0.68° for "south 10". From visual check (gauging from the appearance of the mountain ridge) a visibility (="4-e-length"[3]) for the two days in May of at least 10 km could be estimated, though averaged over the VIS wavelength region and on a path not precisely reproducing the line of sight for "south 10". This would relate to an e-length of ≥ 2.5 km, this in turn to an extinction coefficient of ≤ 0.4 km^{-1}. On one hand, the spectral window used for evaluation certainly has a lower visibility than the average of the VIS region, on the other hand, the extinction along the lowest two elevations may be significantly larger, since near to the ground, the aerosol particle number densities usually is highest, following an e.g. log-curve (or similar) with height.
Let us use the vertical discretization imposed by the tomography retro reflector altitudes; this defines boxes between 0 – 10 m, 10 and 20 m, 20 and 30 m. This is justified by the fact that the tomography division's preliminary results [*Mettendorf, pers. comm.*] show the LP signal on the light paths to the 40 m retro to be lowest, indicating the majority of the NO_2 of the plume to be located below 40 m. Table 9.2.2 gives the distances covered within the boxes henceforth named "B10" – "B30".

Table 9.2.2 Distances covered by the geometrical lines of sight within the boxes defined[4]

Telescope	LOS distance within B10, B20, B30 [m]
north 10	707
north 20	352
north 30	235
south 10	843
south 20	421
south 30	280

The air parcels over and around the motorway are continuously perturbed by the vehicles rushing by; resulting turbulences influence the vertical distribution of the motorway plume rather than that of Heidelberg. Due to the time delay between NO emission and oxydation to NO_2 in conjunction with the turbulence and wind induced movement, it seems a feasible

[3] Four times the distance after which a light beam's intensity has fallen to e^{-1} times its initial value [*Roedel 1991*]
[4] Uncertainties for elevation errors not considered for this estimate

assumption that the maximum of NO_2 is first, not directly at the ground of the motorway and second, not over the motorway, but shifted to the side, away from the motorway axis.
This is supported by [*Bernhard Vogel, pers. comm. 2002*] as well as [*Bäumer et al. 2003*]. The latter provided calculation results on the plume shape for given emission rates of NO for conditions of stable layering which prevailed on May 11th, up to 8:30 UT. The emission rates underlying the calculations may be different, but the plume shape information provides useful insights. Figure 9.2.18 shows the vertical plume shape for different distances *x* to the motorway centre line in leeward direction. *x* = 100 m is near the distance of the towers carrying the retro reflectors. We see the NO mixing ratio to be highest immediately at the motorway, which is understandable, and dropping off with distance, while the NO_2 shows the opposite behaviour.

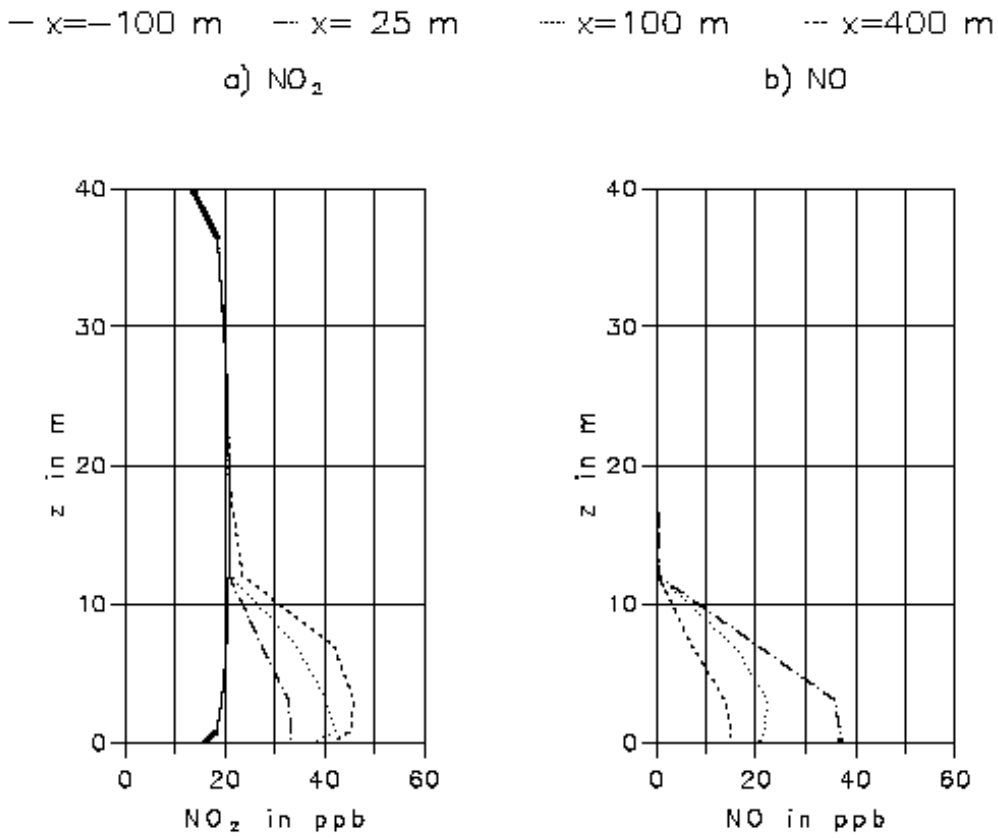

Figure 9.2.18 Vertical shape of the motorway plume for NO and NO_2 from model calculations by [Bäumer et al. 2003]. The NO_2 mixing ratio increases with distance x to the motorway centre line. Moreover, the maximum for a given x is located slightly above th ground. The dotted line for x=100 m represents best the location of the crane towers.

Figure 9.2.19 focuses on the evolving of the plume in *x*-direction for different altitudes above ground. We find the layering of NO_2, once established, to be prevailing up to 400 m away from the motorway, meaning "B10" – "B30" contain similar concentrations even beyond the crane towers as seen along the telescope lines of sight. The altitude of the plume (i.e. where the plume is greater than the background of 20 ppb in Fig. 9.2.18) is no higher than 20 m.

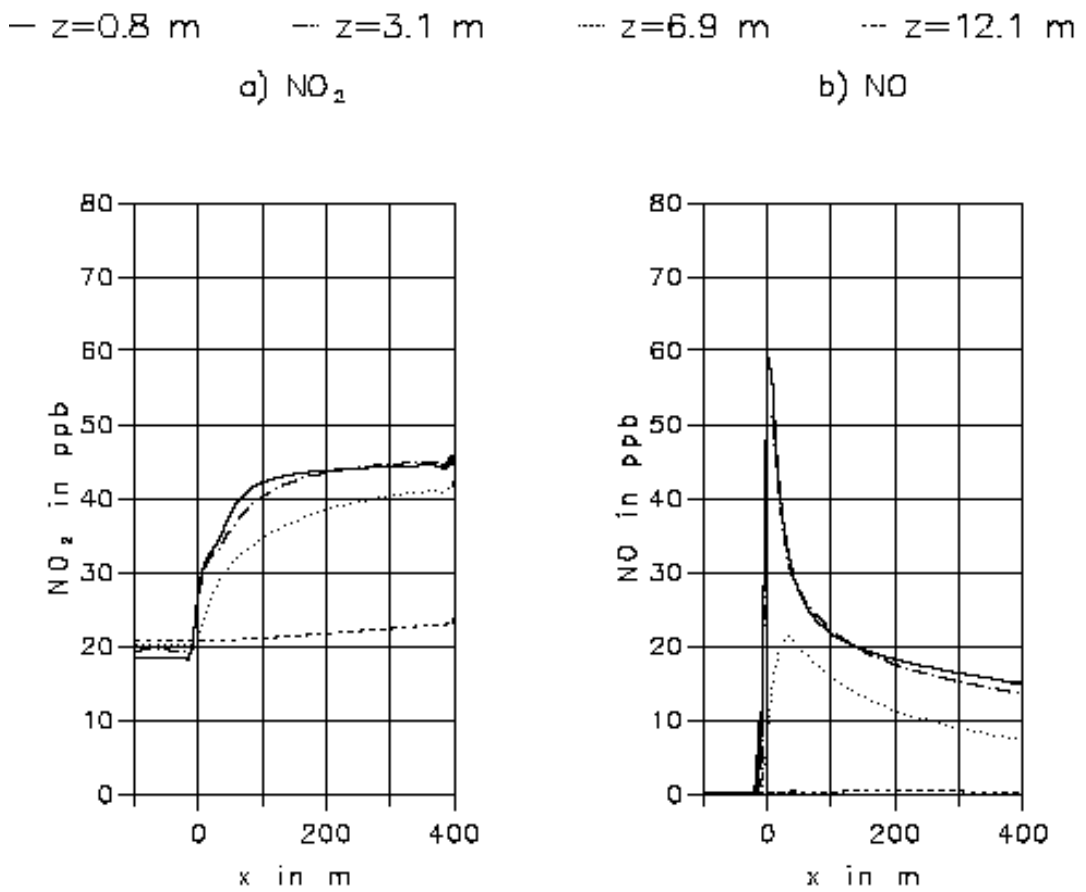

Figure 9.2.19 Horitontal plume development, again under "stable layerin" conditions, by [Bäumer et al. 2003]. The vertical layers of the plume are stable beyond the crane towers in x-direction, i.e. perpendicular to the motorway centre line.

The fact that the signal of "south 10" is smaller than that of "south 20" indicates an aerosol load over the motorway and on its leeward side high enough to reduce the *LSA* of "south 10" to a height low enough to to reduce the light path through the plume as compared to "south 20", which would explain the relation between their two signals. If the model by [*Bäumer et al. 2003*] correctly reflected the plume shape with height 20 m, this *LSA* would have to be around 10 m or smaller, which would relate, with the elevation of 0.68°, to a *LSD* of around 850 m, indicating an indeed high aerosol load near the ground with extinction coefficient of even greater than 1 km^{-1} for the measurement wavelengths.
When comparing, again geometrically first, the lines of sight of "south 20" and "south 30", we find a theoretical factor of 1.5 relating their paths through the plume. But in Figure 9.2.15, we find the ratio between their signals to be smaller, i.e. about 1.3 at 4:30 UT, and even smaller after this time. This can be attributed to shortening of the light path affecting "south 20" stronger than "south 30". Furthermore, since the line of sight of "south 30" is not limited by the mountain ridge, it also probes a part of the plume above Heidelberg with the slant line, which yields an increase in NO_2 slant column that is denied the two lower elevations. With the mixing layer altitude increasing with proceeding time of the day, the plume above Heidelberg extends to higher altitudes as well, increasing the signal for "south 30".

The Heidelberg plume does not generate a plot like 9.2.16; the signal ratios between "north 10", "20" and "30" seem to follow the lengths of the geometrical lines of sight, with "north 30" also looking over the mountains. But this fact indicates that for the "north" telescopes the effect of aerosols shortening the light paths is much weaker on the luvward side of the

motorway, i.e. if the wind prevents the greatest part of particulate matter to cross the lines of sight of the "north" telescopes.
One last comparison be added here to conclude this section. The Heidelberg background plume cannot be considered homogeneous in the horizontal dimension. (E.g. the northern lines of sight cross other motorways that the southern pendants do not.) Hence it is not identical for the southern and northern telescope battery.
With the tomography-derived 4D motorway plume (this effort being underway), it can be subtracted from the southern group and directly compared to the background plumes.
But under the assumption that the Heidelberg plume horizontal variations are smaller than difference to the motorway plume, we can subtract the former from the latter, i.e. form the difference in signal "south 10"-"north 10" etc. (Figure 9.2.20).

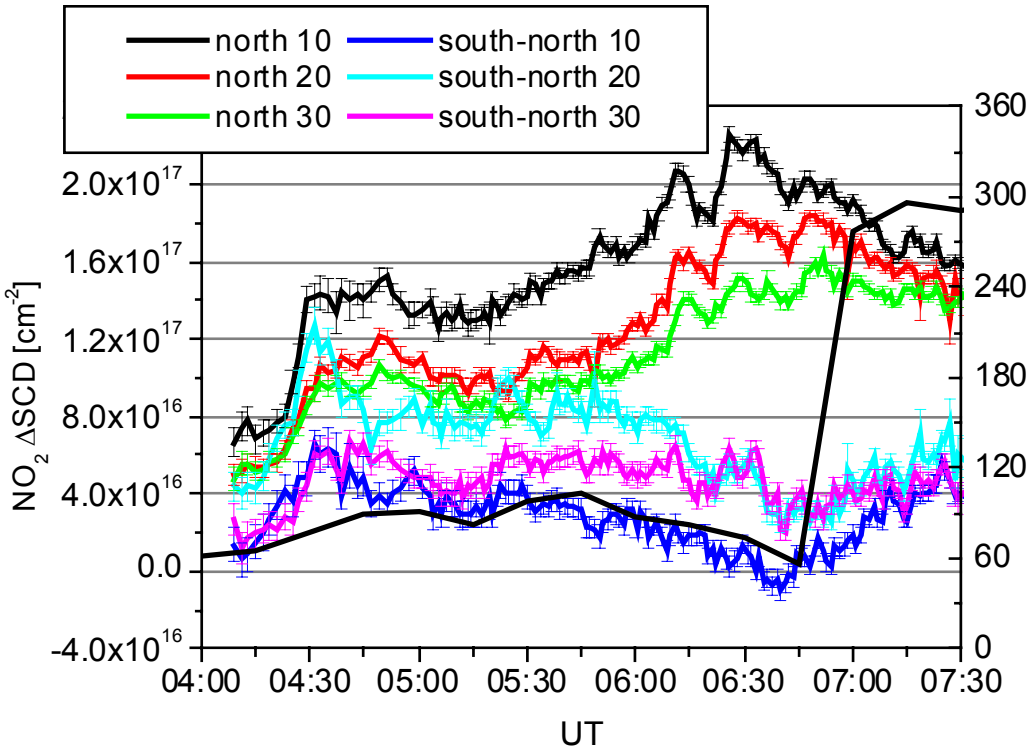

Figure 9.2.20 Signal of the southern-looking telescopes with the "north" signals subtracted retro-wise as compared to the "north" signals; in the beginning of the rush hour the slant columns from the Heidelberg and motorway plumes are comparable.

The information gain from comparison between the "10" telescopes may be questionable, since, according to above considerations, "south 10" may only "see" very little of the Heidelberg plume located mainly behind the last scattering event. But the "20" and "30" telescopes qualitatively show the same behaviour.
We find that at the onset of the rush hour the Heidelberg plume signal is comparable in strength to the motorway; with more traffic rushing in, the Heidelberg plume gets significantly stronger. This kind of comparison is denied the Long Path devices, and one of the advantages of simultaneous MAX DOAS, together with immediate and direct comparability of all lines of sight.
These investigations are not concluded, as stated, and constitute a case study so far. With the aerosol parameters available, RT modelling will be able to deliver vertical data on motorway and Heidelberg plumes on the time scale of the measurement.

9.3 Simultaneous MAX-DOAS of HCHO and O_4, Milano/Italy 2002

The FORMAT (Formaldehyde as a tracer of photooxidation in the Troposphere) campaign was focused on Formaldehyde, HCHO, as well as other urban trace gases, such as nitrogen dioxyde in the heavily polluted Milan area. The diurnal series of the species was to be investigated to assess the chemical relations and the transport of the plume.
For details refer to the FORMAT homepage[1] and references therein.
Of great relevance also are aerosols, such as dust and soot, as well as droplets; radiometric measurements, e.g. with the calibrated spectro-radiometer, were performed to obtain data on photolysis rates as well as on aerosol optical poperties. The evaluation of these data is still in progress. The duration of the campaign was July 23th , to August 17th, 2003.
Among the devices deployed was the MAX DOAS device described in the preceding section; the operator was Thomas Wagner, who also evaluated the data. In this section we will attempt to gauge the aerosol load from measurements of O4. For an investigation on aerosol effect on zenith-sky measurements see [*Wagner et al., 2002*].

9.3.1 FORMAT campaign and the Chemistry of HCHO

Among the objectives to accomplish were:
1. to employ and compare several new measurement techniques to use for the measurement of formalde-hyde on the ground and from aircraft,
2. to use these measurements in order to get a best possible picture of the horizontal, vertical and temporal distribution of formaldehyde in the planetary boundary layer in a photochemically polluted area, the Italian the Po Valley,
3. to thus obtain a better knowledge of the concentrations and distribution of formalde-hyde in the troposphere over Europe and globally and compare it to / to improve chemical models,
4. to validate satellite measurements (GOME, SCIAMACHY) of formaldehyde,
5. to improve the algorithms for obtaining HCHO from satellite measurements by GOME and SCIAMACHY,
6. to inform end users of the results of the FORMAT project [*Campaign proposal 2001*].

Formaldehyde (HCHO) is the most abundant of carbonyl compounds in the atmosphere.
Formaldehyde is found both in the remote background atmosphere and in polluted urban air masses. It is mainly generated by photooxidation of hydrocarbons [*Atkinson, 1994*]. In the background troposphere, methane is the dominant formaldehyde precursor. Close to the surface, local sources of non-methane, e.g. biogenic, hydrocarbons, NMHC, also become important in producing HCHO. Formaldehyde is also anthropogenically generated directly from incomplete combustion processes. Figure (9.3.1) shows some of the reactions involved in the oxidation of hydrocarbons via HCHO to CO.
Accurate HCHO measurements are thus important in constraining and validating photochemical models of the troposphere, in understanding the budgets and cycling among various reactive species and the global budget of CO. Despite this importance and the relatively large number of techniques employed, there is still considerable uncertainty in measurements of ambient HCHO.

[1] [*www.nilu.no/format/*]

Photochemical smog is one of the most, if not the most, serious air pollution problem in Europe today. Episodes with high concentrations of ozone and NOx cause harm to human health and to vegetation. The key to abatement of such pollution as well as prediction and warning protocols are one of the biggest challenges to environmental authorities. A better understanding of the abundance of HCHO in urban plumes is a requirement for this. In addition to it, also nitrogen oxydes were measured, both so from ground as well as from aircraft.

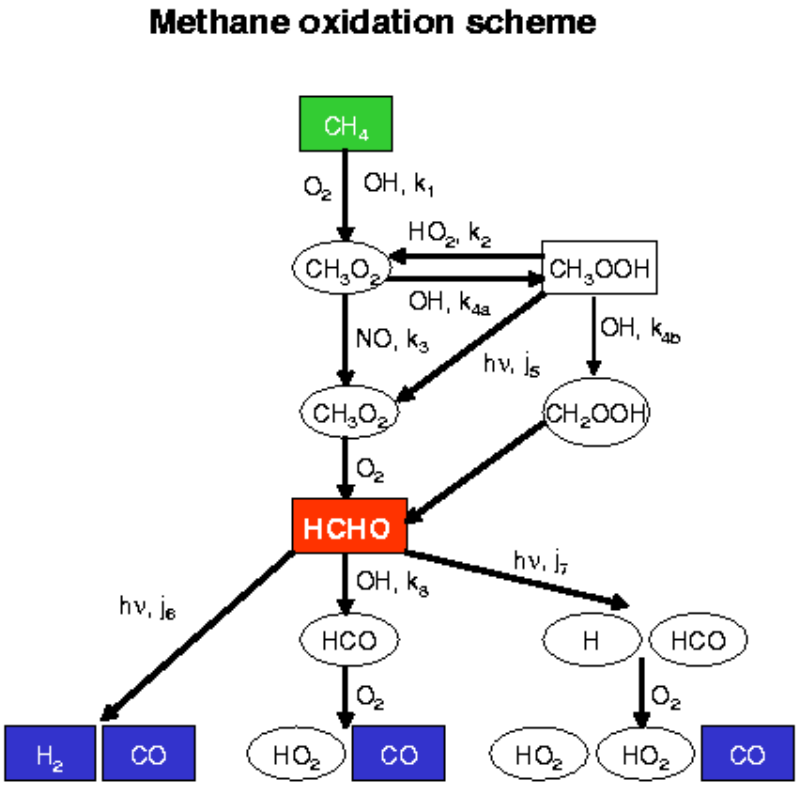

Figure 9.3.1 Overview on methane oxydation; HCHO is a stable intermediate. Taken from FORMAT press release document.

9.3.2 Instrumental Setup

The MAX DOAS was first placed near the village Alzate (45.76° N, 9.16° E); After the 5th of August, it mas moved to Bresso (45.54° N, 9.20° E).
Eight telescopes were employed, with viewing directions 3°, 10° and 90°. Viewing direction was south, i.e. resulting in azimuth directions (relative to the sun) of about between 0° and 105°.
To provide better straylight protection, the tubes were fitted with plastic extensions.
Temporal resolution was between 50 s and 400 s, 120 s on average.
Following the findings concerning evaluation of spectra of this device, once per day all telescope tubes were directed into the zenith to obtain zenith sky spectra with which the measured spectra were evaluated.
The wavelength range for HCHO (and NO_2) evaluation was 337-358 nm, for O_4, it was 338.5-364.5 nm.

9.3.3 Measured SCD

The evaluation was performed in a way similar to the algorithm described in section 9.2.3; i.e. a zenith sky reference was subtracted, recorded around noon of the respective day.
The total dataset shows strong variation with e.g. time of the day. An investigation of all measurements is beyond the scope of this work[2]. Selected here for investigation be a series of days in August showing the effect of the varying aerosol load.
During 10th and 11th of August, heavy rainfalls cleared the air from almost all aerosols. After this, during the following days, the aerosol load increased again, affecting the AMF for O_4 as well as HCHO. Shown in Figure 9.3.2 are DSCD for HCHO, in Figure 9.3.3 for O_4 for the four following days.
Notable are the following facts: The differences between the elevations for HCHO (distinguishable even without further processing of the DSCD) are clear to see, indicating a location of the HCHO close to the ground, where different elevations have their greatest effect on sensitivity.
For O_4, however, two developments can me made out: First, the DSCD drop during the four days, for 3° elevation and the values in the morning by about a factor of two. Second, the differences between the slant elevations decrease. These two findings are in agreement with the investigation results in section 9.1.4. The developments are caused by the increasing aerosol load and the resulting shortening of the *LSD*.

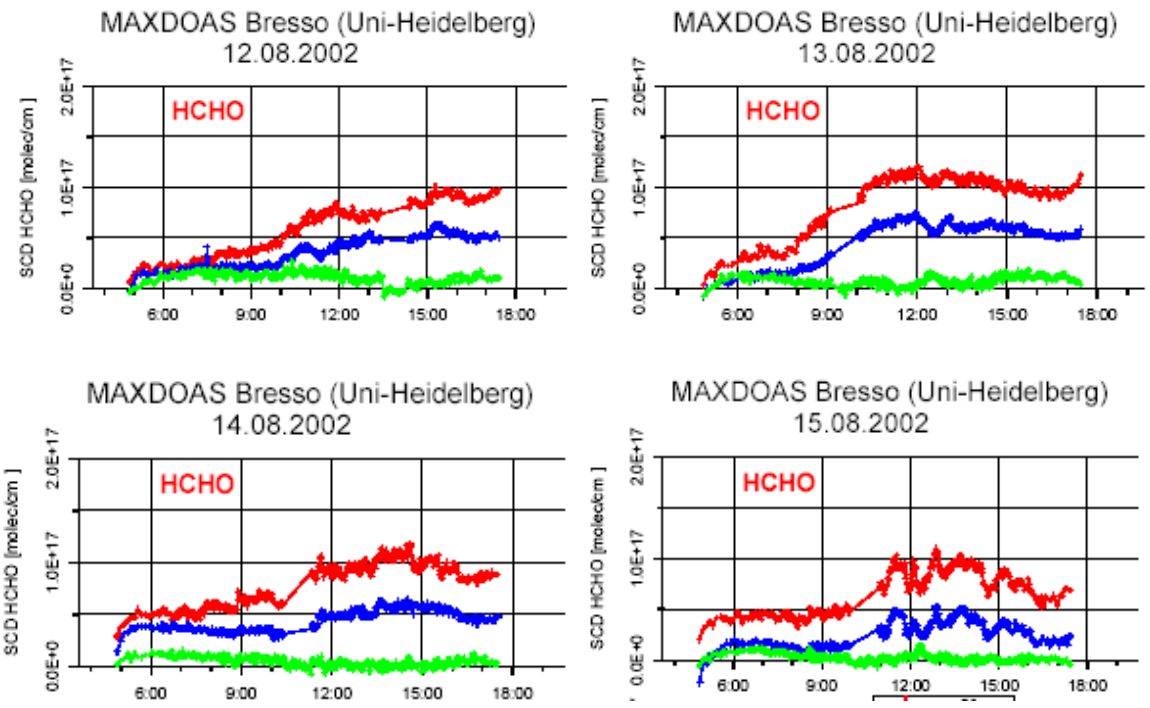

Figure 9.3.2 DSCD for HCHO for days 12th to 15th of August, 2002, [Wagner, pers. comm.] Please note that a zenith sky reference has been subtracted for each of the days.

[2] Thoug, it is not beyond the capabilities of TRACY.

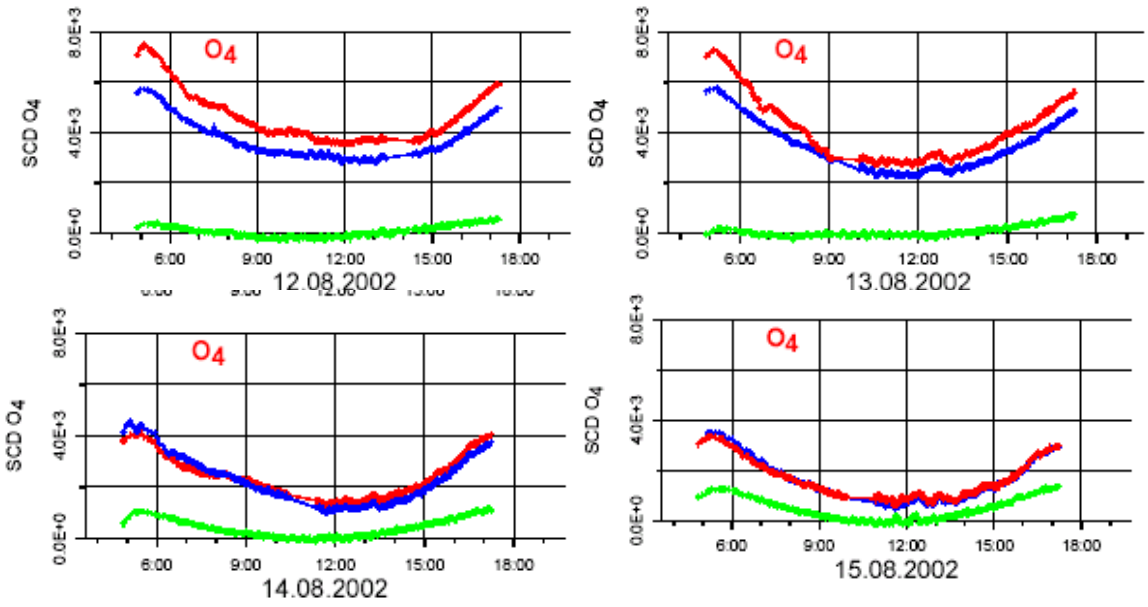

Figure 9.3.3 DSCD for O_4 for days 12th to 15th of August, 2002, [Wagner, pers. comm.] Please note that a zenith sky reference has been subtracted for each of the days; unit is absorptance.

9.3.4 Modelled AMF

To qualitatively model the situation, the chemical profile of HCHO from the QUILT comparison (see section 7.2) was used with the discretization used in this exercise. Also the NO_2 and O_3 profiles were taken into account, together with the two aerosol loads in the MAX investigation in section 9.1., and a standard atmosphere; the model was run for SZA between 30° and 90°, and for pure Rayleigh, low aerosol and high aerosol case. Elevations chosen were 3°, 10° and 90°, azimuth 90°; the albedo was 10%, half aperture angle 0.15°, wavelength 352 nm. Figure 9.3.4 shows the DAMF for HCHO. The AMF for 90° elevation and 30° SZA (≈ 11:27 UT[3]) has been subtracted to make the DAMF comparable to the DSCD.
We see the DAMF to be varying only little with SZA, as expected. The behaviour of the DAMF of different elevation towards each other reproduces in principle that of the measured O_4 DSCD.
Figure 9.3.5 shows the modelled O_4 DAMF, i.e. they also have been subtracted from the value for 90° elevation, 30° SZA. Clearly the fall-off of both absolute DAMF as well as ratio between elevations can be seen. When comparing the DAMF and the DSCD for morning/evening, maximum values, and noon, minimum value, for 3°, we see in the measured data the ratio (averaged over morning and noon) for 13th of August for 3° to drop by a factor of 2.2; this is not reproduced by the clear-sky scenario, but, though not perfectly, by both the low aerosol load scenario (factor 1.7) and the high load (factor 2.56).
This may serve as first indication of already rising aerosol load in 13th of August. On the other hand, the fact that we see a small but significant difference in the measurement O_4 DSCD points toward an aerosol load smaller than the low load, since already for this load the modelled AMF show the two signals to be nearly identical.

[3] To facilitate comparison, the SZA have been converted into UT using high precision software (see 8.1)

This discrepancy in aerosol interpretation statements may be caused by diurnal variation of the aerosol load, e.g. in turn caused by meteorology and wind. Another factor is the phase function; it was taken the one of the RT comparison scenario, as was the input profiles, which may be wrong. But the effect of phase function was found to be small as compared to the aerosol uncertainty.

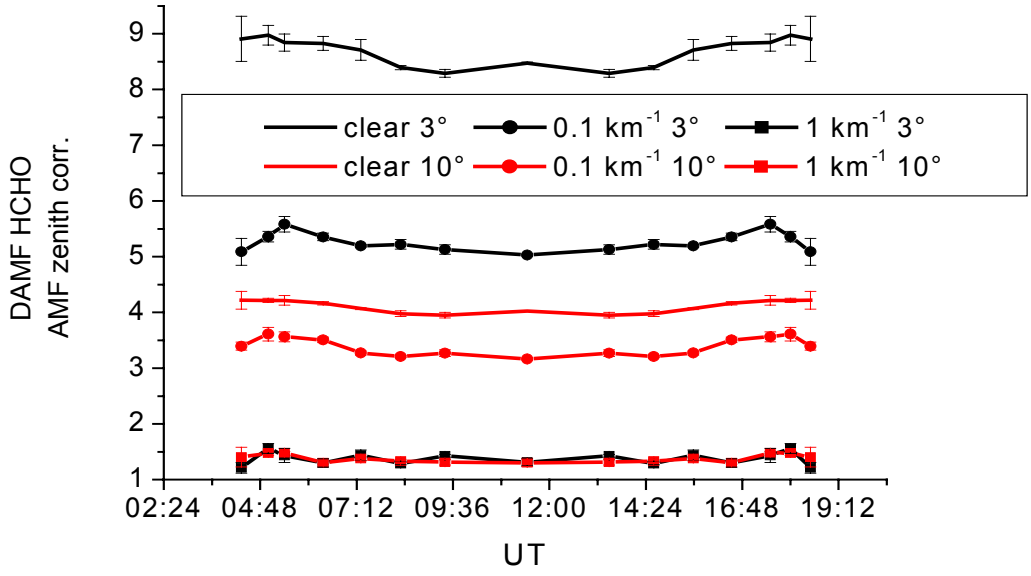

Figure 9.3.4 O_4 DAMF (AMF with AMF for 90° elevation, 30° SZA subtracted) for each model case.

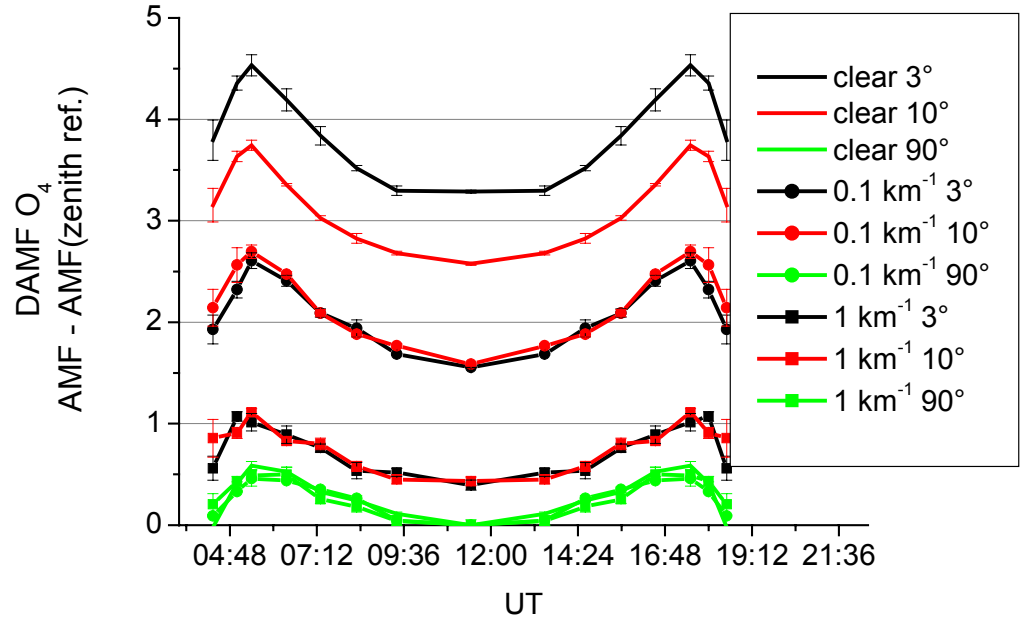

Figure 9.3.5 DAMF (AMF with AMF for 90° elevation, 30° SZA subtracted) for each model case. The SZA has been converted into UT using high precision software (see section 8.1.)

In spite of this, we may again attempt a profile estimate.
We chose the data for August 13th, 11:27 UT, around the time the zenith reference was recorded. We reproduce this by subtracting, in Figures 9.3.4 and 9.3.5, the DAMF for 90° elevation from the other signals. By doing so, we again remove uncertainty induced by albedo, as well as any signal contained within the zenith reference.
By concentration on a dataset for one UT, we deal with one given meteorological condition.
Then we can form the ratios between the zenith-corrected ΔAMF and ΔSCD, respectively, for elevations 3° and 10°, and compare these (equivalent) ratios for measurement and the three scenarios (see Table 9.3.1).
We see that the measured ratio is in between the clear atmosphere case and the case for low aerosol load. This seems to confirm the assumption of a still low aerosol load, lower than for the "low load", but significant even so.

Table 9.3.1 ΔSCD and ΔAMF for O_4 for the dataset investigated

Dataset (11:27 UT, 30° SZA)	ΔSCD (meas.) ΔAMF (mod.) O_4 [a.u.] Zenith-corr. 3°	ΔSCD (meas.) ΔAMF (mod.) O_4 [a.u.] Zenith-corr. 10°	ratio ΔSCD(3°)/ΔSCD(10°) (meas.) ΔAMF(3°)/ΔAMF(10°) (mod.)
meas. 13th Aug.	2823	2359	1.2
model clear	3.3	2.6	1.28
model low load	1.6	1.6	0.98
model high load	0.4	0.43	0.91

When now performing the same exercise on the DAMF and DSCD of HCHO, we find the following numbers (Table 9.3.2):

Table 9.3.2 ΔSCD and ΔAMF forHCHO for the dataset investigated

Dataset (11:27 UT, 30° SZA)	ΔSCD (meas.) ΔAMF (mod.) HCHO [cm^{-2}] Zenith-corr. 3°	ΔSCD (meas.) ΔAMF (mod.) HCHO [cm^{-2}] Zenith-corr. 10°	ratio ΔSCD(3°)/ΔSCD(10°) (meas.) ΔAMF(3°)/ΔAMF(10°) (mod.)
meas. 13th Aug.	1.14E17	7.02E16	1.62
model clear	8.5	4.0	2.10
model low load	5.0	3.2	1.59
model high load	1.3	1.3	1.01

We again find the measured ratio to be in better agreement with the ratio modelled for the low load than for the clear sky. It has to be kept in mind, though, that the ratio is biased by strong variation with time, and that the measurement noise of the ratio is about 15%.
Furthermore, we must take O_4 as "gauging trace gas". Hence if the HCHO profile used for this modelling was correct, the ΔSCD ratio should be larger, and closer to the clear sky case.
This "too low" ratio indicates a HCHO profile different from the one used in the model in the respect that it reaches up higher into the sky, i.e. that a greater part of the trace gas is located higher than the *LSA*. This would be fulfilled e.g. by slower drop-off of the mixing ratio with altitude. Because of the uncertainties, we do not try to estimate a concentration. But this exercise shows the principal algorithm to obtain trace gas distribution data from O_4 measurements. To take more advantage of it, the use of more slant elevations such as 2° and 5° can be recommended from section 9.1.

10. Aircraft measurements of NO_2

Airborne DOAS platforms also are used to probe trace gases in the lower troposphere and the PBL. As part of the FORMAT campaign, the research aircraft DLR/Partenavia was operated carrying several instruments to perform the airborne part of the campaign objectives.
Among them was an AMAX DOAS instrument (for Air Multi Axis) to measure NO_2.

10.1 Instrument

The instrument was a simultaneous Multi-Axis device essentially of the same type as the one used for the ground based operations during BAB II and FORMAT described.
It was integrated into a research aircraft. Figure 10.1.1 shows the aircraft with the upper cylindrical part containing the telescopes of the instrument protruding from the hull. An identical cylinder is located on the lower hull side.

Figure 10.1.1 Partenavia aircraft with the AMAX DOAS instrument fitted to it. The telescope housings can bee seen on top and botton of the hull [Heue et al. 2001].

As with the ground based system, the light measured from the different telescopes (under different viewing directions) is transmitted to an imaging spectrograph via quartz fibres; the end of the fibre bundle forms the entrance slit of the spectrograph, an imaging spectrograph Acton 300i was used. A CCD detector with 512 by 2048 pixels by Andor was chosen. For details see [*Heue at al. 2001*].

The spectral window for 335-480 nm was used for measurements of HCHO and NO_2. The central wavelength of the evaluation window for NO_2 was 345 nm.
The elevations were –4°, -7°, -10°, -14°, -17° and –20°, i.e. looking down on slant paths, and in aft direction, and –78° (=-102°) ahead. The azimuth depended on the flight direction. Several flights were performed at altitudes between 1 and 2 km. Some of them lead the plane through the NO_2 a plume of a plant. For a qualitative investigation we will focus on this.

10.2 Measured SCD

For the evaluation algorithm see [*Pundt 2003*]. Figure 10.2.1 shows the NO_2 SCD for the times of the plume traverse. The SZA was 32° at this time, the SAZ 200°, flight altitude was 1400 m, flight direction was 345° (northwards), hence the azimuth of the telescopes 35°.
The elevation –10° and –7° have the highest signal, -102°, in spite of looking down most "directly" , the lowest.
In contrast to the balloon situation in the previous chapter, the AMF cannot be expected to be as simple in terms of similarity to geometrical considerations.
Figure 10.2.2 is a typical image on the situation below. Pollution aerosols (e.g. droplets and dust, as in the case near the motorway) reduces visibility for both the human eye and any instrument. The strong Rayleigh scattering also took its toll. The sensitivity for a given volume along the lines of sight decreased rapidly with distance from the instrument.

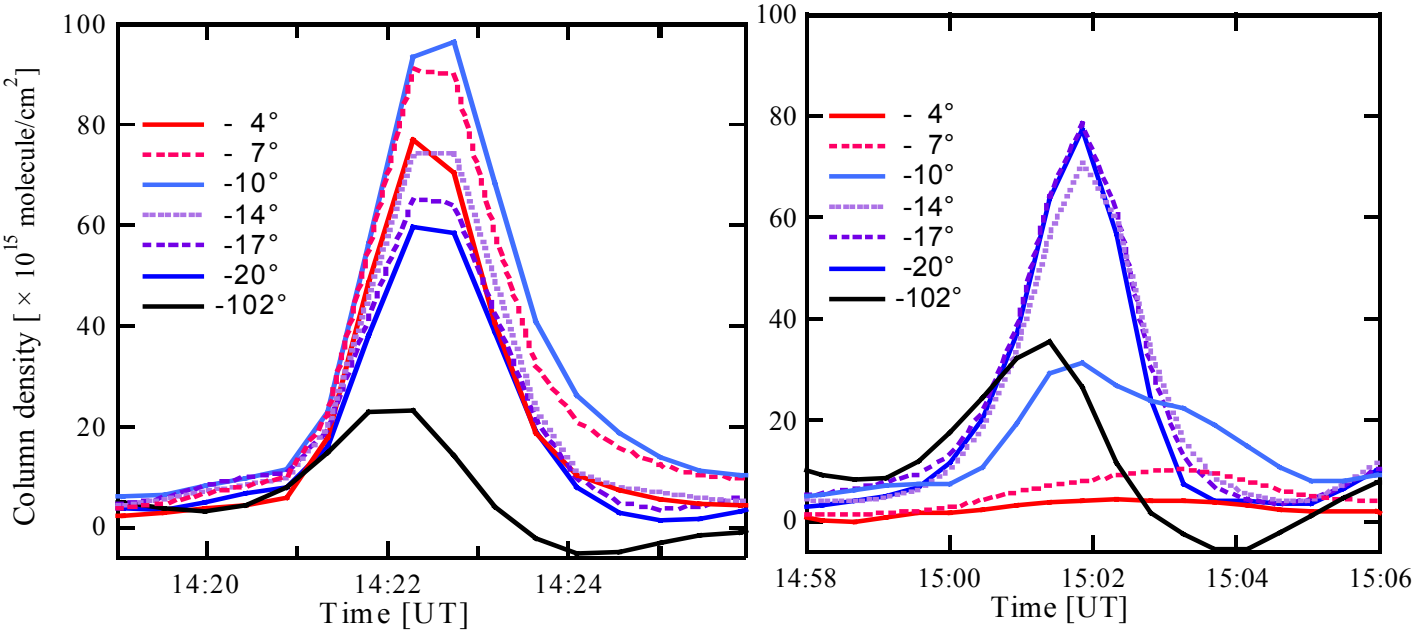

Figure 10.2.2 NO_2 (Differential) SCD for the aircraft measurement of a plant plume during FORMAT campaign [Pundt 2003, Wei-Der Lee, pers. comm. 2003]. Left panel: overpass at altitude 1400 m, right panel: overpass at 1700 m.

Figure 10.2.3 Example SMOG event with large aerosol load below the aircraft, taken from [Campaign proposal 2001, FORMAT website]

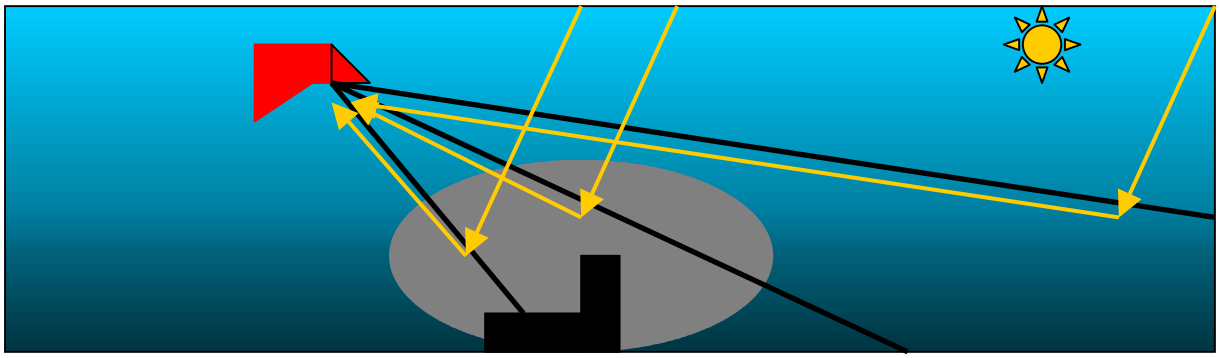

Figure 10.2.4 Lines of sight and light paths in relation to a plume close to ground; slant lines look over the plume; less slant ones cannot penetrate into the layers of dense aerosols and high air density (denoted by darker colour).

A plume which is mainly located close to ground (considering scales defined by the flight altitude) is thus difficult to see. Figure 10.2.4 gives on overview on the sensitivities to it expectable for AMAX DOAS. The slant lines of sight look over it, or only skim it, without "taking up" much spectroscopic signal. Elevations less slant enter the plume, but also the layers of dense aerosol and air, which reduces their *LSD*. The telescopes looking most straight down may penetrate further down, but on a short geometrical path, which again reduces the (Box) AMF. It is this what we see in Fig. 10.2.5.

10.3 Modeled Box AMF

In this qualitative sensitivity study the flight and measurement parameters were reproduced. Only the flight direction was set to due north to simplify the 2D discretization.
Again a standard atmosphere was used with a discretization of 200 m between 0 and 3 km, and 500 m between 3 km and 5km, 1 km above up to 70 km TOA.

This vertical discretization was the same as used in the comparison of ground based HCHO Off-Axis SCD. Also the aerosol scenario from this exercise was used. The elevations listed above were used with azimuth 90° and half aperture angle 0.1°, albedo 0.1, λ 348 nm.
The speed was 144 knots; the average time difference between two spectra recordings was 30 sec., which relates to a distance passed within this time of 2.2 km. To take account of this fact a 2D grid was modelled with vertical (= spherical) layers in the **Z**-axis and separations in ϑ-axis spaced in 2.2 km distances. Box AMF were calculated for these boxes. The number of photons needed was high, i.e. 20000 photons. This is to attribute the small voxels extensions, of which the Box AMF react sensitively to statistical light path variations, as well as the high Rayleigh scattering for 348 nm, which increases the light path variability. The –102° LOS is named –78° for consistency reasons. Figure (10.2.6) shows the setup of the spatial discratization, (10.2.7) the resulting Box AMF. The error is <=5%.

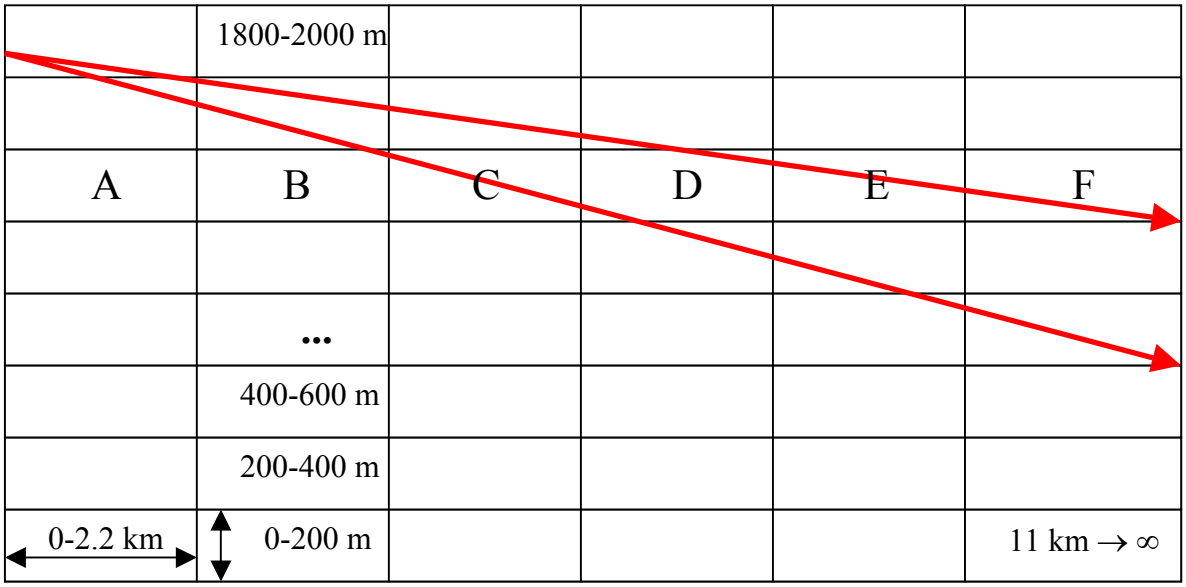

Figure 10.2.6 Organization of the boxes with respect to the lines of sight (red arrows). A denotes the (vertically layered) boxes located immediately in front of the telescope nozzle, F the airspace beyond the box system.

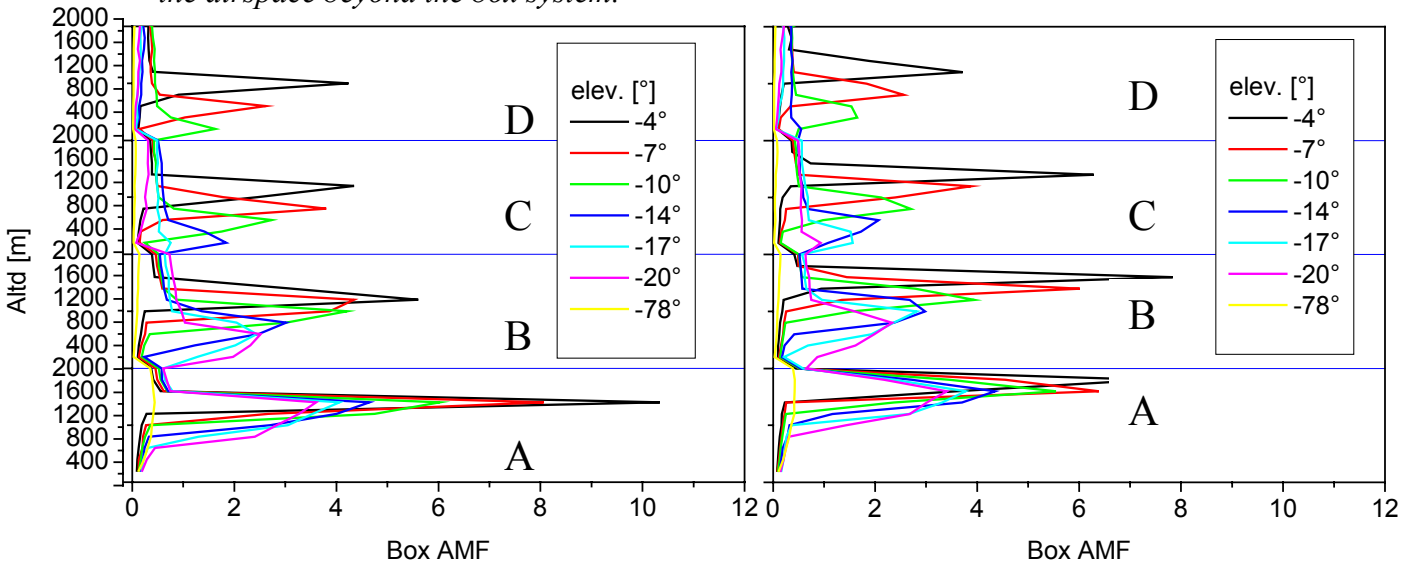

Figure 10.2.7 Box AMF for the lowest 2 km and the discretization described (200 m in Z-axis, 2.2 km in ϑ-axis). Left panel: flight altitude 1400 m, right panel: 1700 m.
The layers in the plot denote the ϑ-axis-boxes; for the letters refer to Fig. 10.2.6.

The letters in Fig. 10.2.7 refer to the ones in Fig. 10.2.6. The Box AMF are largest for A, and larger for flight altitude 1400 m than for 1700 m.
The findings again be summarized.

- The sensitivity of a DOAS device for a given air volume decreases with increasing vertical and horizontal distance to it.
- The slantest lines of sight of sight, i.e. with the smallest negative elevations, are sensitive only for trace gases located immediately below the instrument.
- Again for each line of sight, an altitude of maximum sensitivity (=Box AMF) does exist, and again it is correlated with the *LSA*; it is largely governed by scattering, since for e.g. operation altitude of 1400 m and elevation –4°, there are around 2.5 Rayleigh scattering events the recorded light on average has suffered.
- The greater a (negative) elevation, the deeper the box of highest Box AMF is located.
- For lines of sight resembling nadir, neither of the boxes are probed with an high Box AMF.

Due to the adversary effects on the sensitivity (penetration depth vs. geometrical path through a box) the sensitivities by far are not as different for adjacent boxes as they are in case of the balloon experiment. The best sensitivities for the lowest boxes obviously are given for elevation –10°. It must be kept in mind that the aerosol load once again represents a large uncertainty; without detail aerosol vertical profiles in size distribution, number density and phase function a matrix based retrieval can not be performed.
However, with this information available, from e.g. additional ground based data or O_4 measurements, this seems to be possible, since the Box AMF for the slant elevations show a clear gradient even for vertical layers adjacent to each other, supporting the assumption that the matrix to compose from the Box AMF may be well conditioned.
In the measurement, for 1400 m the elevations of –10° and –7° deliver the highest signal. Given the chosen aerosol load was correct, this would indicate the plume to be lower than 1200 m, because if it would extend higher, the telescope with elevations –4° would deliver, with the high Box AMF for 1200-1400 m, a strong (as compared to –7° and –10°) SCD signal as well.
For the 1700 m overpass, the elevations –10°, -14° and –17° degree “see” an SCD of comparable strength. If we refer to the Box AMF, we find the box with high Box AMF for these three telescopes to be 1200 – 1400 m, indicating the plume to be reaching up higher at this time. This can be explained with the rise of the mixing layer between the two overpasses.
A potential for quantitative profile retrieval must be noted as primary result of this investigation. Future work may assess quantitatively the impact of varying aerosol load.

11. Application to Balloon DOAS

One of the applications of DOAS to investigate the stratospheric chemistry is the opartion of devices aboard balloons. The following will display Box AMF for a typical balloon situation and will discuss the variation of them with measurement parameters. We chose as wavelength 435 nm, which is within wavelength ranges probing for NO_2.

11.1 Role of Stratospheric Nitrogen Oxydes

This section briefly covers the chemistry of stratospheric NO_2 to be "probed" with the wavelength chosen for study in this chapter. For a detail discussion see e.g. [*Bösch 2002*], of which the relations described here are taken. A more detail overview on NO_3 chemistry can be found in [*Geyer 2000*] and [*v. Friedeburg 1999*]. Be it included here as well since it is to play a role in the chapter on a Monte Carlo based retrieval technique.
The dominant net source of stratospheric NOx (=NO+NO_2) is the reaction of excited O* with N_2O:

$$O^* + N_2O \rightarrow 2NO \qquad (11.1.1a)$$

$$\rightarrow N_2+O_2 \qquad (11.1.1b)$$

The NO fractional yield is 58 %. N_2O has both natural and anthropogenic sources with a ratio of 2:1. The major contributions come from oceans and tropical forests. Resulting from biomass burning and the use of artificial fertilizers, the N_2O level has increased from a preindustrial 260 - 285 ppb to 311 ppb today with a mean growth rate of 0.25 % per year during the 1980s. The growth rate varied in recent decades for reasons not clear so far. N_2O is an inert gas with a lifetime of 120 ± 30 years for which no destruction processes in the lower stratosphere are known apart from photolysis:

$$N_2O + h\nu \rightarrow N_2 + O^* \ (\lambda <= 398 \text{ nm}) \qquad (11.1.2)$$

(11.1.1) accounts for only 10% of the N_2O removal.

There is another significant, but highly variable source of NOy[1] in the mesosphere and lower thermosphere (see chapter 1) by solar proton events (SPEs), galactic cosmic rays (GCRs) and energetic electron precipitations (EEP), which produce atomic nitrogen through dissociations, predissociations or dissociative ionizations in collisions with N_2. The observed NOx formed can enter the stratosphere during winter and early spring and can descend to 20-25 km,

[1] NOy is the sum of the reactive nitrogen species, i. e. NOy = NO + NO_2 + NO_3 + N_2O_5 + HNO_3 + $ClONO_2$ + HO_2NO_2 + $BrONO_2$ + aerosol nitrate

causing an anomalous enhancement of NOx in the middle stratosphere. During daytime, NO and NO2 are in photochemical steady-state mostly via the reactions (see also section 9.2):

$$NO + O_3 \rightarrow NO_2 + O_2 \quad (11.1.3)$$

$$NO_2 + O \rightarrow NO + O_2 \quad (11.1.4)$$

and NO_2 photolysis. In addition, primary NO oxydation can also take place with oxidants other than O_3 (R denoting an organic compound):

$$NO + HO_2 \rightarrow NO_2 + OH \quad (11.1.5)$$

$$NO + RO_2 \rightarrow NO_2 + RO \quad (11.1.6)$$

$$NO + ClO \rightarrow NO_2 + Cl \quad (11.1.7)$$

In the stratosphere, the only relevant organic peroxy radical RO is CH_3O_2 in turn formed in the oxidation of methane. With the onset of the night, and the absence of direct light in the stratosphere, NO_2 builds up. Reaction with ozone generates NO_3, an important nighttime oxydizing species:

$$NO_2 + O_3 \rightarrow NO_3 + O_2 \quad (11.1.8)$$

Which in turn suffers rapid photolysis at sunrise:

$$NO_3 + h\nu \rightarrow NO_2 + O \ (\lambda <= 630 \text{ nm}) \quad (11.1.9a)$$

$$\rightarrow NO + O_2 \ (\lambda <= 590 \text{ nm}) \quad (11.1.9b)$$

NO_3 in turn reacts with NO_2 to form the reservoir species N_2O_5

$$NO_3 + NO_2 \rightarrow N_2O_5 \quad (11.1.10)$$

N_2O_5 is destroyed through collisional decomposition

$$N_2O_5 + M \rightarrow NO_3 + NO_2 \quad (11.1.11)$$

And also by photolysis during the day

$$N_2O_5 + h\nu \rightarrow NO_3 + NO_2 \ (\lambda <= 1252\text{nm}) \quad (11.1.12)$$

The species NO_2, NO_3 and N_2O_5 form a chemical equilibrium. During the night, a major part (e.g. 80%, this fraction being highly dependent on temperature) of the NO_3 produced can get "stored" in N_2O_5. When NO_3 is rapidly photolysed and removed as N_2O_5 educt, N_2O_5 "reacts" by a net increase in decomposition releasing NO_3.
But it is largely the NO_2 photolysis responsible for the diurnal variation of NO_2, notable for the U- or tub-shape of e.g. ground based SCD (see [*Otten 1997*] as well as section 9.2).
The part NO_2 plays in the stratospheric ozone chemistry is twofold. NO_2
Contributes to the ozone depletion in an own cycle ("NOx cycle"), on the other hand, it "traps" reactive species in reservoir species.

$$NO_2 + OH + M \rightarrow HNO_3 \quad (11.1.13)$$

$$NO_2 + ClO + M \rightarrow ClONO_2 \quad (11.1.14)$$

$$NO_2 + BrO + M \rightarrow BrONO_2 \quad (11.1.15)$$

HNO_3 is the dominat Noy species in winter. Release of the oxides can take place by photolysis. But a more important process is the following:
During winter, circumpolar air currents generate the "polar vortex" which encloses the circumpolar stratospheric air masses. Within, temperatures drop to minimum temperatures of around 200 K in the northern and below 190 K in the southern hemisphere, respectively. These values promote the generation of particle clouds, "polar stratospheric clouds", consisting mainly of water, H_2SO_4 and HNO_3 ice particles. At their surfaces, heterogeneous reactions "free" the halogens, which are released as halogen oxides BrO and ClO into the gas phase. The following reactions convert the halogens (X) into radicals[2]:

$$XO + O \rightarrow X^* + O_2 \quad (11.1.16)$$

These radicals attac ozone by:

$$X^* + O_3 \rightarrow XO^* + O_2 \quad (11.1.17)$$

The radicals may react with atomic oxygen to become atomic radicals again:

$$XO^* + O \rightarrow X^* + O_2 \quad (11.1.18)$$

This catalytic reaction is what leads to the wintertime ozone depletion until, in spring, the halogens can be trapped in the reservoir species again. The cycles are described in detail in e.g. [*Solomon 1998*]. To conclude this section, Figure 11.1.1 gives an overview on the losses inflicted on ozone by the attacking species.

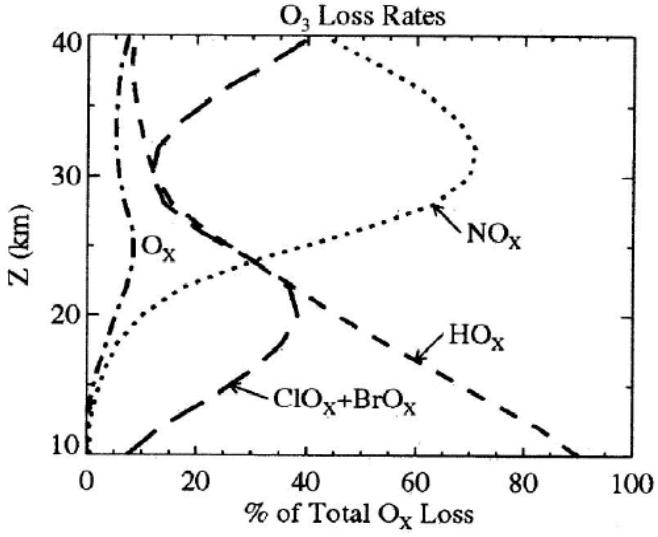

Figure 11.1.1 ozone depletion during Antarctic winter due to catalytic ozone destruction; the curves show the importance of the different cycles with altitude.

[2] a molecule with an uncoupled free outer electron; highly reactive;

11.2 Instrument

One of the balloon borne instruments used to probe the stratosphere is installed on board the LPMA gondola. The LPMA/DOAS balloon gondola is based on a gondola developed for astronomical observations by the Observatoire de Genµeve and was further optimized for atmospheric measurements by Camy-Peyret et al. [1995]. The gondola can be stabilized in azimuthal direction with an accuracy of about 0.5 - 0.1° or better using a gyroscope aligning the gondola to the magnetic field of the earth. The gondola also can be rotated with respect to the much larger balloon.

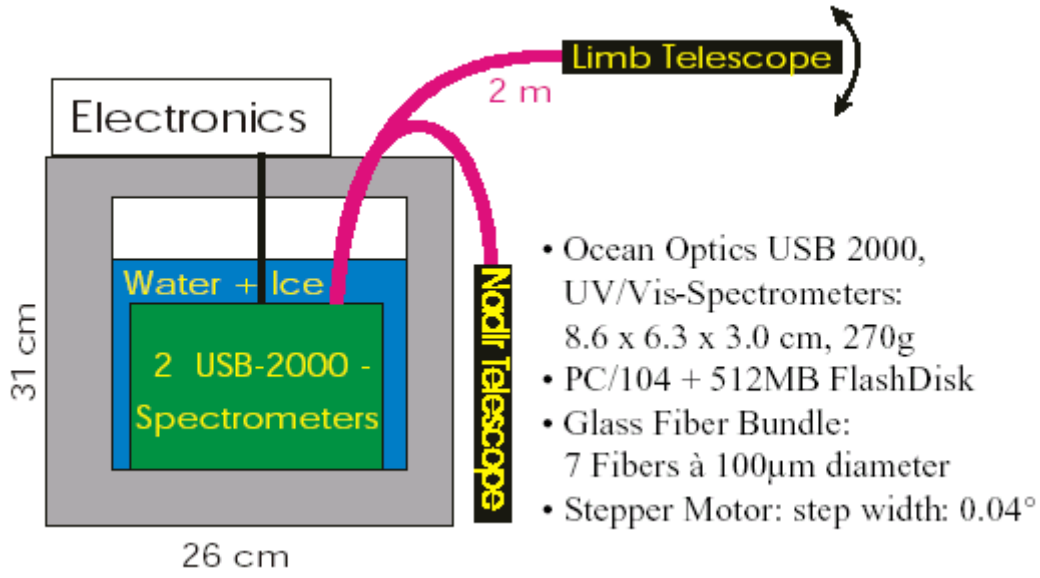

Figure 11.2.1 USB spectrograph instrument installed on board of LPMA balloon gondola [Weidner et al. 2003]

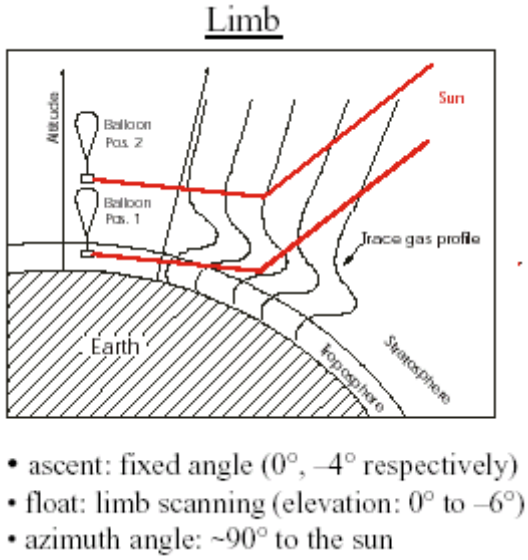

Figure 11.2.2 Scetch of limb viewing geometry (taken from [Weidner et al., 2003])

The DOAS setup aboard is “Mini-DOAS” using a miniature Ocean Optics USB 2000 spectrograph, operating within range 327-527 nm, resolution 0.8 nm. For details see [*Weidner et al., 2003a,b*].
The study of this section is meant as sensitivity study for this kind of instrument.

11.3 Box AMF

11.3.1 Model scenario

The Box AMF were calculated for a balloon-mounted instrument operating at different altitudes and employing different viewing geometries. The SZA is 70°; the wavelength is 435 nm, which is used for NO_2 evaluation, the albedo set to 30%. The absorption of the trace gases NO_2 and ozone were taken into account[3]. The used vertical profiles are shown in Figure 11.3.1. A pure Rayleigh U.S. Standard Atmosphere with TOA at 70 km was used with a vertical discretization of 1 km. Positive elevations denote lines of sight "looking up", negatives looking down. Azimutal angles are stated with respect to the direction of the sun. For the definitions of these geometrical parameters also refer to chapter 6.
In the Box AMF plots, the abscissa denotes the centre altitude of the respective layer, the ordinate the Box AMF for this layer.

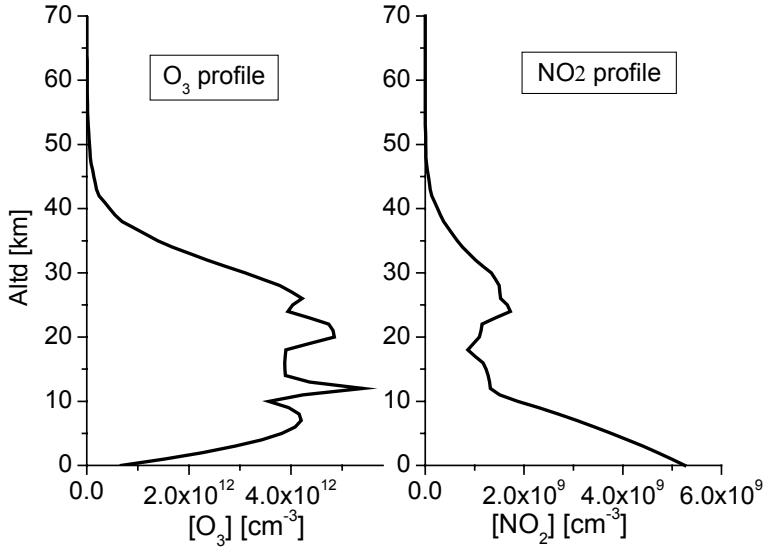

Figure 11.3.1 Ozone and nitrogen dioxyde vertical profile used for the modelling of Box AMF for balloon geometry

11.3.2 Error estimate

The Box AMF errors were calculated like the other parameter's errors as outlined above as intensity weighted standard deviation.
The error therefore decreases with increasing number of valid paths. The error's absolute value depends on the shape and extension of the layers or grid cells the trace gas is contained within, their distances from the instrument, and the influence of multiple scattering and albedo effects. For the investigation presented a set of BOX AMF was calculated using different path numbers. The geometrical parameters were: floating altitude 10 km, elevation –4°, azimuth 90°, half aperture (circular) 0.5°. Fig. 11.3.2 shows the result. We find that the error is

- smallest for the highest levels, e.g. above 50 km
- largest for ground level,
- between these extremes for the altitude of maximum Box AMF, here 10-11 km, and
- dropping gradually for the altitudes above.

[3] Using the input profiles for the zenith sky exercise in chapter 7

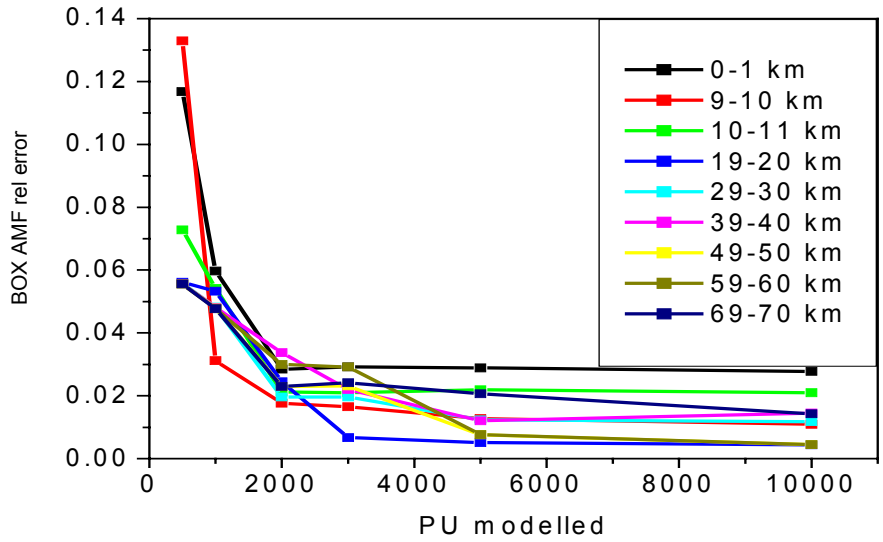

Figure 11.3.2 relative error in Box AMF with increasing number of valid photon paths

All errors drop below 5% for photon numbers of 2000. Based upon the finding, the number of 2000 PU was used for the calculations to follow. For an explanation of the errors of different altitude refer to Figure 11.3.3. It displays the balloon sonde as red circle, the geometrical line of sight as black arrow and a set of possible light paths as red arrows.
The highest atmosphere layers house very few scatterings altering the light path and thus the Box AMF. Nearly all light passes these layers on a straight path. It of course depends on SZA and wavelength above which level scattering becomes unimportant.
The geometrical line of sight does touch the ground for 10 km floating altitude; but there scattering contributes a major part to the recorded light. Since scattering occurs in a variety of angles, multiple scattering increases the variability of light paths, which leads to a larger relative error of AMF and Box AMF.
The levels between 9 and 11 km where the floating altitude is within are a mixture of well defined geometrical light path along the geometrical line of sight and a variety of contributions of scattered light from above and, to a larger extent, from below. This leads to a relative error which is of size between the magnitude of the highest and lowest errors.

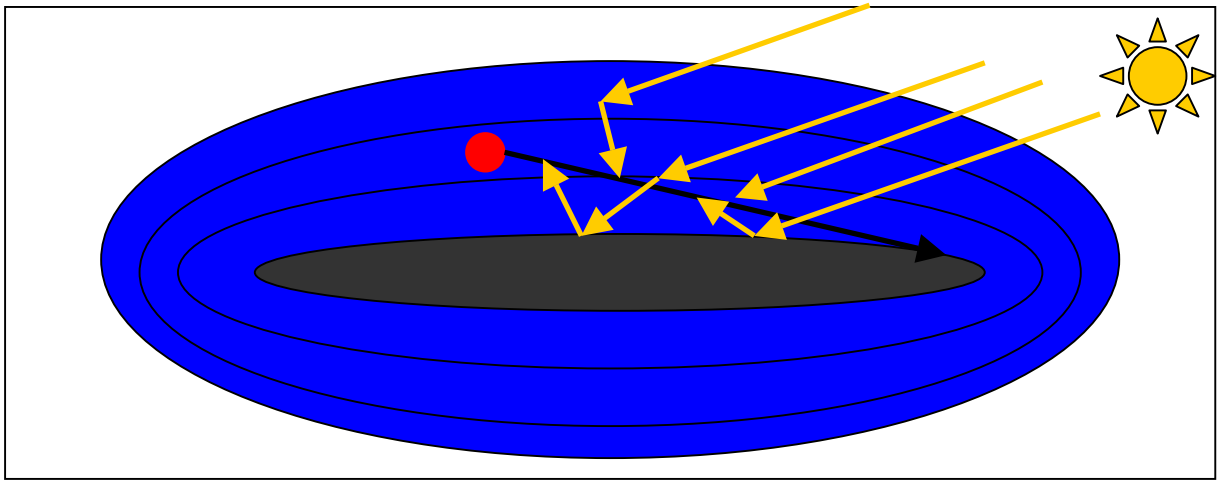

Figure 11.3.3 Explanation for the behaviour of the Box AMF error; it is lowest for the high stratosphere, where few scattering perturbs the straight photon paths, and highest for the ground level where only scattered photons pass on various paths.

11.3.3 Sensitivity to floating altitude

For the investigation of the Box AMF with different floating altitudes the following geometrical parameters were used as fixed: SZA = 70°, elevation = -4°, azimuth = 90°, half aperture (circ.) = 0.5°.
Figure 11.3.4 shows the results for several altitudes between 10 and 40 km.

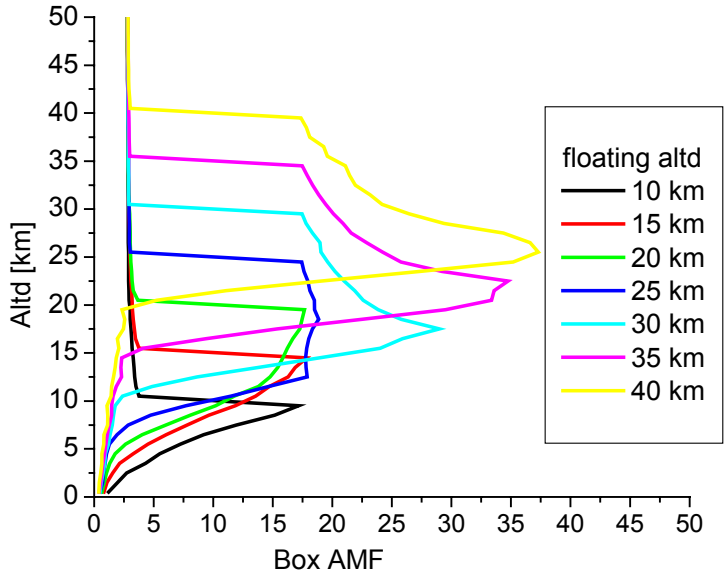

Figure 11.3.4 Box AMF for different floating altitudes, line of sight fixed. With increasing altitude the line of sight no longer touches the ground; a level with Box AMF higher than that of the floating altitude begins to develop.

The black line denotes the Box AMF for 10 km floating altitude. The layer housing it is passed by most of the light on a slant long path. This leads to a large Box AMF. Below floating altitude, the geometrical LOS passes through, but the Box AMF gets, with decreasing altitude and increasing scattering centre density, more and more governed by scattering. This means that the average light path differs from the slant one, and that, from the lowest layers, only small contributions are received due to the attenuation along two passages. The noise also increases, as can be seen at the lowest part of the black curve.
With increasing floating altitude, though, the curve shape below floating altitude alters. Below floating altitude, an increase in Box AMF is observed. For this see Figure 11.3.5.
Due to the lower air density, the photons can travel a long way along the geometrical line of sight which reaches far into the atmosphere. For pure geometrical reasons, as indicated in the picture, the intersections of the LOS with layers below floating altitude get larger, reaching a maximum at the geometrical tangent altitude (the minimum altitude of the LOS). The Box AMF get even larger due to a second pass behind the tangent point.
Below the tangent altitude, only scattering (by air molecules and by the ground) govern the radiative transfer; the lower the altitude, the higher the attenuation of light reaching the ground and travelling up to the LOS. The AMF decreases in a similar way as for 10 km floating altitude. Above floating altitude, for all altitudes shown, the SZA governs the Box AMF which could be calculated, in good approximation, with geometry alone.

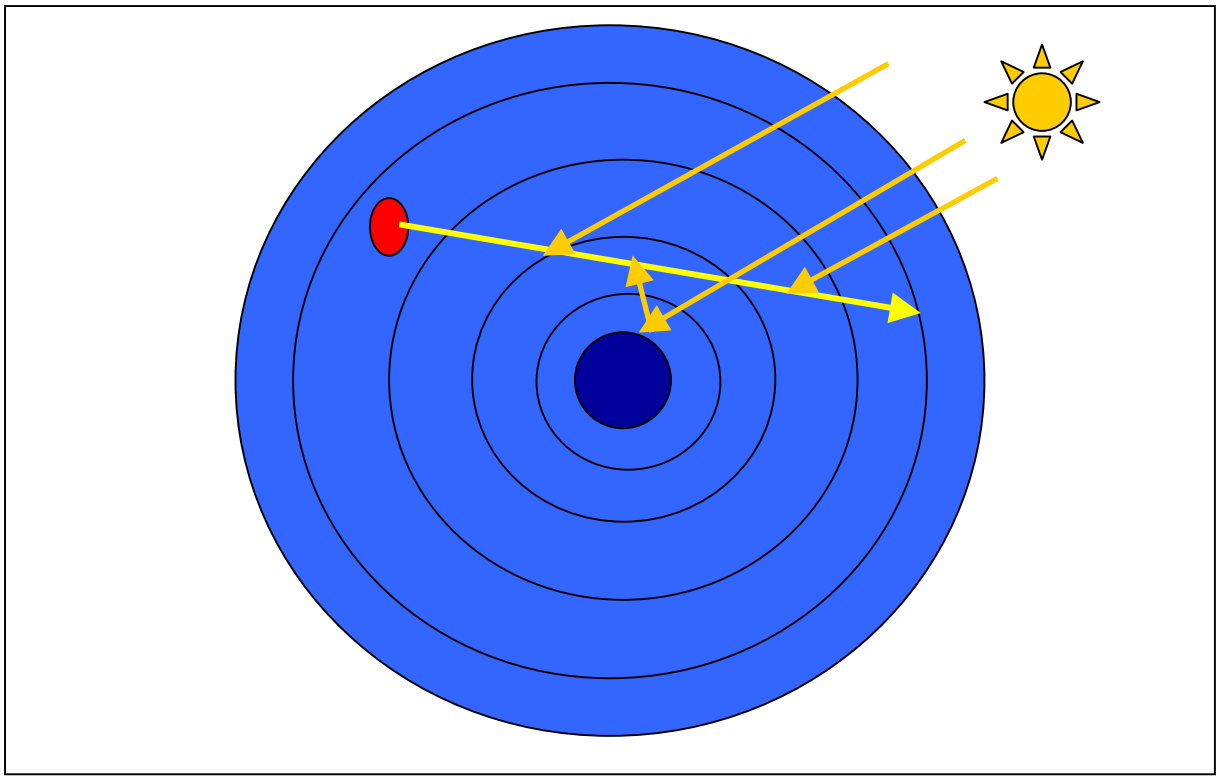

Figure 11.3.5 The development of the Box AMF with high floating altitudes. The geometrical LOS no longer touches the ground; any Box AMF > 0 arise from scattering in the lower atmosphere. At floating altitude, the LOS can penetrate far into the thin atmosphere; the geometrical intersections with the layers below increase to a maximum.

It is instructive too look at some scattering parameters derived by the program, especially on the number of Rayleigh scatterings (NRS), the last scattering distance LSD as well as the last scattering altitude LSA. See Figure 11.3.6.

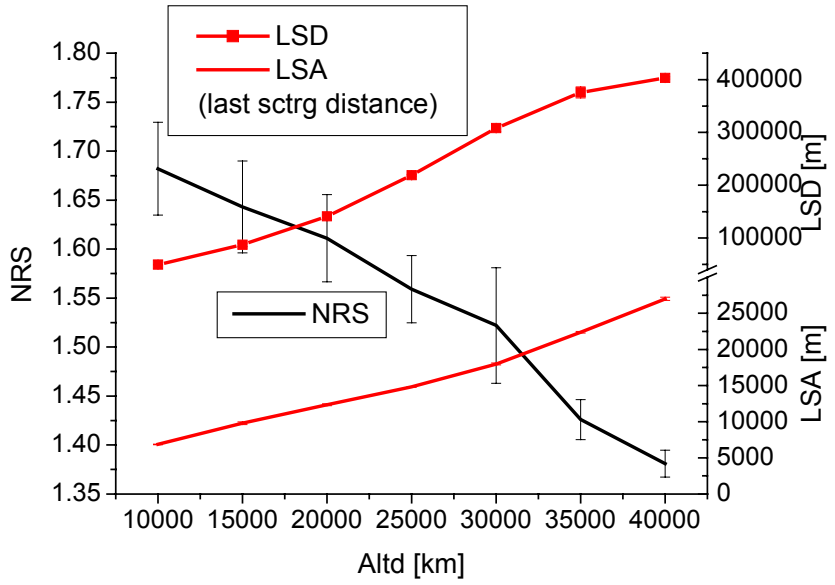

Figure 11.3.6 LSD, LSA (Last Scattering Distance and Altitude) and NRS for different floating altitudes (abscissa)

As expected from above considerations, the LSD increases from 100 to 400 km when raising the floating altitude from 10 to 40 km. This leads to high Box AMFs as shown in Fig. 11.3.5.
The location of the last scattering event is the place where the straight line of sight is terminated. It denotes the effective tangent altitude. For low wavelengths, this can well be different from the geometrically derived tangent altitude.
For low floating altitudes, where the LOS touches the ground, we find the LSA to be larger than zero, at about 5 km, indicating that below this altitude the Box AMF is entirely governed by multiple scattered light.
For high floating altitudes, where the increase in Box AMF below floating altitude develops, we find that the LSA complies well with the altitudes of the highest Box AMF.

11.3.4 Sensitivity to elevation

For high floating altitudes, the geometrical LOS plays a significant role for the derivation of Box AMF for altitudes at and below floating altitude. For this study the SZA has been fixed to 70°, the azimuth to 90°, the half aperture angle to 0.5°, while the elevation has been varied for two floating altitudes. Figure 11.3.7 shows the results. We see that the altitude of highest Box AMF raises near the floating altitude when elevation is increased from negative values to zero. At elevation 0° the two heights are identical (see Fig. 11.3.7).

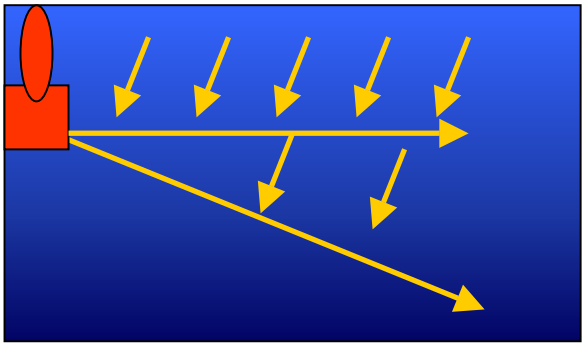

Figure 11.3.7 illustration to the behaviour of Box AMF with elevation 0°. The altitude of highest Box AMF is at or above floating altitude.

For the altitude of maximum Box AMF the Box AMF changes by more than 100 %.
With elevations > 0° we have a geometrically induced increase in Box AMF above floating altitude. Gradually it decreases to the SZA derived value for the high stratosphere. These principal findings are valid for both floating altitudes modelled.
All this highlights the necessity for a precise determination of the viewing geometry during a balloon flight. Assumption of a wrong elevation in retrieval can lead to large errors in the resulting profile.
Especially when the LOS points sideward with respect to the floating direction of the balloon, a tilt of the gondola induced by the driving wind combined with small rotating oscillations may be the cause for a large uncertainty in elevation during a given measurement.
On the other hand, if the elevation is well known, it can be chosen to specifically manipulate the sensitivity for altitudes where the trace gas in question is expected.
This issue is important also for satellite limb geometry.

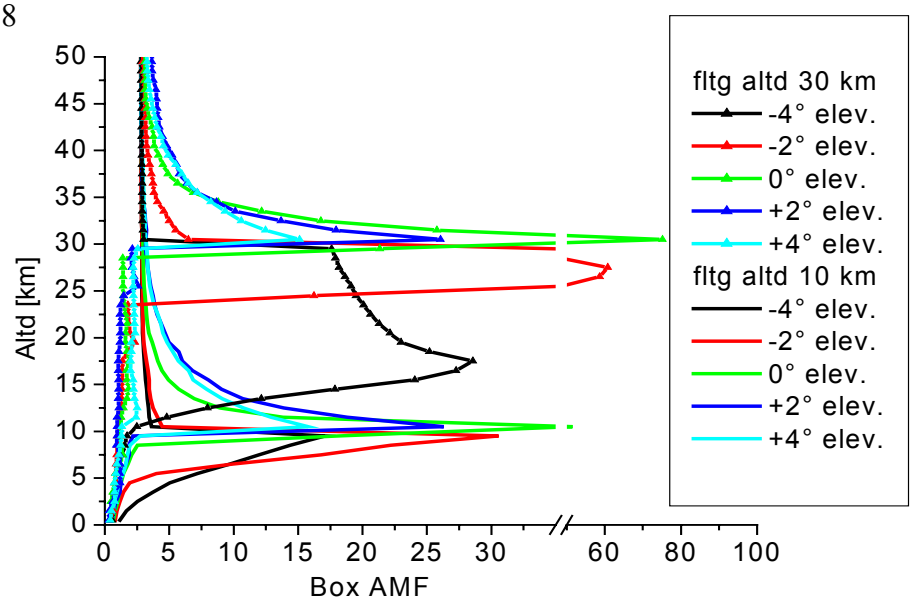

Figure 11.3.8 Box AMF for varying elevations and two floating altitudes; the Box AMF above and below floating altitudes are highly sensitive to variations in this parameter.

11.3.5 Sensitivity to azimuth

The variation of the azimuth only causes minor variation as compared to the elevation. But small effects are notable. For this study the following parameters were fixed: SZA = 70°, elevation -4°, half aperture angle 0.5°. Then the azimuth was varied for again two floating altitudes. Figure 11.3.9 shows the results. We find that above floating altitude, the Box AMF are highest for 180° azimuth. The light, coming in from the sun, must cover a longer distance, past the balloon, before meeting with the LOS, than it is the case for azimuth = 0°. The maximum Box AMF is slightly higher for azimuth 90° than for the other values modeled.

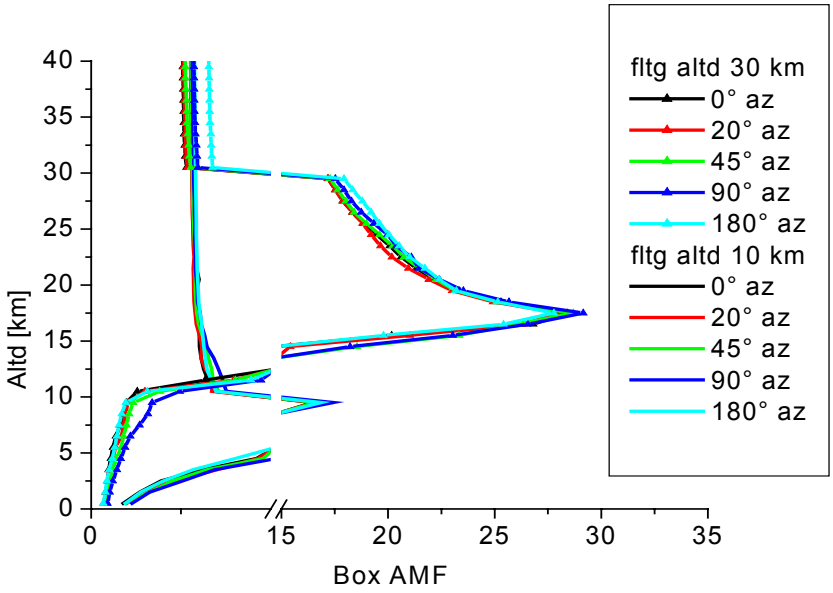

Figure 11.3.9 azimuth-dependency of the Box AMF for two floating altitudes

11.3.6 Sensitivity to aperture angle

As may be concluded from the high sensitivity of the Box AMF to elevation, the aperture angle has a potentially large effect as well. Increase in aperture angle includes light paths which are tilted by a larger angle to the geometrical LOS; this equals the averaging over measurements with smaller aperture angle but different elevations.
The other parameters (SZA = 70°, elevation = -4°, azimuth = 90°, floating altitude 10 km) have been fixed for this study. Figure 11.3.10 shows the results in the usual format.

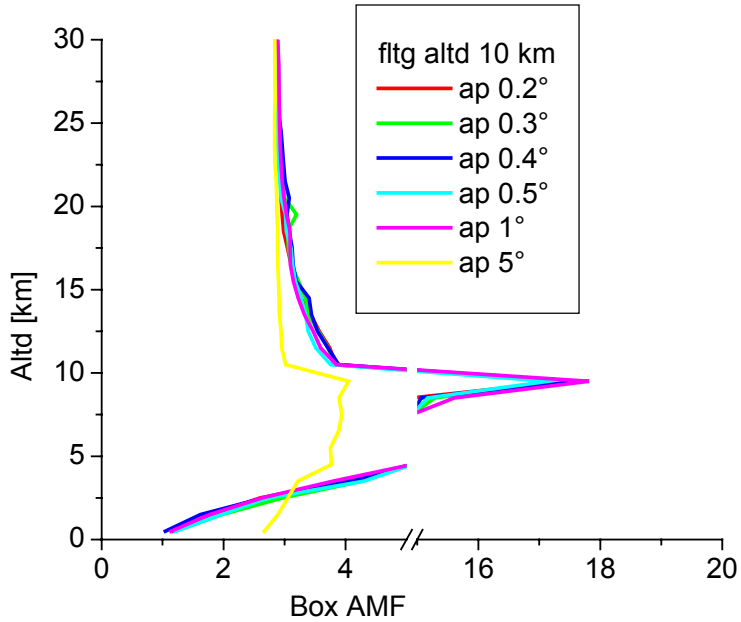

Figure 11.3.10 Aperture dependence of Box AMF for balloon geometry; in the given atmosphere discretization, only half aperture angles > 1° have a significant effect.

We find that below 1°, the aperture angle has very little effect; the largest is to be observed for the altitude of maximum Box AMF, since the cone into which the measurement light enters is narrower with smaller aperture angle. See also Fig. 11.3.11.

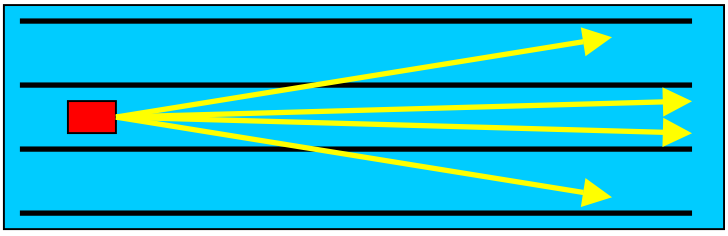

Figure 11.3.11 With smaller aperture angle, a larger fraction of the recorded light has travelled along paths close to the LOS which increases the Box AMF.

But for aperture angles >2° the effect is apparent, significantls smearing out the Box AMF for the floating and the adjacent altitudes.

11.3.7 Influence of cloud covers

Cloud covers, and lack of knowledge about their parameters, presents a major uncertainty in profile retrieval. The primary effect is a shielding of trace gas abundances located below them. This study varies the cloud cover to assess the effect on the Box AMF. For again

floating altitudes 10 km and 30 km the geometry parameters were fixed to elevation = -4°, azimuth = 90° , half aperture angle = 0.5°, SZA = 70°. Figure 11.3.12 shows the outcome.
The cloud cover parameters were: altitude 5 km, albedo 80%, transmission zero, coverage varied between 0 and 1.

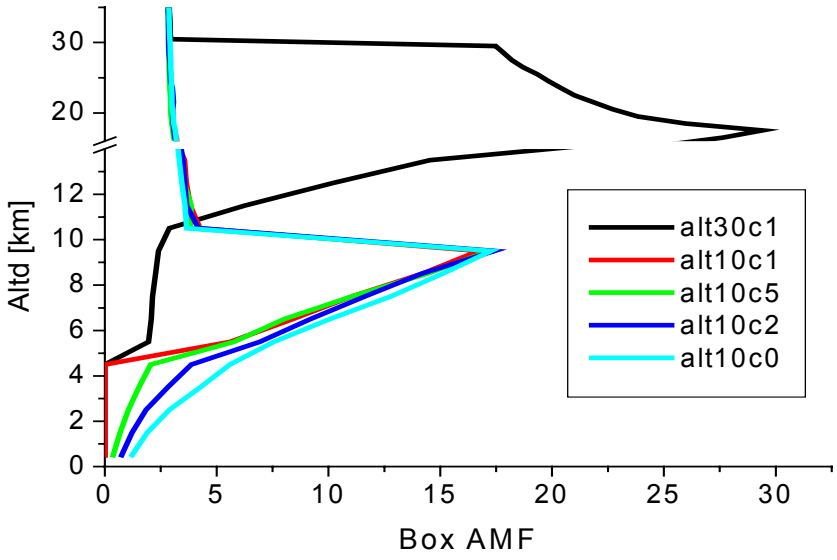

Figure 11.3.12 Box AMF variations due to cloud cover. "c1" denotes cloud coverage 1, "c5", "c2" and "c0" denote coverages 50%, 20% and 0%. Clearly the shielding of the altitudes below 5 km can be seen.

As clearly can be seen, the cloud cover shields the altitudes below it, and the trace gases that may be present there. This is true for both floating altitudes.
It is just important to have parameters in the measurement which react sensitively to cloud covers; they can be used to conclude on the cloud cover. For satellite geometry research has already yielded successes in usage of the O_4 absorbtion [e.g. *Wenig 2001*]
As second part of this cloud study we consider two parameters generated by the model, the O_4-AMF and the measurement radiance signal (Figure 11.3.13).

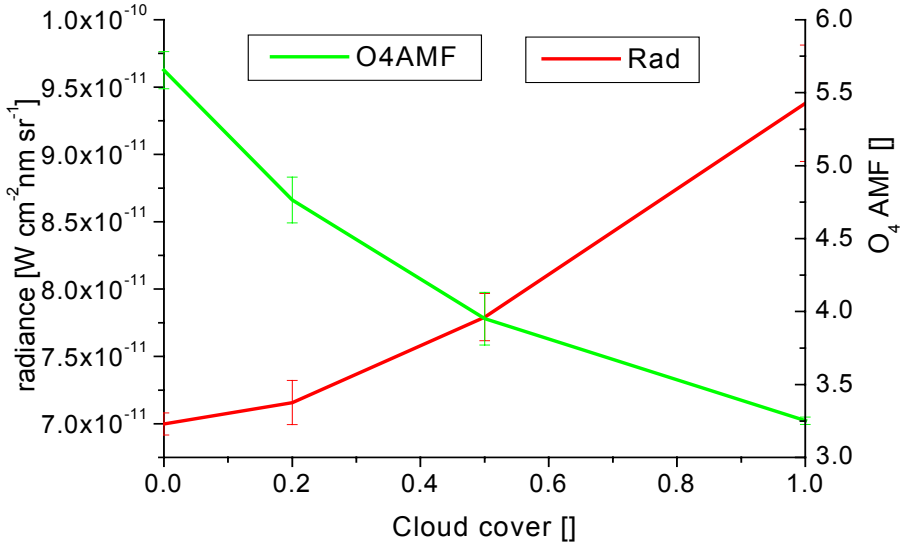

Figure 11.3.13 O_4 and radiances for varying cloud cover, floating altitude 10 km

With increasing cloud cover, the O_4 in the lower troposphere is more and more shielded, resulting in a smaller AMF. At the same time, the radiance increases due to the higher cloud albedo.
The most altitude-specific information is derived with narrow field of view. This implies two things: First, the location of the trace gas must be roughly known to adjust the viewing geometry and, if possible, the operation altitude. Second, precise pointing, and stabilizing, is as least as important for scattered light DOAS as it is for direct light geometry.
TRACY provides a tool to test the sensitivity to line of sight variations for instruments and wavelengths.
As already stated, the findings of this chapter can as well be used for satellite geometry, e.g. in the case of the limb mode of SCIAMACHY on ENVISAT.

12. Application to Satellite DOAS

The application most "global" in the sense of geographical coverage is the operation of DOAS devices aboard space borne platforms. The upcoming of sensors such as GOME and SCIAMACHY provide NRT SCD on a broad variety of traces gases.

12.1 Instrument

SCIAMACHY (for Scanning Imaging Absorption Spectrometer for Atmospheric CHartographY) is a spectrometer for measurement scattered sunlight in several channels of the UV, VIS and IR (240 nm - 2380 nm) at a spectral resolution of between 0.2 nm and 1.5 nm. These soundings measurements yield the amounts and global distributions of O_3, BrO, OClO, ClO, SO_2, H_2CO, NO_2, CO, CO_2, CH_4, H_2O, N_2O, as well pressure, temperature, and aerosol data. A special feature of SCIAMACHY is the combined limb-nadir measurement mode, which enables the tropospheric column amounts of several trace gases to be determined. Figure 12.1 shows the instrument.

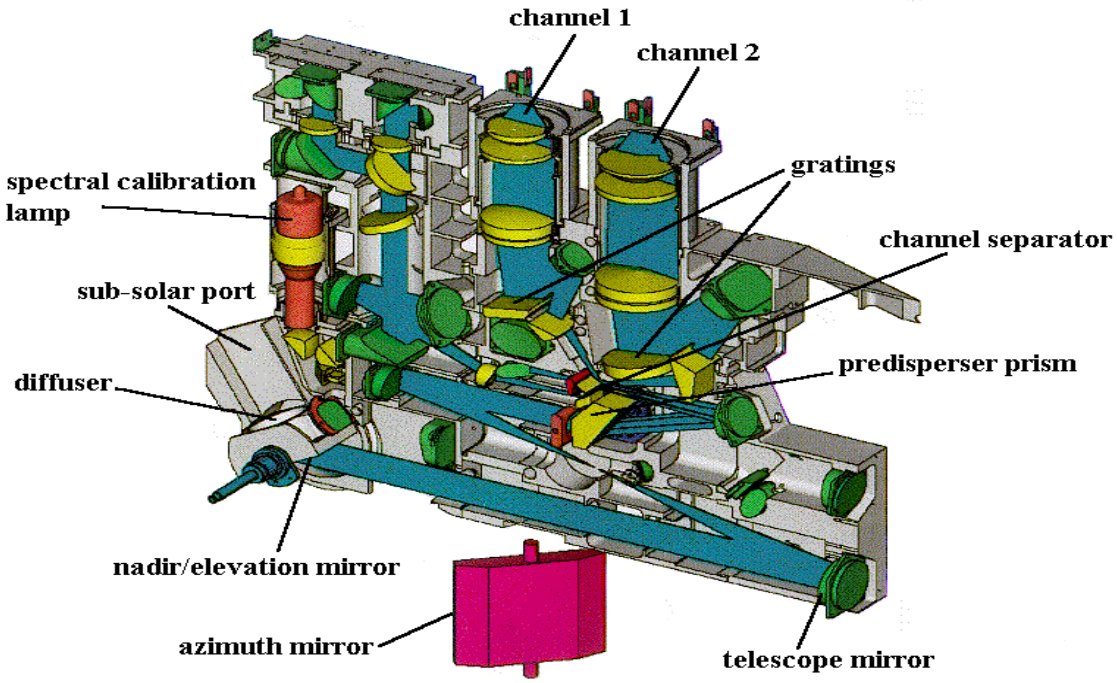

Figure 12.1. Schematic view of SCIAMACHY ob board of ENVISAT, taken from [Homepage IUP Bremen[1]]

[1] http://www.iup.physik.uni-bremen.de/

12.2 Cloud coverage and retrieval efforts

A major issue is cloud coverage which shields absorbers near ground, such as boundary layer NO_2 [*Leue et al. 2001, Velders et al., 2001*].
The first attempt to conclude on clouds using satellite data was to take advantage of the white "colour" of the clouds, as a contrast to the blue of the ocean or the green and brown soil. This works well over e.g. urban areas; but when trying to investigate e.g. halogen compounds in the arctic, the problem of the ice surfaces underneath being white as well hampers this approach (Figure 12.2).

Figure 12.2 The distinction between (fractional) clouds and ice surfaces can be performed using O_4 absorption. (here: clouds over glaciers on one of the South Shetland Islands off Antarctica, picture taken off R/V "Polarstern" on ANT XIX cruise 2001/2002)

To retrieve cloud data for measurement correction, a different approach is to use O_4 [*Kuze and Chance 1994*]. Being located in the lower atmosphere and with a known profile shape, it is shielded by clouds in a similar way as are the trace gases to probe. The strength of the O_4 absorption, which can be measured with DOAS, is then related to an AMF, which in turn can be modelled, as a function of cloud parameters, with an RTM.

The most novel and sophisticated effort in this direction uses the O_4 AMF [*Grzegorski 2003*].

12.3 modelled O_4 AMF

As all retrieval approaches, be it of trace gases or clouds shielding them, using light paths, this one as well depends on RTM. Figure 12.3.1 exemplary shows O_4 AMFs modelled by TRACY for satellite geometry for following parameters:

- Geometry satellite nadir, half ap. angle 0.1°

- cloud cover 40%
- ground albedo 2%
- cloud albedo 80% (transmission zero)
- wavelength 630 nm

The parameters SZA and cloud altitude were varied in the way as stated in the Figure.
As expected, the AMF decreases with rising cloud altitude and increases with SZA; while the fomer effect is readily explained by shielding, the latter must be attributed to path elongation at low sun; since the light at 630 nm can penetrate far into the atmosphere, it does probe it until the cloud cover is hit, and thus traverses the O_4 abundance above the cloud on slant paths.

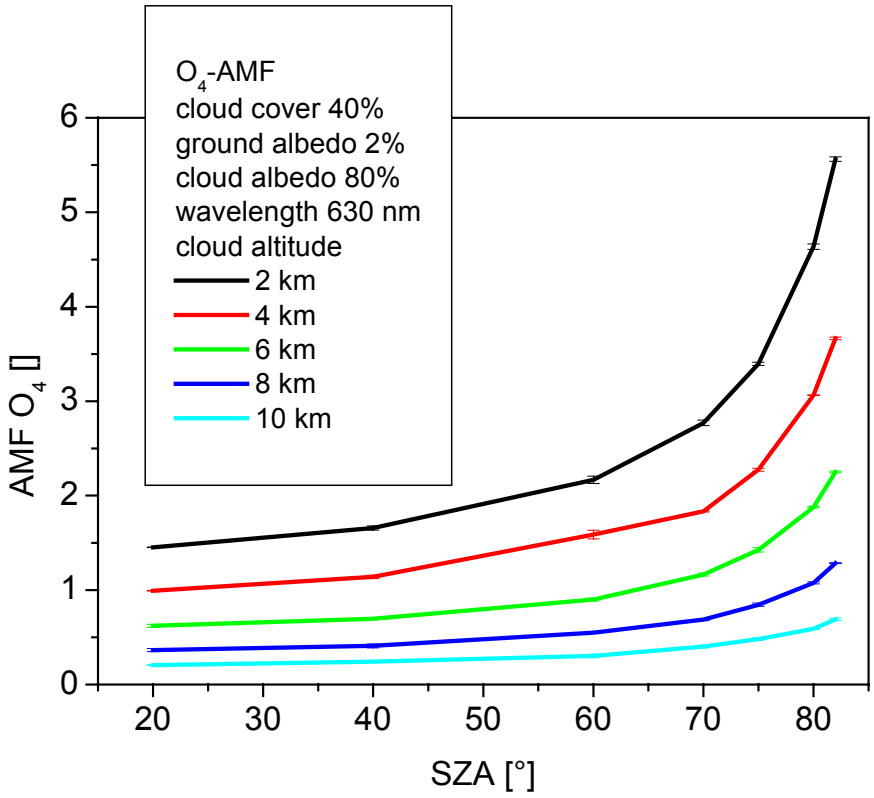

Figure 12.3.1 modelled O_4 AMF for satellite geometry and varying SZA and cloud cover altitudes; the behaviour can be explained straight in straight forward ways.

The situation can be expected to be more complicated when taking e.g. the following features into account:

1. multiple (fractional) cloud layers,
2. of varying individual thickness
3. multiple scattering within cloud, resulting path elongation and in turn resulting additional O_4 absorption compensating for the shielding effect
4. modulation of the multiple scattering by varying droplet size distributions and number densities as well as refractive indices.
5. Effect on polarization
6. horizontal photon transport between clouds by either reflection off vertical cloud patch "walls" or by leakage out of those walls
7. transmission of photons through 100% coverage clouds and thus increase in O_4 absorption

12.4 Future work on TRACY cloud treatment

In spite of the fact that there will be a "future work" section in the terminal chapter, this section will specifically treat the improvements planned for cloud treatment in TRACY.
Based upon the 3D voxel grid, every voxel (or set of voxels adjacent in one or more axes) may be filled by number densities of droplets of parametrization described for the aerosols (see sections on e.g. *AlterPhoton* and *ForcePhoton*) in Appendix A.
But this effort can be expected to be very time consuming due to the large number of scatter events to be calculated. A more promising, i.e. cost effective approach is the enhancement of the layer approach used in the above brief investigation.
Be the above features addressed in the listed order if not already implemented.

1. In the same way as one layer is parametrized so far, more layers can be implemented straight forward based upon an appropriate array object of same layout as the scatterer objects.
2. This parameter set can be enhanced by the thickness. In case of transmission, the photon is placed at the point the previous trajectory (or any other, e.g. one chosen by random numbers itself) exits the opposite cloud surface
3. Extensive modelling using voxels filled with droplets of representatively chosen parameters could generate a lookup table containing effective "within-cloud" paths for a variety of wavelengths and photon incident angles. Also established and more elaborate cloud models could be used for this, e.g. the GESIMA model [*e.g. Eppel et al. 1995*] Taken from this lookup tables, the path elongations can be added to the photon *Path* objects, and the calculation of the resulting absorption is done straight forward in the *SCDCalculator*.
4. and 5.: The cloud objects can, in case of fractional cover, be attributed a virtual horizontal surface; i.e. if a photon enters an altitude layer occupied by (one of) cloud layer(s), and the first random number decides that the photon hits the cloud layer, the incident angle defines the projections of the horizontal and vertical "walls" presented the incoming photon, and thus the probabilities of a hit of either the one or the other, between which another random number can decide. The procedure after hitting the cloud (either reflection, transmission or absorption) then can be carried out in a way analoguous to the treatment for horizontal cloud surfaces only.
5. The polarization by Mie scattering off cloud droplets is as dependent on e.g. size parameter as is the phase function. The treatment of polarization has been developed and implemented for Rayleigh scattering; in the same way, it can be reproduced and used for (known) droplets.

The O_4 measurements provide a promising tool for the sounding of these cloud parameters.

13. A Forward Monte Carlo radiative transfer implementation

The Backward Monte Carlo technique is efficient in the sense to optimize the ratio of successful paths to modelled ("launched") photons.
The drawbacks however have been mentioned:
E.g. in zenith sky geometry and in the UV, the emitted photons are scattered near the detector rather than higher in the stratosphere, which reduces the number of photons taking paths typical for this geometry, i.e. scattered first in the stratosphere and into the detector. Though this in theory is compnesated by applying different weighs for photons scatterered deep, but the problem of low signal-to-noise ratio remains.
The second drawback is related to the refraction. The approach of lookup tables is promising, but time consuming, since strictly for each model atmosphere a new table will have to be calculated.
A way to solve these problems is to use Forward Monte Carlo modelling, FMC. When modelling photons incoming from the sun like in reality, the statistical distribution of first scattering locations is reproduced. The refraction at each voxel transition can be calculated for the entire path accurately.
Since strict FMC is not applicable for reasons stated above, though, an approximation or forcing must be applied here as well. A method is to count the photons passing a given location, i.e. "measuring" the irradiance at this location, and then analytically calculate the fraction of this irradiance scattered in the direction of the detector and the attenuation on their way to it.

13.1. Simple two stage Forward model and application to a solar eclipse

On August 11th 1999, a total solar eclipse passed over southern Germany. During this eclipse, spectroscopic measurements were performed from a place within the zone of totality. This eclipse offered the chance to investigate the possible formation of the nitrate radical, which is photolytically destroyed rapidly by sunlight, but forms during night, i.e. in the darkness.
To compare the measured NO_3 SCD series with a modelled one, a simple two-stage RT estimate model was devised and successfully tested. The calibration parameters were the relative measurement radiance integrated over the spectral window, and a parameter related to the Solar Centre-To-Limb Darkening effect, CLD.
The chemistry of NO_3 will be addressed in chapter 14. The next sections of this chapter will focus on the development of the two stage forward model. It is based upon the algorithm of AMFHD, but uses different input for the radiances at the scattering point.

13.1.1 Instrument

The measurement was performed on August 11th, 1999. The instrument was installed on the roof of the main building of the Institute for Meteorology and Climate Research (IMK) of the

Karlsuhe Research Center (FZK) 20 km north of the major metropole of Karlsruhe. To the south and east, motorway pass by near the site; the sorroundings, though, are rural with forests and agricultural areas. The roof's altitude was 80 meters, thus well above the surrounding treetops.
The eclipse crossed southern Europe on an east-south-easterly course; the core shadow had a width of 109 km, its velocity vecl was 851.56 m/s. At the site, the phenomenon commenced at 9:12:12 UT with the "First Contact" between the sun's and moon's apparent outer rims. From 10:31:39 UT („Second Contact") till 10:33:47 UT („Third Contact") the site was within the core shadow; at 11:55:21 UT the eclipse did end with the „Fourth Contact".
In the following, time will be given as seconds or minutes after First Contact.
The sky was covered with a broken cloud cover. This situation is very complicate to implement in models, since light can be reflected off the cloud tops as well as be transported sidewards within and between the cloud patches. After the Third Contact, the cloud cover grew denser, the gaps closed. 20 minutes after the Fourth Contact rain set in, terminating the measurement phase. According to balloon sensor probings, the cloud cover was located at 750 m. This altitude thus marks the mixing layers upper limit, which also sets the upper limit for the vertical range nitrate radical could be formed in on this day. [*Bernhard Vogel, pers. comm.*].
The instrument was the same as the one described in chapter 9.2. The grating was set to cover the wavelength range between 646 and 676 nm at a spectral resolution of 0.25 nm (full width at half maximum).
After readout and conversion to a digital signal each column of 256 pixels on the CCD chip of the instrument is co-added to form a spectral channel. The digital 'count number' in each channel is thus proportional to the integrated light intensity received during each exposure time interval. Depending on the available light intensities, integration times between 100 and 400 s were used. As usual, the wavelength calibration and the instrumental function were derived by taking spectra of Neon emission lines. Spectra recorded in total darkness were used for the detector's electronic offset and dark current correction, which were found to be stable with time even over several days.
The telescopes were directed along and against the movement axis of the shadow, with an elevation of 2°. The reason for this was as follows.
The formation of nitrate radical during a solar eclipse in general can be expected to be strongest along the track of the central spot of the core shadow, where the total darkness prevails longest.
Obviously the maximum of the nitrate radical formation at a given point along the movement line cannot be expected to occur at the time between the Second and Third Contacts, but at the time of the Third, henceforth called t_{max}, with the phase of maximum darkness preceding. This point of the maximum formation, x_{max}, must be expected to follow the core shadow with the phenomenon's velocity v_{ecl} along the eclipse's track.
Immediately behind the x_{max} at a given time, that is behind the aft rim of the core shadow, which marks the Third Contact, the light from the solar rim impinging on the track quickly destroys the formed NO_3. Further behind, the light intensity grows since in this place, a greater fraction of the solar disk is visible. The zone of significant nitrate radical formation ends.
From these considerations it becomes clear that the highest NO_3 concentration accumulates along the direction of the solar eclipse. The selected viewing geometries of our instrument thus ensures the maximum signal to noise ratio. Since the light intensities tend to decrease during a solar eclipse, all telescopes were directed parallel to each other, not with different elevations. This was done in order to expose all CCD chip lines available to the measurement light of one direction to reduce the noise by coadding them.

With the telescopes trained as described, there thus must be a point of time when the zone of c_{max}, following the shadow center, is located immediately in front of the telescopes, with very little light impinging on it, but when the area of higher light intensity following x_{max} provides light to be scattered through c_{max} over a short distance into our instrument. We did not know the vertical distribution of the nitrate radical formed, but could reasonably expect it to form in the boundary layer, where the educt concentrations are greates. In order to have our line of sight cross the vertical layer of greatest formation, we applied an elevation of 2°.

13.1.2 The CLD effect

During the eclipse, the part of the solar disk covered by the moon changed with time. In [*v. Friedeburg 1999, v. Friedeburg et al. 2001*] a formula to derive the coverage as a series of time is developed (Figure 13.1.1).

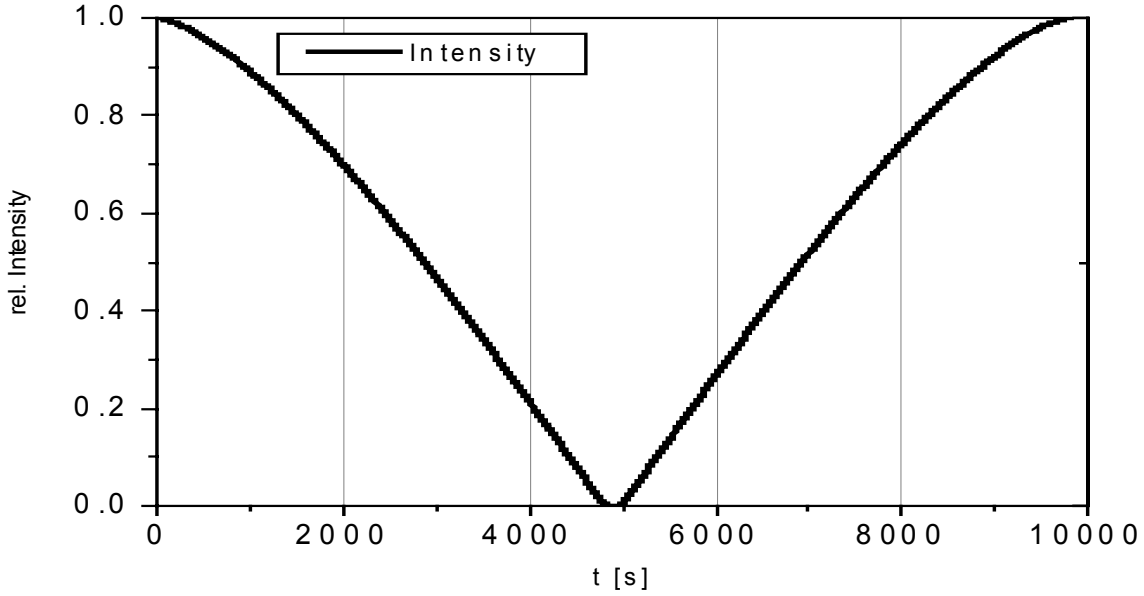

Figure 13.1.1 Calculated time series of the relative solar light intensity. Sun and moon are treated as overlapping disks. The small plateau in the middle represents the phase of totality. Scattering and the coronal light are neglected.

Correlated with the change in coverage of the solar disk is the variation in coverage of areas close to the centre and close to the rim of the solar disk.
A known effect of this is the variation of the solar spectrum emitted from the uncovered part, especially measurable in the change of the optical density of the Fraunhofer lines.
The optical density of the Fraunhofer lines depends on the point of the solar disk looked at by the observer [*Unsöld and Baschek 1999*]
The photosphere is characterized by a negative temperature gradient from the inner layers to the outside. All layers absorb radiation from layers below as well as emit radiation. The physics follows from theory of radiative transfer in stellar atmospheres, using Eddington-Barbier's approximation and the assumption of Local Thermal Equilibrium (LTE). The source term of the emission of a layer depends on its temperature T by means of the Kirchhoff-Planckh-function $B\lambda(T)$. According to E.A. Milne, the relation between T and the optical depth τ^* of the photosphere is:

$$T^4(\tau^*) = \frac{3}{4} T^4{}_{eff}(\tau^* + \frac{2}{3}) \tag{13.1.1}$$

Here, T_{eff} is the temperature of the light emerging from the solar surface. This means that this temperature is realized in an optical depth of 2/3.
For a given λ, $\tau^* = 2/3$ is reached at a specific geometrical depth $z_{2/3}$. Be $z_{2/3,l}$ and $z_{2/3,w}$ this depth for the wavelengths λ_l at the line center and λ_w at the line wings and the continuum, respectively.
$z_{2/3,l}$ and $z_{2/3,w}$ each depend on the slantness of the line of sight by the factor $1/\cos(\vartheta)$, which means it decreases when the path is more slant. Here ϑ is the angle between the normal at the considered point on the solar surface and the line between the centers of the sun and the earth (the line of sight).
When looking at the center of the solar disk, $z_{2/3,l}$ is located in the outer layers of the photosphere, since light at λ_l from lower altitudes cannot penetrate the overlaying photosphere due to the high absorption coefficient. The emission of radiation depends on the temperature $z_{2/3,w}$ is situated deeper inside the photosphere, where higher temperatures prevail. These do imply higher emission compared to the outer layers; this fact in turn leads to a large difference in emitted intensity which implies a large optical density of the Fraunhofer lines at the solar disk center.
In contrast, when looking at a spot at the disk's outer rim, $z_{2/3,l}$ still is located in the outer layers; but due to the slant line of sight through the photosphere, the optical path is longer for light from below, and $z_{2/3,w}$, too, now moves up into cooler layers with lower emission. This in consequence implies a lower optical density at the rim of the sun.
A general consequence of this also is the Rim Darkening. At 660 nm (continuum wavelength), the intensity emitted by a point at with distance $0.8*R_s$ from the center (R_s as solar radius) equals about 45% that of the respective value at the centre.

The formula for the optical density used in DOAS is:

$$\tau = \ln \frac{I_w(\vartheta)}{I_l(\vartheta)} \tag{13.1.2}$$

where already the intensities for line wing and center, respectively, are inserted.
If we assume the light from the line wings to come exclusively from the solar surface, it will, in first approximation, not change over the solar disk. So τ depends merely on $\ln(I_w)$, which in turn depends, for a given wavelength, on the temperature by the term $\exp(kT/hf)$.
Since the logarithm and exponential cancel out, we have:

$$\tau \propto T \tag{13.1.3}$$

Let us now consider the dependence of ϑ on the point of solar disk looked at, this being positioned at a distance r from the center, expressed as fraction of the solar radius r/Ro.
The relation between ϑ and r/Ro reads:

$$\cos\vartheta = \sqrt{1 - \left(\frac{r}{R_o}\right)^2} \tag{13.1.4}$$

When we solve (13.1.1) for T and using (13.1.3), we obtain

$$\tau \propto \sqrt[4]{\frac{3}{4}\left(\cos\vartheta + \frac{2}{3}\right)} \tag{13.1.5}$$

This is the qualitative relation that relates the optical density of the Fraunhofer lines to the point on the solar disk considered and itself identified by ϑ.

We can subdivide the solar disk into an arbitrary number N of concentric rings r_i, each of which assigned to a $cos(\vartheta)_i$ and hence, an optical density τ_i calculated as outlined above. Now at each point of time, following the algorithm outlined in the preceding section, the absolute free area f_i of each of the r_i can be derived by successively calculating the free area $F_i(t)$ of a disk with the radius of r_i and subtracting the $F_{i+1}(t)$, the free area of a disk with the same center as r_i, but with radius $r_{i+1} = r_i - \Delta r_i$. Δr_i is the parameter of the discretization.
For each of these rings, the intensity I_i per unit area can be calculated, and attributed the respective ϑ.
For any point of time of the eclipse, the intensity seen by an observer thus is:

$$I(t) = \sum_{i=1}^{N} I_i F_i(t) \tag{13.1.6}$$

and the optical density follows as:

$$\tau(t) = \frac{1}{I(t)} \sum_{i=1}^{N} \tau_i I_i F_i(t) \tag{13.1.7}$$

13.1.3 A simple Forward model

The following simple Forward Model was devised to calculate the NO_3 absorption signal along the line of sight used during the solar eclipse measurement. As stated, it is based upon AMFHD. AMFHD (and generally single scattering models) computes the radiance along the line of sight extending from a ground based detector to the TOA. It does so because the radiance is altitude dependent, due to different extinction along the slant path from the sun, and so is the scattering probability.
In our case, as first step, the extension of the line of sight was limited to 50 km. This is the maximum visibility (4-e-length) in clean continental air (for polluted continental air, it is 15 km) [*Hugh Coe, pers. comm.*]. Furthermore, it ran close to the ground. So the radiance impinging on the points along it could be considered constant for an uncovered sun, and only a small variation in air number density had to be taken into account. In the wavelength region chosen for measurement, i.e. in the red, the radiance can be considered dominant by the direct beam, so contributions of horizontally scattered light from neighbouring points were neglected. These assumptions governed the radiances along the line of sight, the “first stage”.
The AMFHD algorithm now computes, as “second stage”, the contributions from each line of sight point from the radiance computed for this point, the local scattering probability and the attenuation on the way to the detector, and the trace gas SCD signals of these contributions to average over. The problem with validating this method is that the trace gas profile is unknown; only the intensities can be compared with measurements, when both are performed for a set of SZA.

Now the solar eclipse modified the irradiances at the scattering point, the "first stage" of the model, in two respects. Eqs. (13.1.6) and (13.1.7) relate the intensity (or radiance) of the direct solar beam as well as the optical density of Fraunhofer lines to the time t as observed from one given point. Using the $t = s/v_{ec}$ this relation is converted to the values recorded along a given point along the line of sight in distance s to a reference point for one specific time t. Each point on the line of sight is characterized by a specific "local" phase of the solar eclipse, which is shifted by $t = s/v_{ec}$ against the phase observed at the detector site: E.g. 10 seconds before the Third Contact, the measurement site still is facing the totality, while in 8.5 km distance, the solar disk becomes visible again. Each point can therefore be assigned an intensity (relative to the intensity for the uncovered sun) and an optical density of Fraunhofer lines. The latter can be used as a fingerprint of each segment of the line of sight, defined by the point the segments are centered at. Since these quantities could be calculated with reasonable accuracy using Eqs. (13.1.6) and (13.1.7), this fingerprint could be used to test the single scattering approach in a trace gas independent way, which was desirable since also the absorption of eventually formed nitrate radical was to be simulated with this model.
Unfortunately for this test, a broken cloud cover prevailed as stated above, which had an altitude of 2 km at maximum. This indicated an inversion layer, chemically known to terminate the NO_3 educt rich environment below. The nitrate radical can be expected to form exclusively within that mixing layer enclosed. With the elevation of 2° the distance where an altitude of 2 km is reached is 50 km, when accounting for the earth's curvature, which matched the planned maximum visibility.
An important approximation that must be used in the following considerations is that differences above the cloud cover in radiance transfer itself through the clouds. This means that we ignore horizontal transfer by means of Mie scattering, or we assume the transfer to exist on spatial scales small compared to the dimensions of the boxes.
The 50 km were subdivided into an arbitrary number of M boxes or segments x_j with mean distances (centered at points with distances) d_j to the measurement site.
For each x_j, the phase of the eclipse depends on its distance d_j so each x_j can be assigned a timeshift $t_j = d_j/v_{ecl}$.
For each x_j and a given time t, the intensity $I_j(t)$ is calculated by (13.1.6) using $I_j(t) = I(t+ t_j)$.
In an analoguous manner, a $\tau_j(t)$ can be derived.
From the $I_j(t)$, the relative amount of light scattered into the direction of the instrument as fraction of the amount with uncovered sun is calculated; since the scattering angle is the same, and we only consider relative values, these amounts are identical to the $I_j(t)$, up to a proportionality factor modulated by a small variation in air number density, thus they are henceforth called $I_j(t)$ themselves.
The attenuation term of each $I_j(t)$ is $exp(-d_j/dmax)$. d_{max} can assume values between 15 and 50 km; but this choice is neither relevant to the resulting relative intensity reaching the instrument nor to the optical density.
This relative intensity is:

$$I(t) = \sum_{j=1}^{M} I_j(t) \exp\left(\frac{-d_j}{d_{\max}}\right) \tag{13.1.8}$$

The optical density measured follows to be:

$$\tau(t) = \frac{1}{I(t)} \sum_{j=1}^{M} \tau_j I_j(t) \exp\left(\frac{-d_j}{d_{\max}}\right) \tag{13.1.9}$$

The application of this model to derive the slant column density of an absorber along the line of sight is as follows:
A trace gas concentration $c_j(t)$ existing in a given box j, at a given time t can only be probed by the light crossing this box. For each box j' the fraction of the light $I_{jT}(t)$ reaching the instrument which has traveled through the box can be calculated using (13.1.8) starting with $j = j'$, and reducing d_j appropriately, and dividing by $I(t)$. This yields a visibility factor $v_j(t)$.
When we now multiply the nitrate radical with the length b of the box, which is uniform, and its $v_j(t)$, we can easily derive the slant column density SCD, $S(t)$, measured with our instrument:

$$S(t) = \sum_{j=1}^{M} c_j(t) b v_j(t) \tag{13.1.10}$$

In case of the nitrate radical, the formation and destruction as a function of time, hence phase of the solar eclipse and resulting impinging solar radiation, at a given point along the line of sight can be modelled [*Geyer et al. 2002*].
The point of the modelled nitrate radical curve found at a specific time at a given x_j , yielding $c_j(t)$, depends on the specific phase at this x_j. When normalizing the curve at each x_j to 1, the curves are identical, but shifted by time t_j.
Figure 13.1.2 shows the model result for the Fraunhofer line variation, as well as the SCD signal for one of the NO_3 model scenarios, as obtained using the Forward Model explained. For comparison, the intensity time series for the detector location is displayed as well.

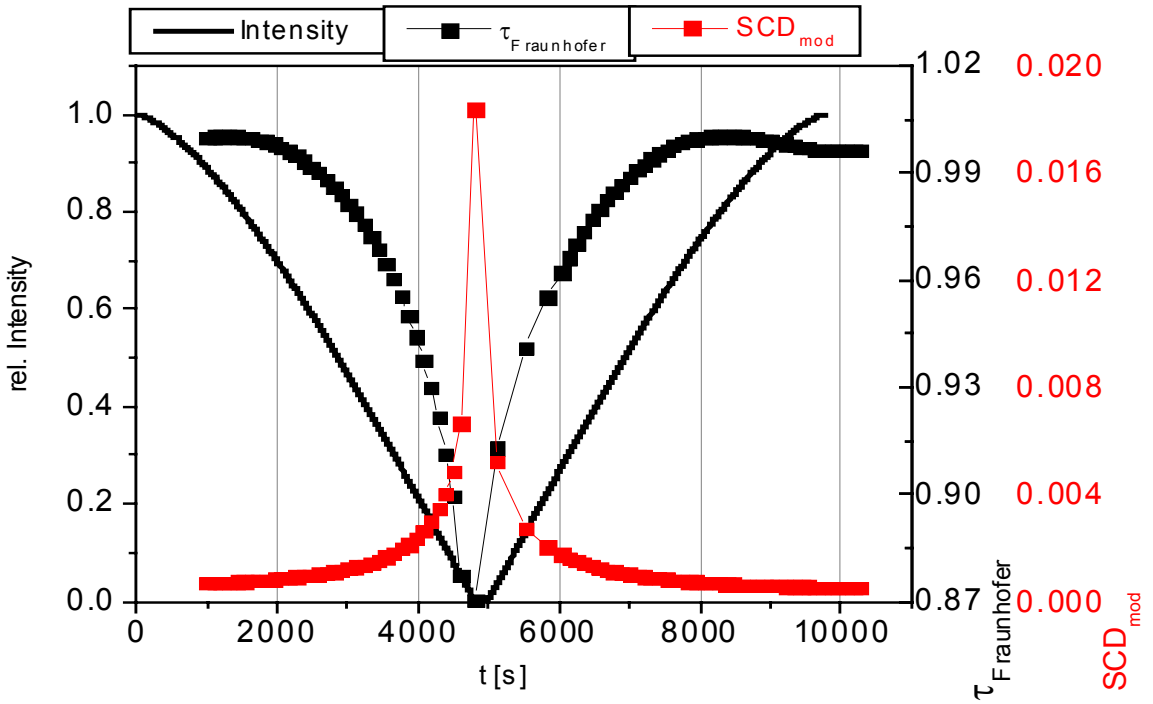

Figure 13.1.2 Modelled Intensity at the measurement location, optical density of Fraunhofer lines modelled for he perspective of the instrument , and modelled SCD

13.1.4 Spectral evaluation

The spectra were recorded from the beginning to the end of the solar eclipse.

The relative radiance series to compare to the model was readily available from the spectra, using the average over the count numbers of the spectral channels.
To derive a parameter correlated with the CLD effect, as well as the optical density of the nitrate radical, the spectra needed to be evaluated.
The evaluation was made complicated of course by just the Fraunhofer OD variation. This section outlines the technique developed to overcome this difficulty. It can be applied to other measurements as well affected by the CLD effect [*v. Friedeburg 2001*]. [*Bösch 2002*] devised, based upon similar findings obtained during the solar eclipse measurement, another correction algorithm using highly resolved Fraunhofer spectra taken with telescopes directed exclusively on parts of the solar disk.
The spectra were evaluated using the DOAS method [*Platt 1994*]. The interfering structures in this case are: The Fraunhofer structures, Ring structures resulting from the filling in of the Fraunhofer lines due to rotational Raman scattering [*Grainger and Ring, 1962, Bussemer, 1993; Fish and Jones, 1995*], and water vapor absorption features. For the following, see [*Weaver et al., 1996, Solomon et al., 1989; Platt et al., 1981*]
To first remove the Fraunhofer structure, each spectrum was divided by a daytime spectrum, i.e. a spectrum with only negligible nitrate radical concentrations, recored at t = 995 s.
Of the spectra recorded in the 20 minutes after the eclipse, two spectra could be found with different water absorption optical densities. The ratio of the spectra contains the difference of their water vapor absorptions, while most of the Fraunhofer absorptions cancel out [see also *Wagner et al., 2000*]. This spectrum was fitted to the respective measured spectrum. So was a Ring spectrum calculated from the daytime spectrum used.
For the structure of the NO_3 cross section spectrum to be fitted the spectrum published by Yokelson et al. [1994] was used. For our instrument's resolution we determined a value for the differential absorption cross section σ' [*Platt 1994*] of 2.09×10^{-17} cm² at 662 nm and 298 K. To ensure a direct comparison with previous studies for the determination of σ' we chose the widely used recommendation in [*Wayne et al. 1991*] for the broad database leading to this averaged value [see also *Geyer et al., 1999*]. Compared to the value derived from the Yokelson cross section this results in about 6% larger SCD.

For the compensation of the Fraunhofer line variation, finally, we applied an approach similar to the one used for the water vapor. In Figure 13.1.2 we see that during certain times of the eclipse, spectra do already or still contain significant Fraunhofer line variation, but not yet, or not any more significant nitrate radical signal. We used a spectrum at t = 2267 s seconds, see Fig. 13.1.2, and formed the ratio with the daytime spectrum. The result is henceforth called Fraunhofer Difference Spectrum (FDS). This FDS is fitted to the spectrum.

The reference spectra are smoothed each in the same way and then fitted to the measured spectrum after subtracting the daytime spectrum.
Figure 13.1.3 shows a typical result of a NO_3 evaluation; Also displayed are the absorptions found by the fit in this spectrum of the water vapour, the ring effect and the nitrate radical in solid thick lines. In red lines the same absorptions with the residual of this evaluation added are overlaid to provide comparison between residuals and absorptions. Figure 13.1.4 shows the resulting time series in optical density of nitrate radical absorption. Additionally shown in Figure 13.1.5 is the comparison of the residuals of the evaluation with and without the fit of the difference spectrum. The improving effect can be seen clearly, making the approach a technique usable for similar measurements where the Fraunhofer line variation occurs.
It has the advantage to exclusively use spectra recorded by the device, which avoids the problems of convolving spectra from other sources.

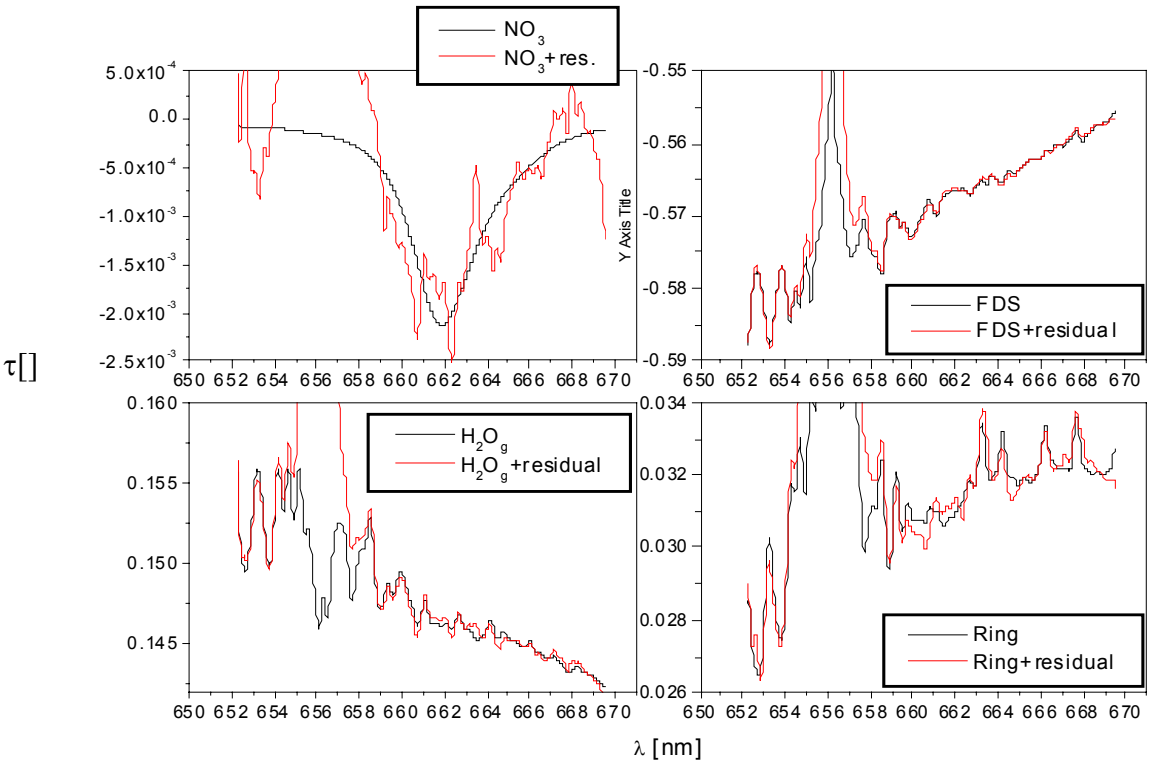

Figure 13.1.3 Typical DOAS evaluation as described in the text. The spectrum was recorded at the time t=Please note that the area from 655-658 nm has been excluded from the fit, since the prominent H-Alpha line could not be corrected for its variation even by the approach described.

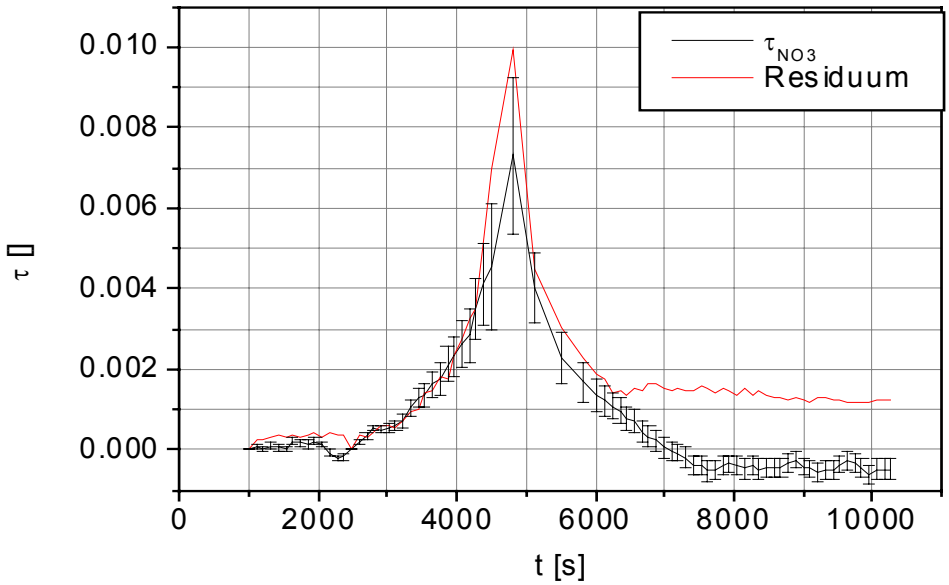

Figure 13.1.4 Time series of NO_3 absorption optical density with 2-σ-error. The residual allows for significant nitrate radical absorption for most of the spectra, though for the time t > 6000 s, the residuum becomes too large, which is due to the cloud cover becoming denser, altering the radiative transfer.

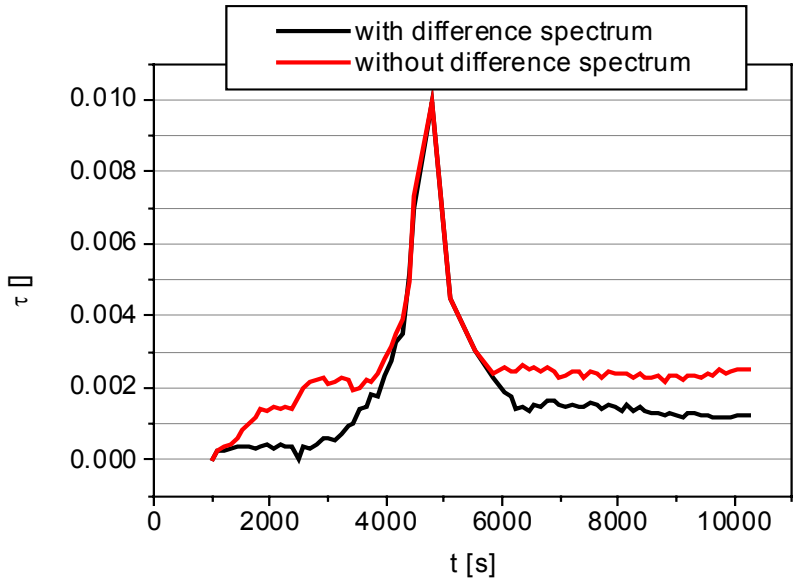

Figure 13.1.5 Comparison of the residuals obtained with and without fitting the Fraunhofer Difference Spectrum FDS. Even for the spectra taken after t = 6000 s the effect is clearly seen.

With the evaluation done, we now can compare the measured/derived spectroscopic quantities to the modelled ones. Figure 13.1.6, left panel, shows the measured relative intensity, normalized to unity at the beginning of the eclipse, compared to the modelled quantity. After the totality, when the cloud cover grew significantly more dens, the agreement is less good than between the 1st and 2nd contact. The V-shape, though, is well reproduced. For a more specific quantity we now consider the Fraunhofer optical density.

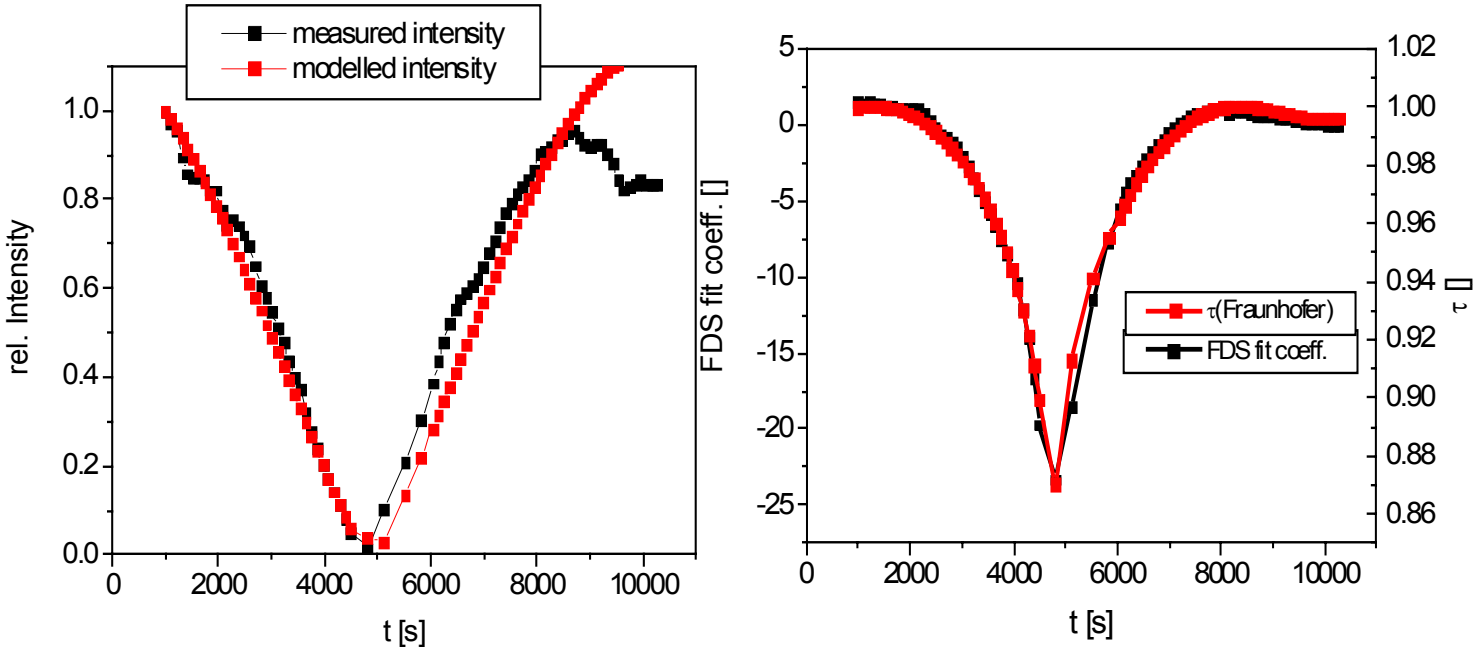

Figure 13.1.6 Left panel: Comparison between measured and modelled relative intensity time series (left panel). The measured curve is the underground-corrected average count value of the respective spectrum divided by its integration time.
Right panel: Comparison between measured and modelled Fraunhofer optical density time series. The measured curve actually is the fitting coefficient of a FDS

Figure 13.1.6, right panel, displays the comparison of the modelled Fraunhofer variation with the fitting coefficient obtained for the Fraunhofer difference spectrum FDS. Since this difference spectrum covers all Fraunhofer lines within the fitting range, absolute comparisons do not yield useful information. But clearly can be seen that the principal behavior, especially the assymetry that arises from the measurement geometry, is reproduced quite well. Differences can be caused by the cloud cover's radiative transfer effects, these having been neglected as stated above.
These figures show the success of the simple model. It seems promising to develop a Forward model for the Monte Carlo RTM.

13.2 A FMC concept

Based upon the apparent successes of a forward model, the following two-staged concept was devised for "Tracy". The two stages are:
1. Calculation of the impinging radiance at points along the line of sight using Monte Carlo
2. Analytical derivation of the radiance scattered into the direction of the detector and of the attenuation on the respective way from the given point to the detector.

13.2.1 Principle of a Monte Carlo based two stage Forward Model

In the model, the solar position is defined using the detector location, as well as the SZA and the SAZ "seen" from this location. For a given solar position, all points "seeing" that same SZA form a ring (henceforth named SZA-ring) running around the model earth. I.e. if the sun would be located over the north pole, at a point above TOA on the **Z**-axis, all points of e,g, "latitude" 42° would have SZA of 42°.
Let us assume horizontal homogeneity in atmosphere parameters and trace gas profiles, then a detector, given a specified viewing direction, would measure the same signal at each point defined by this ring. If there are horizontal variations, the detectors must be placed at a distance small as compared to the variation's scale. The detector's distance must also be smaller than the scale for horizontal photon transfer (see below).

The two lines of sight of these two detectors define a plane reaching from the location of the detectors to the TOA (in case of ground based measurements), or, for airborne and space borne sensors, from the detectors either to the TOA as well or down to the surface (e.g. in nadir mode). This plane can also be defined by one detector's line of sight and the local tangent of the SZA ring. The plane can be given a width which is equivalent to the distance of two detectors at the sides of the plane.
This "plane of sight" can be calculated to take account of refraction since any radiance scattered in the line of sight and into the direction of the detector will on the way to it be subject to refraction. So the plane will actually consist of segments ("line of sight plane segments" or "plane segments", PS) which are tilted with respect to each other.
Along the segment of the SZA ring connecting the two detectors more instruments can be imagined to be placed. If their mutual distance approaches zero, each photon passing the plane will pass one of the lines of sight. Since all detectors (under the assumptions made) measure the same signal, the signal of all of these detectors may be summed (in the limes integrated) over before deriving the spectroscopic quantities from this integrated signal.

The plane of sight can be imagined as flat detector area of a spectro radiometer measuring the irradiance (without any cosine weighting) along the line of sight.

Now we can model a "sun" placed in the location calculated as solar position, and have it emit photons like the detector does in backward MC. The photons have an initial direction which is the inverse of the solar position vector. The sun may also be modelled as a disk with finite radius, and the photon launch positions also may be equally distributed across this disk.
Since the apparent half solar aperture angle of 0.27° is resulting from the solar radius and the distance, photons from the rim of the sun will reach the earth under just an angle of 0.27°. So when calculating from the launching position of the photons on thedisk this angle as deviation from the inverse solar direction vector, we take account of the solar aperture.
We also can assign the photons a parameter *RimOrigin, RO*, which is distance of the photon launch position from the solar disk centre divided by the solar disk radius. I.e. $RO = 0$ denotes a photon coming from the sun centre, $RO = 1$ a photon from the rim.
These photons are then, along their initial directions, projected onto the TOA and the model calculates their path through the atmosphere until they either leave the atmosphere or get absorbed e.g. by a surface of zero albedo.
If a photon passes one of the plane segments, it contributes to the irradiance "measured" in the "plane of sight" of the arrayed detector battery.
The fraction of irradiance scattered into the direction of the detector (usually with a small aperture angle and a detector area small as compared to the dimensions of model discretization) is considered negligible. So the photon may pass the plane, get reflected e.g. off a cloud and again pass the plane a second time, being counted a second time. This represents the situation of increased radiance in the vicinity of reflecting clouds or surfaces of high albedo.
At each plane pass, three quantities must be calculated
1. The probability to get scattered in the volume the plane passes through
2. The probability of scattering into the detector
3. The transmission from this scattering point to the detector along the line of sight.

Before considering them, we must keep in mind two limitations:
First, that we model detectors with zero aperture angle, i.e. with aperture angles that do not influence the measurement significantly when changed from their value to e.g. a small fraction of it. This means the measurement setup must allow for approximation of a finite aperture angle by a zero one.
Second, that usually DOAS devices with small aperture angles do not measure absolutely calibrated radiometric quantities (for reasons related to the e.g. temperature stability); since a detector with aperture angle zero (hence detector are zero as well) could not measure radiances or irradiances because these quantities are not defined for such cases. So we will not attempt to model radiances with the FMC approach outlines here.

#1 of the probabilities is calculated from the sum of aerosol scattering coefficients plus the Rayleigh scattering coefficient along an arbitrary but fixed distance (1 m chosen in the model) for the aerosol load and air density in the voxel containing the PS in question.
#2 The probability that a photon scattered at a given distance from a detector gets scattered into the detector depends in turn on two probabilities:
A. that the scattering location is located within the cone defined by the aperture angle, i.e. within the sphere segment (disk for small aperture angles) defined by the cone aperture angle and the distance photon-detector
B. the solid angle occupied by the detector area as seen from the remote photon.

Both probabilities can be expressed as fractions of these disks of the surface of the unity sphere as we did when deriving the relation between solar irradiance and modelled photon weighs.
In case of A, it is $F_D = sin^2(\alpha_D)/4$ with α_D as half aperture angle of the detector;
In case of B, it is $F_A = r_A{}^2/4$ with r_A the radius of the (assumed circular) detector area.

The distance between detector and scattering locations is not found in either quantity. So the probability of our photon to get scattered into the detector is not depending on it. Since we are not attempting absolute radiometric calculation, we can set it to 1.
Finally,
#3 can be derived straight forward in the same way we use when forcing photons into the sun.

To derive the spatial scale of horizontal photon transport, photons were targeted at points of the earth surface and modelled with forward Monte Carlo. The surface normals of the target points were chosen for a set of angles with the initial photon direction, thus they represented different SZA with respect to the impinging light. Then the distance between the photon impact points on the surface and the selected target point (which would, without scattering, have been zero) was recorded. The study yielded that even with 350 nm (UV) more than 95% of the photons impacted within a 100 km radius around the target point. So this was chosen as an estimate for the spatial scale of horizontal photon transport. To ensure that this lateral transport was taken fully account of, in the following the distance between the two detectors at the two sides of the plane was set to 50 km.
With this value, also the earth curvature between the two detectors, 0.45°, can be neglected in reasonable approximation.
This choice also reduced the curvature between the detectors at its sides and the middle to 0.225°

13.2.2 Implementation

These section covers the additional modules for the forward MC implementation.
First, two more parameters were added, to be modified by the user in the program control file.

13.2.2.1 *SoundLOS* routine

For each viewing geometry the *SoundPlane* routine is called. It successively calculates the line of sight from the detector to either the TOA or the surface; if the user employs refraction, the appropriate tilt is calculated at every transition between voxels with different z-index.
For each segment of the line of sight, the following parameters are calculated and stored:

- Direction of line of sight segment
- Surface normal of SP segment
- Point in the centre of the LOS segment, i.e. between the two points defining the LOS segment, henceforth called “centre point”
- Optical density and column density for each trace gas from the detector to the point where the current segment begins
- Total aerosol absorption from the detector to the point where the current segment begins
- DistUp = distance between the detector and beginning of the LOS segment
- DistLo = distance between the detector and end of the LOS segment
- Voxel indices of the voxel the SP is contained within.

All these parameters are stored to a path object.

The user can chose a parameter *DetectionRadius* in the program control file. It defines the maximum distance allowed between the intersection point of a photon with one of the plane segments and the line of sight to contribute to the measurement. A recommended value (see above) is 50 km.
After this, the maximum area spanned by all the lines of sight used in the model is derived from the beginning and end points.

13.2.2.2 *Reshuffle* routine and *Plane* object

The path object containing the above list of parameters can have the first entry at the TOA (for satellite geometry), on the ground (ground based measurement) or in between (balloon and aircraft operation).
Now for each photon on a way through the model atmosphere and for each path segment the distance to the intersection with the appropriate PS, i.e. for the correct voxel, must be derived; for doing so, a routine must be devised to find the appropriate entry, and do so fast since this routine is called often.
The straight forward solution would be a while-loop "running" along the LOS segments and comparing e.g. the voxel indices using if-clauses until the appropriate segment is found.
But this approach is out of question due to the high CPU time consumption.

So the LOS segments are rearranged in the following way.
Case A: Only lines of sight are used passing each vertical atmosphere only once; this is e.g. the case for ground based Off-axis geometry.
Then a path object *Plane* is allocated of the same type as the one used in *SoundLOS*. It contains $g*n_Z+1$ elements, with g number [0,..,g-1] of viewing geometries (up to 10, as the reader my recall) and n_Z as number of vertical layers (e.g. $n_Z \in [1,..,70]$ in the model atmosphere).
These elements can later be adressed by the successive number, i.e. the first element has number 0, the second 1 etc.
The first entry to the Plane object is a dummy, containing –1 as values of parameters.
Now the PS are inserted into the *Plane* path object in a way that the PS in voxel of index z of geometry g becomes path entry number $g*n_Z + z$.
In case a line of sight does not traverse all layers, e.g. with positive elevation from airborne sensor, the respective *Plane* segments are filled with dummies like the 0^{th} one.

Case B: Among the viewing geometries, one or more traverses a given vertical layer twice, e.g. for limb geometry.
In this case *Plane* is allocated $2*g*n_Z+1$ elements. For each geometry which scans vertical levels twice, an integer flag l is set to 2 instead of 1.
The segments of the line of sights are then divided into two branches, the downward branch B_D and the upward branch B_U. The segment which contains the geometrical tangent height of the line of sight is contained in both branches.
The segments of B_D are then assigned the numbers $2*g*n_Z + z$, the segments of B_U accordingly $2*g*n_Z + n_Z + z$.

Again *Plane* segments with voxel indices of altitude levels not passed by a given branch are filled with dummies.

13.2.2.3 *Sun* routine

This routine performs the tasks described above.
It accepts the area defined by the lines of sight. Then it uses another user-defined parameter, *FiringRange*. By this range it extends the area on the earth surface defined by the lines of sight. This ensures that also photons transferred laterally can contribute to the measurement.
If for DetectionRadius 50 km are chosen, a recommended value for *FiringRange* is 100 km.
This extended area is projected along the solare vector to the TOA. Random numbers distribute the "incoming" photons over this projected area. Additionally, a "launch point" on the solar disk of the photons is random selected determining the above explained *RimOrigin* parameter as well as an appropriate deviation of the initial photon directions from the solar vector.
After the photons have thus been launched into the atmosphere, their paths are modelled in the same way as in the backward MC case.

13.2.2.4 *HitPlane* routine

This routine is called for each photon, each path segment and each geometry after derivation of the next voxel intersection.
HitPlane selects, using the geometry number and the voxel z index, the appropriate plane segment and calculates, using the *GetPOI* routine, whether the photon hits the plane prior to leaving the voxel. If this is the case, the respective plane segment number is returned.
The calculated intersection point, if valid in terms of a positive elongation parameter *d* derived (see section 6.5.4), must pass two tests:

1. The distance *d* to it must be smaller than the one to the next voxel boundary, otherwise the point is not hit within the current voxel.
2. The point must have a distance to the line of sight smaller than the *DetectionRadius*, otherwise there is no contribution to the measurement.

In case of limb geometry, there may be intersection points with planes defined by the parameters of two plane of sight segments, i.e. by the two passing the same vertical layer. In this case, the two parameters *DistUp* and *DistLo* are taken into account for a third test:

3. The distance between the intersection point with the considered segment and the point where the line of sight, begun at this point and followed in reverse direction, reaches the detector that "emits" this line of sight, must be within the interval [*DistLo, DistUp*].

Tests 2 and 3 require additional calculation. In case of a valid segment intersection, test 2 is only performed if test 1 has been passed.
If there are valid intersection points with two plane segments, first test 1 is used to decide between the two, then test 2 and after this test 3 are performed if the respective preceding tests has not brought about a decision.
In case of a positive Segment, The *SCDCalculator* is called for each of the geometry a valid PS hit has been derived.
First of all, the photon path and the accompagnying spectroscopical quantities are calculated to the point of the intersection
Then an additional routine is called; it accepts the *Plane* segment number, and calculates the additional columns (of trace gases, aerosols and air) and attenuation from the intersection point down to the detector using the Plane segment information as well as the local voxel information adressed using the voxel indices.
Additionally, taking into account the local voxel air density and aerosol scattering coefficient, the scattering probability is calculated, and from the ratios between the individual coefficients, the absorber causing the "scattering" in the same way as the scatterer is selected in the *ExtinctionDecider*.

The photon weight (actually the weight of a photon copy) is scaled with attenuation and scattering probability and then the parameters are stored to the *Result* object.
After leaving the SCDCalculator, the photon path is continued to model until the photon, as mentioned leaves the atmoshere or gets extincted.
The processing of the data, e.g. the AMF calculation, is the same as in case of BMC.

13.3 Application to balloon – limb geometry

As a first and preliminary application, we apply the Forward scheme to the balloon situation modelled in chapter 11.
Figure 13.3.1 shows the Box AMF for the parameters:
Albedo 30%
Flight altitude 30 km
Elevation –4°
Azimuth 90°
Half aperture angle 0.001°.
SZA 30°, 50°, 70°.
The choice of the aperture angle serves to reduce differences caused by the "zero" aperture angle of the Forward scheme and the non-zero one of the Backward model; they are to expect in the light of the derived sensitivity of the balloon Box AMF to aperture angle.
Figure 13.3.1 shows the result.
We find a reasonable agreement. The maximum Box AMF we find to be larger in Forward mode as in Backward, which was expected.

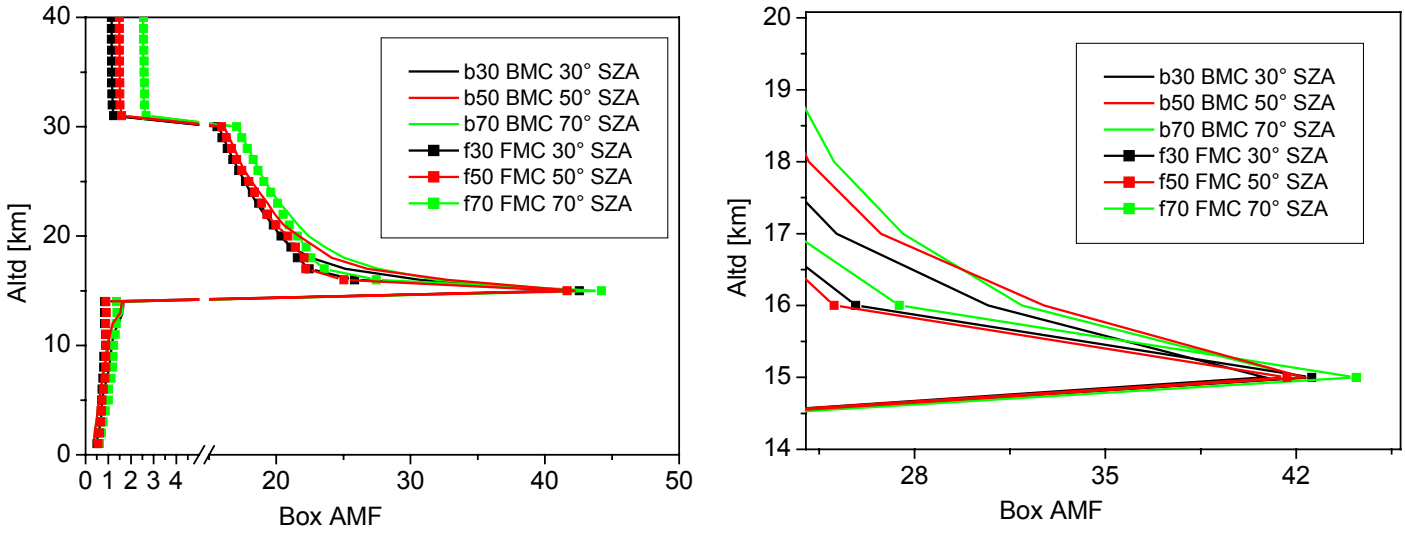

Figure 13.3.1 Balloon geometry Box AMF, modelled in Backward and Forward MC. The agreement is reasonably good, even for the critical part around the altitude of maximum Box AMF.

The briefly presented Forward MC scheme certainly has drawbacks, such as limitation to zero aperture angle. Ways have to be found to e.g. average over several runs encompassing any aperture angle. But also advantages have to be noted, especially the potential of better account of atmospheric refraction.

14. A Monte Carlo based Retrieval Approach for ill-posed problems

In numerous of the preceding sections it was mentioned that lack of additional data, i.e. beside the trace gas SCD measured, prevents the actual profile retrieval or make sit difficult. The aerosol load is the most prominent uncertainty, being highly variable in each parameter with time and location. It is easy to see how the uncertainties can lead to ambiguities. E.g. a profile confined within an altitude layer lifted off the ground may with a given aerosol load lead to the same AMF for a MAX measurement as a different load with a profile which is located on the ground, but extending high enough that the majority of the gas is located above the *LSA* of the lower elevations.
If no other data or reliable a priori information is available, the measurement data itself must be exploited in a way to use parameters different from the mere SCD to constrain the problem. In chapter 9, it was the ratio between AMF that was used to obtain a quantitative estimate. Of course spatial discretization must be sacrificed to retrieve one (or more) unknown parameters (e.g. the aerosol load at ground level) other than the concentrations which are the primary goal to obtain.
An a priori information that can be used is the knowledge, or well founded assumptions, on the photo-chemical reactions, e.g. productions and sinks, between a given target species and other trace gases abundant in the considered air mass. In chapter 9 such information as used to support a distribution estimate derived from the AMF. But it can also help in the derivation itself.
In this chapter we will present an algorithm using a modified matrix approach in conjunction with a Monte Carlo algorithm to retrieve vertical profiles of nitrate radical, NO_3. The chapter focuses mainly on the algorithm itself. For more details see [*v. Friedeburg 2002*].

14.1. Chemistry of the Nitrate Radical in the PBL

A large part of the chemistry of the nitrate radical has already been listed as part of the stratospheric nitrogen oxyde chemistry in section 11.1. In addition to these reactions, in the PBL more channels become important. The most relevant are:
Oxydation of volatile organic components:

$$NO_3 + VOC \rightarrow \text{organic products} \qquad (14.1.1)$$

heterogeneous uptake of N_2O_5 by aerosols:

$$N_2O_5 + \text{Aerosol (heterogeneous uptake)} \rightarrow \text{products} \qquad (14.1.2)$$

and homogeneous hydrolysis of N_2O_5:

$$N_2O_5 + H_2O \rightarrow \text{products} \qquad (14.1.3)$$

The latter two channels apply to N_2O_5, not to NO_3 directly, but vie the reactive equilibrium between the two species any scavenger on N_2O_5 also removes NO_3. A fast gaseous removal channel is the reaction with NO:

$$NO_3 + NO \rightarrow NO_2 + NO_2 \qquad (14.1.4)$$

During day, NO_3 cannot exist in significant concentration due to the rapid photolysis (the photolytic lifetime τ_1 in direct sunlight is ≈ 5 s), especially not in urban areas because of the NO emissions. At night, after the NO has been oxydized by ozone, NO_3 can build up. To which extent depends on the other direct or indirect removal channel. The buildup continues until sunrise. Then, NO_3 is photolyzed again. See also [*Geyer et al. 1999, Geyer 2000, Geyer at al. 2001 a, b, 2002,2003*].

14.2 Measurement of PBL Nitrate Radical

The DOAS measurement is done during sunrise in Off-Axis geometry [*Weaver et al. 1996*] with a slant elevation of in our case 15°. The azimuth angle is around 180°, i.e. poiting away from the sun. This geometry ensures a long light path through the atmosphere layers at the ground, and as well through air masses which are illuminated with time delay as compared to e.g. the air volume directly overhead. Refer to Fig. 14.2.1 for the following.
The photolysis of NO_3 in the morning does not take place at all altitudes simultaneously. At a given SZA ϑ_1 (Figure 14.2.1, top), the line of sight through the dark volume of air, and hence, through the area containing significant nitrate radical concentrations, extends from the observation point C to B, which is the intersection point of the line with the direct light zone. In the aera directly illuminated, the NO_3 is photolyzed; but a part of the light is scattered along the line of sight into the detector. A SCD value S_1 is obtained.
At the next, lower SZA $\vartheta 2$ (Figure 14.2.1, bottom), the zone of direct light has lowered, and the path through the not directly illuminated layers is shorter (C – B'), yielding a smaller S_2. In a first approximation (henceforth called „geometrical" one), subtraction S_2 from S_1 and dividing by the respective difference in the light path lengths, yields the NO_3 concentration in the layer between the altitudes of B and B'. The vertical resolution of this method is governed by the ϑ-dependence of the intersection point's height as well as the sampling rate of the measurement. The geometric calculations were done including spherical geometry as well as atmospheric refraction [*Meeus, 1992*]. *Weaver et al.* [*1996*] showed, comparing direct moon and scattered solar light in off-axis geometry with a similar line of sight, that multiple scattering effects are not significant for their location.

In the present study, The measurements were performed in spring and summer 1999. The instrument was installed on the roof of the 6th floor of the institute building (altitude 30 meters) in the northern part of the city of Heidelberg.
Clouds in the instrument's line of sight can temporarily 'hide' parts of the tropospheric NO_3 column. In addition they can strongly modify the photolysis frequency. For these reasons only clear days were selected.
The instrument was the same as the one described and in sections 9.2, 9.3 and 13.1. The grating was set to cover the wavelength range between 646 and 676 nm at a spectral resolution of 0.25 nm. This contained the strongest absorption line at 662 nm of the broad-band and weak absorber NO_3.

For details of the evaluation, see [*Weaver et al., 1996, Solomon et al., 1989; Platt et al., 1981*] as well as [*v. Friedeburg 2002*]. To first remove the Fraunhofer structure, each spectrum was divided by a daytime spectrum, recorded at a SZA smaller than 80º, containing no significant NO_3 absorption. Then a fit including a NO_3 cross section spectrum [*Yokelson et al. 1994*] yielded the optical density and the SCD. The measurements were started around SZA 95° and continued until SZA < 80°. The result was a series of NO_3 SCD falling off monotonuously with decreasing SZA, as expected from the measurement setup.
The intensity during sunrise is varying rapidly within the integration time of a single spectrum, thus for each spectrum an effective ϑ is calculated: The average spectral intensity of the spectrum, along with those of the preceding and succeeding spectra, is used to derive a time-dependent intensity function. From this the time is derived at which 50% of the recorded light has entered the measurement device; this time is adopted as the effective recording time of the spectrum. From the effective time ϑ is calculated with high numerical precision (0.3 arc seconds) using the software application based on the NOVAS astronomical software by the United States Naval Observatory [*Gernot Burkardt, pers. comm. 2000*].
Figure 14.2.2 shows an exemeplary series of optical density.

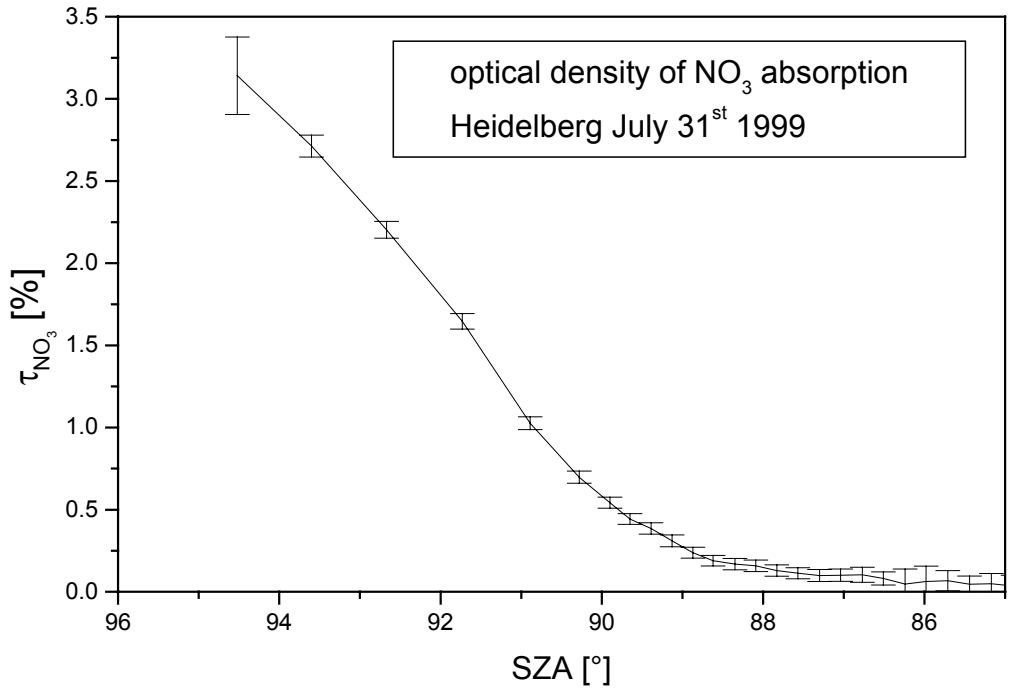

Figure 14.2.2 Typical NO_3 optical density series for a clear sky sunrise.

14.3 Matrix approach and solutions

The geometrical approximation cannot be correct; neither is the NO_3 photolyzed instantaneously in direct sunlight, nor is it unaffected in areas where not yet direct light is present, since scattered light also photolyzes NO_3. To overcome these shortcomings, a modified variation of the matrix algorithm [*Smith and Solomon*, 1990] was developed.
The forward problem is formulated:

$$M \bullet \overrightarrow{c(z)} = \overrightarrow{S(\vartheta)} \tag{14.3.1}$$

The components of M are the product:

$$M = f(\vartheta_i, z_j)A(\vartheta_i, z_j)\Delta z_j \tag{14.3.2}$$

- A part of the atmosphere within which the target species (here NO_3) is assumed to exist is divided into *m* vertical layers numbered with *j*, of thickness Δz_j, centered at z_j.
- The $c(z_j)$ are defined as target gas concentrations within the layers, normalized to unity at SZA = 97°, when the photolysis has not yet set in. They form the vector $\overrightarrow{c(z)}$.
- The SCD recorded at ϑ_i, $i = 1,..,n$ are S(ϑ_i), forming the right-hand-side vector $\overrightarrow{S(\vartheta)}$.
- The matrix components mij consist of three factors:

1. The vertical extension of Δz_j of the layer
2. The Box AMF $A(\vartheta_i, z_j)=A_{ij}$
3. The chemical degradation factor $f(\vartheta_i, z_j)$

The negligibility of multiple scattering due to the long measurement wavelength allowed for the radiative transfer model AMFHD [*Frank, 1991*] to be used to calculate the relative light contributions of vertical layers at a given ϑ. From these data, based upon the Forward technique outlined in chapter 13, the $A(\vartheta i, zj)$ were derived. Studies of the influence of air pollution on the AMFHD results yielded variations of 10% in $A(\vartheta i, zj)$. This contributed to the Box AMF error. The other error sources were the error in ϑi as well as in elevation (which governs the geometrical light path). The linear equation system is thus written as:

$$\begin{pmatrix} f(\vartheta_1, z_1)\cdot\Delta z_1\cdot A_{11} \cdots f(\vartheta_1, z_m)\cdot\Delta z_m\cdot A_{1m} \\ \vdots\cdots\vdots \\ f(\vartheta_n, z_1)\cdot\Delta z_1\cdot A_{n1} \cdots f(\vartheta_n, z_m)\cdot\Delta z_m\cdot A_{nm} \end{pmatrix} \bullet \begin{pmatrix} c(z_1) \\ \vdots \\ c(z_m) \end{pmatrix} = \begin{pmatrix} S(\vartheta_1) \\ \vdots \\ S(\vartheta_n) \end{pmatrix} \tag{14.3.2}$$

Thus each measured SCD S(ϑi) is given by:

$$S(\vartheta_i) = \sum_{j=1}^{m} f(\vartheta_i, z_j)\cdot\Delta z_1\cdot A_{ij}\cdot c(z_j) \tag{14.3.3}$$

A box model for nighttime radical chemistry developed by Geyer et al. [*2002*] was applied to a typical continental atmosphere. The degradation of a given NO_3 concentration was calculated as a function of altitude level (for altitudes zj = 0, 0.5, 1, 2, ... ,10 km) and SZA. All reactions listed in this section adn section 11.1 were incorporated. The behaviour of the species involved is modeled for the duration of a simulated night with both photolysis frequencies set to zero. During sunrise J_{NO3} and $J_{NO2} > 0$ are introduced. The model calculations were made at a time resolution of 10 seconds.
The modeled ϑ-dependent NO_3 concentrations for each altitude zj were normalized to the value at the 'end-of-night' (ϑe = 97°), which yields the ϑ- and zj-dependent relative

remaining fractions *f(ϑ, zj)* of the end-of-night nitrate radical concentration. From them, the degradation factors *f(ϑi, zj)* were interpolated.

Here we were facing the problem of lack of input data. No measured vertical profiles for the relevant species (e.g. NOx, O_3, aerosols, VOCs, etc.) were available for the measurement location. Thus we derived upper and lower estimates of the different parameters based on data available for other locations. The margin between the upper and lower estimate values was governed by the uncertainty of the respective parameter and set generously in order to encompass the situation of Heidelberg. Figure 14.3.1 show the reactant profiles.

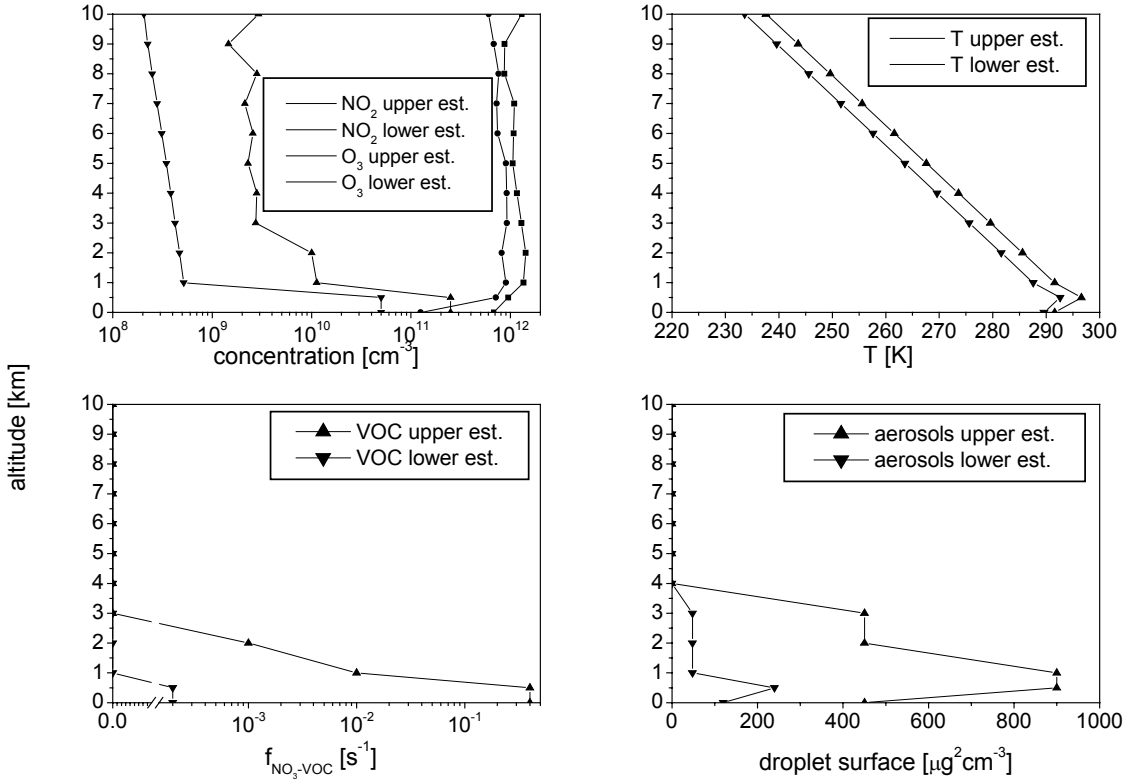

Figure 14.3.1 Upper and lower estimated for the reactant profiles relevant to NO_3 chemistry for Heidelberg. The VOC is given in degradation rates of NO_3 against them, the aerosols in droplet surfaces governing their N_2O_5 uptake.

The profiles of NO_3 and N_2O_5 are assumed to be zero at the beginning of the night.
The temperature at ground level was taken from the temperature sensor installed at the weather station on top of the institutes building. The vertical decrease above the mixing layer was assumed as 0.6 K per kilometer (see e.g. U.S. standard atmosphere for middle latitude summer [AFGL-TR-86-0110]). Since no data was available for higher altitudes, and the time resolution of the ground data is limited, we assumed an uncertainty of 1 K at ground level, and 2 K above.
The photolysis frequencies J_{NO3} were calculated [*Hugh Coe, personal comm. 2000*] using the radiative transfer code PHODIS [*Kylling, 1995*], like DISORT based on the discrete ordinate method [*Dahlbeck and Stamnes, 1991*]. The model takes into account the atmosphere's curvature. In order to estimate the uncertainty in J_{NO3}, the photolysis frequencies were calculated for clean and polluted continental air with accordingly different visibilities (50 and 15 km, respectively), thus upper and lower estimates of J_{NO3} were derived. The calculations

were performed for ϑ between 97 and 80° in 0.5° steps and for altitudes between 0 and 10 km in steps of 1 km (Figure 14.3.2). For the photolysis frequencies of NO_2, (3.3 ± 0.3) % of J_{NO3} was used determined from spectroradiometer measurements performed at the same time of the year on the roof of a building near Berlin by (Eva Eckstein, pers. comm.). The spectroradiometer measured the spectral irradiance with absolute calibration, and both J_{NO3} and J_{NO2} were calculated from these data, which made it possible to derive a proportionality factor.

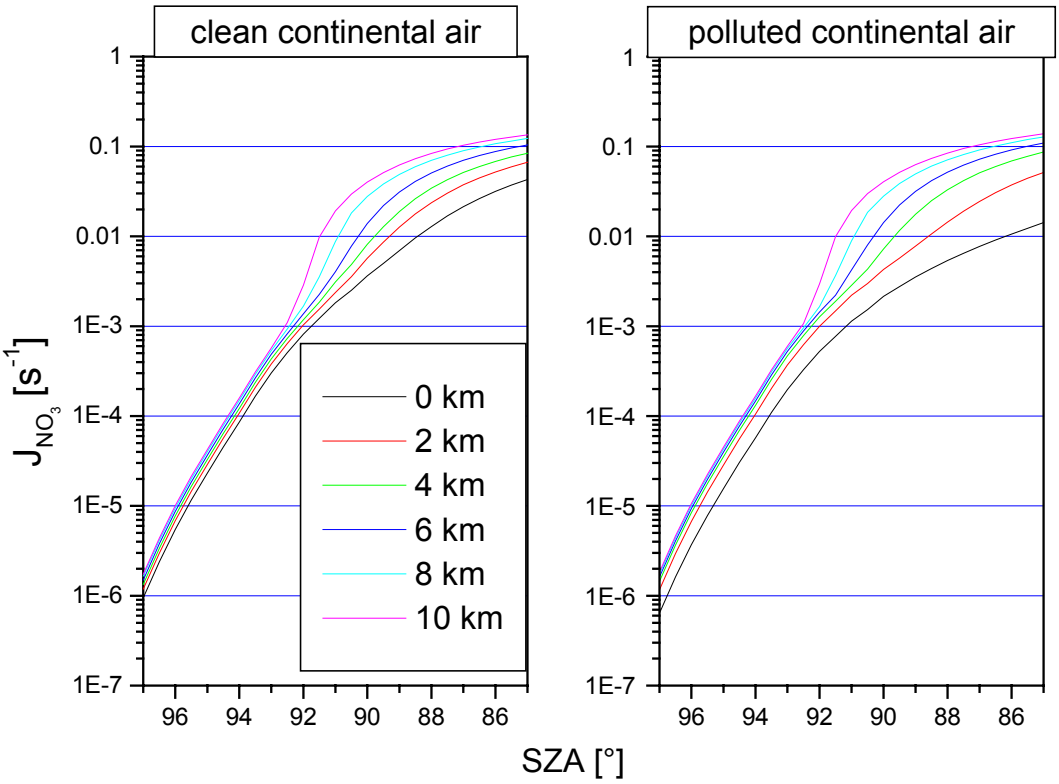

Figure 14.3.2 NO_3 photolysis frequencies calculated with PHODIS [Hugh Coe, pers. comm.]

With the same model, a possible influence of stratospheric nitrate radical on our measurements was investigated. Due to the high photolysis frequency of NO_3 in the stratosphere even for large ϑ (around 94°) the remaining stratospheric NO_3 concentration is less than 1 % of the nocturnal value in spite of the uncertainties; e.g. for the assumed stratospheric NO_3 slant column density at ϑ = 94° is typically $<10^{13}$ cm^{-2}, [*see e.g. Norton and Noxon, 1986*]. In contrast, the NO_3 slant column density measured with our instrument at ϑ = 94° is typically $\approx 10^{15}$ cm^{-2}, about two orders of magnitude larger than the stratospheric NO_3 slant column density. Hence, our measurements and the following considerations (chemical modeling and profile retrieval) address the troposphere only. Also the model confirmed the NO_3 to be unaffected in the troposphere at SZA = 97°.

Now we had to devise a method to solve the linear equation system in spite of the large uncertainties in the chemical degradation factors. It was found that the variation in all of the input parameters of the model lead to a modification in the *ϑ*-derivative of the *f(ϑ, zj)*.
I.e. a higher photolysis frequency lead to a sharper drop off of the initial concentration. A higher initial NO_2 abundance lead to a larger fraction (up to 80%) of the NO_3 formed from NO_2 and ozone during the night being stored in N_2O_5. NO_3 photolysis in the morning causes N_2O_5 to release NO_3, but with time delay, exposing the NO_3 released to even more rapid

destruction by the risen sun as would be the case without N_2O_5. This causes a sharper decrease.
All parameters were investigated to determine whether a higher abundance lead to a sharper or smoother decrease. At ground level, the VOC concentration uncertainty was found to be causing the greatest steepness variability, while above the PBL, the NO_2 uncertainty assumed this role.
As next step, two sets of *f(ϑ, zj)* were calculated: The first with all parameters set to their values leading to the sharpest „steepest" decrease; the second leading to the „smoothest" decrease possible within the uncertainties. Figure 14.3.3 shows the resulting sets of *f(ϑ, zj)*.

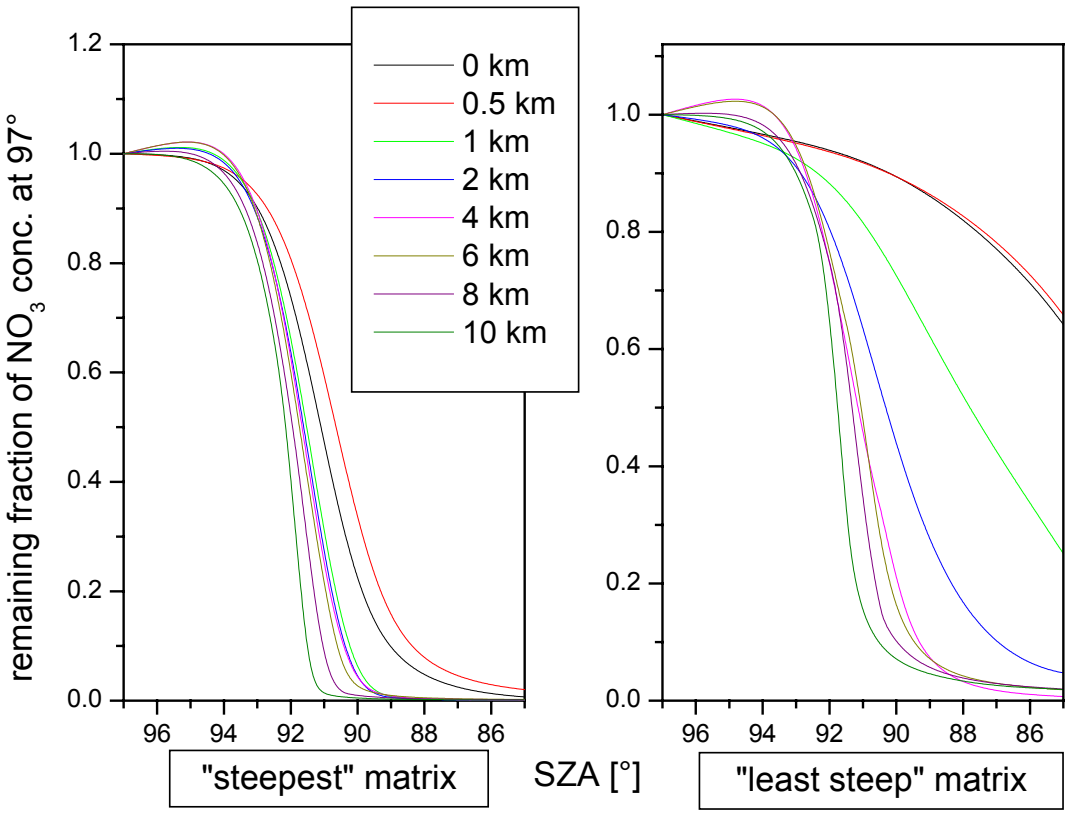

Figure 14.3.3 Sets („matrices") of f(ϑ, zj) calculated with the chemical model. The „steepest" matrix leads to the sharpest decrease of initial NO_3 abundances in the morning, the „smoothest" matrix to the slowest decrease.

The two *f*-matrices can be understood as representing two extreme environments, parametrized by the destruction velocity of an initial nitrate radical abundance in the morning. While the *ϑ* are governed by the measured data points, the vertical levels can theoretically be arbitrary. We did select a discretization with less vertical levels than data points, and with high resolution in the lower troposphere than in the higher, thus reflecting both the actual gradients in e.g. air density and concentrations of e.g. VOC as well as the higher resolution of the geometric approximation at lower altitudes (the geometrical path differences become smaller per unit SZA when the illuminated zone approaches the ground).
This discretization constitutes a second constraint [*Rodgers, 1976*] we apply to the problem, which must be prevented to exclude solutions. When varying our choice in the frame of sensitivity studies, we did either obtain the same principal profile structures as final solutions or no solution at all, indicating a gross mismatch between the resolution chosen and the

chemical gradients of the real atmosphere. We also conducted a sensitivity study on the effect of variations in profile structure on the modeled $S(\vartheta)$. Among several other cases investigated, we a) shifted the enriched layer of model profiles e.g. from the second lowest to the two adjacent boxes, and we b) used a uniform concentration throughout the troposphere, and compared the resulting $S(\vartheta)$ with each other. We found, e.g. at $\vartheta = 90°$, differences of up to 80% between the $S(\vartheta)$ obtained with a given matrix.

The next task was to find possible solutions for the equation system without knowledge which of the above chemical environments, or which one within the range (along the „steepness“ axis) represented by them, was the true one for a given measurement.

To probe the range of chemical environments with these mappings, we composed a set of N matrices representing the whole range of the modeled degradation curves, multiplied component-wise with the respective Δz_j as well as the A_{ij}; the components of those matrices are linear, equidistant interpolations between their counterparts in the two “extreme” matrices. E.g. the i^{th} and j^{th} component $m_{ij,M}$ of the M^{th} matrix is N-(M-1) times $m_{ij,ST}$ plus (M-1) times $m_{ij,LS}$, divided by N, and with $m_{ij,ST}$, $m_{ij,LS}$ as respective components of the steepest (ST) and least steep (LS) matrix. We did select N = 30, but did not obtain other solutions with N=50 or higher. We henceforth call M the degree of steepness.

Additionally, to account for the fact that at different heights the chemical conditions might fit different matrices, we introduce a further pattern of variation. The columns of each matrix are systematically varied depending on the altitude range represented by them.

1. The leftmost column (representing the uppermost altitude level) is increased by 50% of the difference to its counterpart in the next neighboring (smoother) matrix; the rightmost column (ground level) is analogously decreased.
2. The operations are performed in the opposite way.
3. The columns are increased (decreased, respectively) by 25% of the difference to their counterparts in the nearest neighbor matrix.

This leaves us with 150 matrices altogether (30 original matrices + 4 variations of each).

With these matrix variations the system is offered a range of photo-chemical environments, thus mappings from measurement space into profile space, to “choose” from. The straight forward way to facilitate this choice is to probe the range systematically using the parameter M. The final step was to find the solution(s) of a given equation system.

In principle an analytical algorithm using direct matrix inversion is preferable to solve equation (14.3.2).

Unfortunately the following facts constitute a potential obstacle to do this. First, the mapping used can be wrong, that is the degree of steepness may be the wrong one for the given measurement day’s chemical conditions. Second, the measured data points cannot be considered independent from each other, since e.g. the lowermost profile box influences, in theory, all data points due to scattered light photolysis from the very beginning of the measurement. In addition, the errors in the measured $S(\vartheta)$ values have to be considered.

Another reason for the failure of a direct inversion attempt is the very character of the degradation curves, which are reflected in the f-matrix components (see 14.3.3). The components range between 1 and 10^{-4}, which renders the matrix ill-conditioned, causing large oscillations to occur in the inverted matrix.

So direct analytical solution of the equation system is not feasible due to the model uncertainties and the measurement noise.

A possibility would be a least squares or maximum likelihood approach to obtain a profile for a given matrix. In that case, a first guess would be needed. Since these approaches usually find the next minimum in solution space, and not the true best fit to the data, we would not have found more than one solution per run. Since we have noise, we could not a priori rule out multiple solutions for a given matrix.

Non-standard ad hoc approaches have also been addressed by [*Rodgers 1976*]. He points out that they bear the danger of being nonoptimum, but may deliver solutions which agree with the optimum solution within its covariance, that is *S(ϑ)* modeled from the result profile which agree with the measured *S(ϑ)* within its errors. Here again, the possibility of multiple solutions must be considered.

We wanted our retrieval approach to meet the following criteria:

1. Only profiles which yielded, multiplied with one of the matrices, a modeled *S(ϑ)* with all data points located within the 2-σ-error ranges of the respective measured data points are used for further processing.
2. The number and magnitude of the measurement errors must be reflected in the profile error; this process must not minimize the error of one part of the profile vector at the expense of the others, since the location of interesting features within this vector is not a priori known.
3. Profiles yielding modeled *S(ϑ)* vectors which are in better agreement with the measured one shall contribute more to the finally resulting profile vector.

We therefore decided to use a Monte Carlo technique as follows. The NO_3 concentration in each vertical layer was selected randomly and the NO_3 profile vector was multiplied by the degradation matrix M. By performing a large number of runs, the absolute minimum in solution space is, within the measurement errors, found with greater certainty.

For each matrix random profiles are generated as outlined above. Each random-generated profile is multiplied with the matrix yielding a modeled S(ϑi) series. Only if for each ϑi the calculated SCD value is located within the 2-σ-errors of the measurement, the respective profile is kept as valid, otherwise rejected. This procedure is performed for all 150 matrices. For each of the valid profiles, χ is calculated as square sum of the absolute deviations between measurement and modeled SCD (for N measured SCD values):

$$\chi = \sqrt{\sum_{k=1}^{N} (S_{k,\mathrm{mod}} - S_{k,meas})^2} \tag{14.3.4}$$

Using 1/χ to weight the respective profiles a mean profile is calculated from all valid profiles. Analogously, for the error of this final profile a modified standard deviation using the same 1/χ as weighting factor is used. These errors thus are largely governed by the measurement errors. It is obvious that the more measured data points are available, and the smaller their errors are, the fewer possibilities exist to obtain a valid profile, the smaller its variations are, and the smaller the resulting profile errors are.

The method turned out to be ambiguous. Valid profiles (as defined above) were obtained from groups of different matrices representing contradicting chemical conditions. In most cases the matrices yielding valid profiles were found to be grouped around one or two points on the „steepness“ axis (parameter M). (One day, the 26th of July, represents an exception as valid profiles were obtained from virtually all matrices.) The profiles belonging to one group were similar to each other but systematically different from the other group's profiles.

Figure (14.3.4) exemplary shows the resulting NO_3 vertical profiles for three clear days for which measurements were performed in Heidelberg in summer 1999.

The color coding of the profiles indicates the matrix group from which they were derived. The horizontal bars denote the statistical error as calculated above; the vertical bars indicate the thickness of the vertical layers.

The red profiles belong to the steepest matrix group (first third of the steepness axis); for this group the NO_3 maximum is located at altitudes around 350 meters; the blue profiles refer to the smooth matrix group; the NO_3 maximum of this group is situated at altitudes around 2.5 km. The green profiles belong to the matrices in between of the extremes, being similar in

shape and concentrations to the blue group. In most cases no valid profiles were found in this area of the steepness axis, and if so, the resulting profiles resembled closely the blue ones. Although the profiles belonging to the "steepest matrices" can be very probably regarded as the true profiles (see below), some important conclusions can be drawn without any selection between the two solutions; first, for all cases an enriched layer is found, that is a pronounced nitrate radical concentration maximum within the lower troposphere; the respective maximum concentrations range from (100 to 900) x 10^7 cm^{-3}. Above this layer, the concentrations sharply drop to less than 50 x 10^7 cm^{-3}. Below the layer, especially near the ground, all derived profiles show very low concentrations of typically far less than 10 % of the enriched layer's concentration. This is a clear confirmation of suggestions of Aliwell and Jones [1998] and Fish et al. [1998].

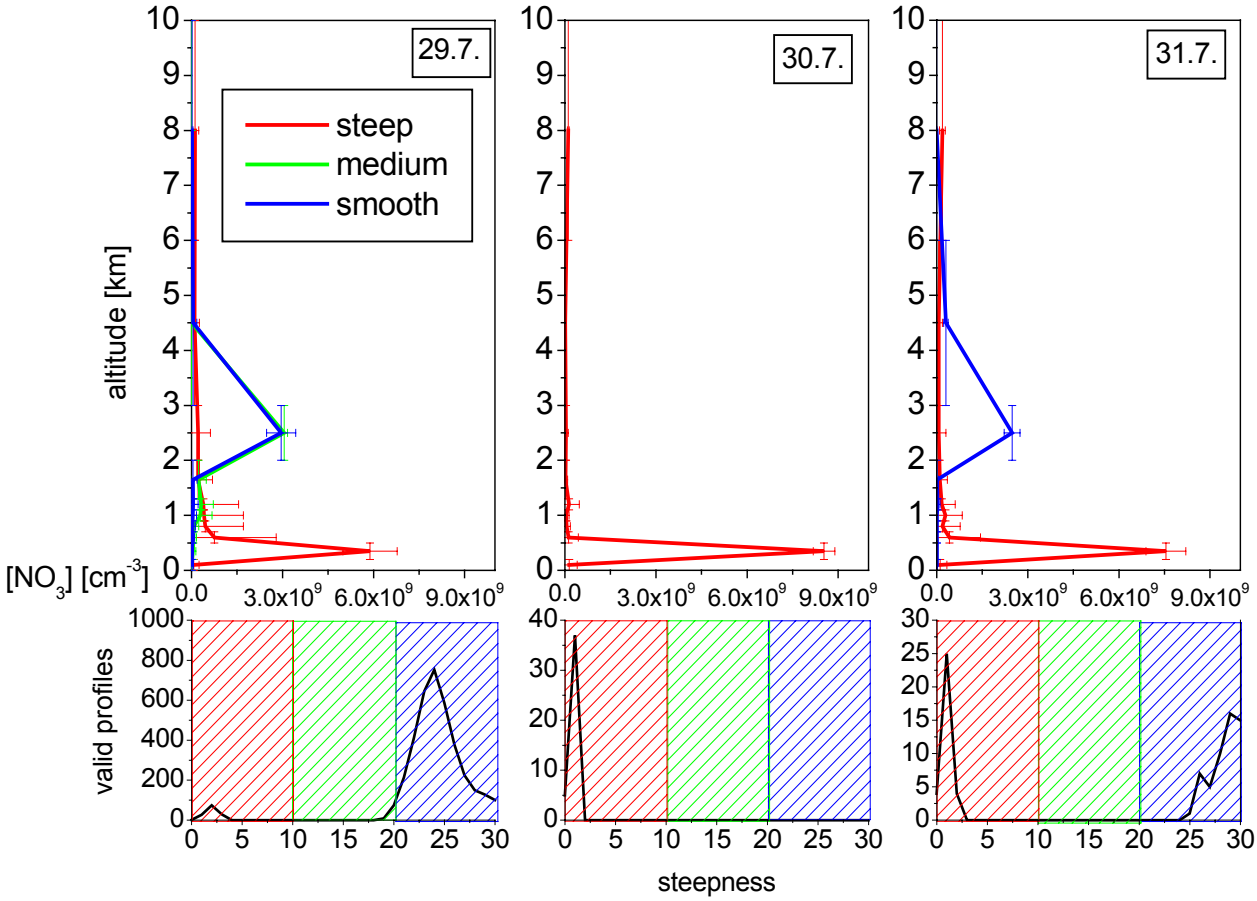

Figure 14.3.4 Weighted mean nitrate radical vertical profiles derived from DOAS-SCD-measurements in summer 1999 using the modified matrix method (2nd of April, 26th and 27th of July). The profiles are grouped according to the position on the steepness axis of the matrix, which yielded the profiles. Shown below each profile graph is the number of valid profiles found for the matrices represented by the axis number. The red profiles refer to the red (steepest) section of this axis, and show their concentration maximum at around 350 m altitude; the blue profiles belong to the smooth matrices (blue section) and possess their maximum within the 2.5 kilometres altitude box. The green profiles refer to the matrices in between, which in most cases did not deliver valid profiles. Please note that the profile shape is controlled by the vertical extensions of the boxes holding the randomly generated concentrations; these boxes's sizes were chosen according to the tropospherical chemistry's spatial variability being higher near the ground than in the free troposphere. The vertical bars represent the vertical resolution of the model, while the horizontal bars describe the statistical error in concentration. According to the meteorological condotions at the measurement site, we conclude that the red profiles (steepest matrices) are the true profiles.

The mathematical algorithm gives no direct indication which profile is the true one. However, one can find some indirect indications considering which environment the different matrices represent. Due to the strong influence of the VOC at low altitudes the steepness is largely governed by VOC. The matrices which correspond to the blue profiles represent the cases with very high VOC concentrations and, hence, degradation rates $f_{NO3\text{-}VOC}$ of NO_3 against them of up to 0.4 s^{-1} throughout the mixing layer, whilst the matrices corresponding to the red profiles are associated to $f_{NO3\text{-}VOC} <= 0.13$ s^{-1}, which is still larger than the great majority of the derived data in [*Geyer et al., 2001a*]. The VOC which are relevant for NO_3 depletion are mainly emitted by trees, i.e. at an altitude of about 20 m [*Geyer et al., 2001a*]. Even with low ground level nitrate radical concentrations the lifetime of these VOC against NO_3 and ozone does not allow them to reach altitudes higher than 200 m within the mixing layer. Under standard meteorological conditions at night (no convection) the transfer of VOC to higher levels is restricted. It cannot completely be ruled out, though, that unusual upwind situations can carry VOC to higher altitudes within the mixing layer. For this reason, due to the lack of on-site data, we had to include this possibility in our choice of the upper estimate of $f_{NO3\text{-}VOC}$.

To resolve for this ambiguity, an additional modelling was performed with an elaborate model, the comprehensive non-hydrostatic mesoscale model KAMM/DRAIS [*Vogel et al., 1995, 1999*]. For details see again [*v. Friedeburg et al. 2002*]. The results confimed the „red“ profiles in both the shape and the concentrations. The only difference was a slower decrease in concentration with altitude above the enriched layer.
The „green“ and „blue“ profiles could not be reproduced by KAMM/DRAIS with any input parameter set used. For these reasons we conclude the blue (and, if applicable, the green) matrices to represent chemical conditions which are very unlikely (e.g., strong upwinds above the forest during night).
Thus, we conclude that the red profiles must be the ‘true’ atmospheric profiles. The results indicate that the majority of the tropospheric nitrate radical during the night is accumulating within an enriched layer in the lower troposphere. The absolute values of the maximum concentration range from 100 to 900 x 10^7 cm^{-3} , while the concentrations below this layer and above are much smaller.

14.4 Conclusions on the Monte Carlo matrix technique

The technique presented was capable of deriving a vertical profile from DOAS SCD using a matrix with components combined from Box AMF and chemical factors accounting for the variation in the concentration vectors with time.
These factors were calculated from sets of reactant estimates and known relationships between them and the target species. One additional a priori data was needed, i.e. the information from KAMM/DRAIS that no NO_3 can form above the PBL with any realistical chemical situation.
But the algorithm at least delivered knowledge on a possible second solution rather than converging on to the the nearest minimum in solution space, i.e. along the steepness axis.
By projecting all chemical processes on to this axis, the need for vertical profile data on any specific species was reduced and made less critical.
This steepness is the magnitude determined to give the best fit to the data, and it is the result from the combination of a number of vertical profiles of the relevant species, which as a whole form a specific chemical situation or environment “towards” NO_3. This means that the reactant profiles do not have to be known in full detail. An error in e.g. NO_2 may be compensated for by an error in VOC, for example, to yield the same degree of steepness, as

stated. Thus it is only necessary to chose the upper and lower reactant concentration estimates large and small enough, respectively, to encompass the real situation with the steepness range obtained. This fact makes the modified matrix algorithm a method for profile retrieval, which is applicable to a wide range of atmospheric conditions. However, if the uncertainties in the parameters are too great, more than one solution can occur, which stresses the need for at least a limited set of chemical data, including of course some knowledge on the chemical relations.

In case of the measurements and/or RT calculations presented in chapters 9, 10, 11, 12, we find that an uncertainty parameter similar (mathematically) to the VOC-degradation are constituted by the aerosols. Their load, and their optical properties are largely unknown for most cases, if standard scenarios and approximated values are left apart. Be it, as concluding part of this chapter, outlined how a target species retrieval could be performed in spite of this uncertainty using the algorithm described in 14.3.

By means of reducing the *LSD*, aerosols alter both the AMF for the target species as well as of O_4. A parameter comparable to the steepness parameter could be a function of the O_4 AMF for slant elevations, e.g. the ratio of the slantest two ones. Be M_{O4} this parameter.
This mapping could be used to conclude on the aerosols. Data on all aerosol properties, i.e. number density vertical profile, phase function, single scattering albedo of the aerosol type(s) present must in the first step be collected, and upper and lower estimates on them (in case of the phase functions, e.g. parametrized using the assymetry coefficient) composed. Then they, and other unknown parameters, are investigated regarding their effect on M_{O4}. Then they are composed in two groups, the one yielding the largest possible M_{O4}, the other group the smallest.
It must be investigated, though, whether the compensation of the decrease in e.g. the aerosol load by e.g. a change in phase function can lead to the same M_{O4}, but to different AMF for the targest species. In this case M_{O4} may have to be modified, e.g. by incorporation of more elevations, sensitively react to this variation as well. Hence M_{O4} becomes 2- (or more) dimensional.
This done, a fitting can conclude from the measured M_{O4} on the aerosol load, within a given uncertainty interval due to e.g. O_4 measurement noise.
As second step, AMF or Box AMF can be modelled for the aerosol loads represented by the interval. Then the retrieval matrix can be attempted to solve for the profile vector in the same way as described above.

15. Conclusions and future work

DOAS applications utilizing direct light, be it artificial or natural, are hardly affected by e.g. multiple scattering; but they are limited to operation near the ground or dependent on the position of the sun. Scattered light DOAS can be realized with simpler hardware and operated from various platforms, including satellites, and can probe the entire troposphere and stratosphere. But the interpretation of the data relies on realistic radiative transfer modelling.
The main topic of this thesis is the development and application of a Backward Monte Carlo Radiative Transfer Model (RTM) TRACY (**T**race gas **RA**diative Monte **C**arlo **Y**(I)mplementation). It is capable of:

- calculating the radiative transfer in full sphericity and three dimensions,
- supporting all measurement geometries, including aperture characteristics
- taking account of full multiple scattering by Rayleigh and arbitrary aerosol scattering, refraction, albedo and polarization,
- offering a phenomenological approximation of cloud cover treatment
- deriving Air Mass Factors, Slant Column and Optical Densities of trace gases, aerosol and air column data, numbers of scattering events and scattering location parameters as well as radiometric quantities including error treatment
- and usable with any Windows PC or notebook with straight forward ASCII files for parameter input and model mode control.

Existing and well established RTMs, e.g. SCIATRAN and DISORT, solving the radiative transfer equation with analytical algorithms suffer from deficiencies since they are based upon certain approximations, e.g. limitation to spherical layers or treatment of the atmosphere's sphericity and refraction only for the direct solar light beam. Furthermore, they so far do not support all DOAS measurement geometries, and also do not calculate scattering locations and event numbers. Hence they cannot be used for the interpretation of all DOAS applications.
The Monte Carlo method, in contrast, does not require simplification of either geometry or the physical processes involved in radiative transfer. The Backward Monte Carlo scheme "launches" photons out of a detector and calculates their path through the atmosphere. This is much more efficient, hence faster, than Forward Monte Carlo. The derived additional scattering parameters, like the numbers of scattering events, see above, serve to explain the dependencies of Slant Column Densities on e.g. measurement geometry and environmental conditions. For the derivation of vertical profiles in a linear equation system, a weighting function equivalent, the Box Air Mass Factor, is developed and applied. The fundamental drawback of Monte Carlo methods, high computation time consumption, becomes less significant with the progress of computers. For certain situations, Forward Monte Carlo can be faster; for this reason, a Forward RTM scheme was developed and preliminarily tested.
In the case of features that could not be fully developed within the limited time frame of this work, approaches were sketched to treat them within the structure of the data objects and algorithms of the program. These are:

- rotational Raman scattering,
- polarization by aerosol scattering,
- refraction after the last scattering event of a modelled path.
- a user interface to ease the reading of 4D trace gas fields

- Also an operational data interface to incorporate the model into the data analysis pipeline for satellite data needs to be developed without sacrificing flexibility and user accessibility.

TRACY model results agree well with established analytical RTMs. For large Solar Zenith Angles and stratospheric absorbers, differences are to be noted, which could be attributed to approximative treatment of sphericity in the analytical models.
The usability of TRACY for ground based, airborne and space based DOAS applications is demonstrated with several examples and sensitivity studies. It also offers interpretation for new DOAS methods such as the Imaging DOAS or the scanning of gas plumes.
An extensive investigation was performed to interpret data derived with the novel Multi Axis DOAS method. It uses the varying measurement sensitivities of different line of sight elevations, probed either sequentially or simultaneously, to derive profile data on tropospheric absorbers. The effects of environmental parameters and especially of aerosol scattering on the Air Mass Factors and Slant Column Densities of trace gases and O_4 were investigated. These calculations show that geometrical approximations of the Air Mass Factors lead to large errors. However it is shown that Air Mass Factor ratios and O_4 absorption measurements provide a tool to quantify the aerosol load from the measured data and constrain the trace gas retrieval problem.

- The effects predicted were confirmed by existing Multi Axis data of tropospheric BrO.
- Measurements of NO_2 at a motorway were performed with a Multi Axis instrument simultaneously probing multiple lines of sight. Two evaluation techniques are presented to evaluate spectra recorded with this device.
- Existing data recorded with the same instrument of O_4 and HCHO in the Milano area were also compared to model results.

The results support and confirm the predictions on the effects of aerosols on Air Mass Factors and Slant Column Densities. In case of the BrO and the HCHO measurement, a statement on the actual vertical profile was derived. Future work must expand the investigation to optimise the measurement geometry and the retrieval.

- Spectra recorded during a solar eclipse were evaluated and a technique was developed to overcome the solar Centre to Limb Darkening effect. The results agree well with a simple single scattering RTM. This did lead to the idea of the Forward Monte Carlo RTM.
- Software for a commercial calibrated spectro radiometer was devised to provide an operational package including user-friendly measurement control, data evaluation and high precision solar position calculation. It offers the capability to measure simultaneously trace gas photolysis frequencies in addition to the trace gas data measured with DOAS.
- Measurements of directional irradiances with the instrument were compared to model results by TRACY. They quantify the dependency of irradiance on aerosol load.
- The effects of combining the spectro radiometer with a polarization filter were briefly investigated, paving the way to take advantage of polarization as well when comparing measurements and model results.

Future work must assess the potential to use the radiometer for not only photolysis frequency measurement but also for additional aerosol data retrieval in field campaigns.
Finally, a Monte Carlo method to derive vertical trace gas profiles with input data only known within large uncertainty intervals was developed and applied to NO_3 measurements. The technique can be adapted to Air Mass Factor ratios and O_4 absorptions of other measurements.

The investigations show the necessity of realistic radiative transfer modelling for the interpretation of scattered light DOAS. With the increase of the importance of various scattered light applications radiative transfer modelling will become an indispensable requirement.

Appendix A: TRACY objects and implementation

A.1 Introductory remarks on Object-Oriented Programming

The Object-Oriented Programming (OOP) is a strategy possible with high level programming languages such as the C++ employed. For details and concepts on C++ see [*Stroustrup 1998*].
Non-OOP High Languages, such as Pascal, Turbo-Pascal or C, on which latter C++ is based concerning syntax, treat as different entities variables holding data and result values, and functions and procedures used to calculate results from values. The variables may be grouped in arrays (of in theory infinitely dimensional depth) or records, the latter comprising variables (or arrays of them) of different type.
The functions and procedures must be given all the relevant variables or arrays, or copies of them, in order to enable them to perform the desired operations. Furthermore, for each operation being similar in task, but different bin realization, either a different routine must be written and called, or if-clauses must be used to discern between certain cases by use of the variable contents.
C++ has added features of treat variables, or groups of variables, and the routines designed to work with them as parts of „objects“. These objects form classes which can „inherit“ properties from each other, that way reducing the necessity to implement identical routines several times. The classes form variable types, these types comprising in itself sets of variables as well as the functions. An object of given name may be declared as object of a given class type. From this line of code being processed, it possesses all variables assigned to the object as well as the related functions which can be addressed using the name of the newly created objects. The declaration, also named „initialization“, may be performed with variables, or with other objects with variables defined, so that these variables become part of the newly created object.
The objects may also be grouped as arrays, such as variable declared in C syntax as eg „float“ or „integer“ variables.
Since the functions are defined for and adressed through their respective classes, two functions may bear the same name, although performing different algorithms for different objects. The best way, though, to make use of this possibility is to use identical names for routines tasked with the same type of operation, e.g. the calculation of an intersection point of a line with a surface of different types.
In combination with the grouping of objects in arrays a highly efficent way to adress routines is feasible, as explained in the example to follow.
In the source code of TRACY, one important object class is the “surface” class. They consist of two “SpaceVector” variables, in turn fomed from three double precision floating point variables. These two vectors define each of the following objects belonging to the “surface” class (see below section on geometrical structure):

- planes,
- cones,
- and spheres.

In the course of the algorithm of modelling a photon path within a geometrical structure of grid cells, which are defined by pairs of these surfaces, an operation perfomed with high frequency is the derivation of an intersection point of the current photon trajectory and the next boundary surface of the grid cell the photon is located within.
This task is perfomed by the routine “GetPOI”. Of this routine there are several ones bearing this name; the one originally called up is the “GetPOI” which is part of the grid cell’s object. It is passed the photon trajectory.
This routine now uses the voxel indices (which also belong to the grid cell object’s attributes) to identify the boundary surfaces enclosing the grid cell and to initialize them by mapping these index numbers to the spatial discretization chosen by the user along the three coordinate axes. In spherical geometry, these surfaces are two planes, two spheres and two cones. These six initialized surfaces are grouped in a six-element array of class type “surface”.
After this, the “GetPOI” routines defined on the three surface types are called up one by one by use of the array name, the array number and the function name “GetPOI”.
Each of this routines receives the photon trajectory and uses the appropriate algebraic techniques to calculate an intersection point between trajectory and surface. The return variable is a parameter with a value by which the trajectory must be elongated to intersect the respective surface. If there is no intersection along the photon flight direction, the parameter is negative.
The voxel “GetPOI” routine receives the six parameters and choses the smalles non-negative one of them. This parameter is returned to the calling routine.
This way, the task of finding the next intersection point is decomposed into single sub-tasks of similar but different nature which are performed by specifically written, but uniformly adressed functions.
A similar structure was established concerning the different scatterers, Rayleigh, aerosols, earth surface and clouds, which each possess their routines performing the direction change or probability calculations. For more details on this object structure see [*Morgner 2000*].
Another feature of the OOP is the encapsulation and the principle of secrecy.
They address the implementation of routines with a very limited set of variables used as interface to other routines or the main program. The actual algorith performed within is “encapsulated” from the outside program code and kept “secret”. Consequent use of this doctrine facilitates the rapid exchange of routines by updated or enhanced versions when they have the same interface since the interaction with the rest of the program does only depend on that interface. The encapsulation also leads to an easily understandable and expandable code.
The inherent drawback of this is that the strict limitation of the interface parameter set easily leads to duplication of computation, since calculations, e.g. of a scattering coefficient sum within a grid cell, may be needed in not only one but in several routines. Duplication and repetition especially of parameter derivations needed with high frequency significantly reduces the modelling speed of the code. Since speed is critical when high photon numbers are needed to reduce the noise of Monte Carlo modellings the strict principle of secrecy was decided to abandon, and the set of interface parameter was expanded for most of the routines conceived by [*Morgner 2000*]. Other routines were entirely rewritten to support new features such as Box-AMF derivation. In the following sections, the crucial algorithms and routines of TRACY in their current form are explained.

A.2 Fundamental objects

The following sections describe the decisive objects and routines used in TRACY. The listing is not complete, as there are several routines tasked with internal data handling of which a description does not add to the understanding of the algorithms. They are commented, though, in the source code.
Also not listed below are routines concerning the forward MC implementation (see chapter 13), since this is still under development and so far has not been fully validated.
For a manual on TRACY see Appendix B.

A.2.1 Voxel and geometrical structure

The model employs full spherical three-dimensional geometry.
The definitions of the coordinate system, and the vectors of detector position, line of sight and solar position have been explained in chapter 6. The discretization is freely chosen by means of an ASCII file („space.txt“, see manual in Appendix B) with the numbers of discretization steps for the ϑ-, the Φ- and the **Z**-axis, N_ϑ, N_Φ and N_Z in the first line and the selected coordinate values ϑ_i, Φ_i (in units radian) and $\mathbf{Z}_i$ (in unit km, above earth surface) of the limiting surfaces in the three lines below. The “Top Of Atmosphere”, TOA, can thus be chosen by the value $\mathbf{Z}_{Nz}$. Three numbers address a given voxel:

- *X* for the latitude, 0 for the voxel between latitude 0° and the first chosen latitude step
- *Y* for longitude, 0 for the voxel between latitude 0° and the first chosen longitude step
- *Z* for altitude, 1 addresses the voxel between ground level and the first vertical step. A voxel with Z=0 can be implemented in the future to account for e.g. radiative transfer effects below an ocean surface

The defined voxels are assigned

- air number densitiy in [cm^{-3}], relevant to scattering and refraction
- pressure in [mb], not used in this work, but useful for later modifications
- temperature in [K] , not used in this work, but useful for later modifications
- trace gas concentrations in [cm^{-3}] of the absorbers used
- aerosol type extinction coefficients in [km^{-1}]

From these initialization parameters, others are derived such as refractive indices and total extinction coefficients. From the aerosol extinction coefficients, the scattering and absorption coefficients are taken. Also clouds can be inserted here, as number densities of droplets of different sizes. A different cloud treatment, and the one used in this work, is the definition of a cloud layer of parameters altitude, coverage, albedo and transmission, see section 4.4. The parameters can be obtained and worked with by any routine that is given the respective voxel object.

A.2.2 Photon unit PU

Apart from this “*Intensity*”, the direction and the location vectors, the PU objects have the following attributes:

- *Lambda*: the wavelength in [nm];
- *Nlamb*: the refractive index term dependent on the wavelength; the total refractive index is derived from this in conjunction with the air number density of a given voxel;
- *RaylCSlamb*: the wavelength dependent Rayleigh cross section in [cm^2];
- *Geometry*: an integer with the number of the actual measurement geometry currently modelled; e.g. if there are three telescope LOS, they are numbered 0-2; the photons launched in these carry with them this number in the *Geometry* variable;

- *Dist*: The distance from the actual position/path point to the last position/path point, updated at every position shift/path point generation;
- *FracDev*: the deviation in [°] of the photon direction by atmospheric refraction at a voxel boundary;
- *EntryAngle*: the angle in [°] between the emerging photon's direction after forcing, i.e. the solar vector, and the surface normal at the exit point; for a real photon it would be the atmosphere entry angle;
- *ScattAngle*: the scattering angle θ in [°] of the last scattering event (initially set to zero);
- *ForceScattAngle*: the scattering angle in [°] of the scattering introduced by the forcing;
- *ActualAbsorber*: the number of the scatterer that is selected for forcing by the respective local extinction coefficients and random numbers;
- *ForceAlt*: the altitude above sea level in [m] of the scattering point introduced by the forcing;
- *LastPhotDir*: the photon direction prior to forcing that led the photon in a "wrong" direction out of the atmosphere;
- *IsForced*: a flag initially of value 0, but set to 1 when the photon gets forced; if it is 1, it prevents further scatterings when the user wants to allow for only one forcing;
- *IsScattered*: a flag initially of value 0, but set to 1 when the photon gets forced; if the user sets the program to allow for only one scattering event, the flag prevents scatterings once it has value 1;
- *LastScatterType*: the type of the last scatterer; 1 for Rayleigh, 2 for aerosol, 3 for albedo, 4 for cloud interaction;
- *X, Y, Z*: the indices of the voxel the last scattering event took place within;
- *NRS, NMS, NAS*: integers containing the number of the Rayleigh, aerosol and albedo scatterings the photon has suffered so far in its path;
- *TNS*: the total number of scatterings so far in the photon path;
- *ScattNumber*: since there are multiple possibilities for aerosol scattering (one for each aerosol type) and for cloud scattering (reflection and transmission), these subtypes get assigned a number stored in this integer;
- *FSP*: The location vector of the last scattering event modelled; for a real photon, it would be the first;
- *LSP*: The location vector of the first scattering event modelled; for a real photon, it would be the last;
- *FSA, LSA*: The scattering altitudes in [m] above sea level of the first and last scattering event, respectively;
- *LSD*: The distance in [m] between the detector and the last scattering event;
- *NPP*: the number of path points modelled for this photon so far;

The photon paths are calculated only taking the elastic scattering processes (Rayleigh, aerosol, albedo) into account. The albedo is modelled by reflecting the PU considered off the ground in a direction governed by the Lambertian characteristics, and reducing the intensity by multiplying it with the albedo.
The second alteration of weight is the forcing applied at the end of the photon path.
The attenuation by trace gas absorption and aerosol absorption is calculated analytically using the segments of the complete path.

A.2.3 Detector

The detector is the "source" in backward MC modelling. The most important characteristics already have been listed: latitude, longitude, altitude, elevation, azimuth and aperture angle.

The angle and the position and LOS vectors are stored to arrays of floating point and vector variables, respectively, with 10 elements each to support up to ten viewing geometries of a MAX DOAS operation.
Also the wavelength is stored, since it governs the wavelength of the emitted photons. Apart from these attributes, the following variables are part of the detector object, of which the ones with "[10]" are stored in arrays.:

- *XIndex, YIndex, Zindex*: the voxel index of the detector location;
- *LOSVec[10]*: the LOS vectors;
- *LOSRight[10]*: it is calculated as vector product from the LOS and the local surface normal; in zenith and nadir viewing geometries, it is the "east vector", pointing to the local "east" and at the "north pole" it is the cartesian vector (0,1,0). This vector thus points in "left-right" direction, in slant viewing geometry parallel to the local surface plane, and is used to orient the initial photon direction vector in the case of elliptical aperture characteristics.
- *LOSUp[10]*: the vector formed from the LOS vector and the *LOSRight* vector; it is perpendicular to the LOS and pointing upwards; for zenith and nadir viewing geometries it is the "north vector", at the north pole it has cartesian coordinates (-1,0,0). This is the second vector necessary to orient photon directions by when the aperture characteristics is elliptical.
- *DetApertureRight[10]*: The detector aperture angle along the LOSRight vector; this accounts for detector aperture characteristics which are elliptical rather than spherical. In this case the ApertureRight value differs from the aperture angle;
- *CosineFlag[10]*: an integer flag that if set to 1 weighs the emitted photons with the cosine of the angle between their initial direction and the detector LOS vector;
- *DetectorArea[10]*: the area in [cm^2] of the detector; usually the telescope front lens area is used for this value; for AMF, SCD amd radiometric quantities defined as per unit area the quantity is in excellent approximation meaningless.
- *LOSNumberElements[10]*: the number of segments of the LOS from the detector to either the earth surface or the TOA; it is defined by the voxel discretization;
- *ActualGeometry*: the number of the actual geometry (the array number of the detector array object) that is currently worked with;
- *BoxSystemLimits[9]*: the minimum and maximum voxel indices in the three spatial dimensions for which the program should derive Box AMF;
- *BoxSystemArray[]*: the array to store products of distances covered by photons within a given voxel with their final intensity weight in order to derive Box AMF;
- *TotInt*: the total intensity "received" by detector to derive the Box AMF;

The detector object can be passed to routines which calculate model output data and need the detector and viewing parameters for their task. But at the beginning of each backward MC photon path run, the detector parameters govern the initial photon vectors

A.2.4 Fire

The *fire* routine is what each single backward MC path begins with.
It is passed the detector object and its parameters.
The photons is "equipped" with the wavelength and ist parameters are set to their default or start values, e.g. the *IsScattered* flag is set to 0, so are the scattering numbers *NRS*, *NMS*, *NAS* and *TNS*.

Then the photon location and voxel indices are set to the detector`s. Depending on the aperture characteristics, *fire* generates the random numbers necessary to derive the initial direction's deviation from the LOS according to the scheme described in section (6.4.2).
Ultimatly, the routine "fires" the photon into the model system by assigning the new direction to the photon.
If the detector is space borne, the point where the photon "enters" the atmosphere is taken as initial location.

A.2.5 GetPOI

The *GetPOI* routine actually consists of several routines, with one calling up the surface-object related ones. It receives

- the voxel indices of the photon,
- its location and
- direction vectors.

The it calculates the next intersection point with the boundary surfaces of the current voxel.
Each *GetPOI* computes a parameter d_S by which the photon direction vector, which is always normalized, must be elongated in order to reach the intersection point; this at the same time is the distance which the photon must cover until it reaches this surface. The calling GetPOI then chooses the smalles non-negative parameter *d*. This parameter is the distance the photon will cover before leaving the voxel. It returns:

- the derived intersection point
- the parameter *d*
- the indices of the voxel which is entered at the intersection point

The routine has been modified not to check "blindly" the intersection with six surfaces, but only for the surfaces in existence in the spatial discretization used. This increases computational speed when modelling in 1D or 2D discretization instead of 3D.

A.2.6 Extinction decider

The *ExtinctionDecider* is the routine deciding on

- whether a scattering occurs,
- where along a given distance,
- and by which scatterer

to a photon on its way to the next derived voxel boundary.
It receives as input variables:

- The distance d the photon has to cover within a given voxel,
- the voxel in question,
- the photon with its wavelength and Rayleigh cross section.

The output variables are

- a distance d_s the photon will travel without either a scattering or a voxel intersection,
- the number of the scatterer: 0 if there is no scattering, 1 for Rayleigh, 2 for aerosols, 3 for ground reflection, 4 for cloud interaction. It also modifies the photon's *LastScatterer* and *ScatterType* parameters according to the outcome of the following algorithm.

From the photon the Rayleigh-cross section σ_R is fetched. From the voxel it obtains the air number density ρ and the scattering coefficients κ_S of the N_A aerosols.
The aerosols (up to ten different types) are parametrized not only by their phase function a vertical profile of extinction coefficients, but also by a ratio $\varpi' = \kappa_{Abs}/\kappa_{Ext}$, which is

equivalent in information to the single scattering albedo ϖ (see section 4.2.4), and must be chosen from appropriate data or reference. This parameter allows for the separation of a given aerosol type into a scattering part and an absorbing one. E.g. with a given number density *n* (equivalent, for a given cross section, to the extinction coefficient), a given ϖ' means that a fraction ϖ'of all interactions photon-aerosol lead to absorption of the photon, as in the case of a trace gas, while (1-ϖ') results in elastic scattering. Hence we can treat the fraction ϖ' of the aerosol particles as additional trace gas to be accounted for when deriving spectroscopic parameters from the completed paths, and (1-ϖ') of the aerosol particles as scatterer like Rayleigh particles.
From these data the probability *t* of transmission without scattering is derived by:

$$t = e^{-d\left(\rho\sigma_R + \sum_{i=1}^{N_A} \kappa_S\right)} = e^{-d\kappa_{S,tot}} \tag{A.2.1}$$

This formula denotes a function *f(x)* which is always unity at $x = 0$ and $f(x) = t$ at $x = d$.
This done, the decider generates a random number $R_T \in [0,1]$ and bases the further algorithm upon two cases:
$R_T <= t$: the photon does not get scattered. The output parameter is set to *d*, the absorber number of the photon to 0.
$R_T > t$: the photon is scattered. In this case the the function (6.5.1) is inverted to map R_T (which is within the interval defined by the function values of *f(x)* with $R_T \in [0,d]$) to the abscissa:

$$f^{1}(R_T) = x \tag{A.2.2}$$

Due to the exponential character of the function a large enough number of experiments will place more x per unit abscissa axis near the value $x = 0$ than near $x = d$. This reflects real photons to be scattered out of a direct path rather at the beginning of the way along a scattering distance than at the end.
This *x* derives denotes the place along the photon direction and within *d* the photon scattering takes place. The output parameter d_s is set to this *x*.
After this, a second random number R_S is generated with $R_S \in [0,\kappa_{S,tot}]$; $\kappa_{S,tot}$ is the total extinction coefficient introduced in Eq. (6.5.1). This R_S now gets successively compared first to the Rayleigh scattering coefficient, then to the Rayleigh coefficient plus the first aerosol scattering coefficient, then to the sum of the Rayleigh and the first two aerosol coefficients and so forth until it is found to be smaller than one of these sums. If it is smaller than the Rayleigh coefficient, Rayleigh scattering is identified as "responsible" for the scattering of which the existence has been established in the first algorithm step. The *LastScatterer* is set to 1. If it is larger than (or equal to) the Rayleigh coefficient plus *i* aerosol coefficients, but smaller than this sum plus the $(i+1)^{th}$ aerosol scattering coefficient, the $(i+1)^{th}$ aerosol is decided to be the scatterer. In this case, *LastScatterer* is set to 2, the *ScatterType* to i+1, to be used as event subtype in the next calculations.
If clouds are present in the model, the vertical index of the cloud cover is compared to the one of the current voxel. If they agree, it is checked using the *GetPOI* routine whether the distance d_c to any valid intersection point of the photon trajectory with the cloud cover is shorter than *x*. If this is the case, the scatterer is set to 4 (for cloud interaction) instead of determining either Rayleigh or an aerosol type as scatterer. The output parameter d_s is accordingly set to this d_c.
A different treatment is used when the program is running in the single scattering mode and already one scattering event of either kind has taken place, as recognized from the *IsScattered* flag of the photon. In this case, the output number of the scatterer is set to 0 to prevent the

code from actually performing a scattering. But the intensity weight is scaled with the transmission *t*. If a cloud cover is encountered, the weight is scaled with the transmission probability of the cloud cover as well. The same is done in "single forcing mode" when the photon has been already "forced" once.

A.2.7 AlterPhoton

The *AlterPhoton* routines perform the scattering operations. They are another kind of functions belonging to different objects. There are five of them: For Rayleigh (named *Rayleigh*), aerosol (named *Mie*), surface reflection (named *Albedo*), and cloud interaction (*Cloud*); the fifth one is a dummy with routines of the same names and interfaces as the others, but performing no operations concerning the photon direction and weight.

These five types of scattering objects belong to a class named *Extinction.* They are grouped in an array of type *Extinction*. The routines assigned to the different objects can be adressed by the array number. The first array element is the dummy; the second one (addressable by number 1) is the *Rayleigh* object, the third the *Mie*, the fourth the *Albedo*, the fifth the *Cloud*.
The number to be used here is the scatterer type number generated by the extinction decider. It is used in a called composed from the array name, the scatterer type number in brackets and the name of the routine which is needed here, in our case the *AlterPhoton*.
All the *AlterPhoton* routines perform the following task:

- Set the photon to the point which is defined by the parameter d_s generated by the extinction decider, i.e. move the photon along its current track by d_s.

The following tasks are only performed by scatterer objects # 1 to 4:

- Generate a random number $R_\theta \in [0,1]$.
- Map this R_θ to the scattering angle abscissa by the inverted antiderivative Φ of the phase function of the repective scatterer. This phase function is multiplied by $sin(\theta)$ since otherwise there would be a clustering of altered photon directions per steradian at small θ due to the decrease in area or ring segments of a given thickness near the "pole" of the surrounding sphere into which an individual photon is scattered. The result is the scattering angle θ ; the higher the phase function value for a given θ, the higher the probability for the occurence of this angle with the scheme described.

$$\theta = \Phi^{-1}(R_\theta) \tag{A.2.3}$$

- Alter the direction in accordance with the randomly selected scattering angle. This could be performed with a rotation matrix. This matrix contains 3 by 3 components of combined sine- and cosine terms. Their calculation is performed by a standard PC using the trigonometric expansion series consisting of a large number of ratios and products. This approach is too time-consuming for frequent operational use. The following algorithm called "tilting" was devised which needs only one trgonometric term:
- Generate a random vector with three random variables generated independently.
- Form a "tilt" vector from the vector product of the direction and the random vector. This "tilt" vector is now (by the very definition of vector products) perpendicular to the direction vector, but points into a random azimuth direction.
- If θ is > 90°, invert the photon direction vector.
- Normalize the "tilt" vector T to the value:

$$|T| = \tan(\theta) \tag{A.2.4}$$

- Form the vector sum of the scaled *T* and the direction vector. When keeping in mind the the direction vector is always kept normalized, we find that the vector product of the direction vector and the scaled *T* is a new vector which is "tilted" by θ with respect to the direction vector and "along" *T*, i.e. in an arbitrary azimuth direction.
- Assign the photon the new vector as direction vector.
- Increase the *TNS* and either *NRS*, *NMS* or *NAS* variable, as appropriate.
- Set the *IsScattered* flag to 1.

The *Rayleigh-AlterPhoton* uses the Rayleigh phase function as defined in section (4.1.3).
The *Mie-AlterPhoton* uses the aerosol phase functions input by the user in an ASCII file (see appendix B). According to the *ScattererNumber* which has been derived in case of an aerosol event, and which denotes the number of the aerosol type of the particle which is scattered off, the phase function is loaded and used in the described scheme.
The *Albedo-AlterPhoton* uses the phase function as defined in section (4.4); it additionally scales the intensity weight of the photon with the albedo value. This retains the number of photons, hence photon paths, which would with low albedoes become too low to support a given signal-to-noise ratio for the Monte Carlo experiment. But it obeys the necessity to reduce the total energy reflected by the albedo factor.
If the program is running in "single scattering" and/or "single forcing mode, and already one scattering event or one "forcing" has taken place and no additional one is allowed, the encounter of the surface causes the path to be aborted.
The *Cloud-AlterPhoton* has to decide whether the photon in question gets reflected, transmitted or absorbed. The user has supplied values for two variables, the cloud albedo and the cloud transmission. The routine generates a random number $R_C \in [0,1]$; in the same way as the extinction decider selects the aerosol type for the scattering, the routine now selects one of the three possible events with this R_C.
In the case of reflection, the same phase function as in *Albedo-AlterPhoton* is used.
If transmission is chosen, the photon is placed at a point along its current trajctory which is at the other side of the cloud cover; then an arbitrary direction pointing into the semisphere is selected using a random scattering angle.
In the case of absorption the path is aborted.
A *Raman-AlterPhoton* is not yet implemented (see section 4.1.5), but could be incorporated using the object types for the other scatterers and the appropriate cross section and phase function. The inelastic scattering would result in a wavelength change of the photon. Taking full account of Raman scattering would include to model also for a set of wavelengths in an interval centered at the selected wavelength to conclude e.g. on eventual line-filling. The width would have to be derived from sensitivity calculations.

A.2.8 Refractor

If the photon reaches a voxel boundary, the Refractor routine is called when atmospherical refraction is chosen to be taken account of by the user. The routine compares the refractive indices of the voxels which have been, during program initialization, calculated using the air number densities in conjunction with the wavelength. Usually the voxel of a given Z-index has a higher refractive index n_1 than a voxel with higher Z-index, and n_2, and vice versa.
From Snell's law we obtain:

$$\sin\alpha n_1 = \sin\beta n_2 \tag{A.2.5}$$

with α and β as angles between the incident and emerging directions and the boundary surface normal. This formula has the drawback of yielding total reflection events and

polarities at small α. This effect, which does not occur in the real and clear atmosphere, is a consequence of the discretization of the atmosphere which makes the smooth decrease in number density with altitude a stepwise one.
A solution is the treatment of the entering into the new voxel as covering of a distance of arbitrary small value ε which contains the actual voxel transion point. In the real atmosphere, the refractive index changes smoothly along any such small path segment, and does so only along the component perpendicular to the local refractive index gradient. In case of a vertical gradient, it is the vertical component. In case of a entering with $\alpha = 0°$, the gradient has the maximum value $\Delta n = n_2 - n_1$.The slanter the incoming photon enters the new voxel, the smaller the refractive index change is along the segment. If the photon moves horizontally, the refraction in theory is infinite, but in reality the photon trajectory is not changed at all, since there is no change in vertical position. This relates to the re-formulation of n_2 in Snell's law:

$$n_2 = n_1 + \Delta n \cos(\alpha) \tag{A.2.6}$$

This formulation avoids any singularities. It was tested "firing" photons in ground based Off-axis geometry from elevation angles between 0 and 50°, preventing scattering and calculating the deviation between the initial photon direction and the direction of the emerging photons which has been caused by successive refraction at the voxel boundaries.
A united states standard atmosphere was used and a vertical discretization of 1 km up to a TOA of 70 km. The values were compared to experimentally derived ones from an observatory which compared the true and the apparent solar elevation [*Zimmermann et al. 1999*]. The result is shown in Fig. (A.2.1).
According to the angles derived from the photon direction and the surface normal of the voxel intersection point the routine calculates the deviation and uses the above described "tilting" to apply it to the photon direction. The treatment of refraction is continued after the "forcing", see section A.2.12.

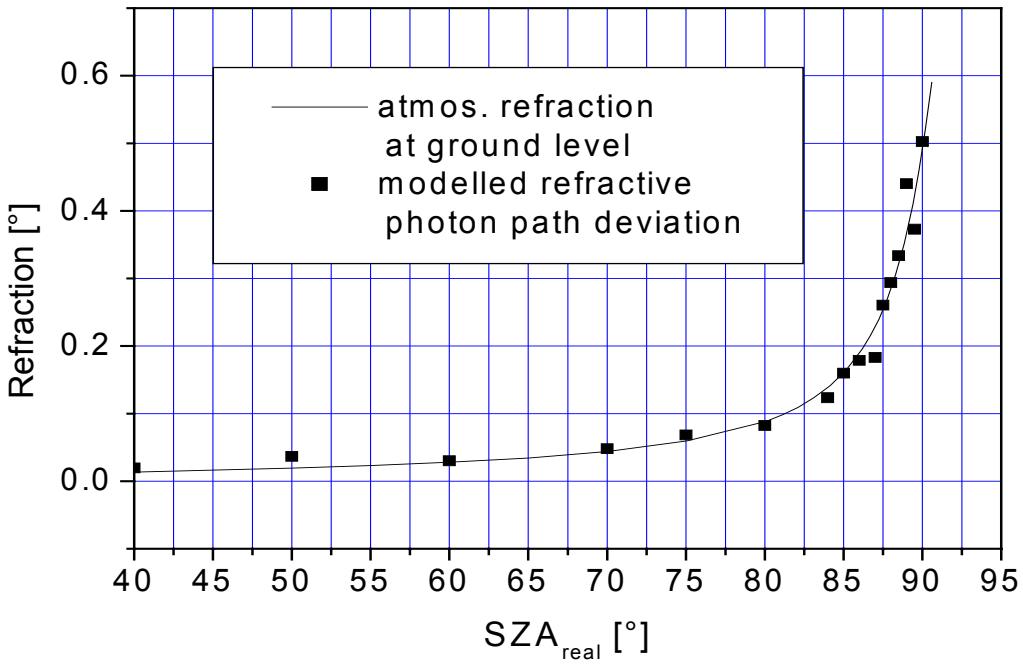

Figure A.2.1 Comparison between observed and modelled photon path deviations caused by atmospherical refraction. The approximation used is neither perfect nor can be improved with a finer vertical discretization. This causes a scattering of the model points around the experimental value which indicates the error of the technique which is up to 0.05° for high SZA.

A.2.9 Photon path

Three vectors are defining the beginning and terminating segment of each photon path. These are the current photon location and direction, and the direction vector of the sun, which by definition is the terminating element of any photon path modelled in backward Monte Carlo with forcing. The initial photon location is the one of the "emitting" or "firing" detector.
After each distance covered by a photon either a scattering event or a voxel transition occurs. They form the waypoints of the photon path. Each of these points is defined by

- A photon position reached
- The distance covered to get to this position
- The number of the scattering event (0 for no scattering and refraction) that took place at this position.

The waypoints be henceforth be more accurately referred to as "segments".

These three variables are stored to a dynamicall memory construction of type *Path*, which consists of a series of vectors of arbitrary length; at each new photon path point, the memory for a new vector is allocated and the parameters are written to its components.
After the successful termination of the path with a valid terminal segment, i.e. taking the photon into the sun, this path is used to calculate the spectroscopic quantities.

A.2.10 Scatter list

All scattering events (i.e. of type 1-4) are stored, with the positions and type numbers, to another *path* type object, the *ScatterList*. After a successful termination of the path, the first and last component are used for the derivation of the altitudes of the first and last scattering events as well as of the distance between the last (in backward MC the first) scattering and the detector.
For completeness be here stated that the numbers of events of a specific scattering type are taken directly from the respective photon variables which are updated in the respective *AlterPhoton* routines.

A.2.11 HasPhotonHit

This is a quite simple routine deriving the angle between the direction of a photon emerging from the atmosphere and the solar vector. Only if it is smaller than the half solar aperture angle (0.28°), the photon is considered to "hit" the sun, and the path is successfully terminated.

A.2.12 ForcePhoton

This routine performs a crucial task in backward MC, the "forcing". It connects the photon paths at the last scattering point to the solar radiation field.
The *ForcePhoton* routine is, just as the *AlterPhoton*, differently implemented for each scatterer. It also is called using the *Extinction* object array and the number of the last scatterer, which has "sent" the photon into the "wrong" direction.
A prerequisite is the *CalculateScatterNorm* routine; called during initialization, it calculates the phase function value for each scatterer (including sub-events such as cloud reflection and transmission) with a wavelength stepsize reflecting the aperture of the photon target, which is in backward MC the sun. Hence the phase functions are calculated with a discretization of 0.52°. Then the average over all the values is stored to the extinction object.

The common task of all is as follows:
Set the photon to the randomly selected location the last scattering has taken place at, taking the location vector from the photon path

- Change the direction to the solar vector
- Calculate the scattering angle necessary to change the direction the photon followed prior to reach this point into the direction of the sun, and the necessary scattering probability
- Derive the phase function value for the respective scatterer;
- Divide it by the average of all values; in isotropical scattering this leads to the same value for all scattering directions
- Multiply with the fraction the solar disk occupies on the unity sphere; this yields the probability of an individual photon to "hit" the sun; this probability is modulated with the normalized phase function;
- Set the photon *IsForced* flag to 1.

The latter operation prevents, if the "Single Forcing" mode is used, further scatterings and causes the *ExtinctionDecider* to scale the intensity weight of the photon with the transmission probability through each voxel the photon has to pass.

At this point an uncertainty is involved, related to the atmospheric refraction. When taking this into account, we must send the photon not in the precise direction to the sun, but in a direction tilted away from the local earth surface tangent in an angle representing the refraction of the direct solar beam from the scattering location to TOA.
Two precise approaches are possible. The first would use an estimate of the refractive deviation $\vartheta_{Ref,est}$ at the last scattering point and apply it to the forced photon's direction. From the error ϑ_{error}, i.e. the deviation of the direction the finally emerging (from the TOA) photon to the solar vector, a corrected deviation is computed and the process is repeated until ϑ_{error} falls below a selected threshold, e.g. the half solar aperture angle. Since this would involve the computation of several direct paths between the last scattering point and the TOA for each photon, this approach would be time consuming.
Another precise solution would be to calculate a large number of photon paths in a forward MC model, prevent scattering, and calculate the deviation from the initial direction at each point of the atmosphere; these points can be characterized by

- their altitude
- the angle ϑ_{Loc} between their location vector and the solar vector.

These two values govern the refraction necessary to take account of, which increases with the angle and decreases with altitude.
The photon number must be chosen high enough to ensure a sufficiently densed spacing of photon trajectories to obtain a dense grid of data points. These then can be stored in a lookup table, and for each last scattering altitude, an appropriate value could be interpolated.
Due to the dependency of the refractive index on wavelength such a table would have to be calculated for the entire wavelength range for which modelling is planned, also in a sufficient spacing, and for a representative set of atmospheres with their individual total air number density profiles.
These undertakings could not yet be performed and tested in the time scope of this thesis, since the tasks performed in this thesis did not require it as a necessity (see below). But the derivation of such a set of table certainly is among the future work.
To implement an approximative scheme for a sensitivity test the following was done instead.
For two wavelengths, 350 nm and 550 nm, 10.000 photons were launched in ground geometry with a local SZA on the surface of 92°. Refraction was engaged. For each last scattering event used for forcing, the two parameters named above were stored. Additionally, refraction was allowed to curve the path to the TOA. The resulting deviation angle ϑ_{Ref} between photon exit direction and solar vector was calculated and stored as well.

From the resulting data, the ratio R_{Ref} of the scattering point altitude [m] divided by ϑ_{Loc} [°] was fitted against ϑ_{Ref} [°]. The quality of the fit was not sufficient to prefer a polynomial of higher degrees, so a linear fit was performed.
The coefficients were for the formula

$$\vartheta_{\mathrm{Ref}} = \mathrm{A} + \mathrm{B}\, R_{Ref} \tag{A.2.7}$$

were for 350 nm: $A_{350} = 0.95$, $B_{350} = -0.003$, regression coeff. 0.86
and for 550 nm: $A_{550} = 1.07$, $B_{550} = -0.005$, regression coeff. 0.71.

As stated, the fit is not very good; the modified equation for refraction treatment at voxel boundaries still bears uncertainties (see the noise in Fig. 6.5.1) causing such uncertainty. The coefficients are influenced e.g. by the average altitude of the scattering point different for both wavelengths. The distances between the modelled data points and the fitted line projected onto the ordinate were around 0.2°, for some points 0.3°. Fortunately, this is in the order of magnitude of the solar aperture angle.
This approximation was implemented in the following subroutines which are called after the forcing if refraction is switched on.

CalculateForceSZA calculates, accepting the location vector of the scattering event off which the photon is forced, the angle between this position vector and the direction to the sun.
CalculateFracDev in turn gets passed this angle, derives $R_{Ref,}$, then interpolates coefficients A and B from $A_{350,}$ $B_{350,}$ $A_{550,}$ B_{550} for the wavelength used, to calculate ϑ_{Ref}.
ExecuteFracDev finally applies this deviation to the new photon direction using the *Tilt* routine.
Subsequently, the refraction is allowed to bend the remaining photon path to the TOA; the resulting deviation was found to compensate for ϑ_{Ref} within the uncertainties stated.

A.2.13 Polarization

The polarization has not yet been validated against measurements or other RTMs. Also the polarization effects of aerosols needs to be included. For completeness, the changes made to the above routines for the inclusion of Rayleigh polarization be stated here. They can be straight forward adapted to other polarization processes.
The photon object was given two more normalized vectors, named *Polaris* and *AntiPolaris*. The former represents the electromagnetic wave's E-field vector, the latter accordingly the H-field vector. Accordingly they are perpendicular to each other. In the Rayleigh-*AlterPhoton* routine, the algorithm was changed as follows:
Instead of the scattering angle θ the angle θ' is calculated as angle between previous and new photon direction in the plane defined by the previous direction and *Polaris*. The phase function is

$$\phi(\theta') = \cos^2(\theta') \tag{8.4.1}$$

The second angle necessary for a 3D scattering now is the angle between the new direction as projected onto the plane defined by the previous direction and *AntiPolaris*. The phase function for this is unity. Both angles are derived using the phase functions and random numbers. In the Rayleigh-*ForcePhoton* routine, the phase function $\phi(\theta')$ is used as a basis for the forcing operation and all sub routines related to it.
In all *AlterPhoton* routines, the routine *TurnPolaris* is called. It performs the following steps:

1. From the vector product of AntiPolaris and the new direction, the new Polaris is derived and normalized, which must be perpendicular to both for the photon on the new course.
2. The vector product of the new *Polaris* and the new direction form the new *AntiPolaris*.

In the control file, two parameter to input have been added:
ODPolarisUp and ODPolarisDown. They are assigned as arrays the *Detector* object's LOS.
The former is the optical density of the detector system for light polarized along the *UpDown* vector, the latter treats the OD for light polarized along the *LeftRight* vector. These two quantities are composed from the OD of a polarization filter oriented in a given way and the detector itself (see below).
In the *Fire*-routine, the following changes are made: Each photon is given a *Polaris* oriented randomly, but of course perpendicular to the initial direction. The vector product of this with Polaris forms the *AntiPolaris*. Using the vector component of *Polaris* parallel to the *LOSUp* and *LOSRight* vector, respectively, the initial weight is modified according to the optical densities input by the user.

A.2.14 SCDCalculator

After each successful termination of a photon path the *SCDCalculator* is tasked with calculating the DOAS quantities. It accepts the completed photon path and reads in segment by segment. For each segment, chemical and environmental quantities of the voxel which houses this segment are multiplied by the segment's length.
The multiple routines tasked each with deriving one single of the path parameters have been combined into one which reduces computational time by reading in the photon path only once instead of several times.
The segment contributions are summed up. The following parameters are listed to a *path* type *result* object:

- The SCDs,
- The SODs,
- The aerosol optical density (obtained from the aerosol absorption coefficient)
- The air column density
- The O_4 column density (as derived from the air number density)
- The geometrical path length of the photon path

Subroutines of the *SCDCalculator* are involved with the forward implementation as well as with a modification of the backward method; they shall be outlined later in the appropriate sections.
The derived aerosol extinction reduces the photon intensity weight.
Also for the trace gases the user has chosen so the extinction due to the molecular absorption is taken into account to reduce the intensity weight of the photon; e.g. for UV wavelengths it is advisable to take into account the ozone absorption since it is strong enough to alter the effective light path and thus the SCD and AMF.
A similar routine is the VCDCalculator launched at he beginning of a modelling. It calculates the VCD and VOD of the trace gases as well as the vertical "versions" of the quantities listed above. It does so along a vertical path starting at the detector location.
If the detector is a satellite sensor, the vertical path is the "nadir" LOS, whether the user actually calculates in "nadir" geometry or not.
For a balloon or aircraft, two cases are distinguished:
For elevations $\geq 0°$, the VCD is derived along the vertical way from the detector to the TOA; otherwise, it is determined from detector to ground.
If both types of elevations are used, two VCD are derived; the AMF then are derived for the SCDs along upward- and downward looking geometries separately using the appropriate VCD and VOD, see below.

A.2.15 Result path

The results derived by *SCDCalculator* are stored to an entry of another *Path* object, named *the Result path*.
Additionally, this entry receives the following parameters from the photon:

- Intensity weight,
- The atmosphere entry angle (the angle between photon's atmosphere exit direction and the local surface normal), called *Entry Angle, EA*
- The angle between the first scattering location vector and the detector location vector, called *First Scattering Angle, FSAN*
- *NRS, NMS* and *NAS* as defined above.
- *Last Scattering Altitude, First Scattering Altitude* and *Last Scattering Distance (LSA,FSA,LSD)* as defined above.

Other parameters are relevant only to the forward MC and shall be described in the appropriate section.

A.2.16 BoxAMFCollector

A second routine called for a successful path is the *BoxAMFCollector*; it also uses the photon path objects; reading them in segment wise in the same way as does the *SCDCalculator*, it multiplies the segment length with the intensity weight of the photon (which eventually has been modified with the trace gas and aerosol extinction) and increases the value of the *BoxSystemArray* component assigned to the respecive voxel.

A.2.17 BoxAMFCalculator

After all of the user-chosen number of photons have been modelled, the *BoxAMFCalculator* reads in the *BoxSystemArray* components, and, according to the definition of Box AMF in the final DOAS chapter section, divides them by the vertical extension of the voxel as well as by the total intensity received by the detector. The error is calculated as intensity-weighted standard deviation.
The results are written in a line to an ASCII file with name "Box" plus suffixes specified by the user. The line also contains the measurement geometry parameters (elevation, azimuth and aperture angle), the wavelength and the total intensity. A header names all these parameters and contains a number for each Box AMF.
Additionally, an ASCII file "BoxDef" (plus suffix) is generated relating these numbers to the limiting latitude, longitude and altitude values of each voxel for which the Box AMF has been calculated. They can be used to derive from the Box AMF any other quantity the user may need to e.g. interpolate values to a different grid system. Both files can be readily read in by any data processing porgram such as Microcal's "Origin" or MS "Excel".

A.2.18 AMFCalculator

The *AMFCalculator* receives the completed result path object to calculate the intensity weighted averages over the quantities stored to it, i.e. the trace gas absorption-related quantities as well as the geometrical light path and photon scattering parameters.
From the sum over the intensity weights and a spectrum of the extraterrestrial solar irradiance it calculates the irradiance recorded by the detector.
For the trace gases, the SODs in conjunction with the appropriate VOD are input into the AMF formula, see AMF section of the DOAS chapter; the SCD then are derived as the VCD multiplied by the AMF. The error, here also, is the intensity weighted standard deviation.

The results are written in a line to an ASCII file with name “AMF” plus suffixes specified by the user. Here again, the line of data is preceded by modelling parameters; they are:

- SZA
- wavelength
- elevation
- detector azimuth
- detector aperture
- detector area
- number of successful paths
- solar irradiance value for the wavelength

The following parameters, excepted the vertical quantities, are accompagnied by their respective statistical error:

- Intensity sum
- Irradiance
- Geometrical path length
- vertical air column
- air column AMF
- vertical O_4 absorption
- O_4-AMF
- *FSAN*
- *FSA*
- *LSA*
- *LSD*
- *EA*
- *NRS*
- *NMS*
- *NAS*
- VODi
- VCDi
- ODi
- CDi
- AMFi

The last five parameters are actually a list of as much entries as trace gases are considered in the model run. The quantities are given out in the same order as they are initialized by the user in the ASCII control file. The “i” denotes the number of the gas, e.g. “AMF0” for the AMF of the first trace gas to appear in the control file, “SCD1” for the SCD of the second gas.

A.2.19 Raytracer

The *Raytracer* is the control routine tasked with the modelling of photon paths. Called from the main program for as many times as photons are to be modelled, it performs the following tasks:

1. Call *Fire* the photon from the detector; in case of satellite geometry
2. Call *GetPOI* to calculate the next voxel intersection and the distance to it
3. Call *ExtinctionDecider* to assert whether and where a scattering of any kind takes place

In case of a scattering

4. Call *AlterPhoton* for the appropriate scatterer number

If no scattering occurs along the distance,
5. Place the photon at the intersection point,
6. Change the voxel indices
7. and call *Refractor* if wished

If the photon gets absorbed by a cloud cover or hits the surface in spite of further scatterings or forcings not allowed
8. Abort the path

If the photon is still within the model grid system
9. Return to 2. The repetition of steps 2 to 8 is called a loop.

If the photon leaves the atmosphere
10. Call HasPhotonHit

If the photon does not hit the sun
11. Call *ForcePhoton* with the type number of the last scattering

Otherwise
12. Terminate the path
13. Call *SCDCalculator* which stores the path and photon parameters to *ResultPath*
14. Call *BoxCollector* if wished which updates the *BoxSystemArray* elements
15. Return to the main program

The raytracer contains an additional routine involved with the forward MC to be explained later.

A.2.20 Main program

The *main* essentially has four tasks:
1. Read in the ASCII control file with the geometrical
2. and the modelling parameters
3. and the spatial discretization, environmental and chemical data from ASCII files
4. perform preparatory calculations, e.g. of
- the photon parameters such as refractive index and Rayleigh cross section,
- the scattering norming constants necessary for the "forcing"

5. Write the input data and the preparatory calculation results to an ASCII control file
6. Call Raytracer for as many times as photons are chosen to be modelled
7. Perform previous step 5 for each matrix file entry, e.g. for each SZA, selected in the control file
8. Call BoxAMFCalculator if wished
9. Call AMFCalculator

A.2.21 Control output

ASCII control file contains an integer parameter *debug*. It governs how many data prior to and during the modelling are stored to an ASCII file „rtlog.txt".
If it is set to 0, only the initialization control data according to step 4 in the *main* program.
- In case it is set to 1, the following information are written to the file for each loop modelled:
- loop number for current photon path
- voxel indices
- indices of voxel to be hit
- distance to intersection point
- direction
- altitude of photon

- current NRS, NMS and TNS
- Parameters relevant to the ExtinctionDecider, e.g. air number density and Rayleigh cross section, aerosol and total extinction coefficients and resulting transmission probabilities
- Type of scattering event
- The output of the data is not decided upon with an if-loop, which is time-consuming during operation, but by an array-grouped output object.
- If the debug flag is set to 2, also parameters relevant to the calculation of intersection points with single voxel surfaces are given out.
- The control file serves to backtrace single photon paths to assess the reason of an effect or a result. It is recommended to set it to 0 for standard operation since the file access is time consuming.
- In model mode 4, the initialization data are written to the file and the modelling is not begun. It is recommended to run the program in this mode prior to modelling to ensure all input files have been read in appropriately.

In addition to the control output written to file if desired, during the runs the number of the measurement geometry worked on is written to screen, followed by letters indicating the mode the program is running in ("BMC" for Backward Monte Carlo), the number of photon path modelled; after this number, letters indicate the events of the path: "R" denotes a Rayleigh scattering, "AS#" a scattering off an aerosol of number #, "G" a surface scattering, "E" an exiting from TOA, "F" a forcing operation, and "S" the calculation of SCD and the other outputs, this letter concluding a successfull photon path. It is illustrative to spend a few minutes watching the lines of letters to scroll by and assess the influence and importance of e.g. aerosols with e.g. Off-axis geometries.

Appendix B: TRACY Manual

Three-dimensional Monte Carlo Radiative Transfer Model (3D MC RTM)
Operation Manual

1. Coordinate system and „voxel“ definition

The model employs full spherical three-dimensional spherical geometry.
When measuring with high solar zenith angles or with slant viewing geometries, the light paths are affectd by the atmosphere's sphericity. Even when investigating situations for which sphericity is not of significant importance it strictly first has to be proven to be of insignificance by modelling with sphericity and comparing to cartesian geometry model results. The derivation of latter is, though, abundant since the spherical calculation already exists. For this reason, the cartesian geometry has been abandoned, and the model was fixed to spherical geometry, although with variable discretization in all of the three dimensions.
The earth sphere is modelled with realistic size, ist central point being the cartesian coordinate system's origin. The z-axis runs thrugh the model earth's north and south pole, being positive in the „north“, negative in the „south“. Three coordinates are used:
ϑ, the angle between the z axis and the location or direction vector in question; it also represents the geographical latitude of any modelled location.
Φ, the azimuth angle. $\Phi = 0$ is valid for all vectors with y = 0 in the cartesian system. Thus it represents the longitude of a given location vector.
Z, the amount axis. It represents the distance from the earth centra, and thus the altitude of any given location. In the following, these coordinates be addressed with bold-printed letters.
The coordinates define three dimensional grid cells, or volume pixels „voxels“ within which the modelled detecors are located, and the modelled photons are to operate.
All points with a given ϑ-value form a cone, of which the tip is the system's origin. All points with a fixed Φ form a plane, which rotates, when Φ is varied, around the z-axis of the cartesian system. An finally any vectors with same **Z** value form a sphere.
This means each voxel is enclosed by three pairs of geometrical surfaces: two cones, two planes, and two spheres. It can be defined by two ϑ, two Φ, two **Z** values, which are in turn defined by the respective axis's chosen discretization. This leads to a three-dimensional numbering of the voxels used in the model. For the ϑ- and Φ-axis, the first voxel coordinate numbers, i_ϑ and i_Φ, are zero, for the Z-axis, i_Z, it is 1.
This preserves the option for the implementation of a ground voxel, within which e.g. radiatiave transfer processes within the earth's surface could be modelled. The voxel with $i_Z = 1$ is the lowest one, extending from altitude $\mathbf{Z}_1$=0 (above earth surface, as stated) to $\mathbf{Z}_2$.
The first values of the ϑ- and Φ-axis, ϑ_0 and Φ_0, are fixed to zero. If the next one, e.g. ϑ_1 is e.g. 0.785 rad (45°), the voxel with ϑ-coordinate number i_ϑ=0 is limited by the cones defined by ϑ_0 and ϑ_1 and include the „north pole“.
The voxel with i_ϑ=1 are enclosed by the ϑ_1 and ϑ_2 cones and thus form a „collar“ running around the „earth“. The voxels with $i_\vartheta=N_\vartheta$ encompass the „south pole“.
The voxels with i_Φ=0 are limited by the plane which contains the „0-meridian line“ on their one side, and the plane defined by Φ_1 on their other side.
The voxels with i_Φ=1, being defined by the Φ_1- and Φ_2-planes, are adjacent to the voxels with i_Φ=0; so are the voxels bearing $i_\Phi=N_\Phi$, closing the ring around the „earth“ sphere.

2. Geometrical parameters

The discretization is freely chosen by means of an ASCII file („space.txt“) with the numbers of discretization steps for the ϑ-, the Φ- and the **Z**-axis, N_ϑ, N_Φ and N_Z in the first line and the selected coordinate values ϑ_i, Φ_i (in units radian) and $\mathbf{Z}_i$ (in unit km, above earth surface) of the limiting surfaces in the three lines below.
The Top Of Atmosphere, TOA, can thus be chosen by the value $\mathbf{Z}_{Nz}$.
Apart from this discretization choice, the location vector of the detector site is input using the main control file of the program, „profiles.txt“, and in spherical coordinates. These are the altitude of the detector (in units m), as well as ist geolocation coordinates, the geographical latitude and longitude. These values may be chosen freely and are not limited or influenced by the chosen spatial discretization in „space.txt“.
The solar position is defined by the user relative to the detector's by the Solar Zenith Angle (SZA or ϑ) and the Solar Azimuth Angle (SAZ, A), in units [°]. The program converts both angles into a solar location vector.
The detector's line(s) of sight (LOS), also named measurement geometries, are parametrized by their elevation ε in [°] (which is the angle between the LOS vector and the local tangential plane to the earth's surface) and the azimuth φ [°], which is defined in relation to the sun: φ = 0° means the detector is looking into the direction where the sun stands, e.g. to the east if the sun is just rising; φ = 90° denotes the viewing direction to be sidewards, and φ = 180° away from the sun.

3. Environmental and chemical parameters

The program can work with up to ten trace gas profiles [i=1,..,n] and aerosol types [j=1,..,m] simultaneously.
The following parameters are used as program input (with v as voxel number):

- air number density vertical profile $\rho(v)$ in [cm^{-3}]
- temperature T(v) in [K]
- pressure p(v) in [bar^{-3}] or [Pa^2]
- trace gas [i] concentration vertical profile $\rho(v)_i$ in [cm^{-3}]
- trace gas cross section spectrum $\sigma(\lambda)_i$ in [cm^2]
- aerosol extinction coefficient vertical profile $K_E(v)_j$ in [km^{-1}] for the wavelength desired
- ratio absorption coefficient $K_{A,j}$ /$K_{E,j}$ ϖ_j (=f(single scattering albedo ω))
- aerosol phase function spectrum $\phi(\theta)_j$ in a.u., θ as scattering angle

The three quantities are read in as ASCII files („AirDen.dat“, Temp.dat“ and „Press.dat“ with one row of V numbers, V being the number of voxels, and each of them constituting the respective value for the bottom of the voxel v, e.g. for altitude zero above earth's surface in case of the voxels with **Z**-coordinate 1. This parametrization complies with many air profiles in literature, which have been calculated or measured (using e.g. balloon sondes) point-wise. To obtain average values for the extended voxels, the values in the ASCII files are interpolated; e.g. the air density value for the voxel with **Z** = 1 is linearly interpolated between the first and the second value in „AirDen.txt“.
The free choice of concentration values for a 3D structure is possible within the program code, although the access routines proved to be too time-consuming. A more efficient way to specifically address certain voxels on an array basis is under development. The calculation of Box AMFs (see below) can be performed in arbitrary 3D discretization.

4. The „profiles.txt“ file

All parameters (apart from the ones related to the spatial discretization) are input using an ASCII file „profiles.txt“. The entries be described one by one in the following.

4.1 Trace gases

2
The number of trace gas profiles to be considered constitutes the very first entry to the „profiles.txt“; it is followed by the stated number of trace gas entries, each in compliance with the following format:
O3
1 1
3408 0
RTsupport/atmosdata/O32.dat
RTsupport/atmosdata/o3quilt.xs

O3 is the name of the trace gas in question.
1 is the extinction flag, it can be either 0 or 1. If it is one, the extinction induced by absorption of this trace gas profile will influence the modelled SCDs and AMFs of all other trace gas profiles present. It should be 1 when the optical density in the chosen measurement geometry is of significant size (usually in the order of 1 % or higher), as is usually the case for ozone when modelling for wavelengths in the UV.
The following 1 is the interpolation flag, see below;
3408 is the number of entries in the cross section file, see below.
0 is the matrix flag, see below.
RTsupport/atmosdata/O32.dat is the path designation and name of the vertical profile file; it has same format as the „AirDen.dat“, „Temp.dat“ and „Press.dat“ files. The interpolation flag can be 0 or 1. In the former case, the values read in are taken as (already averaged) voxel values. In the latter case, the program interpolates the voxel values in the way it does with the air density file values. The matrix flag can either be 0 or 1. If it is 0, then only one set of concentration values are read in and considered. If it is 1, a situation with chemical enhancement, including the variation of the profile with any other model parameter, is modelled. The profile file is then expected to consist of several lines, each representing one separate profile, of which one by one is read in and modelled in separate runs.
RTsupport/atmosdata/o3quilt.xs finally is the absorption cross section file. It consists of a headerless ASCII file with two columns, the first one with the wavelengths, the second with the cross section. The discretization is arbitrary. The number of entries tells the code how many lines of this file to read before aborting. This makes any end flag to add to the cross section file unnecessary. As soon as two lines are found in the file with wavelengths enclosing the wavelength of the planned modelling the cross section is derived by interpolation, and the read-in process is aborted. So if the precise number of entries is not known, just a number which is larger than the line number of the interesting wavelengths serves the purpose.
The described way to initilaize the trace gases oepns a possibility to derive different AMFs for e.g. the tropospheric and the stratospheric part of a profile. In that case the existing profile file is simply divided into the values for voxels altitudes <= TP and > TP, TP being the tropopause, and the „missing“ values in either file are set to zero. Then, both files are input as two different profiles.

4.2 Aerosols

The aerosols are input in a similar way as the trace gases are. A typical entry (the 1st out of 3):
3
QAer1
3
181 0
0.03979
RTsupport/atmosdata/Qano21.txt
RTsupport/atmosdata/QAERNO21.xs

Again, the preceding number, *3* in this case, states the number of aerosols, the following string the name of the aerosol. The following *3* currently is fixed, it constitutes the parameter combination „$K_E(v)$, ϖ, $\phi(\theta)$“. A comprehensive Mie programming is under way, that, once fully incorporated into the program, can accept any other parametrization obtained from literature or measurement (including e.g. number density and droplet size distribution) and calculate the model-relevant parameters, such as phase function, from the parameters provided.
The *181* states the number of entries in the following phase function file. The *0* after this is the matrix flag, which has the same meaning and effect as in the trace gas case.
The number below this is the ϖ-quantity.
RTsupport/atmosdata/Qano21.txt states the path and name of the extinction coefficient profile file; this is of the same format as the trace gas profile files.
RTsupport/atmosdata/QAERNO21.xs finally gives the code access to the phase function file. It has similar structure as the trace gas cross section file, with the difference that the first column holds the scattering angles in arbitrary discretization, and the second one the phase function value. A normalization is not necessary, since this is computed by the program.
In some cases a profile file with three columns is sent out by modellers to represent an aerosol load the user is interested in. In all cases experienced so far this file consists of a limited set of aerosol types, usually between three and five, each of which being present in one area of the atmosphere, e.g. PBL, FT and stratosphere, and each characterized by a constant value for the single scattering albedo and a constant parameter like the assymetry coefficient of which the phase function can be derived. This datasets are correctly initialized by the division of the aerosol file into e.g. three aerosol file sets and entries.

4.3 Viewing geometry

The viewing angles are also read in from the „profiles.txt“; they must be stated there in the following format:
2
2 0 0.7854 0.1 -5 0 0 0
5 0 0.7854 0.1 -5 0 0 0

The *2* denotes G, the number of viewing geometries to be modelled; up to ten are supported, which is useful for e.g. MAX DOAS devices.
The G lines after this contain the specific information for the g-th geometry: the elevation angle ε_g in [°], and the azimuth angle φ_g in [°] (relative to the sun's direction, as explained above). Together with the detector's location these parameters are converted by the program into the line of sight vector Γ_g of the g-th geometry, which is equivalent to the telecope's central axis. The „0.7854“ is in our example the detector area a_g in [cm^2], the „0.1“ the aperture angle $\alpha_{ud,g}$ in [°]. If the following parameter is <=0, as is the case here, the angle

defines a cone centered around the telescope's main axis and with ist tip at the detector's location. This cone is the area out of which scattered photon are accepted in the real measurement.

The following number is the „left-right" aperture angle $\alpha_{lr,g}$, also in [°]. If it is >0, the aperture characteristics becomes elliptical, with the aperture angle describing the aperture along the detector's location vector, that is in „up-down" direction, while the „left-right" aperture angle describes the aperture along the vector which is the vector product of the „up-down" directio and the telescope axis; for elevations < 90°, this is the local horizontal line. In case of elevation = 90°, for the „up-down" direction the direction vector from the instrument location to the model north pole is used, the „left-right" axis is calculated appropriately.

These data control the deviation of the photon's initial direction from Γ_g.

In case of $\alpha_{lr,g} < 0$ this deviation is chosen with a random number out of the interval $[0, \alpha_{du,g}]$; the direction along which the photon's direction will be tilted is derived by a normalized random vector perpendicular to Γ_g.

The following 0 is the cosine flag; if it is zero, all model photons are launched with the same initial intensity, regardless of their direction within the aperture angle characteristics. If it is 1, each photon is weighted with the cosine of the individual, randomly created angle between the new photon direction and Γ_g.

The two last numbers describe the optical densities for light polarized along the „up-down" direction and the „left-right" direction, respectively.

This feature can be used to model a polarization filter used in conjunction with the measurement device, e.g. to investigate the influence of aerosol scattering on the depolarization of scattered light. The appropriate values must be obtained from the manufacturer or from own measurement.

4.4 location geometry and solar position

In the following the other control parameters are explained. The first eleven of them are followed by a number (0 in this example) of which the meaning will be explained below.

They are geometrical and environmental parameters that may be varied in sensitivity studies or to perform model runs for a series of measurements.

- *600.0 0* wavelength [nm] of the photon modelled
- *30 0* SZA [°] at detecetor's site used for the model
- *0 0* SAZ [°] at detector's site used for the model
- *45 0* geographical latitude [°] of the detector location
- *0 0* geographical longitude [°] of the detector location
- *0 0* altitude in [m] over earth surface of detector location

4.5 albedo and cloud cover

- *0.3 0* ground albedo, dimensionless, e.g. 0.42 is 42 % albedo; upon lambertian reflection off the ground, the photon's current intensity weight will be multiplied by this albedo value.
- *0 0* cloud coverage, dimensionless, e.g. 0.42 is 42 % cloud cover
- *0.8 0* cloud albedo, dimensionless, e.g. 0.42 is 42 % cloud albedo
- *2000 0* cloud cover altitude in [m]
- *0 0* cloud transmission, dimensionless, e.g. 0.1 is 10 % cloud transmission; of the photon impinging onto the cloud cover, a percentage according to the cloud albedo will get reflected (lambertian reflexion) without intensity weight modification, the percentage

according to the transmission will get transmitted through the cloud cover, and the difference to 100% will get swallowed, their paths thus terminated; for details on this cloud cover implementation see below.

4.6 model control parameters

The below parameters are not environmental or model input parameters but the model control parameters. They usually are kept constant for a given series of model scenarios to be investigated.

- *0* Intensity threshold; The photon are originally launched with intensity weight 1, but this value will get reduced by means of albedo scattering and forcing; if the intensity falls below this threshhold, the path is aborted.
- *1000* number of photon modelled; usual values are between 1000 and 10000, depending on parameters such as wavelength, SZA, shape of considered trace gas profile and ist distance from the detector; for a detailed study see below.
- *4* mode of the modelling; most common is –1 (Backward Monte Carlo BMC); –2 is BMC with injection along line of sight, see below; 2 is Forward MC (FMC) with line-of-sight-plane approximation; 4 is control mode to have the code print out all read in input parameters to „rtlog.txt“ to test that all input data has been processed properly. For details see respective section (6.5.19).
- *0* Single Scattering Flag; if the parameter is set to 1, only one scattering event is allowed to happen for each photo path; if a photon path already scattered leads into the earth surface, the path is aborted. In case of a cloud cover intersection the intensity weigth is multiplied by the cloud transmission value (see above).
- *1* Single Forcing Flag; if this flag is set to 1, only one forcing is allowed for each path. If the forced photon path intersects the earth or the cloud cover, it is processed as outlined for the „Single Scattering“ case.
- *0* Refraction Flag; if it is set to 1, the model run is performed including atmospherical refraction.
- *0* Debug Flag; if a model run delivers result parameters which cannot be explained or which are obviously wrong, e.g. negative in case of AMF, this Flag may be set to 1; the code then writes all path relevant information (e.g. altitude, voxel number, distance to next boundary) as well as scattering information (e.g. extinction probability, scatterer type) to „rtlog.txt“; the path can be analysed to find a possible program bug. with value 2, even more detailed information is given.
- *100000* Illumination Radius [m]; in FMC mode, the lines of sight define the area of the model earth where the solar radiation field contributes to the measurement. This area, enhanced by the Illumination Radius in both x- and y-directions, is then targeted by the photon modelled. Only relevant to forward MC.
- *50000* Detection Radius [m]; in FMC mode, any photon crossing the line-of-sight.plain at a distance to the LOS <= the Detection Radius, it will be considered for path result calculation. This value has to be small as compared to any horizontal trace gas variation in the detector’s region. Only relevant to forward MC.
- *0* Box Flag; if it set to 1, Box-AMF will be calculated as defined in the respective section for a set of voxels to be specified with the next six integer parameters.
- *0* denotes the smallest x-coordinate of the voxel set for which Box-AMF shall be derived;
- *0* denotes the largest x-coordinate of the voxel set for which Box-AMF shall be derived;
- *0* denotes the smallest y-coordinate of the voxel set for which Box-AMF shall be derived;
- *0* denotes the largest y-coordinate of the voxel set for which Box-AMF shall be derived;

- *1* denotes the smallest z-coordinate of the voxel set for which Box-AMF shall be derived;
- *69* denotes the largest z-coordinate of the voxel set for which Box-AMF shall be derived;
- *0* Matrix Switch; if one or more of the geometrical or environmental parameters are desired to get read in from a columned headerless ASCII file „Matrix.txt“, this switch must be set to the number of columns contained. In this case, the zeroes behind the considered parameters must be set to the number of the column they are found in; if e.g. for a balloon operation SZA, SAZ and altitude are varied to reflect the course of the flight, the „Matrix.txt“ file may contain three columns, e.g. the first (column #1) holding the SZA, the second (#2) the SAZ, and #3 the altitude; the zeroes behind SZA, SAZ and altitude in „profiles.txt“ then are replaced by a 1, 2 and 3, respectively, and the Matrix Switch is set to 3. The parameters in question are then read in from „Matrix.txt“, their values in „profiles.txt“ are disregarded.
- *0* Matrix File Start Line; the first data set, or line of data, to be read in from „Matrix.txt“ and used as model input.
- *5* Matrix File Start Line; the last data set, or line of data, to be read in from „Matrix.txt“ and used as model input. The difference between these two integers plus one denotes the total number of data sets to be read in from the file and modelled for. If one or more of the matrix switches of the trace gases or the aerosols are set to 1, for each data set from „Matrix.txt“ the corresponding line (e.g. line # 42 for line # 42 from „Matrix.txt“) from the trace gas or aerosol file is read in, and modelled with.

5. Command line usage, „RTManager.txt“

The „profiles.txt“ is tried to get opened and read if TRACY is launched using ist icon or by double-clicking on the Tracy.exe file. It can also be launched from command line, e.g. from the DOS prompt; the command without parameters launches TRACY with „profiles.txt“, which then must be present. But the control file, given the contents and format are as specified for „profile.txt“ can bear any arbitrary name, e.g. be named after the user or a balloon flight number, e.g. „LPMA42.flg“. The appropriate command line command then must read „Tracy LPMA42.flg“. The name of the control file is then recognized, the file is read in, any „profiles.txt“ also present in the program directory is disregarded.
If the control file is „profiles.txt“, the output files are named „AMF.txt“, „BOX.txt“ and „BOXDEF.txt“; if the control file name is different, the output file names are „AMF#.txt“, „BOX#.txt“ and „BOXDEF#.txt“, with „#“ standing for the control file name without extension, e.g. for the AMF-file the name would become „AMFLPMA42.txt“.
If more than one control file shall be worked on, e.g. representing different balloon flights or entirely different measurement campaigns, the „Rtmanager.exe“ can be used in conjunction with the „RTList.txt“ file. The latter contains in ist first line the integer number of the control files TRACY is wished to work with; in the next lines (as many as stated by this number) the command line commands for the control files are written; a typical „RTlist.txt“ thus might read:
3
Tracy LPMA42.flg
Tracy LPMA43.flg
Tracy BrOMax.txt

Upon parameterless launch of „RTmanager.exe“, also by either its icon or using a command prompt, the program acts like a batch file executing the command lines written to „RTList.txt“.

6. Ouput parameters

The output is given out in ASCII files named as stated above.
The AMF file contains the output parameters as intensity weighted means accompagnied by the error as intensity-weighted standard mean if applicable.

- *SZA* Solar Zenith Angle [°]
- *Lambda* Wavelength [nm]
- *Elev* line of sight elevation [°]
- *Azimuth* line of sight azimuth [°]
- *Aperture* half aperture angle [°]
- *Area* detector area [°]
- *SphereFct* factor of total area unity sphere defined by the detector half aperture
- *NumberHit* number of photons contributing to the signal
- *I* sum over intensity weights
- *Rad* irradiance modeled [$Wcm^{-2}nm^{-1}$]
- *ETSF* S_0 for the wavelength modeled.
- *L* geometrical path length [m]
- *VairCD* vertical air column [cm^{-2}]
- *AirAMF* AMF for air column
- *VO4OD* vertical optical density for O_4
- *O4AMF* AMF for O_4
- *FSAN* angle between location of first scattering event and detector location[1]
- *FSA* altitude of first scattering event[1]
- *LSA* altitude of last scattering event[1]
- *LSD* distance between last scattering event and detector[1]
- *EA* entry angle of photons into the atmosphere [°]
- *RO* rim origin (distance of point of origin on solar disk divided by solar radius)
- *Pol* Angle between polarization E-vector to Up-down axis of detector [°]
- *NRS* number of Rayleigh scattering events
- *NMS* number od aerosol scattering events
- *NAS* number of albedo (surface) scattering events
- *VOD#* VOD of species #
- *VCD#* VCD of species #
- *OD#* slant OD of species #
- *CD#* SCD of species # [cm^{-2}]
- *AMF#* AMF of species #.

The first line is a header with all these parameter names.

The BOXDEF file lists the indices and geolocations of the voxels for which box AMF have been calculated.

The BOX file contains the parameters:

[1] „First“ and „Last“ refer to the real situation of photons incoming from the sun, i.e. the first scattering event is actually the last one if a photon path is modeled backward.

- *SZA* SZA [°]
- *Lambda* wavelength [nm]
- *Altd* detector altitude [m]
- *Elev* line of sight elevation [°]
- *Azimuth* line of sight azimuth [°]
- *Aperture* half aperture angle of detector [°]
- *Intensity* sum over intensity weights of contributing photons
- After these parameters, the Box AMF follow in one line.

The first line of the file is a header bearing the parameter names and also the names of the voxels, containing their voxel z-index for easier identification.

7. Control parameters printed to screen

In addition to the control output written to file if desired, during the runs the number of the measurement geometry worked on is written to screen, followed by letters indicating the mode the program is running in ("BMC" for Backward Monte Carlo), the number of photon path modelled; after this number, letters indicate the events of the path: "R" denotes a Rayleigh scattering, "AS#" a scattering off an aerosol of number #, "G" a surface scattering, "E" an exiting from TOA, "F" a forcing operation, and "S" the calculation of SCD and the other outputs, this letter concluding a successfull photon path. It is illustrative to spend a few minutes watching the lines of letters to scroll by and assess the influence and importance of e.g. aerosols with e.g. Off-axis geometries.

References

Aliwell, S. R. and R. L. Jones, Measurements of tropospheric NO3 at midlatitude, J. Geophys. Res., 103, D5, 5719-5727, 1998

Ackermann, R., Auswirkungen von Kraftfahrzeugemissionen in der urbanen Atmosphäre, PhD thesis, University of Heidelberg, 2002

Bäumer, D., B. Vogel, F. Fiedler, Modelling of the dispersion of motorway emissions, in prep., 2003

Blättner, W. G., H. G. Horak, D. G. Collins and M.B. Wells, Monte Carlo studies of the sky radiation at twilight, Appl. Optics 13(3) 534-547, 1974

Bösch, H. Studies of the Stratospheric Nitrogen and Iodine Chemistry by Balloon-Borne DOAS Measurements and Model Calculations, PhD thesis, University of Heidelberg, 2002

Boßmeyer, J., Ship-Based Multi-Axis Differential Optical Absorption Spectroscopy Measurements of Tropospheric Trace Gases over the Atlantic Ocean, PhD thesis, University of Heidelberg, 2002

Brasseur, G., and S. Solomon, Aeronomy of the middle atmosphere, D. Reidel Publishing company, The Netherlands, 1984

Buchwitz, M., Strahlungstransport- und Inversions-Algorithmen zur Ableitung atmosphärischer Spurengasinformationen aus Erdfernerkundungsmessungen in Nadirgeometrie im ultravioletten bis nahinfraroten Spektralbereich am Beispiel SCIAMACHY, PhD thesis, University of Bremen, 2000

Buchwitz, M., V. V. Rozanov, J. P. Burrows, Development of a correlated-k distribution band model scheme for the radiative transfer program GOMETRAN / SCIATRAN for retrieval of atmospheric constituents from SCIAMACHY / ENVISAT-1 data, Proceedings of SPIE, Vol. 3495, Conference on Satellite Remote Sensing of Clouds and the Atmosphere III, Editor/Chair: J. E. Russell, 171-186, European Symposium on Remote Sensing, Barcelona, Spain, 21 - 24 Sep. 1998

Bussemer, M., Der Ringeffekt: Ursachen und Einfluß auf die spektroskopische Messung atmosphärischer Spurenstoffe, diploma thesis, Institute for Environmental Physics, Heidelberg, 1993

Camy-Peyret, C., P. Jeseck, T. Hawat, G. Durry, G. Berubele, L. Rochette, and D. Huguenin, The LPMA balloon borne FTIR spectrometer for remote sensing of the atmospheric

constituents. In 12th ESA Symposium on Rocket and Balloon Programmes and Related Research, 1995

Carslaw, N., L. J. Carpenter, J. M. C. Plane, B. J. Allan, R. A. Burgess, K. C. Clemitshaw, H. Coe, and S. A. Penkett, Simultaneous observations of nitrate and peroxy radicals in the marine boundary layer, J. Geophys. Res., 102, 18.917-18.933, 1997

Chance, K., and R. J. D. Spurr, Ring effect studies; Rayleigh scattering, including molecular parameters for rotational Raman scattering and the Fraunhofer spectrum, Appl. Opt. 36, 5224-5230, 1997

Chipperfield, M. P., Multiannual simulations with a three-dimensional chemical transport model, J. Geophys. Res., 104 (D1), 1781-1805, 1999

Czerny, M. and A. Turner, Z.Phys., Vol. 61, 792, 1930

De More, W.B., Sander, S.P., Golden, D.M., Hampson, R.F., Howard, C.j., Kolb, c.E., Kurylo, M.J., Molina, M.J., Ravishankara, A.R., Chemical Kinetics and Photochemical Data for Use in Stratospheric Modeling. Evaluation Number 12, JPL Publication 97-4, NASA, 1997

Dahlbeck, A., and K. Stamnes, A new spherical model for computing the radiation field available for photolysis and heating at twilight, Planet. Space Sci., 39, 671-683, 1991.

Dundee Satellite Receiving Station, http://www.sat.dundee.ac.uk/auth.html, University of Dundee, DD1 4HN, Scotland, UK, 1999

Eppel, D. P. and Kapitza, H. and Clausen, M. and Jacob, D. and Koch, W. and Levkov, W. and Mengelkamp, H.-T. and Werrmann, N., The non-hydrostatic mesoscale model GESIMA, Part II: Parameterizations and Applications, CAP, 86, 15-41, 1995

Errera., Q., and D. Fonteyn, Four-dimensional variational chemical assimilation of CRISTA stratospheric measurements, J. Geophys. Res., 106 (D11), 12,253-12,265, 2001

Fiedler, F., U. Corsmeier, M. Kohler, B. Vogel, Experimentelle Bestimmung der Emissionen des Kraftfahrzeugverkehrs auf Autobahnen und Vergleich mit berechneten Emissionen. Operationsplan. Selbstverlag des Instituts für Meteorologie und Klimaforschung, Forschungszentrum Karlsruhe/Universität Karlsruhe, pp 45 ff., 2001

Finlayson-Pitts, B. J., F. E. Livingston, and H. N. Berko, Ozone destruction and bromine photochemistry at ground level in the Arctic spring. Nature, Vol. 343, 622-625, 1990

Fish, D. J., D.E. Shallcross and R.L. Jones, The vertical distribution of NO3 in the atmospheric boundary layer, At. Env., 33, 687-691, 1999

Fish, D. J., R. L. Jones, Rotational Raman scattering and the Ring effect in zenith-sky spectra, Geophys. Res. Lett. 22, 811-814, 1995

Frank, H., Ein Strahlungstransportmodell zur Interpretation von spektroskopischen Spurenstoffmessungen in der Erdatmosphäre, diploma thesis, University of Heidelberg, 1991

Frieß, U., Spectroscopic Measurements of Atmospheric Trace Gases at Neumayer-Station, Antarctica, PhD thesis, University of Heidelberg 2001

Geyer, A., B. Alicke, D. Mihelcic, J. Stutz and U. Platt, Comparison of tropospheric NO3 radical measurements by differential optical absorption spectroscopy and matrix isolation spin resonance, J. Geophys. Res., 104, 26097, 1999

Geyer, A. The Role of the Nitrate Radical in the Boundary Layer, PhD thesis, University of Heidelberg, 2000

Geyer, A., B. Alicke, S. Konrad, J. Stutz, and U. Platt, Chemistry and oxidation capacity of the nitrate radical in the continental boundary layer near Berlin, J. Geophys. Res., 106, 8013-8025, 2001a

Geyer, A., R. Ackermann, R. Dubois, B. Lohrmann, T. Mueller, and U. Platt, Long-term observation of nitrate radicals in the continental boundary layer near Berlin,, Atmos. Environ., 35, 3619-3631, 2001b

Geyer, A., and U. Platt, Temperature dependence of the NO3 loss frequency: A new indicator for the contribution of NO3 to the oxidation of monoterpenes and NOx removal in the atmosphere, J. Geophys. Res., 107, doi: 10.1029/2001JD001215, 2002

Geyer, A., K. Bächmann, A. Hofzumahaus, F. Holland, S. Konrad, T. Klüpfel, H. Pätz, D. Perner, D. Mihelcic, H. Schäfer, A. Volz-Thomas, and U. Platt, Nighttime formation of peroxy and hydroxyl radicals during the BERLIOZ campaign: Observations and modeling studies, J. Geophys. Res., 108, doi: 10.1029/2001JD000656, 2003

Gomer, T., T. Brauers, F. Heintz, J. Stutz, and U. Platt, MFC version 1.98 User manual, University of Heidelberg, 1995

Graedel, T. E., and P. Crutzen, Atmospheric change – An Earth System Perspective, W. H. Freeman and Company, New York 1992

Grainger, J.F., and J. Ring, Anomalous Fraunhofer lie profiles, Nature, 193, 762,1962

Grätz, W., Untersuchung polarisierten und unpolarisierten Himmelsstreulichtes mit einem absolut kalibrierten Spektralradiometer zur Validierung eines Strahlungstransportmodelles, high school thesis, 12th class Physics Qualification Course, Gymnasium Ulricianum Aurich, 2003

Greenblatt G.D., J.J.Orlando, J.B. Burkholder, and A.R. Ravinshakara, Absorption Measurements of Oxygen Between 330 and 1140 nm, Journal of Geophys. Res., 95, 18577-18582, 1990

Greiner, W., Klassische Elektrodynamik, Verlag Harri Deutsch, Frankfurt 1991[5]

Grzegorski M., Bestimmung von Wolenparametern für das Global Ozone Monitoring Experiment mit breitbandigen Spektrometern und aus Absorptionsbanden von Sauerstoffdimeren, diploma thesis, University of Heidelberg, 2003

Harder, J.W., J.W. Brault, P.V. Johnston and G.H. Mount, Temperature dependent NO2 cross sections at high resolution, J. Geophys. Res., 102, 3861-3879, 1996

Hausmann, M. and U. Platt, Spectroscopic measurement of bromine oxide and ozone in the high Arctic during Polar Sunrise Experiments 1992. J. Geophys. Res., Vol. 99, 25399-25413, 1994

Hebestreit, K., Halogenoxide in der planetaren Grenzschicht mittlerer Breiten, PhD thesis, University of Heidelberg, 2001

Heismann, B., Eine CCD Kamera zur Messung atmosphärischer Spurenstoffe, diploma thesis, University of Heidelberg, 1996

Hendrick, F., et al.,Simulation of BrO Diurnal Variation and BrO Slant Columns: Intercomparison Exercise Between Three Model Packages, Proceedings of the 5th European Workshop on Stratospheric Ozone, Saint Jean de Luz, France, 27 Sept.-1 Oct. 1999, Air Pollution Research Report n°73, European Commission - DG XII, Brussels, 2000

Henvey, L.G., and J. L. Greenstein, Diffuse radiation in the Galaxy, Astrophys. Journal, 93, 70-83, 1941

Heue, K.-P., M. Bruns, J. P. Burrows, S. Fietkau , F. Finocchi, C. von Friedeburg, G. Hoenninger, U. Platt, I. Pundt, A. Richter, R. Rollenbeck, T.Wagner, F. Wittrock and P. Xie, The AMAX-DOAS instrument, Concept and Instrumental Setup, Poster, Workshop "Emissions of chemical species and aerosols into the atmosphere", CNES, Paris, June 19-22, 2001

Hofzumahaus, A., A. Kraus, and Ma. Müller, Solar actinic flux spectroscopy: a technique for measuring photolysis frequencies in the atmosphere, Appl. Opt. 38, 21, 1999

Hönninger, G., Halogen Oxide Studies in the Boundary Layer by Multi Axis Differential Optical Absorption Spectroscopy and Active Longpath-DOAS PhD thesis, University of Heidelberg, 2002

Jeong, Gill-Ran, The sensitivity of UV radiation to atmospheric aerosols and clouds, contribution to Program in Atmospheric and Oceanic Sciences, University of Colorado, 1999

Kirk, J. T. O., Volume scattering function, average cosines, and the underwater light field, Limnol. Oceanogr., 36, 455-467, 1991

Kreher, K., Messung der Breitenverteilung (50°N – 70°S) von stratosphärischem Ozon und Stickstoffdioxid mittels optischer Absorptionsspektroskopie, diploma thesis, University of Heidelberg, 1997

Kurucz, R. L., I. Furenlid, J. Brault und L. Testerman, Solar flux atlas from 296 to 1300 nm, National Solar Observatory, printed by University Publisher, Harvard University, 1984

Kuze, A. and K. V. Chance, Analysis of cloud top height and cloud coverage from satellites using the O2 A and B bands, J. Geophys. Res., 99, 14481-14491, 1994

Kylling, A., Uvspec: a program package for calculation of diffuse and direct UV and visible intensities and fluxes, available by anonymous ftp to kaja.gi.alaska.edu, cd pub/arve, 1995

Kylling, A., PHODIS, a program package for calculation of photodissociation rates in the Earth's atmosphere, available by anonymous ftp to ftp://kaja.gi.alaska.edu/pub/phodis/phodis.f, 1995

LeBras, G. and U. Platt. A possible mechanism for combined chlorine and bromine catalyzed destruction of tropospheric ozone in the arctic. Geophys. Res. Lett., Vol. 22, 599-602, 1995

Lehrer, E. , Polar tropospheric ozone loss. Ph. D. thesis, University of Heidelberg, 1999

Leue, C., M. Wenig, T. Wagner, U. Platt, and B. Jähne, Quntitative analysis of NOx emissions from GOME satellite image squences, J. Geophys. Res., 106, 5493-5505, 2001

Macke, A. and Mitchell, D. and von Bremen, L., Monte Carlo radiative transfer calculations for inhomogeneous mixed phase clouds, PCE, 24(3), 237-241, 1999

Mie, G., Beiträge zur Optik trüber Medien, speziell kolloidaler Metallösungen, Ann. Phys., 25,377-445, 1908

Levenberg, K., A method for the solution of certain non-linear problems in least squares, Quart. Appl. Math 2, 164-168, 1944

Magnotta, F. and H. S. Johnson, Photodissociation quantum yields for the NO3 free radical, Geophys. Res. Lett., 7, 769-772, 1980

Marquard, L.C., Modellierung des Strahlungstransports in der Erdatmosphäre für absorptionsspektroskopische Messungen im ultravioletten und sichtbaren Spektralbereich, PhD thesis, University of Heidelberg, 1998

Marquard, L.C., and U. Platt, AMFTRAN: A new Monte Carlo radiative transfer model for calculating air mass factors, Proceedings of the NATO Advanced Research Workshop, Athens, 1995

Marquardt, D. W., An algorithm for least-squares estimation of nonlinear parameters, J. Soc. Indust. Appl. Math. 11, 431-441, 1963

Meeus, J., Astronomische Algorithmen, Johann Ambrosius Barth Verlag, Heidelberg, 1992

Mobley C.D., "Light and water", Academic Press, 1994

Morgner, A. Ein objektorientiertes 3D-Monte-Carlo-Strahlungstransportmodell, diploma thesis, University of Heidelberg, 2000

Noxon, J.F., R. B. Norton, and W. R. Henderson, Observation of atmospheric NO3, Geophys. Res. Lett., 5, 675, 1978

Oltmans, S. J. and W. D. Komhyr, Surface ozone distributions and variations from 1973-1984 measurements at the NOAA Geophysical Monitoring for Climate Change baseline observatories. J. Geophys. Res., Vol. 91, 5229-5236, 1986

Otten, C., Messung stratosphÄarischer Spurenstoffe in den Wintern 1992/93 bis 1994/95 über Kiruna in Nordschweden. Ph. D. thesis, University of Heidelberg, 1997

Penndorf, R., Tables of the refractive index for standard air and the Rayleigh scattering coeffcient for the spectral region between 0.2 and 200 μm and their application to atmospheric optics. J.Opt. Soc. Am., Vol. 47, No. 2, 176-182, 1957

Perliski, L. M.,The Role of Multiple Scattering in Twilight Zenith Sky Observations of Atmospheric absorbers: Diurnal Photochemistry and Airmass Factors, PhD Boulder 1992

Perliski, L.M., and S. Solomon, On the evaluation of air mass factors for atmospheric near-ultraviolet and visible absorption spectroscopy, J. Geophys. Res., 98, 10363, 1993

Platt, U. and E. Lehrer, Arctic Tropospheric Ozone Chemistry, ARCTOC, Final Report of the EU-Project No. EV5V-CT93-0318, Heidelberg, 1996

Platt, U., Differential optical absorption spectroscopy, (DOAS), in air monitoring by spectroscopic techniques, M. W. Sigrist (Ed.), Chemical Analysis Vol. 127, John Wiley, New York, 1994

Pundt, I., Mapping of trace gas distributions from ground and aircraft by UV-Vis spectroscopy, AFO Newsletter, BMBF, 2003

Rasmussen, A., S. Kilisholm, J. H. Sörensen, and I. S. Mikkelsen, Analysis of tropospheric ozone measurements in Greenland. Tellus, Vol. 49B, No. 5, 510-521, 1997

Rodgers, C.D., Retrieval of atmospheric temperature and composition from remote measurements of thermal radiation, Reviews of Geophysics and Space Physics Vol. 14 No. 4, 609-624, 1976

Rodgers, C., Inverse Methods for Atmospheric Sounding, World Scientific, London, 2000

Roedel, W., Physik unserer Umwelt - Die Atmosphäre, Springer Verlag Heidelberg, 1991[2]

Sanghavi, S., The influence of aerosols on radiative transfer as calculated with a Monte Carlo RTM (working title), diploma thesis, University of Heidelberg, in prep., 2003

Scheirer, R. and Macke, A.,Influence of the gasous atmosphere on solar fluxes of inhomogeneous clouds, PCE, 25, 73-76, 2000

Schulte, M, DAMF V1.22 direct light airmass factors. Internal paper, University of Heidelberg, 1996

Smith, J.P., S. Solomon, Atmospheric NO3 3. Sunrise disappearance and the stratospheric Profile, J. Geophys. Res. 95, 13819-13827, 1990

Smith, J.P., S. Solomon, R.W. Sanders, H.L. Miller, L.M. Perliski, J.G. Keys and A.L. Schmeltekopf; Atmospheric NO3 4. Vertical profiles at middle and polar latitudes at sunrise, J. Geophys. Res. 98, 8983-8989, 1993

Solomon, S., A.L. Schmeltekopf, and R.W. Samnders, On the Interpretation of Zenith Sky Absorption Measurements, Journal of Geophys. Res.,7, 8311-8319, 1987

Solomon, S., H.L. Miller, J.P. Smith, R.W. Sanders, G.H. Mount, A.L. Schmeltekopf and J.F. Noxon; Atmospheric NO3 1. Measurement technique and the annual cycle at 40° N, J. Geophys. Res. 94, 11041-11048, 1989

Solomon, S., R. W. Portman, R. R. Garcia, W. Randel, F. Wu, R. Nagatani, J. Gleason, L. Thomason, L. R. Poole, and M. P. McCormick. Ozone depletion at midlatitudes: coupling of volcanic aerosols and temperature variability to anthropogenic chlorine. Geophys. Res. Lett., Vol. 25, 1871-1874, 1998

Staehelin, J., K. Schlapfer, T. Burgin, U. Steinemann, S. Schneider, D. Brunner, M. Baumle, M. Meier, C. Zahner, S. Keiser, W. Stahel, C. Keller: Emission factors from road traffic from a tunnel study (Gubristtunnel, Switzerland). Part I: concept and first results, Sci. Total Envir., 169, 141-147, 1995.

P. Stammes, P. (Editor), R. Noordhoek (Layout), OMI Algorithm Theoretical Basis
Document Volume III, Clouds, Aerosols, and Surface UV Irradiance, ATBD-OMI-03, Version 2.0, August 2002

Stroustrup, B., The C++ Programming Language, Addison Wesley, Reading[3], 1998

Stutz, J., and U. Platt, Numerical analysis and error estimation of Differential Optical Absorption Spectroscopy measurements least-squares methods, Appl. Optics, 35, 6041-6053, 1996

Thomas, G. E. and K. Stamnes, Radiative Transfer in the Atmosphere and Ocean, CUP, 1999

Trick, S., Das Bildungspotential Salpetriger Säure (HONO) an städtischen Oberflächen, exam thesis, University of Heidelberg, 1999

Unsöld, A. And B. Baschek, Der neue Kosmos, Springer, Heidelberg[6]

US Standard Atmosphere, NOAA-S/T76-1562, 1976

Velders, Guus J.M., Claire Granier, Robert W. Portmann, Klaus Pfeilsticker, Mark Wenig, Thomas Wagner, Ulrich Platt, Andreas Richter, and John P. Burrows, Global tropospheric NO2 column distributions: Comparing 3-D model calculations with GOME measurements, J. Geophys. Res., 106 , 12,643-12660, 2001

Vogel, B., F. Fiedler, H. Vogel, Influence of topography and biogenic volatile organic compounds emission in the state of Baden-Wuerttemberg on ozone concentrations during episodes of high air temperatures, J. Geophys. Res., 100, 22907-22928, 1995

Vogel, B., N. Riemer, H. Vogel, F. Fiedler, Findings on NOy as an indicator for ozone sensitivity based on different numerical simulations, J. Geophys. Res., 104, 3605-3620, 1999

Vogel, B., U. Corsmeier, H. Vogel, F. Fiedler, J. Kühlwein, R. Friedrich, A. Obermeier, J. Weppner, N. Kalthoff, D. Bäumer, A. Bitzer, K. Jay, Comparison of measured and calculated motorway emission data. Atmos. Environ., 34, 2437-2450, 2000

Vogt, R., P. J. Crutzen, and R. Sander, A mechanism for halogen release from sea-salt aerosol in the remote marine boundary layer. Nature, Vol. 383, 327-330, 1996

v. Friedeburg, Optimierung der NO3-Höhenprofilermittelung mittels Differentieller Streulichtspektroskopie, diploma thesis, University of Heidelberg, 1999

v. Friedeburg, C., T. Wagner, A. Geyer, N. Kaiser, B. Vogel, H. Vogel and U. Platt, Derivation of Tropospheric NO3 Profiles Using Off-axis-DOAS Measurements During Sunrise and Comparison with Simulations, JGR, 107, doi: 10.1029/2001JD000481, 2002

v. Friedeburg, C., A. Geyer, I. Pundt, B. Vogel, T. Wagner and U. Platt, Nitrate Radical Formation during the Solar Eclipse of 1999 over Southern Germany - Measurements and Retrieval Concepts, contribution to EGS 2001 assembly, Nice, 2001

Wayne, R. P., I. Barnes, P. Biggs, J. P. Burrows, C. E. Canosa-Mas, J. Hjorth, G. Le Bras, G. K. Moortgat, D. Perner, G. Poulet, G. Restelli und H. Sidebottom., The nitrate radical: physics, chemistry, and the atmosphere, Atmos. Environ. 25A, 1-203, 1991

Wagner, T., and U. Platt, Satellite mapping of enhanced BrO concentrations in the troposphere, Nature, 395, 486-490, 1999

Wagner, T., C. Otten, K. Pfeilsticker, I. Pundt, and U. Platt, DOAS moonlight observation of atmospheric NO3 in the Arctic winter, Geophys. Res. Lett., 27, 3441-3444, 2000

Wagner, T., C. v. Friedeburg, M. Wenig, and U. Platt, UV-visible observations of atmospheric O4 absorptions using direct moonlight and zenith-scattered sunlight. For clear-sky and cloudy sky conditions, Journal of Geophy. Res., 107, D20, 4424, 2002

Wagner, T., J. Heland, M. Zöger, and U. Platt, A fast H2O total column density product from GOME - validation with in-situ aircraft measurements, Atmos. Chem. Phys. Discuss., 3, 323-353, 2003

Wahner, A., T. F. Mentel, M. Sohn, J. Stier, Heterogeneous reaction of N2O5 on sodium nitrate aerosol, J. Geophys. Res., 103, 31103-31112, 1998

Weidner, F., H. Bösch, A. Butz, C. Camy-Peyret, M. Dorf, Ch. v. Friedeburg, R. Kumar, and K. Pfeilsticker, A New Lightweight Balloon-Borne DOAS Instrument For Stratospheric Trace Gas Study, EGS-AGU-EUG Joint Assembly, Nice, France 2003a

Weidner, F., H. Bösch, A. Butz, C. Camy-Peyret, M. Dorf, C. v. Friedeburg, Konstantin Gerlikowski, Wolfgang Gurlit, and K. Pfeilsticker, A New Balloonborne DOAS Instrument Analyzing Limb Scattered Radiation, International UV/Vis Limb Workshop, Bremen, 2003b

Weaver, A., S. Solomon, R. W. Sanders, K. Arpag and H. L. Miller Jr., Atmospheric NO3 5. Off-axis measurements at sunrise: Estimates of tropospheric NO3 at 40°N, J. Geophys. Res., 101, 18605-18612, 1996

Wehrli, C.; "Extraterrestrial Solar Spectrum"; WMO No. 615; July 1985
http://rredc.nrel.gov/solar/standards/am0/wehrli1985.html

Wenig. M., Wolkenklassifizierung mittels Bildsequenzanalyse auf GOME-Satellitendaten, diploma thesis, University of Heidelberg 1999

Wenig, M., Satellite Measurement of Long-Term Tropospheric Trace Gas Distributions and Source Strengths - Algorithm Development and Data Analysis, PhD-Thesis, University of Heidelberg, Germany, 2001

Yokelson, R.J., J.B. Burkholder, R.W. Fox, R.K. Talukdar and A.R. Ravinshakara; Temperature dependence of the NO3 absorption spectrum, J. Phys. Chem. 98, 13144-13150, 1994

Zimmerman, H., A. Weigert, Lexikon der Astronomie, Spektrum Akademischer Verlag, 1999

Acknowledgements

I wish to express my gratitude and my esteem to the colleagues, fellows and friends with the Air Chemistry Division of the Institute for Environmental Physics, IUP, of the Ruperto Carola.

Especially I wish to address my thank to:

My supervisor Prof. Dr. Platt for the freedom of research in a fascinating field
My Postdoc Thomas Wagner for the arduous assistance and fruitful discussions
My office fellows for their sense of humor

Birger Bohn for his repeated calibration, without which the spectro radiometer was only another spectrograph
Heike and Bernhard Vogel for their cooperation in our publication

My parents for their support
Friederike Eyssel for her accompaniment
Kirsten Pistel for her vast knowledge and patient help in my tasks at the University Council